André Filipe Ventura Cortez

NOVEL TECHNIQUES FOR HIGH PRESSURE NOBLE GAS RADIATION DETECTORS

Tese de doutoramento em Engenharia Física, ramo de Instrumentação, orientada pela Professora Doutora Filipa Isabel Gouveia de Melo Borges e pelo Professor Doutor Sérgio José Coelho do Carmo e apresentada ao Departamento de Física da Faculdade de Ciências e Tecnologia da Universidade de Coimbra

Maio de 2018

· U C ·

Universidade de Coimbra

University of Coimbra

PhD Thesis

Doctoral Programme in Engineering Physics (UC)

Novel Techniques for High Pressure Noble Gas Radiation Detectors

Author:
André Filipe Ventura Cortez
Supervisors:
Prof. Filipa Isabel Gouveia Melo Borges
(University of Coimbra)
Prof. Sérgio José Coelho do Carmo
(University of Coimbra)

2018

The research reported in this thesis was performed with financial support of the following institutions/programs:

- PhD scholarship number SFRH/BD/52333/2013 granted by the Fundação para a Ciência e Tecnologia.
- PhD programme number PD/274/2012 from Fundação para a Ciência e Tecnologia.
- Travelling grant for the participation at RD51 Collaboration from CERN/FP/116392/2010 granted by the Fundação para a Ciência e Tecnologia.
- RD51 Common Project 2014/2015 entitled "Measurement and calculation of ion mobility of some gas mixtures of interest" granted by RD51 Collaboration/CERN.

"Hier sitz' ich, forme Menschen
Nach meinem Bilde,
Ein Geschlecht, das mir gleich sei,
Zu leiden, zu weinen,
Zu genießen und zu freuen sich,
Und dein nicht zu achten,
Wie ich!"
(Goethe in "Prometheus")

Resumo

Esta tese apresenta os estudos realizados com o objectivo de desenvolver e testar um detetor gasoso do tipo contador gasoso de cintilação proporcional (CGCP) baseado em Xe a alta pressão (5-20 bar) com geometria cilíndrica para a detecção de raios-X duros e de radiação gama (100-662 keV), para utilização em ambientes hostis em que a robustez é um requisito, por exemplo em segurança nacional (detecção de transporte ilegal de material radioativo) ou em instrumentação para prospecção geológica. Apresenta também o estudo realizado relativamente às propriedades de transporte de iões em meios gasosos de interesse para detetores de grande volume.

Nos CGCPs, a detecção da radiação ionizante assenta na produção de fotões de cintilação como estágio de amplificação e sua posterior detecção com a ajuda de um fotosensor, geralmente um fotomultiplicador. Os CGCPs são constituídos por uma região de absorção/deriva onde a radiação ionizante é absorvida dando origem a uma nuvem de electrões primários que é guiada por um campo eléctrico baixo (abaixo do limiar de excitação do gás) em direcção à região de cintilação secundária onde, devido ao campo eléctrico mantido acima do limiar de excitação e abaixo do limiar de ionização do gás, são produzidos um elevado número de fotões de cintilação (fotões de VUV). Os fotões emitidos durante o processo de desexcitação dos átomos do meio irão atingir o fotosensor originando um sinal proporcional à energia da radiação incidente.

Convencionalmente, a geometria adoptada é a geometria planar por ser a que apresenta a melhor resolução em energia, mas devido à utilização de fotosensores o seu uso em ambiente de campo é limitada. Recentemente foi desenvolvido um protótipo com geometria planar, mais robusto, tendo em vista esse tipo de aplicações, uma vez que utiliza como fotosensor um depósito de iodeto de césio, sendo a carga originada no mesmo pela incidência de fotões VUV, e recolhida numa grelha colocada na sua proximidade. Contudo, este detector revelou algumas limitações: baixa eficiência de detecção para radiação de energia acima de 50 keV, baixo ângulo sólido e elevada tensão de polarização necessária, que condicionam o seu desempenho e a sua gama de aplicações.

Para resolver estas limitações foi desenvolvido um novo protótipo para detecção de radiação de energia mais elevada (100-662 keV), optando-se por uma geometria cilíndrica, que apresenta inúmeras vantagens. Por um lado, a configuração cilíndrica permite diminuir o número de grelhas metálicas utilizadas no anterior protótipo, reduzindo o impacto da transmissão óptica interna no ganho do detector, e melhora significativamente o ângulo sólido. Não menos importante é a melhoria que esta configuração permite ao nível da eficiência de detecção, já que nesta geometria a radiação é absorvida ao longo do eixo principal do detector. Também diminui significativamente a tensão de polarização quando comparado com a geometria planar.

Depois de um estudo preliminar, o detector foi projetado construído e montado, tendo sido feita a caracterização preliminar do mesmo, à qual se seguiu a verificação do seu desempenho com o recurso a uma fonte de partículas alfa de ^{241}Am, para pressões entre

1 a 3 bar. Numa primeira fase, foi feita a caracterização da fonte de ^{241}Am utilizada nos testes, à qual se seguiu o estudo da carga primária recolhida no ânodo, seguindo-se a caracterização do sinal de cintilação. Com este estudo foi possível verificar que aumentando o E/p para valores acima do limiar de ionização à superfície do ânodo e ligeiramente acima do limiar de excitação na região de recolha a resolução em energia do detector recolhendo o sinal na região de recolha poderia ser melhorada. Neste trabalho foram ainda estudados o ganho e a relação sinal-ruído (SNR) do detector. Em relação ao ganho, o comportamento observado era o o esperado teoricamente, sendo que nas melhores condições possíveis foi obtido um ganho de 1.9 a 1.05 bar o que nos dá boas perspectivas para alcançar ganhos na ordem de 30 para pressões de 15 bar. Já em relação à SNR, nas melhores condições possíveis, o sinal observado foi 10 vezes superior ao ruído, o que permitiu estimar a energia mínima detetável nestas condições de operação.

Em paralelo com o desenvolvimento deste novo detector, foi estudada a mobilidade de iões em diferentes misturas gasosas de interesse ou utilizadas em diversas experiências de grande relevância (ALICE TPC e TRD, CBM TRD, NEXT TPC e a futura LCTPC), uma vez que a informação sobre a mobilidade de iões é relevante não só para o desenho e modelação de detectores, mas também para a compreensão da formação dos impulsos gerados. Este trabalho foi desenvolvido no âmbito da nossa participação na colaboração NEXT e RD51 do CERN. A câmara de deriva de iões positivos utilizada nestes estudos, já existente no laboratório, permite determinar com precisão o tempo de deriva deste grupo de iões e consequentemente a sua velocidade de deriva e mobilidade. Determinada a mobilidade destes iões e utilizando a Lei de Blanc e o limite de polarização de Langevin é possível efectuar a sua identificação. No âmbito desta tese foram feitos estudos relativos a cinco misturas com interesse para as experiências mencionadas: Xe-N_2, Xe-CO_2, Xe-CF_4, Ar-C_2H_6 and Ar-CH_4.

Neste estudo foi também verificada a validade do limite de polarização de Langevin para a estimativa da mobilidade de iões, tendo-se concluído que as suas limitações estão relacionadas essencialmente com a fraca polarizabilidade dos átomos ou moléculas envolvidos como é o caso do Ne, ou pela presença de inúmeros graus de liberdade internos nas mesmas que são responsáveis por reduzir a mobilidade em cerca de 10% em casos como o do dióxido de carbono, CO_2. Esta informação torna-se especialmente relevante pois a introdução de correcções permite obter melhores estimativas para a mobilidade em casos onde não existem medidas experimentais.

Keywords: Detectores gasosos de alta pressão, contadores gasosos de cintilação proporcional, transporte e multiplicação de carga em gases, electroluminescência, mobilidade de iões.

Abstract

This thesis presents the studies conducted with the objective of developing a new and ruggedized Gas Proportional Scintillation Counter (GPSC) based on high-pressure Xe (5-20 bar) with a cylindrical geometry for the detection of hard X- and gamma-rays (100 keV to 662 keV). It is to be used in field applications, where robustness is a requirement, for example in homeland security (detection of illegal transport of radioactive material) or for geological prospection (instrumentation for boreholes). A study of the mobility of ions in gases used in large volume detectors is also presented.

In GPSCs, the detection of ionizing radiation is based on the production of scintillation photons as the amplification stage, followed by their detection with the help of a photosensor, typically a photomultiplier. GPSCs have an absorption/drift region where the ionizing radiation is absorbed, producing a cloud of primary electrons which is guided by a low electric field (kept below the excitation threshold of the gas) to the scintillation region, where the electric field is above the scintillation threshold but below the ionization threshold of the gas. In the scintillation region, they produce a large number of scintillation photons (vacuum ultra-violet photons), emitted during the deexcitation process of the gas atoms. These will eventually reach the photosensor, producing a signal proportional to the energy of the incident radiation.

Conventionally, the adopted geometry is planar, since it displays the best energy resolution, but because of the photosensors usually adopted, its use in field applications is limited. In a recent work, a prototype was developed with a planar geometry with the objective of being more ruggedized for field applications. The main difference consisted of the use of a deposited caesium iodide as the photosensor, with the photoelectrons produced by the VUV photons being collected at a grid close to the photocathode. However, this new detector displayed several limitations: low detection efficiency for high energy radiation (above 50 keV); small solid angle subtended by the photosensor; and the high bias voltage needed, which reduced its performance and its application scope.

So, to solve these limitations a new detector for higher energies (100-662 keV) was developed using a cylindrical geometry, which is expected to display several advantages. On one hand, the cylindrical configuration allows the number of metallic grids used to be decreased, thus reducing the impact of the internal optical transmission in the detector gain. In addition, the fact that the photocathode is deposited on the inner surface of the detector walls significantly increases the solid angle subtended by the photosensor, improving the gain. Also because the radiation is absorbed along the cylinder axis, the detecting efficiency is improved. Moreover, this configuration will, in principle, allow the bias voltage to be minimized for the same gain when compared with the planar geometry.

In this work, this new prototype was designed according to the initial performance requirements, constructed and assembled, followed by its characterization with the assessment of the prototype performance using an alpha particle source of ^{241}Am, varying the pressure from 1 up to 3 bar. In the initial stage, the characterization of the ^{241}Am

source was performed, followed by the study of the charge collection at the anode and the characterization of the scintillation signal.

In this study, it was possible to verify that increasing the E/p above the ionization threshold at the anode surface and slightly above the scintillation one in the collecting region, the energy resolution was improved. In addition, the gain and the signal-to-noise ratio (SNR) of the detector were also determined. Regarding the gain, the experimental values determined were in agreement with the theoretical ones, and at the best possible conditions we were able to reach a gain of 1.9 at 1.05 bar, which gives a good outlook for achieving gains of about 30 at 15 bar. As for the SNR, in the best possible conditions studied, the signal was 10 times greater than the noise, which allowed the minimum detectable energy to be estimated with the detector in the present operating conditions.

In parallel with the development of this new detector, the transport properties of ions were also studied to provide information on ion mobility for different gas mixtures used or considered for several major experiments (ALICE TPC and TRD, CBM TRD, NEXT and the future LCTPC), as the information of the mobility of ions in gases is relevant not only for the design and modelling of gaseous radiation detectors, but also in the understanding of the signal formation. This work was developed in the scope of our participation in the NEXT Collaboration and RD51 Collaboration from CERN. The ion drift chamber used in these studies, already available in our laboratory, allows the drift time of this group of ions to be determined with precision and consequently their drift velocity and mobility. Finally, knowing the mobility of these ions and using Blanc's law with the polarization limit of the Langevin's formula, it is possible to identify most of the collected ions. In the scope of this thesis, 5 gas mixtures of interest for the above-mentioned experiments were studied: Xe-N_2, Xe-CO_2, Xe-CF_4, Ar-C_2H_6 and Ar-CH_4.

Another interesting result coming from this work is related to the validity of the Langevin polarization formula used to predict the mobility of ions and whose limitations are related to the weak polarizability of some neutrals such as Ne, or by the numerous internal degrees of freedom, responsible for reducing the mobility in gases such as CO_2 by about 10%. An alternative method to the use of the Langevin polarization limit, when it fails, is proposed, which will allow a better estimate of the mobility to be obtained.

Keywords: high-pressure gas radiation detectors, gas proportional scintillation counters, charge transport and multiplication in gases, electroluminescence, ion mobility.

Acknowledgments

Since I was a child I've always loved a good story. I believed that stories, like dreams, help us to ennoble ourselves, to fix what is broken inside and to help us become the people we dreamed of being. This work, like those dreams helped me to become who I am today, a person that tries to understand the deeper truth that lies everywhere and that needs to be brought to light, in other words, what we call science. And as all in life, this work and this journey would not have been possible without so many that brought their knowledge and support to this work and that believed in me.

First of all I would like to express my sincere gratitude to my supervisors, Prof. Filipa Borges (UC) and Prof. Sérgio do Carmo (UC), for their guidance and support throughout this work. I would like to especially thank Prof. Filipa Borges for bringing me to LIP, and giving me the chance to work with her and with such an incredible and talented group of people. Thank you for entrusting me with important work and responsibilities. Thank you for all the knowledge and vision shared but, above all, for your high moral values and work ethic that make you an example. Prof. Sérgio do Carmo, I've never met someone so tremendously gifted, always generous, simple and ready to help. This work would not be possible without you.

I also want to express my gratitude to Prof. Carlos Conde (UC) whose availability and help, encouragement and guidance provided the basis for the development of the current work. Thank you for sharing with me your knowledge, advice and wisdom for which I am grateful.

To Prof. Filomena Santos, a special thank you for all the personal advice, patience, constant support and opportunities given. Thank you for providing me with that extra push to believe in myself and always give my best.

I would also thank Dr. Teresa Dias (LIP), Dr. José Escada (LIP/UC), Dr. Pedro Neves, Dr. Alberto Blanco (LIP), MSc. Alexandre Trindade, Dr. Rui Silva (UC), Dr. Jorge Maia (UBI), Prof. Custódio Loureiro (UC), Dr. João Cardoso (UC), Dr. Francisco Neves (LIP), Dr. Luis Margato (LIP), Dr. Luis P. Fernandes (GIAN), Dr. Filippo Resnati (CERN), Dr. Kiwamu Saito (KEK) and Dr. Esteban Santi (Univ. Nacional de Costa Rica) for their precious scientific knowledge that, each shared with me in his/her domain of expertise, for their availability and their important support to the project.

To the team of the LIP workshop and lab facilities, Nuno Dias, Carlos Oliveira, Douglas, MSc. Rui Alves, Luís Lopes, Américo Pereira, Nuno Carolino, Orlando Cunha, thanks for your precious help in the construction of the different components of the detector developed and for always being available to help.

To the GIAN group (UC) for helping with the CsI deposition process, in particular Prof. Joaquim dos Santos (UC), Dr. Fernando Amaro and MSc. Carlos Henriques.

To Prof. Rui Marques (UC) and Prof. Paulo Fonte (ISEC), who made it possible to join CERN (RD51 Collaboration), a dream and life goal that came true - something that I am truly grateful for and that I will never forget.

To Dr. Chilo Garabatos (GSI), Dr. Tapan Nayak (VECC), Dr. Paul Colas (CEA Saclay) and Dr. Jochen Kaminski (Univ. Bonn), thank you for entrusting me with important measurements and for believing in this work.

To Dr. Veenhof (CERN), my gratitude for his invaluable knowledge which he often shared with me, for our countless hours of discussion that, as I see, are responsible in part for the success and visibility that our work on ion mobility gained during the last years and that opened new opportunities for our group, both at CERN and ILC.

To Prof. Francisco Fraga (UC), Prof. Francisco Gil (UC) and Prof. Carlos Correia (UC) for awakening in me the interest for research as an undergraduate student. Thank you for sharing with me valuable lessons throughout my years at the Physics Department of the University of Coimbra. In particular to Prof. Francisco Fraga, whose mastery and knowledge shared gave me the motivation to challenge myself continuously.

To Dr. Ariella Catai (CERN), for the encouragement and kind words, for believing in my work and in me, and for providing me with the opportunities to learn with the best.

To Dr. David Nygren (Univ. Arlington) for the motivational words and for being the role model that you became to me. It was a pleasure and a great honour meeting you, a memory I will cherish forever.

I would also like to thank my Master's students, Pedro Encarnação, José Perdigoto and Miguel Santos, who gave me continuous challenges and with whom I've learned how to guide and teach, and to my colleagues Miguel Moita, João Marcos and Paulo Brás from LIP for their friendship.

Institutionally, I want thank all the elements that constitute the Coimbra pole of LIP and the Physics Department of the University of Coimbra, for providing the necessary conditions and infrastructures which were essential for the accomplishment of my goals.

This work would not be possible without DAEPHYS (Doctorate in Applied and Engineering Physics) and Fundação para a Ciência e Tecnologia for the Ph.D. scholarship SFRH\BD\52333\2013. I would also like to acknowledge the RD51 Collaboration for the "common project" approved on ion mobility.

This work is also dedicated to my long-time friends, whose strong support, presence and spirit gave this work a special meaning: Alberto Cortez, Vânia Rivero, Rui Toulson, Anderson Bulhões, Raquel Reis, Pedro Fonseca, Vítor Tomé, Bartolomeu Rodrigues, Ricardo Silva, Daniel Magalhães, Rui Martins, Pedro Cioga, Pedro Correia, Pedro Matrola, Marco Ribeiro, Danilo Jesus, Mário Ribeiro, Elson Simões, David Costa, João Borba and Alexandre Garcia. A special thank you to Pedro Correia and Pedro Vaz, for sharing the beginning of this incredible journey with me, for your friendship, support and motivation.

Finally, I want to thank Andreia Costa (my north star), my family and in particular my godmother Helena Rivero and my dear godson Rodrigo Toulson, my parents Emídio Cortez and Maria Lá-Salete Ventura and especially my brother, Alberto Cortez, for all the love, kindness, perseverance, belief, effort and unconditional support which made me the person I am today.

You are the ones who made this possible. Thank you for being part of the foundations of this work.

To all of you my eternal gratitude!

Yours faithfully,
André

Contents

List of Acronyms

AE Appearance Energy

ALICE A Large Ion Collider Experiment

CO carbon monoxide

CO_2 carbon dioxide

CSDA Continuous-Slowing-Down Approximation

CsI caesium iodide

EE Extraction Efficiency

EL Electroluminescence

EU European Union

FWHM Full Width at Half Maximum

GEANT4 GEometry ANd Tracking 4

GPSC Gas Proportional Scintillation Counter

H_2 hydrogen

H_2O water

HPXe High Pressure Xenon

HV High-Voltage

ILC International Linear Collider

KCl potassium chloride

Kr krypton

LAAPD Large Area Avalanche Photodiode

MGHP-GPSC Multi-Grid High Pressure Gas Proportional Scintillation Counter

N_2 nitrogen

NaCl sodium chloride

NEXT Neutrino Experiment with a Xenon TPC

NIM Nuclear Instruments Modules

PHENIX Pioneering High Energy Nuclear Interaction eXperiment

PMT Photomultiplier Tube

QE Quantum Efficiency

REE Relative Extraction Efficiency

SF Safety Factor

Si silicon

SRIM Stopping and Range of Ions in Matter

TMA trimethylamine - $(CH_3)_3N$

VUV Vacuum Ultra-Violet

List of Figures

List of Tables

Introduction

Wilhem C. Roentgen (1845-1923), discovered X-rays while working with a cathode ray tube in his laboratory. The radiation was named X-ray because it was unknown. In his discovery Roentgen found that the X-ray would pass through the tissue of humans leaving the bones and metals visible.

–

The University of Coimbra, an historical institution with 727 years of continuous activity has, since the 1960s, been highly recognized for the development of radiation detectors in its Physics Department with pioneering contributions from Prof. Carlos Conde and Prof. Armando Policarpo. That work gave rise to many internationally recognised innovative gas detectors [1]. Research in this area has brought about important developments which resulted in excellent know-how in the field of radiation detection, mainly focused on low-energy X-rays (up to few keV).

Moving to higher energies (hard X- and gamma-rays) raises some challenges. On one hand, we have the detecting efficiency which is dependent on several factors such as the atomic number of the medium and its density and, on the other hand, we have the appearance of additional processes competing with the photoelectric effect (favoured at lower energies) which may imply different detection efficiencies.

For this energy range, semiconductor detectors may be preferred, since they provide better energy resolutions than liquid and gaseous ones [2]. However, they also exhibit some important limitations, such as the detection area and efficiency, which deeply restricts their use. In addition, the need to be cooled down, associated with a much higher cost when compared to other detectors [3], constrains their use in higher energy events.

Considering liquid and gaseous detectors, both have a considerable advantage when compared to the solid state competitors in their customizable geometry (detection area and volume), making them more adaptable to the requirements of high-energy experiment. In terms of energy resolution, as seen before, it is difficult to compare them with solid state detectors, but in both cases the energy resolution can be improved by making use of an internal amplification stage, based either on charge or light multiplication (the latter also known as electroluminescence), allowing these detectors to compete cost-wise with solid-state detectors, even at lower energy.

As for liquid detectors, there are two important limitations: the need to be cooled down and the purity of the liquid, which has a major role in the amplification stage (probably

the main limitation); both affect the energy resolution. Although new techniques have been developed to overcome this last limitation, the problem is not completely solved [3]. Until recently, these limitations were overcome by the higher detection efficiency of these detectors. However, recent developments in high-pressure gas detectors have allowed them to become more competitive when compared with liquid counterparts.

Noble gas detectors display a wide range of unique characteristics that make them the preferred solution for the main applications. The advantages include: customizable detection area and active volume, lower detector cost and adjustable detection efficiency, together with an energy resolution that is usually comparable to that obtained with solid state detectors [4, 5] for some energy ranges.

Objectives and Motivation

The goal of this work is to develop an improved-performance High Pressure Xenon (HPXe) based radiation detector for hard X-ray and gamma-ray spectrometry by perfecting and upgrading a recently developed prototype of a Multi-Grid High Pressure Gas Proportional Scintillation Counter (MGHP-GPSC) [6], making it more ruggedized and cost attractive to be used in field applications such as homeland security (detection of nuclear terrorism, dirty bombs, illegal transport of radioactive material), but also in instrumentation for boreholes in geological prospection.

In addition to the development of the new detector, we intend to study the charge transport properties in gas mixtures, in particular the ion mobility, essential for modelling detectors and for understanding the pulse formation [4, 5, 7], especially in large volume detectors. The choice of the gas mixture for such detectors is determined by several parameters such as high electron/ion velocity and low electron diffusion, which are of key importance [5, 8]. In this work, the experimental results of ion mobility in several gases are presented and a discussion of the choice of gas mixtures, in the context of experiments such as the Neutrino Experiment with a Xenon TPC (NEXT) Experiment, A Large Ion Collider Experiment (ALICE) TPC, International Linear Collider (ILC) Experiment, and ALICE and CBM TRDs, is conducted based on its influence in the performance of these detectors.

Thesis Overview

This thesis is divided into 5 chapters:

- Chapter 1 - Scientific Background: In this chapter some concepts important for the different gaseous radiation detectors (ionization chambers, proportional ionization counters and proportional scintillation counters) are discussed. A short overview of the most important issues that are fundamental to this work such as the interaction of radiation with matter, ionization, transport phenomena and electroluminescence in gases is given, finishing the chapter with the introduction of the Gas Proportional Scintillation Counter (GPSC) working principle, together with the discription of the first prototype and its limitations.
- Chapter 2 - HPXe Gas Proportional Scintillation Counter: In this chapter, the design and characterization of the prototype developed is presented. This chapter introduces the different stages of development of the detector (design, assembly and test).
- Chapter 3 - Detector Performance: In this chapter, the preliminary studies using alpha particles are presented. The detector is characterized and its performance is assessed.
- Chapter 4 - Ion Mobility Measurement in Relevant Gases: The fourth chapter introduces the experiments that have been carried out on ion mobility as well as the results obtained for the different gas mixtures studied, discussing the advantages/implications of the choice of the gas mixtures in the several experiments where they are more commonly used, and a discussion concerning the validity of the Langevin limit.
- Chapter 5 - Conclusions and Future Work: The final remarks are presented in this chapter. The achievements and limitations of the studies and of the detector developed are discussed together with suggestions of how to explore and correct them. Finally, the possibilities for future work are presented.

Scientific Contributions

The scientific contributions resulting from the work of this thesis are summarized in tables 1, 2, 3 and 4.

Awards in the Scientific Communications

The awards received that are directly related to the work of this thesis are presented in table 5.

Table 1: Reference of scientific contributions - Part I.

#	International journal papers
1	A.F.V. Cortez, A.N.C. Garcia, P.N.B. Neves, F.P. Santos, F.I.G.M. Borges, J.A.S. Barata and C.A.N. Conde, *Experimental measurement of the mobility of ions originated in ethane in their parent gas*, *JINST* **8** (2013) P07013
2	A.F.V. Cortez, A.N.C. Garcia, P.N.B. Neves, F.P. Santos, F.I.G.M. Borges, J.A.S. Barata and C.A.N. Conde *Experimental measurements of the mobility of methane ions in Ar-C_2H_6*, *JINST* **8** (2013) P12012.
3	A.M.F. Trindade, A.F.V. Cortez, P.N.B. Neves, A.N.C. Garcia, J.Escada, F.P. Santos and C.A.N. Conde *Experimental study on ion mobility in Ar-CH_4 mixtures*, *JINST* **9** (2014) P06003.
4	A.N.C. Garcia, P.N.B. Neves, A.M.F. Trindade, A.F.V. Cortez, F.P. Santos and C.A.N. Conde *Experimental measurements of the mobility of Xenon- Neon ions mixtures*, *JINST* **9** (2014) P07008.
5	P.M.C.C. Encarnação, A.F.V. Cortez, M.G.A. Pinto, P.N.B. Neves, A.M.F. Trindade, J. Escada, F.P. Santos, F.I.G.M. Borges, J.A.S. Barata and C.A.N. Conde *Experimental Ion Mobility measurements in Ar-CO_2 mixtures*, *JINST* **10** (2015) P01010.
6	Y. Kalkan, M. Arslandok, A.F.V. Cortez, Y. Kaya, I. Tapan and R. Veenhof, *Cluster ions in gas-based detectors*, *JINST* **10**, (2015) P07004.
7	P.M.C.C. Encarnação, A.F.V. Cortez, R. Veenhof, P.N.B. Neves, F.P. Santos, A.M.F. Trindade, F.I.G.M. Borges and C.A.N. Conde *Experimental Ion Mobility measurements in Ne-CO_2 and CO_2-N_2 mixtures*, *JINST* **11** (2016) P05005.
8	A.F.V. Cortez, P.M.C.C. Encarnação, R. Veenhof, P.N.B. Neves, F.P. Santos, F.I.G.M. Borges and C.A.N. Conde *Experimental Ion Mobility measurements in Ne-N_2*, *JINST* **11** (2016) P11019.
9	A.F.V. Cortez, M.A.G. Santos, R. Veenhof, R.N. Patra, P.N.B. Neves, F.P. Santos, F.I.G.M. Borges and C.A.N. Conde *Experimental ion mobility measurements in Xe-CO_2*, *JINST* **12** (2017) P06012.
10	A.M.F. Trindade, J. Escada, P.M.C.C. Encarnação, A.F.V. Cortez, P.N.B. Neves, C.A.N. Conde, F.I.G.M. Borges and F.P. Santos *Experimental ion mobility measurements in xenon-trimethylamine*, *JINST* **12** (2017) P07007.
11	J.M.C. Perdigoto, A.F.V. Cortez,R. Veenhof, P.N.B. Neves, F.P. Santos, F.I.G.M. Borges and C.A.N. Conde *Experimental ion mobility measurements in Xe-CH_4*, *JINST* **12** (2017) P09003.
12	J.M.C. Perdigoto, A.F.V. Cortez, R. Veenhof, P.N.B. Neves, F.P. Santos, F.I.G.M. Borges and C.A.N. Conde *Experimental ion mobility measurements in Xe-C_2H_6*, *JINST* **12** (2017) P10011.
13	A.F.V. Cortez, M.A. Kaja, J. Escada, M.A.G. Santos, R. Veenhof, P.N.B. Neves, F.P. Santos, F.I.G.M. Borges and C.A.N. Conde *Experimental ion mobility measurements in Xe-CF_4*, *JINST* **13** (2018) P04006.
14	M.A.G. Santos, M.A. Kaja, A.F.V. Cortez, R. Veenhof, P.N.B. Neves, F.P. Santos, F.I.G.M. Borges and C.A.N. Conde *Experimental ion mobility measurements for the LCTPC Collaboration - Ar-CF_4*, *JINST* **13** (2018) P04012.

Table 2: Reference of scientific contributions - Part II.

#	International conference proceedings papers
1	A.F.V. Cortez, K. Saito, C.A.N. Conde, S.J.C. do Carmo, F.I.G.M. Borges, *New Developments in Gas Detectors - The Multi-Grid High-Pressure Gas Proportional Scintillation Counter*, *JPS Conf. Proc.* **11**, 020006 (2016).
2	A.F.V. Cortez, C.A.N. Conde, S.J.C. do Carmo, F.I.G.M. Borges, *Dual-Stage Gas Proportional Scintillation Counter - Concept and Experimental Results*, Submitted to *JPS Conf. Proc.* in April 2018.
#	Oral Communications in Scientific Meetings & Conferences
1	A.F.V. Cortez *et al.*, *Ion mobility measurement*, 13th RD51 Collaboration Meeting, 2-5 February 2014, CERN, Switzerland.
2	A.F.V. Cortez *et al.*, *Ion mobility measurement in gases*, Café com Física (Dep. Física / Univ. de Coimbra), 26th of March 2014, Coimbra, Portugal.
3	A.F.V. Cortez *et al.*, *Ion mobility measurement in Ar-CO_2 mixtures*, RD51 Collaboration Mini-week, 16-19 June 2014, CERN, Switzerland.
4	A.F.V. Cortez, F.I.G.M. Borges, S.J.C. do Carmo, C.A.N. Conde, *Novel Techniques for Gaseous Radiation Detectors*, 1st Doctoral Congress in Engineering - Symposium on Physics Engineering, 11-12 June 2015 – DCE 2015, Porto, Portugal.
5	P.M.C.C. Encarnação, A.F.V. Cortez, Y. Kalkan, R.Veenhof, F.I.G.M. Borges, F.P. Santos, P.N.B. Neves, C.A.N. Conde, *Ion transport in CO_2-N2 mixtures*, RD51 Collaboration Meeting, 16-17 October 2015, Trieste, Italy.
6	Y. Kalkan, A.F.V. Cortez, P.M.C.C. Encarnação, R. Veenhof, *Diffusion of ions in gas medium*, 4th International Conference on Micro Pattern Gaseous Detectors, 12-15 October 2015 – MPGD 2015, Trieste, Italy.
7	P.M.C.C. Encarnação, A.F.V. Cortez, Y. Kalkan, C. Garabatos, R. Veenhof, F.I.G.M. Borges, F.P. Santos, C.A.N. Conde, *Ion transport in CO_2-N_2 mixtures*, RD51 Collaboration Mini-week, 7-9 December 2015, CERN, Switzerland.
8	A.F.V. Cortez, P.M.C.C. Encarnação, A.M.F. Trindade, J. Escada, P.N.B. Neves, C.A.N. Conde, F.P. Santos, *Xe-TMA update*, RD51 Collaboration Mini-week, 7-9 December 2015, CERN, Switzerland.
9	P.M.C.C. Encarnação, A.F.V. Cortez, R. Veenhof, F.I.G.M. Borges, F.P. Santos, C.A.N. Conde, *Ion transport in in Nitrogen based mixtures*, RD51 Collaboration Mini-week, 8-11 March 2016, CERN, Switzerland.
10	F.C. Rolo, F.I.G.M. Borges, K. Saito, A.F.V. Cortez, C.A.N. Conde, *Dependence on the incident angle and pressure of the Relative Extraction Efficiency of photoelectrons from CsI photocathode*, RD51 Collaboration Mini-week, 8-11 March 2016, CERN, Switzerland.
11	A.F.V. Cortez , P.M.C.C. Encarnação, R. Veenhof, P.N.B. Neves, F.P. Santos, F.I.G.M. Borges and C.A.N. Conde, *Ion mobility measurements in gas mixtures*, XIth International Conference on Ion Implantation and Other Applications of Ions and Electrons, 13-16 June 2016 – ION 2016, Kazimierz Dolny, Poland.

Table 3: Reference of scientific contributions - Part III.

#	Oral Communications in Scientific Meetings & Conferences
12	A.M.F. Trindade, J. Escada, A.F.V. Cortez, F.I.G.M. Borges and F.P. Santos, *Xenon VUV scintillation wavelength shift by trimethylamine*, IEEE Nuclear Science Symposium, 29 October – 6 November 2016 – 2016 NSS, Strasbourg, France.
13	J.M.C. Perdigoto, A.F.V. Cortez, M.A.G. Santos, R. Veenhof, R. Patra, F.P. Santos, F.I.G.M. Borges and C.A.N. Conde, *Ion mobility in Xe-CO_2 mixtures: recent results*, RD51 Collaboration Mini-week, 20-23 February 2017, CERN, Switzerland.
14	J.M.C. Perdigoto, A.F.V. Cortez, F.P. Santos, F.I.G.M. Borges and C.A.N. Conde, *Influence of Additive Gases on the Ion Transport Properties in Xenon*, 2nd Doctoral Congress in Engineering - Symposium on Physics Engineering – DCE 2017, 8-9 June 2017, Porto, Portugal.
15	A.F.V. Cortez, M.A.G. Santos, M.A. Kaja, F.P. Santos, F.I.G.M. Borges and C.A.N. Conde, *Ion mobility in Ar-CF_4*, LCTPC Collaboration Meeting, 29 November - 1 December 2017, Hamburg, Germany.
16	M.A.G. Santos, A.F.V. Cortez, M.A. Kaja, F.P. Santos, F.I.G.M. Borges and C.A.N. Conde, *Ion mobility for the ILC experiment*, RD51 Collaboration Mini-week, 11-15 December 2017, CERN, Switzerland.
17	A.F.V. Cortez, C.A.N. Conde, S.J.C. do Carmo, F.I.G.M. Borges, *Dual-Stage Gas Proportional Scintillation Counter - Concept and Experimental Results*, International Symposium on Radiation Detectors and Their Uses - ISRD2018, 23-26 January 2018, Tsukuba, Japan.
18	M.A.G. Santos, A.F.V. Cortez, M.A. Kaja, F.P. Santos, F.I.G.M. Borges and C.A.N. Conde, *Alternative gas mixtures for LCTPC: Ar-CF_4-C_2H_6*, RD51 Collaboration Mini-week, 19-22 February 2018, CERN, Switzerland.
19	A.F.V. Cortez, C.A.N. Conde, S.J.C. do Carmo, F.I.G.M. Borges, *Dual-Stage Gas Proportional Scintillation Counter - Concept and Experimental Results*, Frontier Detectors for Frontier Physics - 14th Pisa Meeting on Advanced Detectors, 27 May to 2 June 2018, La Biodola, Isola d'Elba, Italy.
#	Poster Communications in Scientific Meetings & Conferences
1	A.F.V. Cortez, S.J.C. do Carmo, F.I.G.M. Borges, *Novel Techniques for Gaseous Radiation Detectors*, CERN Danube School on Instrumentation in Elementary Physics & Nuclear Physics, 8-13 September 2014, Novi Sad, Serbia.
2	P.M.C.C. Encarnação, A.F.V. Cortez, F.I.G.M. Borges, F.P. Santos, P.N.B. Neves, C.A.N. Conde, *Experimental ion mobility measurements in Ar-CO_2 and Ne-CO_2 mixtures*, 1st Doctoral Congress in Engineering - Symposium on Physics Engineering – DCE 2015, 11-12 June 2015, Porto, Portugal.
3	A.F.V. Cortez, F.I.G.M. Borges, S.J.C. do Carmo, C.A.N. Conde, *Multi-Grid High-Pressure Gas Proportional Scintillation Counter – A New Approach*, 3rd International Summer School on Intelligent Signal Processing for FrontIEr Research and Industry – INFIERI 2015, 14-25 September 2015, Hamburg, Germany.

Table 4: Reference of scientific contributions - Part IV.

#	Poster Communications in Scientific Meetings & Conferences
4	A.F.V. Cortez, F.I.G.M. Borges, S.J.C. do Carmo, C.A.N. Conde, *High-Pressure Xenon based Detectors for Gamma-ray Spectrometry – A New Approach*, Excellence in Detectors and Instrumentation Technologies – EDIT 2015, 20-29 October 2015, Frascati, Italy.
5	A.F.V. Cortez, K. Saito, C.A.N. Conde, S.J.C. do Carmo, F.I.G.M. Borges, *New Developments in Gas Detectors - The Multi-Grid High-Pressure Gas Proportional Scintillation Counter*, International Symposium on Radiation Detectors and Their Uses, 18-21 January 2016 – ISRD 2016, KEK Tsukuba, Japan.
6	P.M.C.C. Encarnação, A.F.V. Cortez, P.N.B. Neves, F.P. Santos, F.I.G.M. Borges and C.A.N. Conde, *Experimental Ion Mobility Measurements in Nitrogen Based Mixtures*, IEEE Nuclear Science Symposium, 29 October – 6 November 2016 – 2016 NSS, Strasbourg, France.
7	F. Rolo, K. Saito, A.F.V. Cortez, F.P. Santos, C.A.N. Conde and F.I.G.M. Borges, *Quantum Efficiency Dependence of a CsI Photocathode with Photon Incidence Angle*, IEEE Nuclear Science Symposium, 29 October – 6 November 2016 – 2016 NSS, Strasbourg, France.
8	A.F.V. Cortez, C.A.N. Conde, S.J.C. do Carmo, F.I.G.M. Borges, *Multi-Grid HPXe Gas Proportional Scintillation Counter - New Developments*, 2nd Doctoral Congress in Engineering - Symposium on Physics Engineering – DCE 2017, 8-9 June 2017, Porto, Portugal.
9	A.F.V. Cortez, C.A.N. Conde, S.J.C. do Carmo, F.I.G.M. Borges, *New Developments in Gas Detectors: Dual-Stage Gas Proportional Scintillation Counter*, European School of High Energy Physics (CERN/JINR) - ESHEP 2017, 6-19 September 2017, Évora, Portugal.
10	A.F.V. Cortez, M.A.G. Santos, R. Veenhof, P.N.B. Neves, F.I.G.M. Borges and C.A.N. Conde, *Experimental ion mobility measurements for the LCTPC Collaboration*, Frontier Detectors for Frontier Physics - 14th Pisa Meeting on Advanced Detectors, 27 May to 2 June 2018, La Biodola, Isola d'Elba, Italy.

Table 5: Awards received for the scientific contributions.

#	Award	Scientific Meeting & Conference
1	Best Poster Award	CERN Danube School on Instrumentation in Elementary Physics & Nuclear Physics, Novi Sad (Serbia).
2	Best Poster Award	Excellence in Detectors and Instrumentation Technologies – EDIT 2015, Frascati (Italy).
3	Young Scientist Contest 2nd place	XIth International Conference on Ion Implantation and Other Applications of Ions and Electrons - ION 2016, Kazimierz Dolny (Poland).
4	Young Scientist Grant	Frontier Detectors for Frontier Physics - 14th Pisa Meeting on Advanced Detectors, Isola d'Elba (Italy).

1

Scientific Background

Heinrich Hertz (1857-1894) was the first to observe that electrodes illuminated with ultraviolet light created electric sparks. This observation lead to the interpretation of the photoelectric effect years later by Albert Einstein for which he received the Nobel Prize in Physics in 1921.

–

1.1 Interaction of Radiation with Matter

The operation of X- and gamma-ray radiation detectors is based on the interaction of the radiation within the detecting medium. The interaction of the radiation within the detection medium can occur through either elastic or inelastic processes.

The interaction of radiation with matter, relevant for this work, is essentially made through three different inelastic processes: *photoeletric absorption*, *Compton scattering* and *pair production* [7, 9]. The relevance of such interaction mechanisms is a function of the photon energy, depending also on the atomic number (Z) of the detecting medium as depicted in figure 1.1.

1.1.1 Photoectric Effect

In the photoelectric process, a photon is absorbed by an atom of the medium and an atomic electron is ejected. Due to the large mass of the recoiling ion when compared to that of the photoelectron, most of the photon energy is transferred as kinetic energy to the photoelectron (E_e), being related to the energy of the incident photon ($h\nu$) by:

$$E_e = h\nu - E_b \tag{1.1}$$

where ν is the photon frequency, h the Planck constant and E_b the binding energy of the photoelectron in its original shell [7].

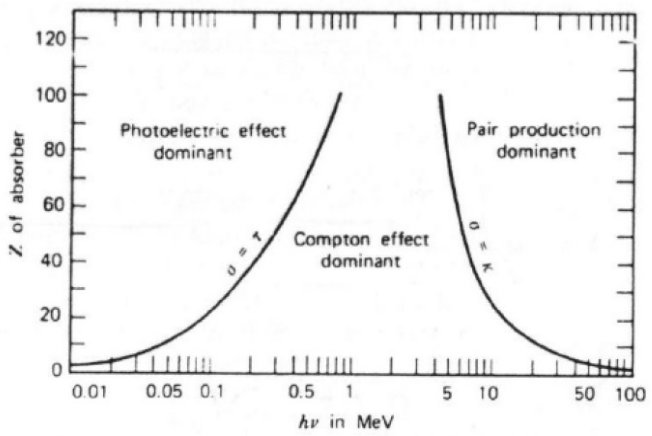

Figure 1.1: Relevance of the different interaction mechanisms as a function of the photon energy and atomic number (Z) of the detecting medium [7].

There is no exact analytical expression for the probability of photon interaction through photoelectric effect for the possible ranges of $h\nu$ and Z but it is known to be roughly proportional to $\frac{Z^n}{(h\nu)^{3.5}}$, with n varying between 4 and 5 over the photon energy range of interest. This relationship shows that the photoelectric effect is more probable for low-energy photons and high-Z materials, which makes it the predominant mode of interaction for X and γ-rays of relatively low energy [7].

1.1.2 Compton Scattering

The Compton effect accounts for the scattering of an incident hard X-ray or gamma-ray photon through collision with an electron of the absorbing material. In Compton scattering, the incoming photon is deflected through a certain angle with respect to its original direction, carrying only part of its initial energy and transferring the remaining to the recoil electron (assumed to be initially at rest) that carries away the kinetic energy and linear momentum lost by the photon in the interaction. Because all angles of scattering are possible, the energy transferred to the electron can vary from zero to a large fraction of the initial photon energy. The probability of Compton scattering per atom of the absorber depends on the number of electrons available as scattering targets and is therefore a function of Z. The angular distribution of scattered photons is predicted by the Klein-Nishina formula for the differential scattering cross-section ($d\sigma/d\Omega$) per free electron [7].

1.1.3 Pair Production

Another interaction process through which gamma-rays can interact with matter is pair production. The pair production process is only possible if the gamma-ray energy exceeds the rest-mass energy of an electron-positron pair (*i.e.* 1.022 MeV). The probability of interaction remains low until the gamma-ray energy approaches several MeV and therefore

pair production is predominantly confined to high-energy gamma rays. In the interaction (which must take place in the coulomb field of a nucleus), the gamma-ray photon disappears and gives rise to an electron-positron pair. All the photon energy above 1.022 MeV goes into kinetic energy shared by the positron and electron. Because the positron will rapidly annihilate in the absorbing medium, two annihilation photons are normally produced as secondary products of the pair production interaction. There is no simple expression for the probability of pair production but its magnitude varies approximately with Z^2. As seen from the example in figure 1.1, the probability of pair-production interaction rises sharply with the gamma-ray energy, becoming the dominant interaction mechanism for gamma-rays with energies above several MeV [7].

1.1.4 The Fundamental Law of Attenuation

As seen before, the relative importance of the processes described depends on the energy of the incident photons and on the absorber material. If we now look at the probability of interaction of a single photon, it is the result of the sum of these probabilities and can be expressed as follows:

$$\sigma_{total} = \sigma_{photoelectric} + \sigma_{Compton} + \sigma_{pair} \tag{1.2}$$

where σ_{total} is the total cross-section, $\sigma_{photoelectric}$ is the cross section for the photoelectric interaction, $\sigma_{Compton}$ is the cross section for the Compton scattering and σ_{pair} is the cross section for the pair production [7]. The linear attenuation coefficient $\mu_l{=}n\sigma$ can be defined for a certain material density, where n is the number of atoms per unit of volume.

As a result of these mechanisms, the incident radiation intensity (I_0) will be attenuated and the intensity of the radiation transmitted (I) by a given absorber of thickness L can be found using the law of attenuation.

$$I = I_0 e^{-\mu_l L} \tag{1.3}$$

where the linear attenuation coefficient (μ_l) is expressed in cm^{-1}. The transmission (I/I_0) depends on the energy and respective total cross section of the incident radiation as well as on the atomic number (Z) and density (ρ) of the absorbing material [7]. The reciprocal of the attenuation coefficient $1/\mu_l$ has units of length and is often called mean free path [7].

Since the linear attenuation coefficient is not usually tabulated because of its dependence on the density of the absorbing material, it is common to use the mass attenuation coefficient, which is independent of the density. The mass attenuation coefficient (μ) corresponds to the ratio of the linear attenuation coefficient to the density (μ_l/ρ) and has dimensions of area per unit mass (cm^2/g) [7]. The units of this coefficient indicate its meaning, which could be considered as an effective cross-sectional area of atoms per unit mass of absorber [7].

1.2 Primary electron cloud

As a consequence of the interaction processes referred to, the resulting energetic electrons and subsequent ones arising from the decay of the ions formed will further ionize and excite atoms or molecules of the medium, until all electrons are thermalized. This resultant primary electron cloud is the basis of the detector's signal since it contains information on the energy of the incident ionizing radiation [4, 5, 7, 9].

1.2.1 Mechanisms of primary charge formation

In fact, the ion arising from the interaction of the ionizing radiation/particle with the medium will decay to the fundamental state through a cascade process with the emission of more electrons - by Auger, Coster-Kronig and shake-off processes, and of fluorescence photons. These processes are represented in figure 1.2.

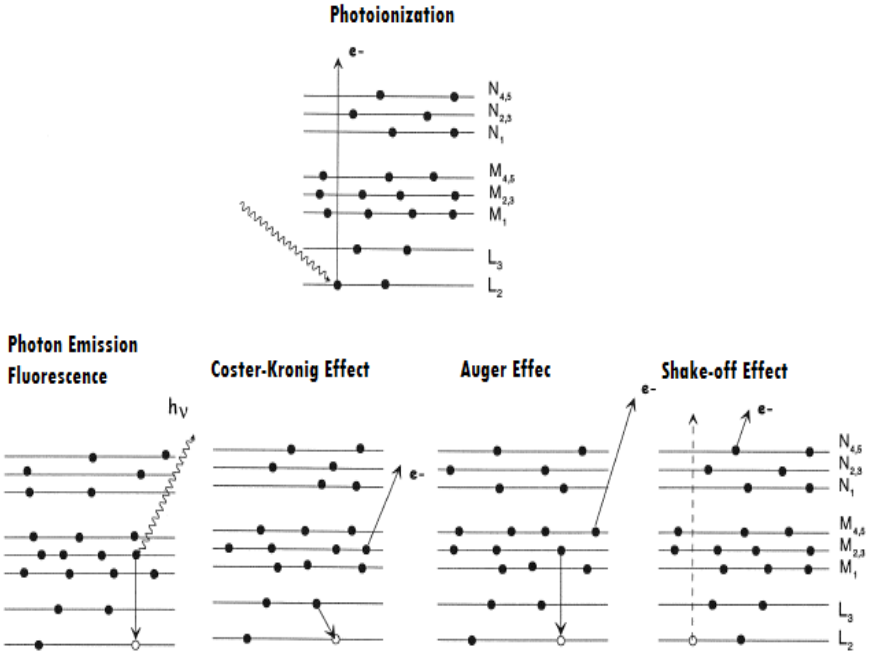

Figure 1.2: Photoionization processes of a gas atom and decay of the resulting ion by fluorescence radiation emission, or through electron emission of electrons by Auger, Coster-Kronig and shake-off effect. Adapted from [10, 11].

After the cascade process, the resulting ion will remain in the fundamental state with a multiple charge, X^{q+}. Additional electrons can be produced through other processes, namely by ionization transfer, between X^{q+} and a neutral [12–14]:

$$X^{q+} + X \rightarrow X^{(q-k)+} + X^{i+} + (i-k)e^{-} \tag{1.4}$$

with a probability that increases with the charge, q.

These electrons may have sufficient energy to further ionize or excite other gas atoms, leading to the formation of further electrons and ions and excited atoms (excimers). These excimers can decay by two processes: through the emission of a photon or by colliding with a neutral atom, giving rise to additional electron-ion pairs through the processes of associative ionization (equation 1.5) or Hornbeck-Molnar (equation 1.6) [15, 16].

$$X^{**} + Y \rightarrow XY^{+} + e^{-} \tag{1.5}$$

$$X + X^{**} \rightarrow X_2^{+} + e^{-} \tag{1.6}$$

Also, fluorescence photons emitted during the decay process may still be able to photoionize atoms of the medium, producing more photoelectrons and ions through the mechanisms already mentioned. The primary electron cloud is completed only when the energy of all these electrons is below the excitation potential of the gas atoms, and the ions have no possibility of extra electron production.

1.2.2 Mean number of ion pairs produced - The w-value and Fano factor

As already mentioned, the detector signal depends on the number of electron-ion pairs created, which is, in principle, proportional to the energy of the incident radiation or charged particle absorbed within the detector. Since the processes involved in the primary electron cloud formation are stochastic, it is usual to refer to mean values and associated fluctuations.

The mean ionization yield is expressed in terms of the w-value, the mean energy required to form an electron-ion pair, and can be defined as:

$$w = \frac{E_{ir}}{\bar{n}} \tag{1.7}$$

where E_{ir} is the energy of the incident radiation and $\bar{n}$ is the mean number of primary electrons produced by an ionization radiation when absorbed in the gas [7]. The w-value depends on the medium and on the energy and type of incident ionizing radiation. In a low-energy region, below few tens of keV, the w-value consistently decreases with the increasing radiation/particle energy, however at well defined energies (atomic absorption edges) this value increases abruptly, resulting in nonlinear effects. Nevertheless, at high energies (well above the atomic binding energy), it reaches an approximately constant value.

The number of ion pairs formed by each incident particle of a given energy has some intrinsic fluctuations related to the variety of possible paths that lead to the formation of the primary electron cloud.

Since the physical processes involved in the primary electron production are correlated, the variance σ^2, associated with $\bar{n}$, is smaller than that expected from pure Poisson

statistics (for which $\sigma^2{=}\bar{n}$) by a factor F, the so-called Fano factor, *i.e.* $\sigma^2{=}F\bar{n}$ [7].

$$F = \frac{\text{observed variance in } \bar{n}}{\text{Poisson predicted variance}} < 1 \tag{1.8}$$

The Fano factor depends on the gas and the energy of radiation and becomes approximately constant for energies above the energy of the atomic levels. At high incident energies the value of the Fano factor is constant, around 0.17 in noble gases [17], and between 0.2 and 0.4 in molecular gases.

1.3 Transport of Charged Particles in Gases

After the energy is deposited in the detector medium and converted into electrons, if an external electric field, E, is applied to this region, the electrostatic forces tend to move the charged particles (electrons and ions) away from their point of origin [7]. Electrons and ions are pulled in opposite directions [7], with their velocity resulting from the superposition of a random thermal motion and a component in the direction defined by the electric field.

The drift of these charges is characterized by a mean free path λ, and the correspondent time interval is the mean time between collisions, τ [18]. The mean free path, λ, can be expressed as follows:

$$\lambda = \frac{1}{\sigma N} \tag{1.9}$$

where N is the gas number density that corresponds to the stationary target particles per unit volume and σ is the elastic scattering cross section [18].

By simply dividing the mean free path by the average velocity, $\bar{v}$ of the incident particle and assuming that the target particle to be at rest, it is possible to calculate the time between collisions τ.

$$\tau = \frac{\lambda}{\bar{v}} \tag{1.10}$$

or alternatively,

$$\tau = \frac{1}{\bar{v}\sigma N} \tag{1.11}$$

In addition, if the energy of these primary electrons and ions is below the excitation threshold, using classic mechanics we are able to calculate the average energy lost in elastic collisions by both electrons and ions with neutrals. In this case ΔE can be expressed as follows:

$$\Delta E = \frac{2mM}{(m+M)^2} E_i \tag{1.12}$$

where m is the incident mass (electron or ion), M is the mass of the atom/molecule of the medium with which the incident particle collides and E_i is the energy of the incident particle. If we now consider the example of pure Xe ($M{=}131.293$ u) and the electron mass ($m_e{=}5.4858{\times}10^{-4}$ u) we are able to find that an electron colliding with a Xe atom loses, in average, a very small fraction of its initial energy, about $8.4{\times}10^{-6}$. If instead of an electron we consider an ion, for example Xe_2^+ ($M{=}262.586$ u), the mean energy lost per

collision is about 0.44 of the initial energy.

If we now consider the electrons and ions moving under the influence the electric field, after a certain number of mean free paths or collisions with the gas atoms/molecules, these will reach a steady state, when the average rate of the energy gained (due to the electric field) equals the average rate of the energy lost (in collisions).

1.3.1 Drift parameters

The drift of these charge carriers (electrons and ions) in a certain medium is characterized by macroscopic physical quantities, called drift or transport parameters, such as: the drift velocity, v_{d}, mobility, $K{=}v_{\mathrm{d}}/E$, average energy, ε_m, transverse diffusion coefficient, D_T (in the plane perpendicular to the electric field) and longitudinal diffusion coefficient, D_L (in the direction of the electric field), and characteristic energies ε_{kT} and ε_{kL}.

To compare the drift parameters for different gases, it is sometimes useful to represent the electric field, E, reduced to the gas pressure, p, the reduced electric field E/p (in units of V·cm^{-1}·Torr^{-1} or V·cm^{-1}·bar^{-1}). The E/p can be written in terms of E/N (in units of Td or "Townsend" where 1 Td is approximately 10^{-17} V·cm^2), where N is the gas density. Still, a conversion relation can be defined as follows:

$$\frac{E}{N} = (1.0354 \times T \times 10^{-2})\left(\frac{E}{p}\right) \tag{1.13}$$

where T is the temperature in K. In this case E/p has units of V·cm^{-1}·Torr^{-1}.

In this work it is also important to make a distinction between two limiting cases - low and high electric fields.

For sufficiently low E, the effect of the loss in collisions prevails over the gain due to the electric field and the charge carriers attain thermal equilibrium with the gas and the drift parameters become dependent on the gas temperature, T. Under these circumstances, the average energy of the charge carriers, ε_m, is equal to the thermal energy of the gas ($\varepsilon_m{=}3/2k_BT$, where k_B is the Boltzmann constant) and as a result the macroscopic diffusion is isotropic ($D_T{=}D_L$), the characteristic energies reach the thermal limit ($\varepsilon_{kT}{=}\varepsilon_{kL}{=}k_BT$), and the reduced mobility $K_0{=}KN_0/N$ becomes independent of the reduced electric field (E/N), while the drift velocity depends linearly on E/N.

For higher E values, the effect of the electric field becomes dominant, breaking the thermal equilibrium and the dependence on the gas temperature. So, for a specific E value, it is possible to verify that both average energy (ε_m) and the characteristic energies (ε_{kT} and ε_{kL}) increase with E, and as a result the macroscopic diffusion becomes anisotropic ($D_L{\neq}D_T$). The behaviour of these parameters with E is essential to characterize the detecting medium, which is closely related to the diffusion processes of the charges involved and the respective cross sections.

For electrons, the drift velocity depends on the frequency of collisions between the electron and the gas atom/molecule, *i.e.*, on the collision cross-section, the gas pressure

and temperature and also on the magnitude of the electric field, or more accurately on E/N [19].

1.3.2 Charge transfer and recombination

During the drift and diffusion process the electrons and ions can participate in different processes that can affect the signal and performance of detectors.

One of these processes is recombination, which can take place if the electrons produced are thermalized very close (within Onsager radius) to their parent ions. This can be avoided or minimized by increasing the applied electric field, so that electrons and ions are separated more efficiently [2]. In this case, the frequency of the collisions leading to recombination is proportional to both concentrations of negative charged particles, n^-, and positive charged particles, n^+, where the constant of proportionality is the recombination coefficient, α_{rec} [7]. The recombination rate can be determined using the following expression:

$$\frac{dn^+}{dt} = \frac{dn^-}{dt} = -\alpha_{rec} n^+ n^- \tag{1.14}$$

Electrons may also be attached to gas molecules, during their drift in the gas, forming negative ions [7]. Whereas noble gases and most organic molecules produce mainly stable positive ions at collision energies of several eV (which is higher than the energies reached during the drift in the gas), some molecules like halogenides and oxygen are capable of attaching electrons at much lower collision energies [4].

Regarding the processes affecting the drift of ions, this issue will be addressed later in section 4.3.

1.4 Detectors

1.4.1 Ionization Chambers

The principle of ion chambers is the simplest of all gas-filled detectors since they do not have an intrinsic amplification stage [5]. Their operation is based on the collection of all the charges created by direct ionization within the gas through the application of an electric field [7].

As a result, they are mostly used for high energy detection (above hundreds of keV), for which the primary charge produced is measurable; although they can reach very competitive performances, they have the drawback of being specially sensitive to electronic noise and vibrations.

1.4.2 Proportional Ionization Counters

The proportional ionization counter is a type of gaseous detector introduced in the late 1940s. In these detectors, after the formation of the primary electron cloud, proportional to the incident radiation energy, the electrons are guided to a region where the electric

field is sufficiently high so that ionization by electron impact occurs, producing additional electron-ion pairs through a process called electron avalanche.

Typical proportional ionization counters have cylindrical geometry, with the anode consisting of a thin wire that is positioned along the axis of a hollow cylinder that works as the cathode. This configuration makes it easier to reach the reduced electric fields required for the electron avalanche to occur. As a result of the electric field configuration, the multiplication region is confined to a very small volume when compared to the total volume of the detector. Therefore, most of the primary electrons are produced outside the multiplication region, undergoing the same multiplication gain on average, generate a charge signal whose amplitude is proportional to the incident radiation energy. Because the signal is considerably larger than that from the ionization chambers, this allows to reduce the impact of microphonic noise and, at the same time, to study a wider range of energies.

1.4.2.1 Charge amplification

As already mentioned, at low electric field, the electrons and ions created by the incident radiation simply drift to their respective collecting electrodes, with the energy gained due to the electric field being lost in the collisions with the gas atoms/molecules. If, between collisions, the energy gained from the electric field reaches a value greater than the ionization potential of the neutral gas atom/molecule, an additional electron-ion pair can be created. Following this secondary ionization, both the primary and secondary electrons will be accelerated by the electric field undergoing the same process over again, eventually creating additional ionizations. This process will continue until all the electrons are collected at the anode.

The charge multiplication process is exponential, taking the form of a cascade, known as Townsend avalanche, where the number of electrons, n, produced per unit path length follows the Townsend equation [4, 7]:

$$\frac{dn}{dr} = n\alpha \tag{1.15}$$

where α is the first Townsend coefficient that represents the ionization probability per drift length which depends on the reduced electric field and on the gas used. Its solution predicts that the density of electrons grows exponentially with distance as the avalanche progresses.

From equation 1.15 it results that, if the electric field is uniform α is constant, and the average number of electrons in the avalanche per primary electron – the gas multiplication factor or gain, M – increases exponentially with the distance travelled by the electrons [7].

$$\frac{n(r)}{N_e} = M = e^{\alpha r} \tag{1.16}$$

Since the electric field in typical proportional ionization counters has a radial depen-

dence, the gain is obtained through the integration along the avalanche average path, Γ [7]:

$$\ln M = \int_a^{\Gamma} \alpha(r) dr \tag{1.17}$$

where a is the anode radius.

The signal amplitude in such detectors can also be estimated, simply by knowing the average gas multiplication factor, M, that characterizes the counter operation, which is subject to fluctuations due to variations in both the number of ion-electron pairs initially created, F, and the ones produced in the avalanche process, b which can be defined, as shown in [51], as:

$$b = \left(\frac{\sigma_A}{\bar{A}}\right)^2 \tag{1.18}$$

where A is the gain in each avalanche, related to M by:

$$M = \frac{1}{N_e} \sum_{i=1}^{N_e} A_i = \bar{A} \tag{1.19}$$

with the variance in M, σ_M^2, given by:

$$\sigma_M^2 = \frac{1}{N_e} \sigma_A^2. \tag{1.20}$$

These fluctuations are introduced by deviations of the electron trajectories relatively to the average path and by the fact that the energy acquired by the electrons from the electric field is shared also with excitations and elastic collisions. Because of the processes involved the variance in the pulse amplitude in proportional ionization counters is dominated by fluctuations in the size of the avalanche produced by each electron [9], with the contribution from the fluctuations on the initial number of primary electrons produced (related with the Fano factor) being much smaller [7]. Additional fluctuations may also be caused by photon-induced effects that can lead to a loss of proportionality and/or spurious pulses.

These factors will limit the performance of these detectors, so one way to improve their performance is to use gas mixtures instead of pure gases.

1.4.2.2 Choice of Filling Gas

The choice of the filling gas of a detector depends essentially on the purpose for which the detector was designed. For example, the choice of a filling gas for proportional ionization counters is governed by factors to be considered like: low working voltage, high gain, good proportionality, high rate capability, long lifetime and fast recovery [5]. In general these conditions are met by using a gas mixture rather than a pure one [5, 7, 9].

To achieve high count rates two principal factors emerge, both related to the charges' velocity, namely the electron drift velocity and the ion mobility - both should be as high as possible [21].

For a minimum working voltage, noble gases are usually chosen, since they require the lowest electric field intensities for avalanche formation and the associated fluctuations are smaller than in molecular gases. Despite having a higher specific ionization, argon is usually preferred due to its lower cost. Pure argon as a filling gas, however cannot be operated with gains of more than about 10^3 - 10^4 without electrical discharges [9]. This problem is usually surpassed by adding a polyatomic gas, such as methane (CH_4), ethane (C_2H_6), isobutane(iC_4H_{10}) or carbon tetrafluormethane (CF_4). These molecules act as quenchers by absorbing the radiated photons and then dissipating this energy through excitation of either vibrational or rotational levels. So, adding a small amount of an additive gas leads to a significant reduction of the instabilities and proportionality loss caused by the production of electroluminescence photons due to the excitation of the gas atoms by the electrons [5, 9].

One way to reduce the fluctuations in the gain in such detectors is by using the so-called Penning mixtures. Adding a gas with lower ionization energy than the excitation of the main one, both the w-value and Fano factor can be significantly reduced. This happens because the energy that would then be lost through excitation processes of the main gas atoms can be converted into ionization of the additive gas molecules, with lower abundance. This process reduces the fluctuations associated with the primary electron production [7]. For example, the w-value for argon can be reduced from 26.2 to 20.3 eV through the addition of a small concentration of ethylene [20]. For this reason Penning mixtures are commonly chosen for proportional ionization counters used in radiation spectroscopy [5, 7].

The use of an organic quencher has, nevertheless, some limitations. The recombination of dissociated organic molecules and polymerization results in the formation of solid or liquid deposits which accumulate on the electrodes of the detector, with a great impact on the lifetime of counters [5].

1.4.2.3 Energy Resolution

Radiation detectors have many applications most of them relying on the analysis of the energy of the incident radiation [7]. The accuracy of the measure is assessed by the energy resolution, a characteristic of a given detector for a given energy. Experimentally the energy resolution can be defined as the Full Width at Half Maximum (FWHM) of the peak in the energy spectra (usually Gaussian shaped), divided by the position of the peak centroid, H_0 [7]. It is dimensionless and expressed as a percentage and indicates the minimum energy difference between two events that the detector is able to detect as separate peaks [7]. There are several potential sources of fluctuations that can affect the energy resolution [7]. In the radiation absorption process, the energy resolution is limited by the statistical fluctuations associated with the formation of the primary electron cloud, *i.e.* by F. The lower limit of R, known as intrinsic energy resolution, R_{int}, can be expressed

by:

$$R_{int} = 2.355\frac{\sigma_n}{\bar{n}} \tag{1.21}$$

where σ_n=$\sqrt{F.\bar{n}}$ as seen before or, in terms of ω and F for an incident radiation with a energy E_{ir}:

$$R_{int} = 2.355\sqrt{\frac{F\omega}{E_{ir}}} \tag{1.22}$$

F and ω have a major role in detectors, as they establish a lower limit to the final resolution attainable [7]. Comparing the Fano factors available in the literature, it is possible to observe that there are great discrepancies between them [17]. These discrepancies result not only from the physical processes involved but also from geometric effects and system used in their determination, which may improve or worsen the energy resolution. Fluctuations in the amplification process in proportional ionization counters can also play a non-negligible role in the attainable energy resolution, R.

As already discussed, in proportional ionization counters, the avalanche multiplication process, introduces fluctuations in the charge gain of a "single electron avalanche" which influences the energy resolution of proportional ionization counters, and there are some indications that avalanche fluctuations, b, increase with the avalanche size (the gain of the counter). Combining the effect of the fluctuations on the primary electron cloud formation with the fluctuations in each avalanche, the expression for the energy resolution can be written as follows [3, 22]:

$$R \simeq 2.355\sqrt{\frac{1}{\bar{n}}(F+b)} \tag{1.23}$$

In addition, the performance of the proportional ionization counters is highly dependent on several factors among them the pressure, filling gas, voltage supply stability, the anode wire's diameter and uniformity [7]. In order to have a good signal-to-noise ratio and energy resolution, the counter has to work in the limited proportionality region and at high gas gain. Nevertheless, these detectors are greatly affected by space-charge effects [7]. The combination of these factors leads to performance deterioration since it modifies the electric field, deeply affecting the charge multiplication [7].

1.4.3 Proportional Scintillation Counters

Instead of having their amplification stage based on electron multiplication, gas proportional scintillation counters (GPSC) have their amplification stage based on light production, using a known phenomenon called Electroluminescence (EL).

So, in a EL-based gas detector, after thermalization of the primary electron cloud, the electrons are guided to a region (secondary scintillation region) where the electric field is high enough to cause excitation of the gas atoms but not enough to ionize them. In these

conditions, the excitation of atoms followed by the de-excitation through the emission of scintillation is enhanced and can achieve a high efficiency. The scintillation photons are then detected by a photosensor, originating a signal proportional to the incident radiation energy. Because the fluctuations associated to the amplification process are generally small, it is expected that detectors based on EL can achieve good energy resolutions [7].

1.4.3.1 Electroluminescence process

Rare gas atoms, when excited, are known to emit light with high efficiency, since the other deexcitation channels like vibrational and/or rotational are not present. In a gas, an electron may undergo one of three processes: elastic, excitation or ionization collision when it interacts with a neutral atom (X) of the gas, depending on the cross sections of each process. In detectors based on EL, excitation is the preferential process, which at pressures above a few hundred Torr is more likely to be due to a three-body collision producing an excited (X_2^*) molecule or excimer. This excited molecule, when vibrationally relaxed, returns to the ground state emitting a photon with a wavelength characteristic of the gas. When this process occurs during the formation of the primary electron cloud it is known as primary scintillation. This process may be enhanced applying the conditions that favour its occurrence, namely adjusting the pressure and the applied electric field. In such circumstances this process is often called secondary scintillation or electroluminescence.

Scintillation in rare gases has a spectral distribution that depends on the excitation mechanism involved which is pressure dependent [23–27]. For pressures below 10 Torr, the scintillation in rare gases is essentially due to atomic de-excitations with well defined energies that correspond to the transitions:

$$X[^1S_0] + e^- \rightarrow X^*[^3P_2, ^3P_0, ^1P_1, ^3P_1] + e^- \rightarrow X[^1S_0] + e^- + h\nu \tag{1.24}$$

where the lower atomic excited states of the gas are $^3P_2$, $^3P_0$, $^1P_1$, $^3P_1$ and the fundamental state is $^1S_0$. However, for pressures above tens of Torr, the formation of excimers through 3-body collisions [24, 25], becomes more probable and the scintillation comes progressively from molecular emissions:

$$X^*[^3P_1, ^3P_2] + 2X[^1S_0] \rightarrow X_2^*\left[^1\sum_u^+, ^3\sum_u^+\right]^\nu + X[^1S_0] \tag{1.25}$$

where $^1\sum_u^+$ and $^3\sum_u^+$ represent the attractive molecular excited states which can be either vibrationally excited ($\nu \neq 0$) or vibrationally relaxed ($\nu = 0$). Although the atomic states directly involved are $^3P_1$ and $^3P_2$, respectively, it is possible that other atomic excited states can be responsible for the formation of these excimers through indirect processes [24]. These molecular excited states decay radiatively to the repulsive fundamental molecular state $^1\sum_g^+$

$$X_2^*\left[^1\sum_u^+, ^3\sum_u^+\right]^\nu \rightarrow X_2\left[^1\sum_g^+\right] + h\nu' \tag{1.26}$$

with a scintillation emission centred in a region of shorter wavelengths (1st continuum) or in a region of longer wavelengths (2nd continuum), depending on whether the excimer is vibrationally excited or relaxed. Since increasing the pressure favours the vibrationally relaxed states due to their collision with other gas atoms, for pressures above 50 Torr, the 2nd continuum becomes the dominant one, this emission being the typical one at working pressures used in GPSC [23].

Figure 1.3 shows the emission spectra of argon (Ar), krypton (Kr), and xenon (Xe) for pressures of 50 Torr and hundreds of Torr.

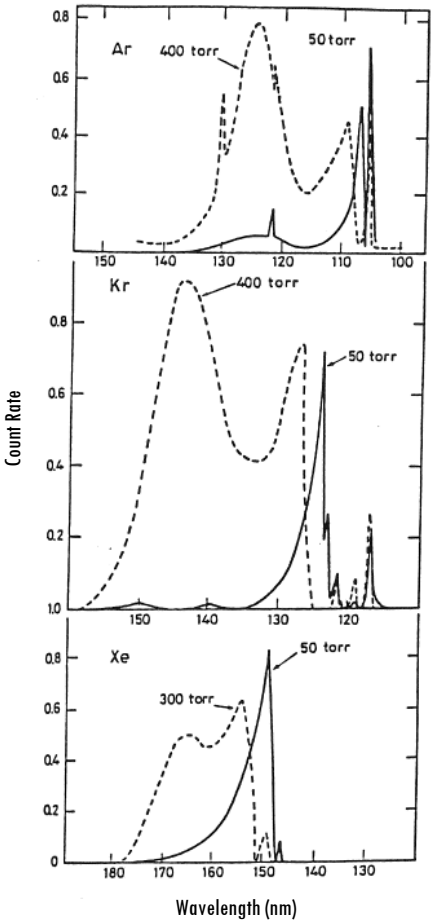

Figure 1.3: Emission spectra of argon, krypton and xenon for 50 Torr and 300 Torr (Xe) or 400 Torr (Ar, Kr) [23, 28, 29].

Looking at figure 1.3, it is possible to observe that the atomic emission lines practically disappear when the pressure increases, being replaced by the continuum of the molecular emission. Another important fact is that the wavelength of the emission increases as the atomic number of the rare gas, with the 2nd continuum being centred at 126 nm, 150 nm

and 175 nm for Ar, Kr and Xe respectively.

The behaviour of the pressure-reduced secondary scintillation yield, $(1/p)(dN_S/dx)$ (where dN_S is the number of photons produced per electron drifting along an elementary drift distance dx), is well established. Above the excitation threshold and below the threshold for ionization, it increases linearly with the pressure-reduced electric field E_S/p in the scintillation region, according to the empirical relation:

$$\frac{1}{p}\frac{dN_S}{dx} = A\frac{E_S}{p} - B \tag{1.27}$$

first reported in [30, 31] and then investigated with Monte Carlo simulations [32–34]. The last paper reports absolute values for the constants A and B (x in cm, E_S in V·cm^{-1}, p in bar, and T = 293 K) of A = 0.139 photons·V^{-1} per electron and B = 101 photons cm^{-1}·bar^{-1} per electron in Xe.

As a result of the process involved in the amplification in GPSCs, the associated fluctuations on the number of photons produced by a single electron are smaller than the ones involved in the charge multiplication process, as it will be discussed later.

1.4.3.2 Choice of Filling Gas

In GPSCs, noble gases are usually the preferred choice due to their high scintillation efficiency and low w-value and Fano factor. Gases such as Xe (Z=54) and Ar (Z=18) are usually chosen because of their relatively high atomic number and associated photoionization cross section, σ_{ph}, with Kr (Z=36) being usually avoided since it has a radioactive isotope. When comparing the rare gases, Xe becomes the obvious choice, due to its low w-value [35–37], relatively low Fano factor [7] and high scintillation yield [38]. Furthermore, the larger wavelength of its secondary scintillation emission is more adequate to most photosensors [39].

1.4.3.3 Photosensors

Since GPSCs have their amplification mechanism based on light production, they require the use of photosensors to detect the resulting electroluminescence. Among the most common is the Photomultiplier Tube (PMT) used in the first scintillation studies with GPSCs [40–42], which gives the best energy resolution. The photosensor was initially separated from the detecting medium which increased the complexity of these detectors, resulting also in some additional drawbacks: a decrease in photon detection due to the absorption of the Vacuum Ultra-Violet (VUV) photons in the window and a smaller solid angle subtended by the photosensor in such cases, as the photosensor would be placed further from the light production point. In order to surpass these difficulties alternatives were devised with the photosensor placed in direct contact with the gas [43–45].

Despite presenting the best energy resolution PMTs exhibit several disadvantages such as their fragility, the fact that they cannot work in the presence of magnetic fields, and

their high cost for large area detectors [46]. The quest for a suitable alternative to the PMTs started with early efforts by Policarpo in the 1970s [47], followed by studies of photosensitive gases by Anderson in the early 1980s [48], photodiodes by Van Standen and de Campos in the late 1970s to the mid 1980s [49, 50] and the use of caesium iodide (CsI) photocathodes [51–53] in the mid 1990s. In the late 1990s and early 2000s Lopes [46] suggested the use of avalanche photodiodes (APDs) as candidates for the scintillation readout, as they are compact and present low power consumption and high quantum efficiency and can be operated in high-intensity magnetic fields [22]. A clear advantage of using APDs relies on their negligible natural radioactivity necessary for a reduced background, a requisite for the next generation large-volume rare event experiments [45]. This solution also allows the development of large area detectors using smaller photosensors, but the need for a high number of these increases the cost of the detector significantly [45]. At about the same time the use silicon (Si) photodiodes was suggested [46] but the noise on such photosensors is too high and their performance is somewhat worse than that of standard GPSCs with PMTs. Even with the recent development of VUV sensitive Large Area Avalanche Photodiode (LAAPD) [43], which allowed the development of high performance GPSCs, LAAPDs have the inconvenience of having a gain which is rather sensitive to temperature fluctuations reducing the scope of applications.

To surpass these problems, instead of using photodiodes as a photosensor another possibility explored was to use deposited photocathodes in direct contact with the gas with the resulting photoelectrons being emitted to the gas and then collected by either a microstrip [51, 52, 54], a GEM [55] or an electrode array [56], all involving charge multiplication or by a properly biased grid where the photoelectrons produced are collected [6]. These solutions have several advantages: a much lower cost, allowing large detecting areas to be developed and avoiding the problems mentioned before, making them more ruggedized for field applications and competitive in terms of performance. In such cases, the photoelectron extraction efficiency has an important role in the signal generation [33]. The mechanism of photon detection with photocathodes can rely either on internal or external photoemission, also known as transmissive and reflective mode. The term internal photoemission is often used when the photoelectron is emitted into a solid, while the external photoemission is used when the photoelectron is emitted into vacuum. For our purpose we are only interested on the external photoelectric effect, where photons with energy above a certain threshold are absorbed by the photosensitive material within a certain depth, generating free charge carriers which can then be ejected from the same photocathode surface that was hit by the photon.

The photoelectric effect occurring in reflective photocathodes can be described by the Spicer Three-Step model [57, 58], which considers three successive steps in the electron photoemission process:

1. Optical absorption of a photon into the bulk of the photocathode leading to the liberation of electrons into the bulk.

2. The motion of the electrons through the bulk of the crystalline structure of the photocathode towards its surface.

3. Escape of the electrons from the photocathode's surface to the vacuum or gas.

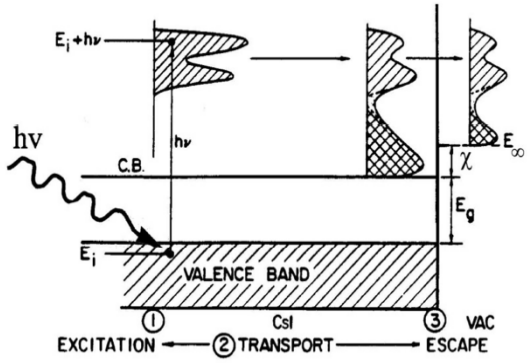

Figure 1.4: Classic representation of the Spicer Three-Step model. Taken from [58].

The energy, E_k, of the electrons ejected from the photocathode, coming from the valence band (thus with maximum energy), is given by:

$$E_k = hv - (E_g + \chi) \tag{1.28}$$

where E_g is the energy bandgap from the top of the valence band to the conduction band and χ is the electron affinity of the material – which is the energy gap from the conduction band minimum to the vacuum energy level. These three steps are depicted in figure 1.4, where it can be observed that electrons reaching the surface of the photocathode can only escape if their energy is greater than that of the vacuum level.

Quantum Efficiency

Since, as explained before, not all photoelectrons produced in the bulk of the photocathode material manage to escape to the surface, the ratio between the number of photoelectrons emitted, n_{phe^-}, and the incident photons, n_{ph}, $QE{=}\dfrac{n_{phe^-}}{n_{ph}}$, is called quantum efficiency of the material and depends on the wavelength of the incident photons.

So, the Quantum Efficiency (QE) of a photocathode is an intrinsic characteristic which is extremely important in detectors whose operation principle relies on the detection of photons, as in GPSCs. In figure 1.5, a comparison of the quantum efficiency for different photocathodes is given.

As can be seen, the photocathode that offers the best performance is CsI, with quantum efficiency values that can reach 20% in the range of wavelengths of interest in the most common gaseous detectors [59, 60]. This is due to its low electron affinity (E = 0.1-0.2 eV) and electron escape length, of the order of 16 nm for 1 eV electrons [61], as illustrated

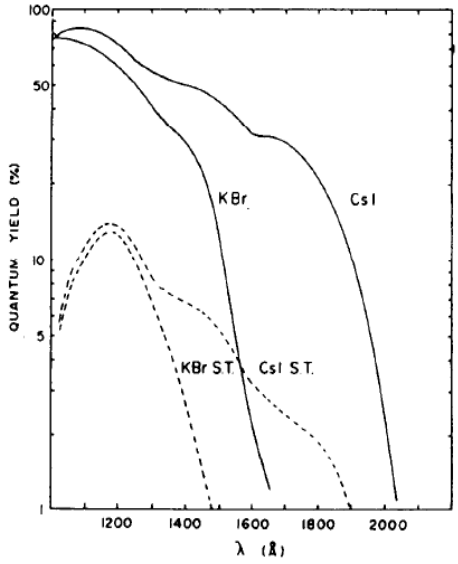

Figure 1.5: Comparison of the quantum efficiency of typical reflective (full lines) and some semitransparent photocathodes (dashed lines). Taken from [39].

in figure 1.6. This effect is the result of an efficient electron transport mechanism, dominated by electron-phonon interactions, characterized by very small energy losses between collisions.

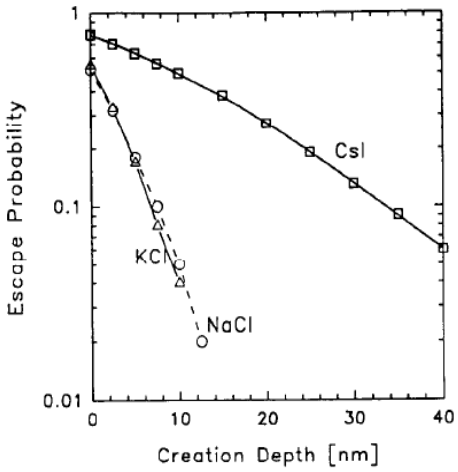

Figure 1.6: Calculated escape probability for electrons with initial energy of 1 eV as a function of their creation depth in caesium iodide (CsI), NaCl and KCl. Taken from [39].

In most cases, a relatively thick CsI film, a few hundreds of nanometers, is deposited on metal substrates, usually stainless steel [39]. The values for the quantum efficiency of CsI can be improved using special treatments, as can be seen in figure 1.7.

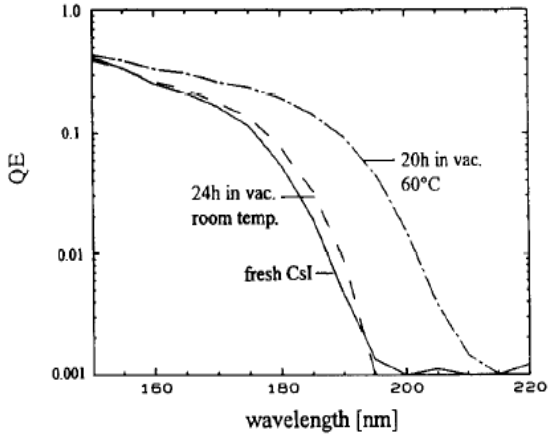

Figure 1.7: Quantum efficiency of a 500 nm thick CsI film on stainless steel substrate, in vacuum of 10^{-7} Torr, immediately after the evaporation, after 24 hrs at room temperature and after 20 hrs at 60°C. Taken from [39].

Apart from their high quantum efficiency, CsI films display several other important characteristics that make their use as photocathode advantageous. These characteristics include:

- Easy production of photocathodes using vacuum thermal evaporation techniques [39];
- Chemically non reactive with most substrates and gases [39];
- Relatively stable when exposed to gases [39];
- Low resistivity (10^{10}-10^{11} Ω·m [62]) that allows its operation in high flux conditions, almost without charge effects;
- Not sensitive to visible light, therefore not requiring special optical isolation [63];

Photoelectron Retrodiffusion

From the extraction point-of-view it is very different if the emission occurs from a photocathode into vacuum (QE) or into a gaseous atmosphere (Extraction Efficiency (EE)). In this last case, photoelectrons can be backscattered and reabsorbed by the photocathode surface [64, 65], thus reducing the photoelectron extraction and consequently the overall efficiency of the detector. Although the retrodiffusion phenomenon has been known since the end of the XIX century [66–69], with important contributions from Thompson [70] and then from Loeb [71], it recently gained growing importance for the scientific community with the appearance of detectors based on microstructures with a photocathode deposit [39, 72].

The elastic backscattering of photoelectrons on the gas molecules is known to be larger in noble gases, due to dominant elastic collisions at low electron energies [64]. The fraction

of the emitted photoelectrons that return to the cathode and that are reabsorbed is usually named the retrodiffusion coefficient.

Associated with the retrodiffusion coefficient is the extraction efficiency, which is defined as the fraction of the emitted photoelectrons that are extracted, which is more adequate for the understanding of the influence of the retrodiffusion process in the signal formation of detectors that make use of photocathodes. So, the extraction efficiency of photoelectrons can be expressed as follows:

$$\eta_{ext} = \frac{n_{phe^- extracted}}{n_{phe^- emitted}} \tag{1.29}$$

The photoelectron extraction efficiency depends on several factors namely, the energy of the photoelectrons leaving the surface, the gas or mixture composition, pressure and electric field at the photocathode surface [63, 71, 73–77].

In spite of the dependence on pressure, it has been experimentally verified that the extraction efficiency is independent of the pressure when the electric field is scaled accordingly [78]. Therefore, it is common to represent the extraction efficiency as a function of the reduced electric field (E/p) which allows a better understanding of the influence of both factors in specific operating conditions.

In figure 1.8, it is possible to observe the influence of the reduced electric field in the extraction efficiency of photoelectrons from CsI in Xe at atmospheric pressure, for incident photons with 7.2 eV [19]. Although in the simulation performed by Escada [19] the extraction efficiency is determined for reduced electric fields above the scintillation and ionization threshold the effect of positive photon feedback as well as the effect of charge multiplication were not considered. From figure 1.8, it is possible to verify that by increasing the reduced electric field above the photocathode, the extraction efficiency is improved.

Photon Positive Feedback

In some gases, if the extraction reduced electric field is above the excitation threshold, secondary scintillation can occur and the resulting scintillation photons hitting the photocathode might be able to further release photoelectrons from the photocathode surface, in a process called positive feedback or photon-feedback. The occurrence of this process is usually avoided in detectors since it worsens the detector performance, eventually leading to electrical discharges.

Solid Angle Compensation Methods

As a result of the solid angle, the number of photons able to reach the photosensor depends on the photon emission position. This makes the detectors' response non-uniform. To solve this issue several compensation methods have been used and are described in the literature. These methods, however, are usually accompanied by an important cost in terms of signal

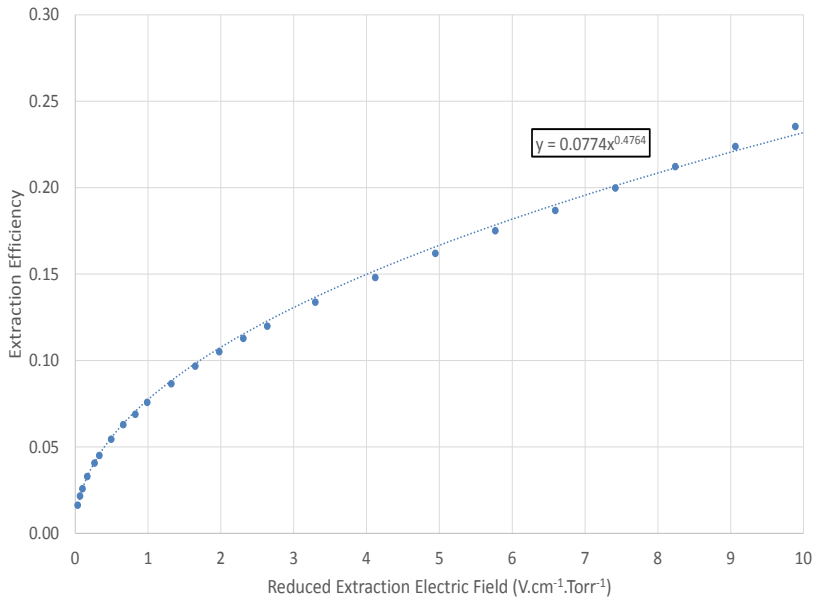

Figure 1.8: Photoelectron extraction efficiency as a function of the reduced electric field for 7.2 eV Xe scintillation photons in CsI. Data used was obtained from [19].

amplitude, compensated by a gain in uniformity in the response that may result in an overall improvement, especially in energy resolution. So far, in GPSCs there are two types of compensations described in the literature: active or passive, depending on whether they affect the signal formation mechanisms or not, respectively.

A typical example of active compensation methods are focusing techniques whose objective is to bring the primary electrons closer to the detector axis [79]. In addition, a curved grid technique was developed in the Physics Department of the University of Coimbra by Conde, dos Santos and Bento [80]. In this technique, the curved grid is used to obtain a non-uniform electric field, with increasing intensity outwards the detector axis, which leads to an increase in the light yield production with the radial distance [30], in a way that compensates for the loss of light collected due to solid angle effects for off-axis events.

As for passive methods, typical examples are masks with a radially-decreasing transparency, which are usually applied on the surfaces of the photosensor or photosensitive materials. The transparency gradient is calculated to produce radially-independent light collection in the photosensor. The use of this technique allows the operation of the standard planar GPSC with radiation window dimensions close to the PMT window size without a significant degradation of its performance [81].

1.4.3.4 Energy Resolution

Similarly to that of the proportional ionization chambers, the energy resolution can be determined for the proportional scintillation counters. In these detectors, the amplification stage, based on light production, introduces fluctuations, J, in the light gain, *i.e.* the number of photons produced, N_S, by a single electron, that will affect the energy resolution of the proportional scintillation counters. As a result, the energy resolution of the proportional scintillation counter can be expressed as follows [51]:

$$R \simeq 2.355\sqrt{\frac{F}{\bar{n}} + \frac{1}{\bar{n}} \times \frac{J}{N_S}} \tag{1.30}$$

where J represents the fluctuations in the light gain process.

As J is much smaller than F, with an optimized design, GPSCs are expected to achieve energy resolutions close to the intrinsic value, so this value establishes the goal for the detector optimization.

However, it is important to recall that there are a few factors that can worsen the energy resolution of such detectors, which include:

- electronegative impurities present in the gas [82], that increase fluctuations in the EL production;
- reduced electric fields above the ionization threshold [51, 83], that increase fluctuations due to $b > J$;
- non-uniform response in the photosensor active area [84, 85];
- variance in the solid angle subtended by the photosensor as a function of the scintillation photon emission [86, 87].

1.4.4 Detector Efficiency

Another important property of detectors is their detection efficiency. Ideally, radiation detectors should have an output pulse for each quantum of radiation that enters its detection volume. However, since the interaction probability of electromagnetic radiation follows an exponential law, radiation such as X and γ-rays do not have a well-defined range or stopping distance [7]. The detector's capability to detect these radiations depends on the interaction probability of the incident radiation within the medium, which is intrinsically related to several factors that were already discussed in section 1.1 and that result in its attenuation.

Nevertheless, two types of detecting efficiency can be defined: absolute and intrinsic. The absolute efficiency of a detector is given by the ratio between the number of photons detected and the total number of photons emitted by the source, so it displays a dependency on the detector properties but also on other geometry aspects like the distance from the source to the detector, entrance window size, and so on [7]. The intrinsic efficiency

is the most useful one as it practically removes the dependence on geometric factors (like the solid angle of the detector), being defined as the ratio between the number of photons detected and the total number of incident photons [7]. The intrinsic efficiency depends primarily on the detector material, the radiation energy and on the medium $density \times length$ in the direction of the incident radiation, i.e. on the absorbed radiation [7]. A simple way of determining the detector efficiency for a certain radiation is by using the radiation attenuation law, expressed in equation 1.3.

1.5 State-of-the-Art

Gaseous gamma-ray spectrometers are standard instruments used in a wide variety of scientific and industrial applications. Several approaches to these have been developed in recent years. As seen before, gaseous radiation detectors can be divided into two distinct categories, namely those that do not use amplification, which include ionization chambers, and those that use amplification and that include the proportional ionization counters (charge amplification) and proportional scintillation counters (light amplification).

Concerning ionization chambers, several configurations have been developed in recent decades by Dmitrenko [88, 89], Bolotnikov [90], Bolozdynya [91] and Austin [92]. Typical configurations include parallel-plate [91, 93] or cylindrical ionization chambers with one anode [88–90], eventually with a shield grid [89, 93], or with two anodes [92]. These configurations exhibit energy resolutions around 4% for 662 keV gamma-rays. In general, cylindrical configurations have better performance than the planar ones. This improved performance results from the better energy resolution and lower sensitivity to external vibrations/acoustic effects. By incorporating a shielding grid the energy resolution is enhanced, due to a significant reduction in the charge induction effect [93].

However, several limitations persist. These limitations are mostly related to vibrations and acoustic effects [88,94], detector asymmetry [92] and small signal amplitude that result in a small signal-to-noise ratio (SNR) [90–93]. This can be avoided using electroluminescence (EL) as the amplification method, which is high-yield, low-fluctuation process if the right gas is used [7]. The low statistical fluctuations in the amplification process in proportional scintillation counters make them usually more competitive than those using charge multiplication with the advantage of the space-charge effects being drastically reduced, and the microphonic effects. Several detectors using electroluminescence have been reported recently namely by Akimov [95,96], Bolozdynya [97], Coelho [44], Borges [6] and Resnati [98, 99], differing mainly in the geometry and readout system used. Table 1.1 summarizes the main characteristics of some of these detectors.

Configurations are either planar [6, 44, 97–99] or cylindrical [95], and concerning the readout system, they typically use photomultipliers [95,97–99], avalanche photodiodes [44] or deposited photocathodes [6]. Energy resolutions below 2% at 662 keV energy have already been achieved [100]. Despite the attractive characteristics already discussed, EL based solutions suffer from a common drawback that results from the use of photosensors.

Table 1.1: Summary of the energy resolutions and Xe densities of Ionization Chambers (IC) and Proportional Scintillation Counters (PSC) developed by different authors. The Full Width at Half Maximum ($FWHM$) is for 662 keV unless otherwise stated.

Work	Method	Geometry	$FWHM$	Density (g/cm^3)
Bolotnikov et. al [90]	PSC	Planar	3.5%	0.6
Ulin et. al [93]	PSC	Cylindrical	2.7%	0.6
Tepper et. al [101]	IC	Cylindrical	1.8%	0.5
Akimov et. al [96]	PSC	Cylindrical	13% (13.9 keV)	0.04
Bolozdyna et. al [91]	IC	Cylindrical	3%	0.5
Coelho et. al [44]	PSC	Planar	3% (60 keV)	0.03
Austin et. al [92]	IC	Cylindrical	2.5%	0.3-0.5
Dmitrenko et. al [89]	PSC	Planar	2%	0.05-0.08
Resnati et. al 2013 [99]	IC	Planar	7.3%	0.13

These drawbacks include: their fragility, the use of windows which also reduces light collection efficiency and the dependency on the quantum efficiency of the photosensor used. The use of the photosensors in direct contact with the gas is a way of reducing some of these effects [46]. The combined effect of the detector solid angle and photosensor quantum efficiency can affect the detector gain (number of photoelectrons produced per primary electron) and also the detector signal-to-noise ratio [46].

In a recent work [6], a multigrid high-pressure gas proportional scintillation counter (MGHP-GPSC) based on the secondary scintillation of xenon and optimized for field applications, using a CsI deposited photocathode as the photosensor, was developed. The prototype described has several interesting features, in particular the fact that it does not require a PMT or any additional photosensor, which would make the detector fragile for field applications. Exploring this possibility with a new prototype might prove rewarding as it may result in the improvement of the energy resolution and of the detection efficiency, making these detectors more competitive.

1.6 HPXe Gas Proportional Scintillation Counter 1^{st} Prototype Planar Geometry

We will now describe in more detail the previous MGHP-GPSC prototype that was developed in [6]. Figure 1.9 depicts the schematic of this prototype.

This detector consists of a cylindrical vessel with four inner circular grids parallel to each other, together with a CsI photocathode (about 500 nm thick) vacuum evaporated in the lower inner surface and a radiation entrance window in the upper surface of the detector. The outer vessel is at ground potential and the grids are biased to obtain the required electric field in the several regions. The ionizing radiation with energy E_r is absorbed in the drift region (A), producing the primary electrons, which drift into the secondary scintillation region (B) between grids G1 and G2, where the reduced electric field is above

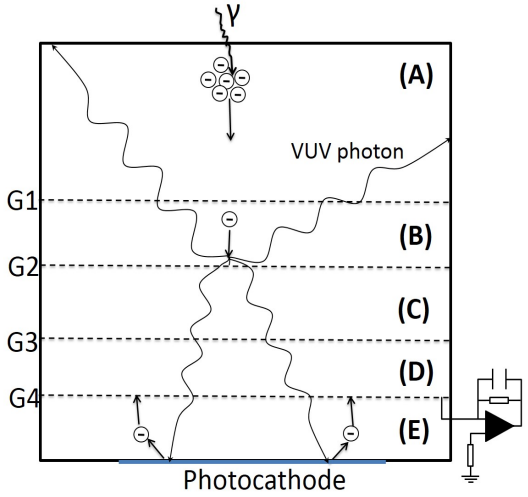

Figure 1.9: Schematic of the 1st prototype of MGHP-GPSC [6].

the scintillation but below the ionization threshold (0.76< E_S/p <4.56 kV·cm^{-1}·bar^{-1}). In this region, they produce a large number of VUV secondary scintillation photons per primary electron, approximately 1100 ph/e$^-$ for an E_S/p of about 2.3 kV·cm^{-1}·bar^{-1} [6], using 5 bar of Xe. These photons will then cross the optical transmission region (C), between grids G2 and G3, the electric field barrier region (D) between grid G3 and G4 and finally the photoelectron collecting region (E), reaching a reflective CsI photocathode where the photoelectrons are produced. Grid G4 sets an appropriate electric field to improve the photoelectron extraction efficiency [102] and collect the produced photoelectrons. The charge signal produced in G4 is then fed to the electronic amplification stages, producing a pulse whose amplitude is proportional to the number of primary electrons and so to the energy of the absorbed radiation. Table 1.2 summarizes the E/p and length of the different regions of the MGHP-GPSC (1st prototype).

Table 1.2: E/p and length of the different regions of the MGHP-GPSC (1st prototype). Adapted from [6].

Regions	Length (1st prototype)	E/p (kV·cm^{-1}·bar^{-1})
Absorption/Drift	4.0 cm	0.075-0.150
Scintillation	0.7 cm	0.76-4.5
Optical transmission	1.2 cm	<0.76
Electric field barrier	2.4 cm	<0.76
Photoelectron collection	1 cm	<0.76

In this configuration the detector solid angle, $\Omega/4\pi$ subtended by the CsI photocathode is about 0.16. The gain with this geometry can, in theory, reach values up to 100 (20 bar of Xe) [6], although the measured value was 10, for Xe at 5.4 bar.

Although the working principle of the detector with this geometry was demonstrated in [6], several drawbacks were also identified, namely the high voltage requirements that limited the detector dimensions (absorption region - 4 cm), affecting the detector active volume (736 cm^3), detection efficiency (<1%) and solid angle (0.16), and the number of grids used that decreases the overall optical transmission of the scintillation photons, reducing the gain of the detector, already affected by the small solid angle.

In order to surpass the limitations encountered with this first prototype a second prototype was developed, based on the same working principle with a different geometry, which is one of the research items of the present work.

2

HPXe Gas Proportional Scintillation Counter

Harold Edgerton (1903-1990) discovered that light is generated by passing a brief electric current through a tube filled with a rare gas, which led to the discovery of the electroluminescence phenomenon by Armando Policarpo and Carlos Conde in the 1960s and subsequent development of proportional scintillation counters.

–

The proposed new prototype of the MGHP-GPSC detector has a working principle similar to the planar one, but with a cylindrical geometry. This new geometry displays several interesting characteristics when compared to the previous one. On one hand, this configuration allows the number of grids used in the definition of the several detector regions to be decreased, consequently reducing the impact of the optical transmission in the detector gain. On the other hand, the fact that the photocathode is deposited on an outer cylinder allows the solid angle subtended by it to be significantly increased, increasing the active volume of detection since the radiation can be absorbed along the cylinder axis, allowing the use of lower biasing voltages. So, this configuration is expected to solve some of the problems observed in the previous prototype regarding the electrical discharges that occur at high bias voltage in the scintillation region, allowing the E/p value to be optimized in this region.

In figure 2.1, a schematic of this prototype is shown (longitudinal and transversal views), with the main regions and components signalled.

The detector has four distinct regions:

- Absorption/Drift Region ($r_s < r < r_d$);
- Secondary Scintillation Region ($a < r < r_s$);
- Photoelectron Collecting Region ($r_b < r < r_c$);
- Electric Field Barrier Region ($r_d < r < r_b$);

The different regions are defined by the anode and cylindrical grids (G1 and G2) or by the reduced electric field intensity values.

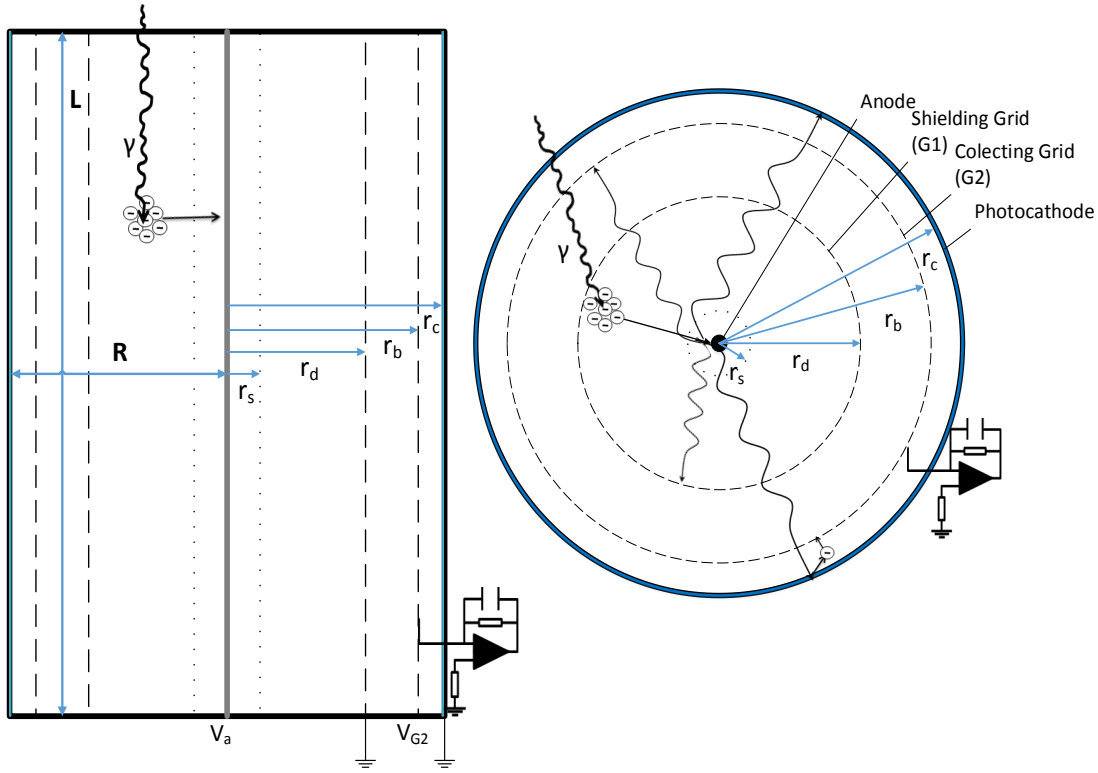

Figure 2.1: Schematic of the prototype of the MGHP-GPSC. On the left: a longitudinal cut with the main structures: anode, shielding (G1) and collecting (G2) grids, CsI photocathode (in light blue) and the bias in each structure. On the right side: a transversal cut of the detector and the working principle of the detector.

The absorption/drift region is the region between grid G1 and the radial distance from the detector axis where the reduced electric field, E/p, is below the scintillation threshold, *i.e.* $r_s < r < r_d$. The radiation entering the detector (X or γ-rays), preferentially in a direction perpendicular to the bases as depicted in figure 2.1, should be absorbed in this region, with the resulting primary electrons, which may be highly energetic, being thermalized preferentially in this region while drifting towards the anode.

As the primary electrons are accelerated towards the anode by an increasing electric field, they will increasingly gain energy from the electric field and when they reach a region where the E/p value is above the Xe scintillation threshold (E/p>1 V·cm^{-1}·Torr^{-1}), these primary electrons will produce VUV scintillation photons upon colliding with the gas atoms which happens for radial distances below r_s, the distance where the E/p is equal to 1 V·cm^{-1}·Torr^{-1}. Since there are no grids to separate the absorption and scintillation regions, their dimensions depend on the voltage applied between the anode and grid G1, on the anode radius, and gas pressure. In fact, the reduced electric field inside a gas

detector with a cylindrical geometry, in the approximation of infinite length, can be given by:

$$E_{(r)} = \frac{\Delta V}{r.ln(b/a)} \tag{2.1}$$

where ΔV is the voltage applied between the anode and grid G1, r is the radial position and b and a are the grid G1 (b = r_d) and anode radius, respectively. So at points near the anode, the electric field can reach very high values even for a moderate ΔV.

It is important that the E/p at the surface of the anode be kept just below the Xe ionization threshold to maximize the electroluminescence yield, and the E/p near grid G1 should be at least 0.1 V·cm^{-1}·Torr^{-1} to avoid charge recombination that would affect the signal formation of the detector.

As in the previous prototype, the VUV photons produced in the scintillation region ($a < r < r_s$) will travel across the detector volume, eventually reaching the reflective CsI photocathode deposited in the inner surface of the outer cylinder at a radial distance r_c from the detector axis. The extracted photoelectrons produced at the photocathode, proportional to the incident radiation energy, are then collected in grid G2 (at a radial distance r_b from the detector axis), which is biased to maximize the extraction efficiency. Grid G1 is also responsible for creating an electric field barrier for the extracted photoelectrons, preventing these from drifting towards the anode and improving the collecting efficiency of the photoelectrons in G2. Grid G1 has also another purpose which is to prevent signal induction by the drifting ions on the collecting grid, G2. As we will describe in the next sections, it is expected that when compared to the previous prototype with planar geometry, this new detector will allow a higher gain with lower applied voltages.

2.1 Detector Design Considerations

In the present section a brief explanation of how the dimensions of the several regions of the detector were determined will be presented. To achieve good performance and obtain a competitive detector, a compromise must be established between the detector dimensions, working pressure and detecting efficiency for a given incident energy range.

The dimensions were established considering that the prototype should allow a good performance in gamma radiation detection from 100 keV up to 662 keV, for 5-20 bar of Xe.

2.1.1 Absorption/Drift region

In this region, the ionizing radiation (X or γ-ray) is absorbed in a 5–20 bar atmosphere of xenon, where a reduced electric field between 0.1 and 1 V.cm^{-1}.Torr^{-1} (the threshold for secondary scintillation) is applied to allow the primary electrons to thermalize and drift to the scintillation region.

2.1.1.1 Absorption region length - Detector length

To determine the dimensions of this prototype, we considered the range of energies between 100-662 keV and a gas pressure of 15 bar, since this is a reasonable pressure value to work with in the laboratory.

To estimate the detector length the fundamental law of gamma-ray attenuation was used (eq. 1.3), from which the detector length, L, can be obtained

$$L = -\frac{ln\frac{I}{I_0}}{(\mu/\rho).\rho} \tag{2.2}$$

where I/I_0 represents the ratio of transmitted radiation, ρ the gas density, while μ/ρ represents the mass attenuation coefficient, which depends on the radiation energy and on the gas. Considering that 20% of radiation absorption for 662 keV would be a good compromise for this first prototype, some calculations were performed and will now be described. Figure 2.2 displays the dependence of μ/ρ with the photon energy for Xe [103]. Using this data, the mass attenuation coefficient (μ/ρ) for 662 keV in Xe was found to be 0.08077 g/cm^2. Figure 2.2 displays the dependence of μ/ρ with the photon energy for Xe.

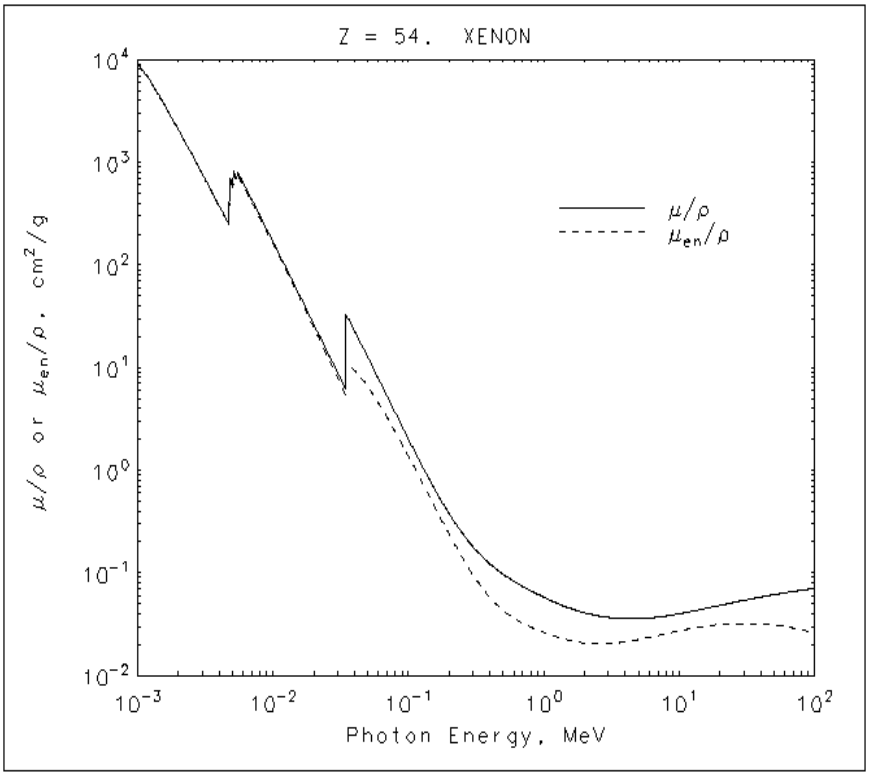

Figure 2.2: Dependence of μ/ρ value with photon energy for Xe. Graphic adapted from [103].

As for the density of xenon at a pressure of 15 bar at room temperature (293 K), a good approximation can be obtained by making use of van der Waals equation. The van der Waals equation (equation 2.3) is an equation of state for a fluid composed of particles that have a non-zero volume and a pairwise attractive inter-particle force, and is most useful for temperatures above the critical temperature, as is the present case:

$$\left(p + \frac{n^2 a}{V^2}\right)(V - nb) = RT \tag{2.3}$$

In this equation p represents the pressure (atm), n the number of moles, V is the volume, R is the ideal gas constant, T is the temperature (K), and a and b are constants related to the attraction between the particles and volume excluded by a mole of them respectively.

For a pressure of 15 bar (∼14.8 atm), a temperature of 293 K, a=0.4156 (m^6.Pa.mol^{-2}) and b=0.0000511 (m^3.mol^{-1}) and using the gaseous equation of state calculator available on [104], the gas density (ρ) of Xe at 15 bar was found to be equal to 0.0877 g/cm^3.

Introducing these values in equation 2.2 for a transmission (I/I_0) of 80%, we obtain L=31.5 cm.

The detecting efficiency, of about 20% for a 662 keV incident radiation, can be easily improved by increasing the pressure of the detecting medium (Xe). Since our objective is to prove the concept, this length and working pressure were considered satisfactory for this purpose.

2.1.1.2 Absorption region radial dimension

The radial dimension of this region, on the other hand, depends essentially on the distance needed for the formation and thermalization of the primary electron cloud and the diffusion of the primary electrons, since these are highly energetic electrons. As a consequence of the electron diffusion it is important to ensure that the highly energetic primary electrons will be thermalized inside the absorption/drift region in order to assure that all electrons are in the same energetic conditions as they reach the scintillation region.

As an initial approach, to define the radial dimension of the absorption/drift region we will assume that this region must be larger than the stopping range of an electron carrying all the 662 keV of the gamma-ray photon (maximum energy limit for which the detector was initially designed).

The stopping range for 662 keV electrons in a Xe medium is approximately 0.3899 g/cm^2 [103], and if we consider a Xe density of 0.0877 g/cm^3, by multiplying the stopping range by the density of the medium, we obtain a stopping distance of less than 4.86 cm. This means that the absorption region should be wider than this, so a distance between 5 and 6 cm between the shielding grid and the beginning of the secondary scintillation region should be enough.

Figure 2.3 displays the Continuous-Slowing-Down Approximation (CSDA) range for energetic electrons with energies between 0.01-1000 MeV.

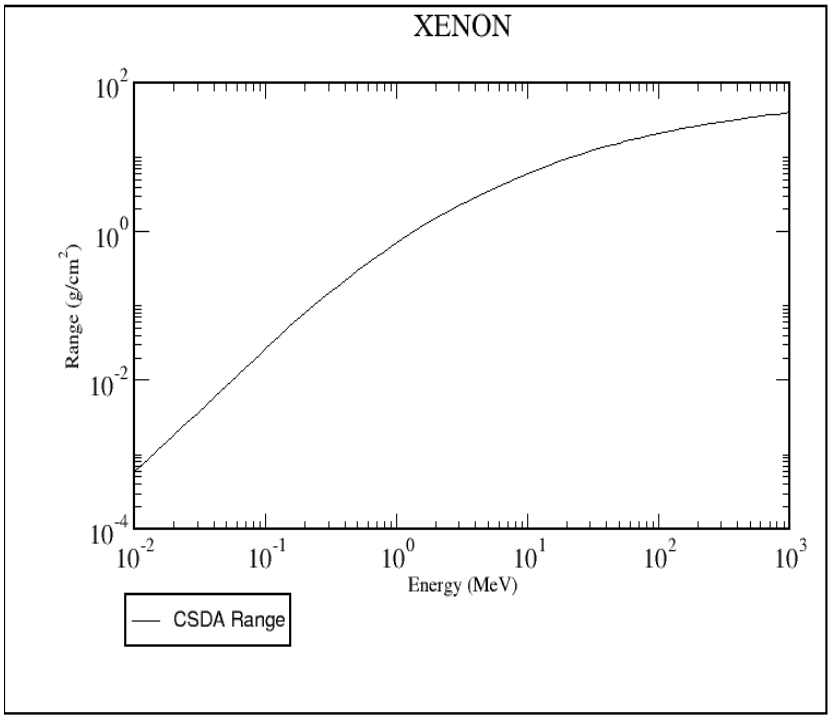

Figure 2.3: Continuous-Slowing-Down Approximation (CSDA) value with the electron energy. Graphic adapted from [103].

Figure 2.4 shows the range of energetic electrons as a function of their initial energy ranging between 100-700 keV for different temperatures: 273 K (circles) and 293 K (rhomb). In this figure it is possible to observe that for an absorption region of 5-6 cm and for pressures above 15 bar of Xe, electrons with energies between 100-700 keV are thermalized, while for lower pressures, only electrons with energies below 350 keV can be thermalized. So, we can conclude that the 5-6 cm absorption distance will be enough for this first prototype.

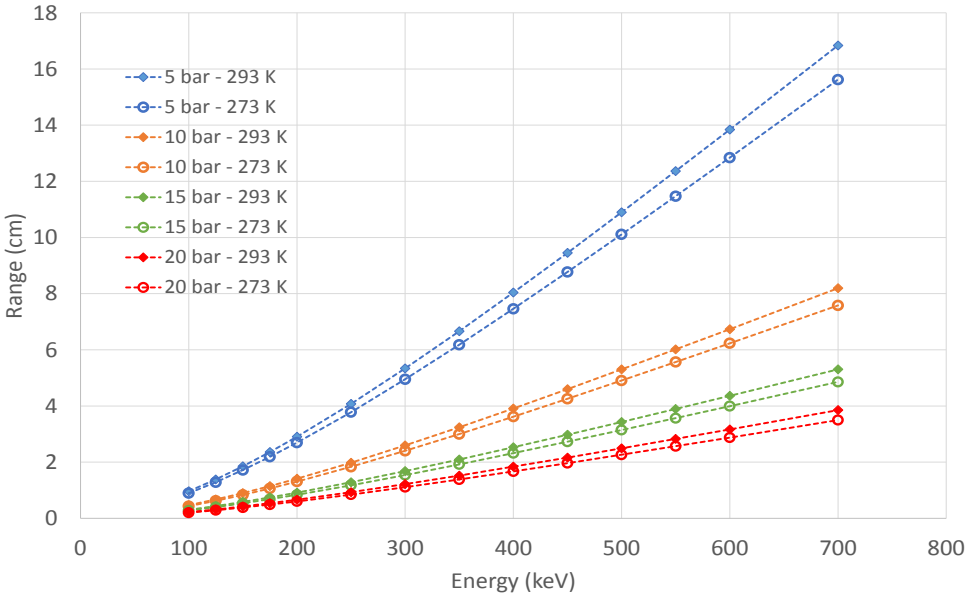

Figure 2.4: Stopping range of energetic electrons as a function of their initial energy ranging between 100-700 keV for different temperatures: 273 K (circles) and 293 K (rhomb).

2.1.1.3 Simulation of the absorption region performance

In the previous sections an estimate of the detector dimensions, both its length and radius, were obtained. Using these values in a GEometry ANd Tracking 4 (GEANT4) simulation, we were able to assess in more detail the full energy peak efficiency of the detector, α, *i.e.* the ratio between the events that are counted in the full-energy peak to the events that are absorbed in the detector, as a function of radiation energy, for different pressures and photoelectron emission angles. A hollow tube of 0.6 cm inner radius, representing approximately the scintillation region, 6 cm of outer radius and 30 cm long, filled with Xe at different pressures (10, 15 and 20 bar) was considered. In this simulation it was assumed that all the energy of the absorbed photon was transmitted to an energetic electron and the energy deposited in the active volume of the detector was determined for energies ranging from 0.662 to 2 MeV. In the first step it was considered that all the electrons were emitted in the direction of the detector axis at the centre of the absorption region. In each run, 1000 events were generated.

The results of the simulation for the full energy peak efficiency α are given in figure 2.5. In figure 2.5 it is possible to observe that an efficiency above 97% for the dimensions established for the absorption region for incident radiation with energies up to 1 MeV is obtained for pressures above 15 bar. A study was also made by varying the radial position

of the initial photoelectron between the limits of the absorption region, for a pressure of 15 bar, and it was found that the full peak absorption efficiency only slightly decreases for energies below 1 MeV, while for energies above this value a significant decrease was observed, in accordance with the fact that the primary electrons are more energetic and so a larger path is needed for their thermalization.

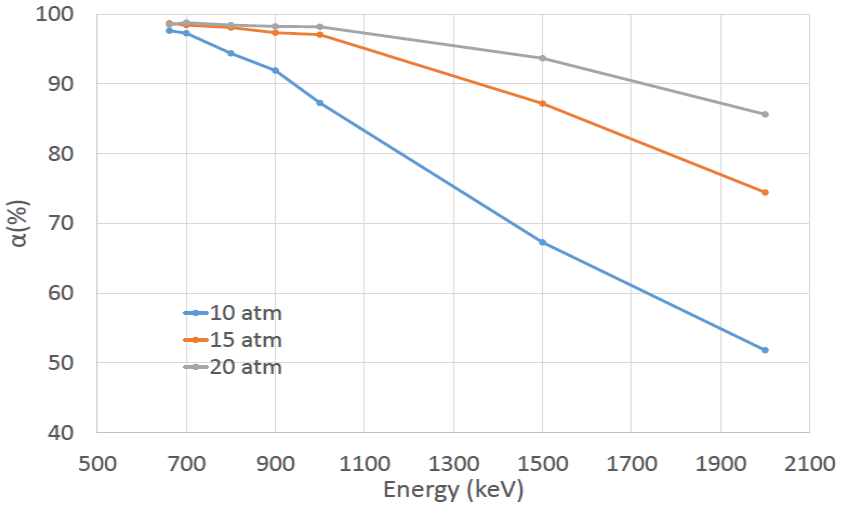

Figure 2.5: Full-energy peak efficiency as a function of the initial energy of the electrons (from 662 keV up to 2000 keV), for different pressures (10, 15 and 20 bar).

Finally, a simulation was also carried out considering that the initial photoelectron is emitted at different angles, from 0° to 90° inside the absorption region (figure 2.6). As expected, results show that the absorption efficiency is better for the lower emission angles, but up to 1 MeV, there is no significant difference between the efficiency values for the different angles. Results show that good absorption efficiencies can be obtained for the different emission angles for energies up to 1 MeV. Overall results have shown that the full-peak efficiency for photoelectrons with initial energy up to 1 MeV stands between 97% and 99%, leading us to conclude that an absorption region with this 5-6 cm dimension is adequate for the detection of radiation in the 0.1-1 MeV energy.

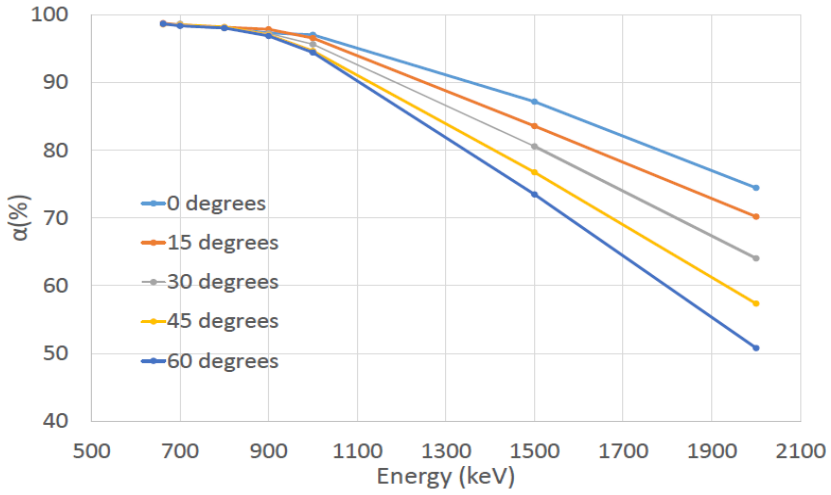

Figure 2.6: Full-energy peak efficiency as a function of the initial energy of the electrons (from 662 keV up to 2000 keV), for different angles of emission of the initial photoelectrons (from 0 up to 90°) and for 15 bar.

2.1.2 Secondary Scintillation region

As mentioned, due to the presence of a radial electric field, after the cloud of primary electrons is thermalized in the absorption region it will be increasingly accelerated towards the anode. When the electrons reach a position, r_s, where the E/p value is 1 V·cm^{-1}·Torr^{-1}, they begin to gain enough energy from the electric field to excite the atoms, but not to ionize them. In the atomic de-excitation process, VUV photons are generated.

Due to the radial dependence of the electric field intensity in this detector, the scintillation region is defined by the voltage applied to the anode with the electroluminescence occurring in a limited region near the anode [3, 6].

So, the scintillation region width depends essentially on the bias voltage between the anode and the shielding grid (G1) (figure 1.9), on the anode radius, a, on the pressure and on the radial distance of the G1 to the detector axis, r_d. With a proper biasing voltage, this region extends from the surface of the anode with radius a, where the E/p value should be close to 6 V·cm^{-1}·Torr^{-1}, to r_s which for all intents and purposes equals $6a$, where the E/p value is about 1 V·cm^{-1}·Torr^{-1}.

The value of the anode wire radius and so the extension of the scintillation region (a to $6a$) can be determined using the expression for the electric field in a cylindrical geometry. Rewriting the expression for the electric field for a cylindrical geometry we obtain:

$$E_{(r)} = \frac{\Delta V}{r.ln(E_a/E_b)} \tag{2.4}$$

where b/a is substituted by the inverted ratio of the electric field in both positions E_a/E_b. Considering a biasing voltage of 30 kV at the anode (which will be the highest voltage applied to the detector), the grid G1 at ground potential, which for a pressure of 15 bar and an anode radius, a, results in an E/p at the anode surface (at $r = a$) of 6 V·cm^{-1}·Torr^{-1} and assuming an $E/p(b)$ of 0.1 V·cm^{-1}·Torr^{-1} at G1 (at $r = r_d$), the anode radius, a, can then be calculated.

$$a = \frac{\Delta V}{E/p.ln(E/p(a)/E/p(b)).p} = 0.10 \text{ cm} \tag{2.5}$$

Once the anode radius a is defined, the secondary scintillation region dimension and the position of grid G1 can be determined. The radial position where the scintillation region starts, r_s, is 0.6 cm. Consequently, if we consider an absorption region with 5.4 cm, the position of the grid G1, r_d, is $r_d = 5.4 + r_s = 6$ cm.

It is also very important that the scintillation region's dimension is uniform along the detector so that no significant changes in light production occur. This uniformity must be assured when designing the detector.

2.1.3 Electric Field Barrier region

This is the region between the shielding (G1) and the collecting (G2) grids and it acts as an "electric field barrier region" essential to ensure an efficient charge collection at G2, since it avoids the escape of photoelectrons from G2 to the anode, at a higher electric potential. G1 also avoids signal induction from the drifting positive ions produced by the ionizing radiation in the absorption region in G2 and shielding it from fluctuations in the anode voltage.

This region's dimensions were established to obtain the best compromise between the smallest possible distance between them to avoid a large detector volume and to give easy access to the internal components of the detector during the assembly or maintenance procedures. Although there are no restrictions in terms of the E/p in this region, to keep the detector more versatile and to facilitate its assembly, a compromise was found for the barrier region dimension, defined at 2 cm. According to the scheme presented in figure 2.1, the position of the second grid (G2) is now defined, having a radius, $r_b = r_d + 2$ cm, equal to 8 cm.

2.1.4 Photoelectron Collection region

In this region, the photoelectrons extracted from the photocathode surface drift towards grid G2, where they are collected, as represented in figure 2.1. As mentioned previously, the extraction efficiency depends on the reduced electric field value near the photocathode, which depends on the voltage difference between grid G2 and the photocathode surface and on the distance between them. The E/p value above the photocathode should be as close as possible to the threshold for scintillation (1 V·cm^{-1}·Torr^{-1}) to optimize the

collection efficiency but below it, to avoid positive feedback, as discussed in section 1.4.3.3.

Since this distance is expected to be much smaller than the curvature radius of both surfaces, the E/p in this region can be approximated to a constant value:

$$E/p = \frac{\Delta V}{d\ p} \tag{2.6}$$

The voltage limit for the collecting grid was considered to be 5 kV, since this was the limit value of the voltage input of the available charge pre-amplifiers, and a reduced electric field of 0.9 V·cm^{-1}·Torr^{-1} above the photocathode was defined. These conditions will define the minimum distance between G2 and the photocathode.

Using the equation above along with mentioned conditions - ΔV of 5000 V and an E/p of 0.9 V·cm^{-1}·Torr^{-1} - for a pressure of 15 bar, a value of 0.5 cm was found for the distance d between G2 and photocathode. Because the distance is very small, possible problems can appear from non-uniformities in the electric field in this region; these problems can be easily surpassed by increasing the distance between the collecting grid and photocathode, but with the drawback of decreasing the E/p value and consequently compromising the extraction efficiency, as previously reported in [6, 19]. So, considering the position of the grid, defined in the previous section, the photocathode position is finally determined. The photocathode will be placed at a radial distance from the detector axis, $r_c = r_b + 0.5$ cm, of 8.5 cm, so the overall internal diameter of the detector will be 17 cm.

2.2 Characterization of the Detector

Considering the dimensions obtained in the previous sections, we will now characterize the detector namely its expected efficiency, gain and energy resolution, for the different possible pressures and defined energies.

2.2.1 Detector Efficiency

For L= 30 cm, and using the expression for the intrinsic detection efficiency of a detector:

$$\eta = 1 - \frac{I}{I_0} = 1 - e^{-\mu\rho L} \tag{2.7}$$

which is the fraction of the incident radiation actually deposited in the detector, η can be found for different radiation energies and different operation pressures.

Figure 2.7 presents the estimated detector efficiency as a function of the incident radiation energy (ranging from 0.1 up to 1 MeV), for different Xe pressures (3, 5, 8 and 15 bar) at room temperature. To estimate the detector efficiency, the NIST database [103] was consulted in order to obtain the attenuation coefficient, μ/ρ, for each energy.

As can be seen, the detector length is adequate for the absorption of gamma rays of energies up to 1 MeV. As expected, the absorption of gamma rays decreases with its energy and increases with increasing pressure, as the attenuation coefficient μ_L depends

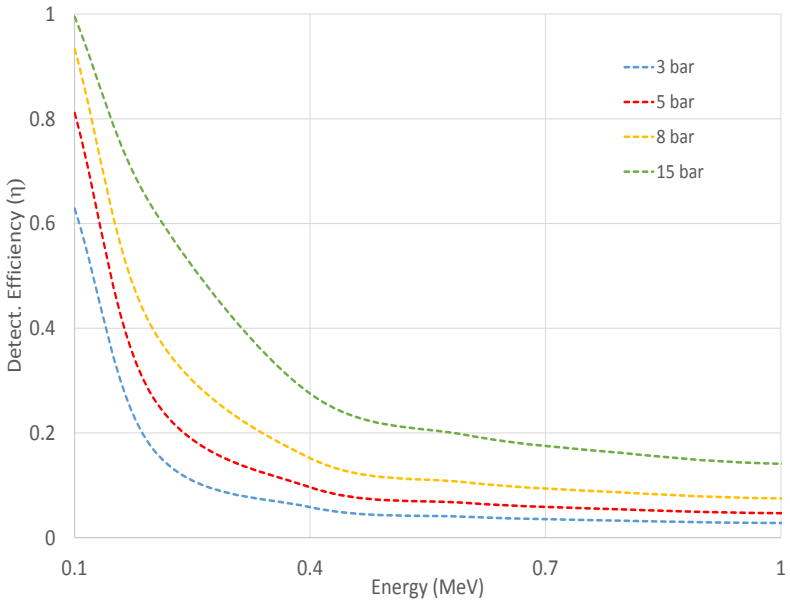

Figure 2.7: Detector efficiency, η, as a function of the incident radiation energies ranging from 0.1 up to 1 MeV, for different Xe pressures - 3 (blue), 5 (red), 8 (yellow) and 15 (green) bar, at room temperature.

on the gamma-ray energy and the atomic number (Z) and density (ρ) of the absorber.

2.2.2 Gain Considerations

The detector gain, defined as the number of photoelectrons produced by each primary electron, was also assessed. There are several aspects that contribute to photoelectron production, so a general expression for the detector gain can be defined:

$$G = N_s.T_{g1}.T_{g2}.QE.\eta_{ext} \tag{2.8}$$

where N_s is the number of photons produced by each primary electron in the secondary scintillation region already corrected due to solid angle effects, T_{g1} and T_{g2} are the transmission coefficients for grid 1 and 2, respectively, QE is the quantum efficiency of the CsI photocathode and η_{ext} is the photoelectron extraction efficiency of a CsI photocathode in Xe gas.

The influence of the different parameters in the estimate of the detector gain will be now discussed, these include:

- Solid Angle
- Anode Shadow
- Optical Transmission of the Grids
- Photoelectron Extraction Efficiency
- Electroluminescence Production

Solid Angle

Because of the geometry involved, not all of the photons produced will be able to reach the photocathode due to several factors. One process that affects the photon collection is the solid angle subtended by the deposited photocathode. Figure 2.8 depicts the solid angle (Ω_0) subtended by the photocathode here represented in light blue, for an isotropic emission occurring at the coordinate (r,z), where z is the position along the direction of the axis of the detector and r is the radial position of the event. In the same figure L represents the detector active length and R, the detector inner radius (distance from the detector axis to the photocathode surface).

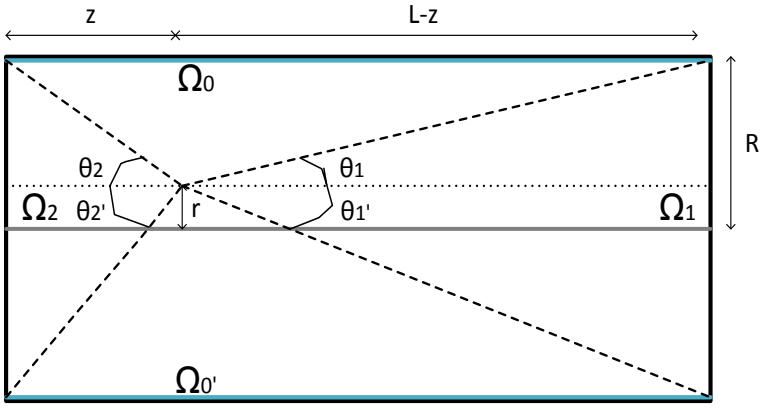

Figure 2.8: Schematic of the solid angle subtended by the photocathode for a photon emission (isotropic) at an arbitrary position (r,z), in the scintillation region.

In order to estimate the solid angle effect on the detected light and the fraction of light collected, a few assumptions were considered. Since the photons are emitted in the vicinity of the anode due to the radial dependence of the electric field, we will assume that the light source is at the z axis which is coincident with the cylinder axis, and so θ'_1=θ_1 and θ'_2=θ_2, with the solid angle, $\Omega_0(z)$, given by the following expression:

$$\Omega_0(z) = 4\pi - (\Omega_1 + \Omega_2) \tag{2.9}$$

where $\Omega_1(z)$ and $\Omega_2(z)$ are the solid angles corresponding to the fraction of light lost at the top and bottom of the cylindrical detector. From the definition of solid angle a generic expression for Ω_i(z) can be determined:

$$\Omega_i(z) = \int_0^{2\pi} \int_0^{\theta_i} sin(\theta) d\theta d\phi = 2\pi(1 - \cos\theta_i) \tag{2.10}$$

performing the integration over all angles between zero and θ_1 for Ω_1(z) and between zero and θ_2 for Ω_2(z), we obtain:

$$\Omega_1(z) = 2\pi(1 - cos(\theta_1)) \tag{2.11}$$

$$\Omega_2(z) = 2\pi(1 - cos(\theta_2)) \tag{2.12}$$

Substituting equations 2.11 and 2.12 in equation 2.9 we get:

$$\Omega_0(z) = 2\pi(cos(\theta_1) + cos(\theta_2)) \tag{2.13}$$

Considering the origin of the z coordinate at the left end of the detector of length L, and substituting θ_1 and θ_2 in the last equation, we obtain:

$$\Omega_0(z) = 2\pi \left(\frac{(L-z)}{\sqrt{(L-z)^2 + R^2}} + \frac{z}{\sqrt{z^2 + R^2}} \right) \tag{2.14}$$

where z is the position where photon emission occurs, which is considered to be at r=0.

Using the MATLAB® code, and considering the dimensions previously determined for the detector length L (30 cm) and for the detector inner radius R (8.5 cm), we obtained the photon's detectable fraction, η_Ω, defined as the fraction of photons emitted in the axis of the detector that can reach the photocathode, which is represented in figure 2.9 as a function of the z position.

In this case, $\eta_\Omega(z)$, is obtained by simply dividing the solid angle by 4π, which results in:

$$\eta_\Omega(z) = \frac{1}{2} \left(\frac{L-z}{\sqrt{(L-z)^2 + R^2}} + \frac{z}{\sqrt{z^2 + R^2}} \right) \tag{2.15}$$

Figure 2.9 displays the resulting detectable fraction for the cylindrical detector, for 0<Z<L.

Considering the detectors dimensions, $\Omega/4\pi$ will range between 48% and 87% of the total emitted electroluminescence. This represents a considerable effect in the detector gain, depending on the absorption position of the incoming photon. A solid angle correction will therefore have to be considered.

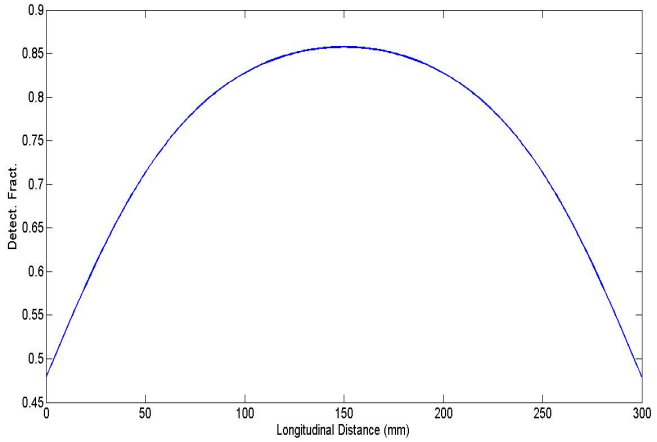

Figure 2.9: Longitudinal detectable fraction for a cylindrical detector.

Anode Shadow Effect

Another parameter to take into account in the detection of light is the influence of the shadow of the anode in the fraction of photons that can reach the photocathode. This depends on the distance of the emission point to the anode, and to calculate this effect, we used the following method. First we need to assume that the radial detectable fraction is not dependent on the longitudinal position, z, and considering the emission only on the xy plane. Let us start by considering that the photon emission occurs at a distance r from the anode axis that ranges from a, anode radius, to r_s, the beginning of the scintillation region, as depicted in figure 2.10.

If θ corresponds to the emission angle for which the photons emitted are tangent to the anode surface, the fraction of photons that will be blocked by the anode correspond to $2\theta/2\pi$ and so the fraction of photons that are not blocked by the anode shadow (radial detectable fraction, η_a(r) can be determined:

$$\eta_a(r) = \frac{2\pi - 2\theta(r)}{2\pi} \tag{2.16}$$

$$\eta_a(r) = \frac{2\pi - 2\arcsin\left(\frac{a}{r}\right)}{2\pi} \tag{2.17}$$

Figure 2.11 depicts the calculated detectable fraction considering the anode's shadow as a function of the radial distance to the anode in this detector, with r_s=6 mm and a=1 mm that results in a scintillation region of 5 mm.

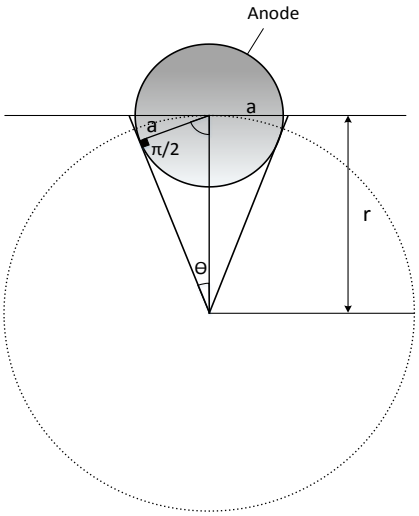

Figure 2.10: Geometric considerations for the anode shadow contribution on the detectable fraction of the photons.

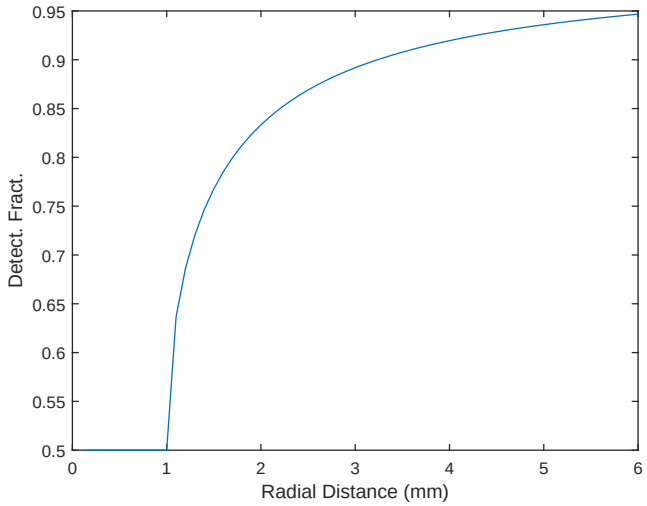

Figure 2.11: Fraction photons radially detected in a cylindrical detector with a anode radius of 1 mm and a scintillation region of 5 mm (r_s-a).

The shadow created by the anode results in a fraction of detected photons ranging between 50% (at the anode surface, r=1 mm) and about 95% (in the beginning of the scintillation region, r=6 mm).

Optical Transmission of the Grids

Another issue that must be taken into account is the optical transmission of the grids.

As already mentioned, this detector has two grids, G1 and G2. G1 is made of stainless steel (100 μm thickness) with hexagonal holes and an optical transparency provided by the manufacturer of T_{grid}=0.78. Grid G2 is made of the same material as G1, but due to its proximity to the photocathode, a thinner mesh (50 μm thickness), was applied to this grid to allow a higher electric field uniformity in the charge collection region. A simulation to study the electrical field uniformity dependence with the open area was made and is available in Appendix A.3.2. The transmission of the mesh according to the manufacturer is T_{mesh}=0.88. Assuming a normal incidence, the combined optical transmission of the grids, T_{opt}, can be simply determined using the following expression:

$$T_{opt} = T_{G1} \times T_{G2} \tag{2.18}$$

where T_{G1}=T_{grid} and T_{G2}=$T_{grid} \times T_{mesh}$, with T_{G1} and T_{G2} being the optical transmission of the shielding (G1) and collecting (G2) grids respectively. In this case, the optical transmission is approximately 0.54.

Photoelectron Extraction Efficiency

After crossing both grids, the photons will impinge on the photocathode producing the photoelectrons that are in the origin of the signal of the detector.

As seen previously in the end of Chapter 1, the performance of a photocathode is characterized by its QE, that is reduced due to backscattering of the photoelectrons by the gas atoms, with this behaviour being described by the extraction efficiency. This effect depends on several factors: energy of the incident photons, gas composition, gas pressure, and extraction electric field intensity [75] [76] [77]. As a consequence, results are different depending on whether the photocathode is placed in vacuum or in a gas atmosphere.

When in a gaseous atmosphere, studies carried out by Escada [75] and Covita [78] have shown that the extraction efficiency (EE) becomes independent of the pressure when the electric field is scaled accordingly and that it can be improved increasing the reduced electric field in the extraction region. In addition to this effect, an increase of the quantum efficiency with the photon incidence angle has already been observed by Lopes and Conde [105] and Tremsin and Siegmund [106], but little information on this issue is available.

In order to understand the influence of the incidence angle in the performance of the present detector, a parallel study was conducted by Rolo [107]. In this study, the role of the angle of incidence on the extraction efficiency was assessed with a dedicated system designed to reproduce the photon to photoelectron conversion stage of this detector, which allows the measurement of the relative extraction efficiency for photon incidence angles from normal incidence (0°) to 50°, which is the highest angle of incidence possible for the detector dimensions. A schematic of the detector used in this study is shown in figure 2.12.

A summary of the results obtained in [107] is presented here since this data can be used to correct the EE values for this detector prototype.

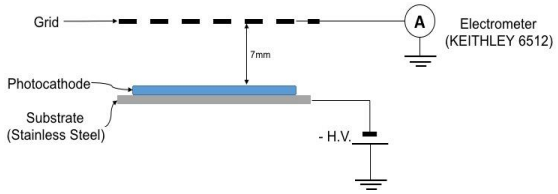

Figure 2.12: Schematic of the set-up used for the study of the photoelectrons' relative extraction efficiency as a function of the photon incidence angle. Taken from [107].

In this study, the Relative Extraction Efficiency (REE), *i.e.* the extraction efficiency relative to the normal angle of incidence (0°), was measured for different Xe pressures. The incidence angle was varied between 0° and 50°, in 5° steps, for different reduced electric fields (E/p) values. Figure 2.13 shows the results for Xe at 5 bar, the error bars are within the symbols used. Each line represents a set of measurements at a characteristic E/p.

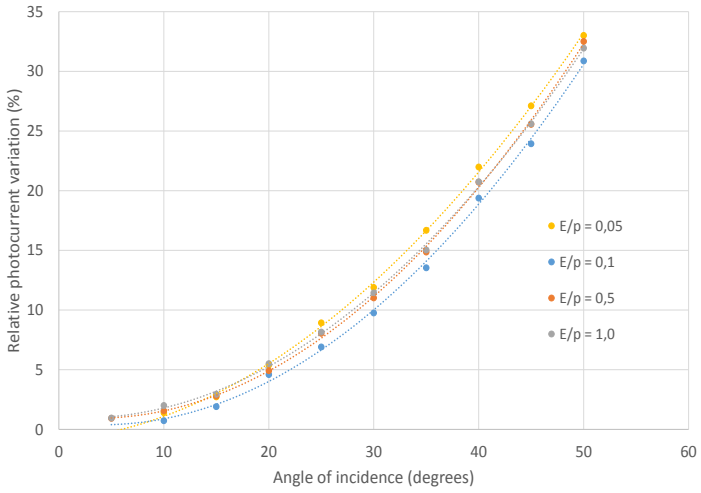

Figure 2.13: The relative photocurrent variation as a function of the light incidence angle for different E/p conditions, for 5 bar of Xe. Adapted from [107].

The results show that the REE increases with the incidence angle. For an incidence angle of 50°, an increase of ∼30% was observed in the relative extraction efficiency. The results are in accordance with the work of Lopes and Conde [105] and Tremsin and Siegmund [106]. Both authors attributed their results to the features of the photocathode, as described by a theoretical model proposed by Fraser [108], based on the absorption and escape length of photoelectrons. One of the most relevant features mentioned is the depth at which the photon interaction occurs, *i.e.*, the depth at which photoelectrons are produced [19, 39]. As the incidence angle increases, electrons are produced closer to the surface, leading to smaller losses of energy in their drift towards the surface of the photocathode, thus to a larger number of photoelectrons that can reach the surface with enough energy to escape the material. This was already suggested by Lopes and Conde, and is compatible with the observations and interpretations made by Tremsin and Siegmund. It was also possible to verify with this study that the behaviour of REE with the incidence angle is independent of the gas pressure for the same E/p, meaning that the energy lost by the photoelectrons in collisions with the gas atoms is balanced by the energy gained from the applied electric field.

Although this was a complementary study, it was conclusive concerning the influence of the incidence angle on the extraction efficiency and will allow a more accurate estimate of the gain of the GPSC detector developed, and so a more adequate compensation of the effects mentioned before in order to obtain a close to uniform detector response.

Electroluminescence Production

To obtain the number of photons, N_s, produced by one electron drifting along an elementary drift distance dx below the ionization threshold, we can use equation 1.27, where E_s depends on the r-value and substituting A and B with their values for Xe [3].

$$\frac{1}{p}\frac{dN_S}{dr} = A\frac{E_S(r)}{p} - B \tag{2.19}$$

As can be seen, the production of photons depends on several features: detector geometry and anode voltage, V_a (since E_S depends on it), secondary scintillation region dimensions, detector filling gas (A and B values) and its pressure. Using this equation it is possible to obtain the information on the number of secondary photons produced per primary electron, in the secondary scintillation region.

We assume that the electrons reach the beginning of the scintillation region thermalized and so their drift is essentially radial, so the number of photons produced by one electron drifting along an elementary drift distance dr, below the ionization threshold, until it

reaches the photocathode, is given by the following integral:

$$N_S = \int_a^{r_s} (AE_S(r) - pB)\eta_a(r)\eta_\Omega(z)dr \tag{2.20}$$

$$N_S = \int_a^{r_s} (AE_S(r) - pB)\left(\frac{2\pi - 2\theta(r)}{2\pi}\right)\frac{\Omega(z)}{4\pi}dr \tag{2.21}$$

where $\eta_a(r)$ corresponds to the fraction of photons that are not blocked by the anode in a given photon emission position (r,z) in the detector scintillation region (see section 2.2.2) and $\Omega(r,z)$ is the solid angle subtended by the photosensor for the position of photon emission, which is divided by 4π in order to obtain the fraction of photon able to reach the photocathode due to the solid angle, in this case $\eta_\Omega(z)=\frac{\Omega(z)}{4\pi}$. Substituting the expression 2.15 of the longitudinal solid angle in equation 2.21 we get:

$$N_S = \int_a^{r_s} \underbrace{(AE_S(r) - pB)}_{\text{Light production}} \underbrace{\left(\frac{2\pi - 2\theta(r)}{2\pi}\right)}_{\text{Radial effect}} \underbrace{\frac{1}{2}\left(\frac{(L-z)}{\sqrt{(L-z)^2+R^2}} + \frac{z}{\sqrt{z^2+R^2}}\right)}_{\text{Longitudinal effect}} dr \tag{2.22}$$

Calculating the integral for the number of photons produced (equation 1.27) with E_S given by equation 2.1 without the $\eta_a(r)$ and $\eta_\Omega(r)$ contributions, we were able to find that approximately 866 photons are produced for each primary electron drifting in the scintillation region (r_s>r>a), for r_s=0.6 cm and a=1 cm with E/p= 6 V·cm^{-1}·Torr^{-1} at the anode surface at p= 15 bar. By introducing the effect of the shadow created by the anode (introduction of the term $\eta_a(r)$) in the integral, it is possible to find that only 705 of the initial 866 photons produced per primary electron can successfully exit the scintillation region, eventually reaching the photocathode. Nevertheless, not all of these 705 photons will reach the photocathode due to the solid angle effect. As discussed previously, the solid angle subtended by the CsI photocathode depends on the point along the axis (z) where the light is produced. The dependence on the z position of the number of photons capable of reaching the photocathode is shown in figure 2.9, and varies between 48-87%.

Finally the gain can be calculated using equation 2.8 for a pressure of 15 bar and a E/p of about 6 V·cm^{-1}·Torr^{-1} at the anode surface and of 0.9 V·cm^{-1}·Torr^{-1} both at the electric barrier field and collecting regions. Considering N_s=0.87×705 or 0.48×705 and assuming that the combined transmission of the grids is approximately 54% (calculated in section 2.2.2), the QE about 20% for the CsI [39] and the extraction efficiency values about 7.2% (for the E/p=0.9 V·cm^{-1}·Torr^{-1} above the photocathode [19]), the detector gain can be estimated to be between about 2.6 phe$^-$/e$^-$ and 4.8 phe$^-$/e$^-$ depending on the z position of the initialphoton interaction.

2.2.3 Energy Resolution

Most of the applications related to the detection of radiation rely on the analysis of the energy of the incident radiation [7]. The accuracy of the measurement is assessed by the energy resolution of the detector, which is energy dependent.

As already mentioned, the limiting energy resolution depends on the fluctuations associated with the signal formation in the detector from the absorption to the charge collection at the grid.

In addition to the fluctuations in the number of electron-ion pairs, the energy resolution in proportional scintillation counters is affected by fluctuations in the gain (number of photons produced, N_S, by a single electron), associated with the EL yield, J, and due to solid angle effects, σ_{Ns} [51]. Another source of fluctuations is associated to the VUV photon-to-photoelectron conversion stage, which is due to two distinct reasons: the intrinsic fluctuations in the extraction efficiency and fluctuations due to the variance in the incidence angle of the VUV photon in the photocathode, σ_q, for a unity gain in the photosensor, G_q [22]. As a result, the limiting energy resolution of the proportional scintillation counter, can be expressed by:

$$R = 2.355\sqrt{\frac{F}{\bar{n}} + \frac{1}{\bar{n}} \times \left(\frac{J}{N_S} + \left(\frac{\sigma_{Ns}}{N_S}\right)^2\right) + \frac{1}{N_e}\left(1 + \left(\frac{\sigma_q}{G_q}\right)^2\right)} \tag{2.23}$$

Or, re-writing $\bar{n} = E_g/w$:

$$R = 2.355\sqrt{\underbrace{\frac{Fw}{E_g}}_{\text{cloud of e}^-} + \underbrace{\frac{w}{E_g} \times \left(\frac{J}{N_S} + \left(\frac{\sigma_{Ns}}{N_S}\right)^2\right)}_{\text{amplification}} + \underbrace{\frac{1}{G} \times \frac{w}{E_g} \times \left(1 + \left(\frac{\sigma_q}{G_q}\right)^2\right)}_{\text{photosensor}}} \tag{2.24}$$

Substituting in this last expression the w-value of Xe for 21.6 eV [17], the F value for 0.17 [17], the J reference value of 0.03 given in [51], N_s value for 705 photons, σ_{Ns} for 0.25 (which results from the variance in the solid angle, as discussed previously in section 2.2.2), the detector gain, G, for 3.7 (here considering the mean value of the solid angle limits - 48% and 87%), and a σ_q of 0.15 (that results from the variance in the extraction efficiency, as discussed in section 2.2.2) the limiting energy resolution for this GPSC can be calculated.

Figure 2.14, shows the energy resolution obtained in 2.24 as a function of the energy of the incident radiation from 100 keV up to 1000 keV in Xe, using the predicted gain of the GPSC calculated in the previous section together with R_{int} (equation 1.22) for the same energy resolution.

The intrinsic energy resolution in a gaseous radiation detector, for an incident radiation of 662 keV is $R = 0.24\%$. However, due to the above mentioned fluctuations the limit energy resolution of this prototype is expected to be about 1% in the conditions mentioned above. One important conclusion is that the energy resolution for this prototype is highly affected and limited by both solid angle and fluctuations in the extraction efficiency.

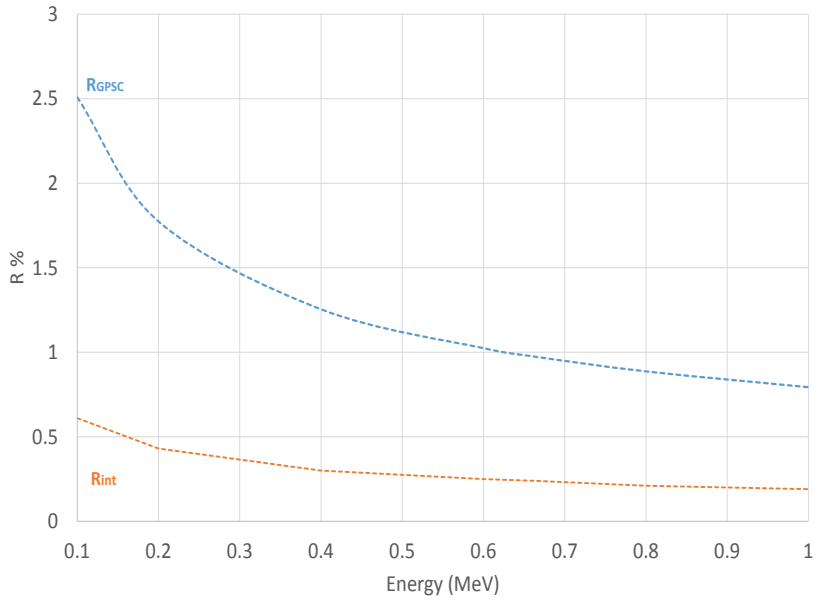

Figure 2.14: Intrinsic resolution (orange dashed line) and estimated limit for the energy resolution for the GPSC (blue dashed line) as a function of the energy of the incident radiation from 100 keV up to 1000 keV in Xe for a detector gain of 3.7.

Other factors not included here may also have a significant contribution further worsening the energy resolution. These factors include: electronic noise and non-uniformities in the electric field in the collecting region. In theory, this value places the detector at a competing level with the existing solutions (section 1.5). Another important fact is the gain of the detector, which affects the energy resolution attainable. The values presented here establish the limiting value for the energy resolution and the goal for detector optimization.

2.2.4 Comparison between 1st and 2nd Prototype

This new prototype of the HPXe-GPSC, as seen before has a working principle similar to the previous prototype but instead of having a planar geometry it has a cylindrical geometry. A comparison of both prototypes will now be made, concerning:

- Detection efficiency
- Gain (Solid angle, Optical transmission and Biasing voltage)
- Energy resolution

2.2.4.1 Detection efficiency

When comparing the detecting efficiency it is possible to see that the 2nd prototype with a cylindrical geometry has a higher detecting efficiency. As mentioned, the detecting efficiency for the same gas and density depends on the path travelled by the photon. If we look at both configurations it is possible to see that in the second prototype, there are 30 cm available to stop the radiation that enters one of the ends of the cylinder, while in the first prototype because the radiation enters perpendicular to the absorption/drift region, there are only 4 cm available and, as a consequence, the resulting detecting efficiency is much worse.

Although the detection efficiency could be improved in the first prototype by increasing the absorption region to about 30 cm, it would imply a much higher ΔV (about 34 kV just for the absorption region for a pressure of 15 bar and an E/p of 0.1 V·cm^{-1}·Torr^{-1}), to which we would need to add about 44 kV to define the scintillation region. This adds up to 78 kV, whereas in the present configuration, the voltage needed for the same conditions is much smaller - about 28 kV.

Also as a result of the geometry involved, the resulting active volume of detection, *i.e.* the gas volume used to absorb the incident radiation, is significantly improved in the 2nd prototype, about 3369 cm^3 when compared with the 726 cm^3 of the previous prototype, which can be important in the evaluation of the detector cost, since most of the gas volume will be used in the radiation detection. Considering the dimensions involved in both prototypes it is possible to see that the active volume of detection in the 1st prototype corresponds to about 43% of the total volume, while in the 2nd prototype it is about 50%. Moreover, this value could still be improved reducing the spacing between the collecting and shielding grid.

2.2.4.2 Gain

The gain of this new prototype is expected to be improved as a result of the improvement in several features such as: the solid angle, combined optical transmission of the grids and biasing voltage, whose improvements will be now addressed.

Solid angle

Another advantage of having a detector with this geometry (and associated configuration) and with these dimensions, is the solid angle subtended by the photosensor. Here again the difference is impressive. When comparing the solid angle between the two we can observe that the solid angle in the cylindrical geometry ranges between 0.48 near the ends and 0.87 at the centre, while in the planar geometry it ranges between 0.10 and 0.16 at the centre. In this case, improving the solid angle in the previous prototype would be challenging as it is already limited to a maximum of 0.5 in the optimal conditions.

Improving the solid angle in the first prototype can be performed using two complementary approaches: one is by getting scintillation region closer to the photocathode and the second by increasing the area of both the photocathode and collecting grid. Both approaches have intrinsic limitations such as ensuring an uniform distance between the grids, and possible problems with discharges, since the grids will be placed at very small distances.

Optical transmission

Another expected advantage introduced by the new geometry is related with the number of grids used to define the different regions that is smaller. In fact, this is a direct result of the electric field geometry. In the cylindrical geometry, both absorption/drift and scintillation regions are defined by the voltage difference applied between the anode and the shielding grid. This is only possible because the electric field is radially dependent and ranging from about 0.1 V·cm^{-1}·Torr^{-1} at the shielding grid to 6 V·cm^{-1}·Torr^{-1} at the anode surface, with the scintillation region being defined by the reduced electric field intensity values, starting where the E/p is above 1 V·cm^{-1}·Torr^{-1}. So, since the secondary photons are produced near the anode, the number of grids that they will encounter on their way to the photocathode is only two, while in the previous prototype (planar geometry), there were three. Using similar grids will result in a better overall optical transmission.

Biasing voltage

This new configuration will allow a reduction in the number of structures to be biased and also a more efficient use of the bias voltage for the scintillation yield, requiring a lower biasing voltage to produce the same detector gain.

In order to understand the influence of the biasing voltage on the gain we will now consider equation 1.27. Looking at this expression, it is possible to see that the production of electroluminescence depends basically on two factors: the energy that the electrons can gain from the electric field, which is related to the ΔV in this region and the scintillation region dimension, d.

Using the same equation it is possible to relate for both geometries the scintillation yield with the applied voltage, ΔV_s, at the scintillation region (for the planar geometry) and ΔV_c between the anode and grid G1 (for the cylindrical geometry).

For the planar geometry:

$$N_s^p = \int_0^d (AE_s - pB)dr \quad (2.25)$$

$$N_s^p = \int_0^d A\frac{\Delta V_s}{d} - pBdr \quad (2.26)$$

$$N_s^p = A\Delta V_s - pBd \quad (2.27)$$

For the cylindrical geometry:

$$N_s^c = \int_a^{r_s} (AE_s(r) - pB)dr \quad (2.28)$$

$$N_s^c = \int_a^{r_s} A\frac{\Delta V_c}{rln(b/a)} - pBdr \quad (2.29)$$

$$N_s^c = A\frac{\Delta V_c ln(r_s/a)}{ln(b/a)} - pB\Delta r \quad (2.30)$$

Assuming that the number of scintillation photons, N_s, produced in the scintillation region and its dimension in both planar and cylindrical geometries are the same, we obtain the relation that will allow us to directly compare the ΔV applied in the two geometries:

$$\Delta V_s = \left(\frac{ln(r_s/a)}{ln(b/a)}\right)\Delta V_c \tag{2.31}$$

As b is greater than r_s, ΔV_s will be smaller than ΔV_c. Nevertheless, ΔV_c refers to the whole voltage applied in the detector (drift and scintillation region) and not only in the scintillation region as in the planar geometry, while to ΔV_s the biasing voltage of the drift region needs to be added. The ΔV is not the same for the scintillation region in the cylindrical and planar geometries. Only in the case when b is equal to r_s, does the scintillation yield on both geometries become the same. As a matter of fact, the main advantage of using a cylindrical geometry resides not in the N_s but, as we can see, in the wider solid angle and the fact that it only makes use of two grids, that allows to compensate for this difference in the scintillation yield. If we look at the general expression for the gain of the GPSC detector (equation 2.8);

$$G = N_s.T_{opt}.QE.\eta.\frac{\Omega}{4\pi} \tag{2.32}$$

the advantage of using a cylindrical geometry becomes evident since, considering just geometrical factors and assuming that the scintillation yield is the same for both configurations, the difference that we obtain is basically the reason between the optical transmission of the grids multiplied by the reason between the solid angles of both structures. So, if we use the dimensions of both prototypes and consider the maximum solid angle we verify that the gain given by the cylindrical geometry is about 4.8 times greater than the planar one. Of course we are neglecting here the effect of the anode shadow. In the worst case scenario, the scintillation loss due to the anode shadow is 0.5, and even considering this additional contribution, the gain would be about 2.5 times higher in the cylindrical geometry considering the same scintillation yield.

Table 2.1: Typical voltage difference, ΔV, for biasing the MGHP-GPSC (1st and 2nd prototypes) absorption/drift and scintillation regions for 15 bar of Xe and for the specified E/p in the last column.

Regions	ΔV (kV) (1st prototype)	ΔV (kV) (2nd prototype)	E/p ($V{\cdot}cm^{-1}{\cdot}Torr^{-1}$)
Absorption/Drift	4.5-45	15.5	0.1-1
Scintillation	7.3-43.9	12.1	1-6
Total	48.4	27.6	-

Please notice that in the determination of the total ΔV for the 1^{st} prototype the E/p values of 0.1 and 6 $V{\cdot}cm^{-1}{\cdot}Torr^{-1}$ were used for the absorption/drift and scintillation region, respectively. If we further increase the pressure to 20 bar, using the same E/p conditions, ΔV will be much higher in the planar geometry (about 64.5 kV) when compared

to the cylindrical one (about 36.9 kV).

Summary

Combining all these characteristics it is expected that this prototype will display improved performance while simultaneously solving practical constraints. Tables 2.2 and 2.3 summarize the main characteristics of both prototypes.

Table 2.2: Resume of the characteristics of the 1st and 2nd prototype of the MGHP-GPSC.

Characteristics	Planar Geometry	Cylindrical Geometry
Pressure Range	5-10 bar	5-20 bar
Det. Efficiency (662 keV 15 atm)	<1%	∼20%
Solid Angle ($\Omega/4\pi$)	0.16	0.48-0.87
Detector Active Volume	726 cm^3	3369 cm^3
Grids Combined Optical Transmission	∼0.62	∼0.54
Detector Gain	1.6-3.2 phe^-/e^-	1.7-6.7 phe^-/e^-

Table 2.3: E/p and length of the different regions of the MGHP-GPSC (1st and 2nd prototypes).

Regions	Length (1st prototype)	Length (2nd prototype)	E/p ($V{\cdot}cm^{-1}{\cdot}Torr^{-1}$)
Absorption/Drift	4.0 cm	30 cm/5.4 cm	0.1-1
Scintillation	0.65 cm	0.5 cm	1-6
Optical transmission	1.2 cm	-	<1
Electric field barrier	2.4 cm	2.0 cm	<1
Photoelectron collection	1 cm	0.5 cm	<1

2.3 Signal characterization and electronic processing

With the detector gain and efficiency characterized and compared with the previous prototype, it is important to characterize the detector impedance as well as the expected signal (amplitude and width), since this is important in the signal formation. For this reason and to choose the best electronic amplification circuit to amplify the detector signal, we calculated the detector capacitance.

2.3.1 Detector Capacitance

A basic concept in the processing of pulses from radiation detectors is the impedance of the devices that compose the signal processing chain. A simple schematic of the detector impedance can be found in figure 2.15.

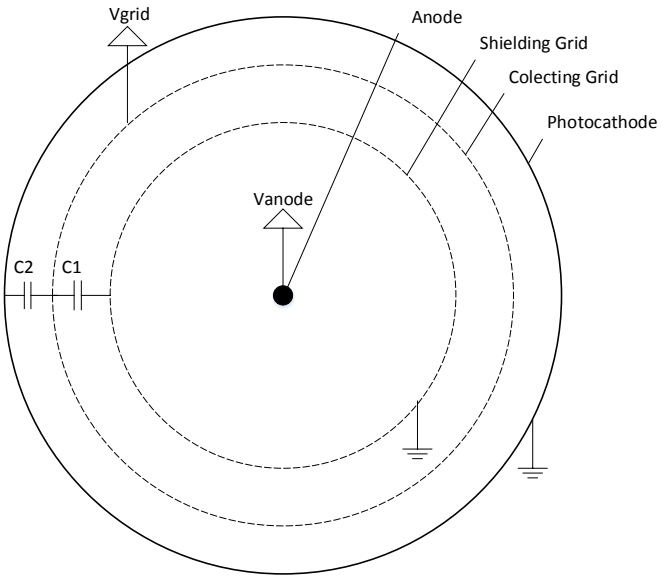

Figure 2.15: Schematic of the detector, including the relevant capacitances and voltage supplies.

From the electronic point-of-view, this detector can be represented by a current source in parallel with two capacitors, since both the shielding grid and photocathode are at ground potential, with a low impedance resistor in series, as can be seen in figure 2.16.

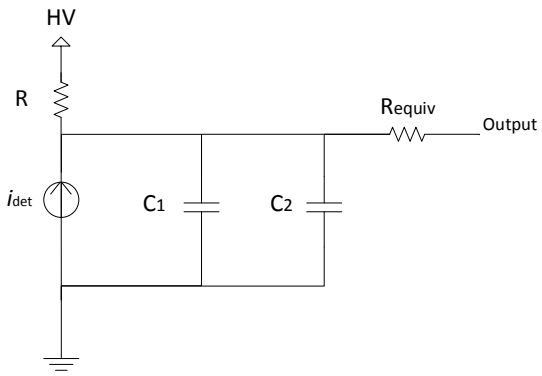

Figure 2.16: Detector electronic equivalent circuit.

Now that the relevant capacitances of the detector have been identified it is important to estimate their value. Applying the general expression that defines the capacitance between two conductors: $C{=}Q/\Delta V$, where Q is the charge in each electrode and ΔV is the voltage difference between them, and using the expression for ΔV for two coaxial

conducting cylinders (of infinite length),

$$\Delta V = \frac{Q}{2\pi\varepsilon L}\ln(r_b/r_a) \tag{2.33}$$

the expression for the capacitance of two coaxial cylindrical electrodes is equal to:

$$C = \frac{2\pi\varepsilon L}{\ln(r_b/r_a)} \tag{2.34}$$

substituting r_a and r_b for the shielding and collecting grid radius, 6 cm and 8 cm respectively, as well as the detector length, L=30 cm, and considering the permittivity of Xe, ε (calculated using ε_r=1.83 [109] and the vacuum permittivity, ε_0=8.854187827$\times10^{-12}$ F·m^{-1} [110]) we are able to determine that the capacitance between the shielding and collecting grids equals 106 pF (C_1).

Substituting in equation 2.34 the radii values, r_a and r_b for the CsI photocathode and collecting grid radii, 8.5 cm and 8 cm respectively, we are able to calculate the capacitance between the photocathode and collecting grid, which is 504 pF (C_2). So, the equivalent capacity of the detector is C_{total}=C_1+C_2=610 pF.

2.3.2 Charge amplitude

In order to estimate the charge signal amplitude after the absorption of a 662 keV gamma-ray photon in the detector, we first need to calculate the number of primary electrons produced, and then the number of photoelectrons extracted from the photocathode.

The number of primary electrons produced depends on the energy of the incident ionizing radiation or particle and on the w-value, which is the mean energy to form an electron-ion pair. Considering the w-value for Xe of 21.6 eV [17], and using equation 1.7, we are able to calculate the average number of electrons, $\bar{n}$, formed following the absorption of a gamma photon of 662 keV in Xe:

$$\bar{n} = \frac{E_{ir}}{w} \simeq 30648 \text{ e}^- \tag{2.35}$$

These electrons will afterwards produce photons through secondary scintillation processes, which will produce photoelectrons in the CsI photocathode. The number of photoelectrons can be easily obtained by simply multiplying the number of primary electrons by the detector gain, G. Considering the estimated gain of 5 for 15 bar of Xe, as a result the average number of photoelectrons extracted, $\bar{n}_{phe^-}$, is given by:

$$\bar{n}_{phe^-} = n.G \simeq 153240 \text{ phe}^- \tag{2.36}$$

to which corresponds a charge of 2.45$\times10^{-14}$ C, collected at the collecting grid, G2. Knowing the expression of the equivalent noise charge, ENC, of the preamplifier and assuming that the equivalent input capacitance is the capacitance calculated for the detector

(610 pF), we are able to find that the ENC will be about 2.56×10^{-16} C (as it will be calculated in section 3.6.5). If we compare the expected signal with the ENC obtained for the operating conditions, we can see that the signal is about 96 times greater than the noise, which suggests that in optimal conditions, *i.e.* without any other noise sources, the signal-to-noise ratio, SNR (using the same definition that will be used in section 3.6.4) is expected to be about 40.

2.3.3 Signal width

Another important characteristic of the signal generated by the detector is the signal width as it will influence the choice of the detector's associated electronics. In the HPXe detector, the signal width depends on several aspects: primary electron cloud dispersion, and drift time in the scintillation and in the collecting regions. Due to the dimensions and reduced electric fields involved, the contribution to the signal width of the drift time in the scintillation and in the collection regions are usually negligible when compared to the primary electron cloud dispersion.

Assuming the worst case scenario, when the primary electron cloud is radially dispersed in the entire absorption/drift region, the signal width will be given by the time it takes an electron near grid G1 to reach the scintillation region.

In order to determine the signal with, Δt_d, since the electron drift velocity depends on the reduced electric field and the electric field has a radial dependence, the following integral was calculated:

$$\Delta t_d = \int_b^{r_s} \frac{dx}{v_d(x)} \tag{2.37}$$

The expression for the drift velocity of electrons in Xe used to calculate the integral was obtained by fitting the data available in [19]. In figure 2.17 is depicted the electron drift velocity and electron mobility in Xe as a function of the reduced electric field.

Calculating the integral on equation 2.37, assuming a reduced electric field at the anode surface of 6 V·cm^{-1}·Torr^{-1}, an upper limit for the signal width expected with this detector is about 100 μs.

2.3.4 Readout Electronics

One of the most important aspects of the detector is the signal conditioning circuitry which, as we saw earlier, includes an amplification stage. In fact, the amplification stage besides providing the shaping to optimize the processing, also provides amplification to the charge signals. The amplification stage is usually separated in two stages, the pre-amplifier and the shaping amplifier (generally referred to as amplifier). The charge pre-amplifier used should be placed as close to the detector output as possible. Its objective is to provide the input signal with a gain to ensure that the signal transmitted has a magnitude well above the electronic noise.

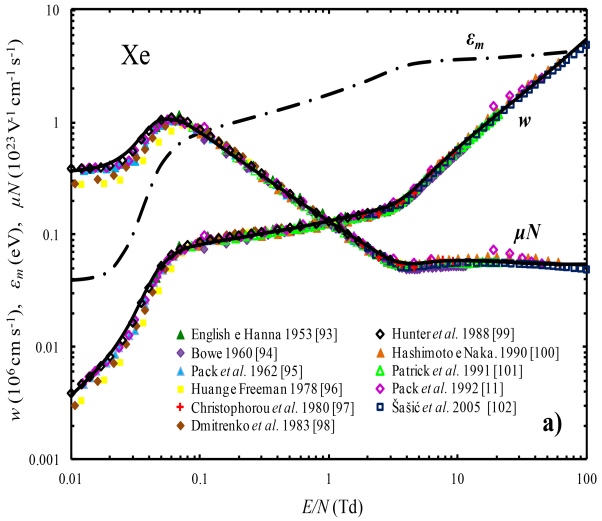

Figure 2.17: Representation of the electron drift velocity and electron mobility dependency on the reduced electric field. Taken from [19].

In the most common configuration, the capacitor introduced in the feedback network forces the signal current to integrate its charge in C_f (feedback capacitor) rather than in C_{in} (input capacitance). The total charge created by the radiation interaction inside the detector in a single event (Q) splits itself between $C_{in}(Q_{in})$ and $C_f(Q_f)$ so that Q=Q_{in}+Q_f. So, the charge integrated in each capacitor is given by the following expressions, where A is the open-loop gain of the pre-amplifier [111].

$$Q_{in} = Q\frac{1}{1+\frac{C_f}{C_{in}}(1+A)} \tag{2.38}$$

$$Q_f = Q\frac{1}{1+\frac{C_{in}}{C_f}(1+A)\frac{1}{1+A}} \tag{2.39}$$

One important observation that can be made is that as A increases to infinity, Q_{in} tends to zero and Q_f to Q, meaning that all the charge is swept from the detector to the feedback capacitor (C_f) if A is much larger than (1+ C_{in}/C_f) [111].

So, the condition for the pre-amplifier to behave as a perfect integrator to the input charge pulse is that A>>1+(C_{in}/C_f) [111].

In addition, it is important for the pulse duration to be shorter than the decay time constant of the pre-amplifier circuit so the output voltage is proportional to the total integrated charge in the pulse [7]. In our case, the pre-amplifier should have a decay time constant of about 100 μs in order to have a voltage signal proportional to the charge signal at its input, which is proportional to the energy deposited in the detector.

Although the charge pre-amplifier already provides some amplification to the signal, the signal shape is inadequate for an appropriate pulse height analysis, setting an unacceptably low upper limit on the count rate. For this reason, the output voltage signal coming from

the pre-amplifier needs to be shaped and amplified by a linear amplifier, before being fed to the oscilloscope and multichannel analyser (MCA), where the analysis of the signal (real time) is performed. The oscilloscope allows us to observe the shape of the pulse coming out of the detector and parameters like the rise time of the pulse and the electronic noise, while the MCA will be used to obtain the spectral distribution of the pulse amplitude. However, there are several factors that may jeopardize the performance of the detector [9]:

- Electronic noise - this is a consequence of the intrinsic electronic noise generated both by the detector and the various electronic components of the biasing and acquisition system.
- Pulse pile-up - when two pulses overlap in time in the signal processing system.
- Ballistic deficit - this is a measure of the inefficiency of charge integration and is defined as the fractional deficit of the output pulse height compared to that for an ideal charge integration.

2.4 Detector Design

According to the previous description and to the considerations made, the detector was designed using the 3D modelling software, Solidworks. The result can be seen in figure 2.18. A detailed description of the detector can be found in Appendix A.

The external structure of the detector consists of a cylindrical tube (made of stainless steel 316 L with an outside diameter of 220 mm, a wall thickness of 20 mm and a length of 340 mm) with two flanges fixed at the top and bottom also with a 220 mm diameter and a thickness of 20 mm each. One of the flanges supports the structure to the electrical feedthroughs selected (21184-01-CF Cerameseal model for the anode and the 18088-01-CF Cerameseal model for the collecting grid).

The main objective of this structure is to support the various components of the internal structure, to provide the needed support to the electrical feedthroughs and also to isolate the detector from the outside environment, allowing the gas to be introduced, circulated and retrieved. Based on our previous discussion, the detector dimensions, which were the basis for the present design, are summarized below.

Radial Dimensions:

- Anode - 0.1 cm
- Absorption plus Scintillation region - 5.9 cm
- Electric field barrier region - 2 cm
- Photoelectron collecting region - 0.5 cm

Length:

- Effective absorption length - 30 cm

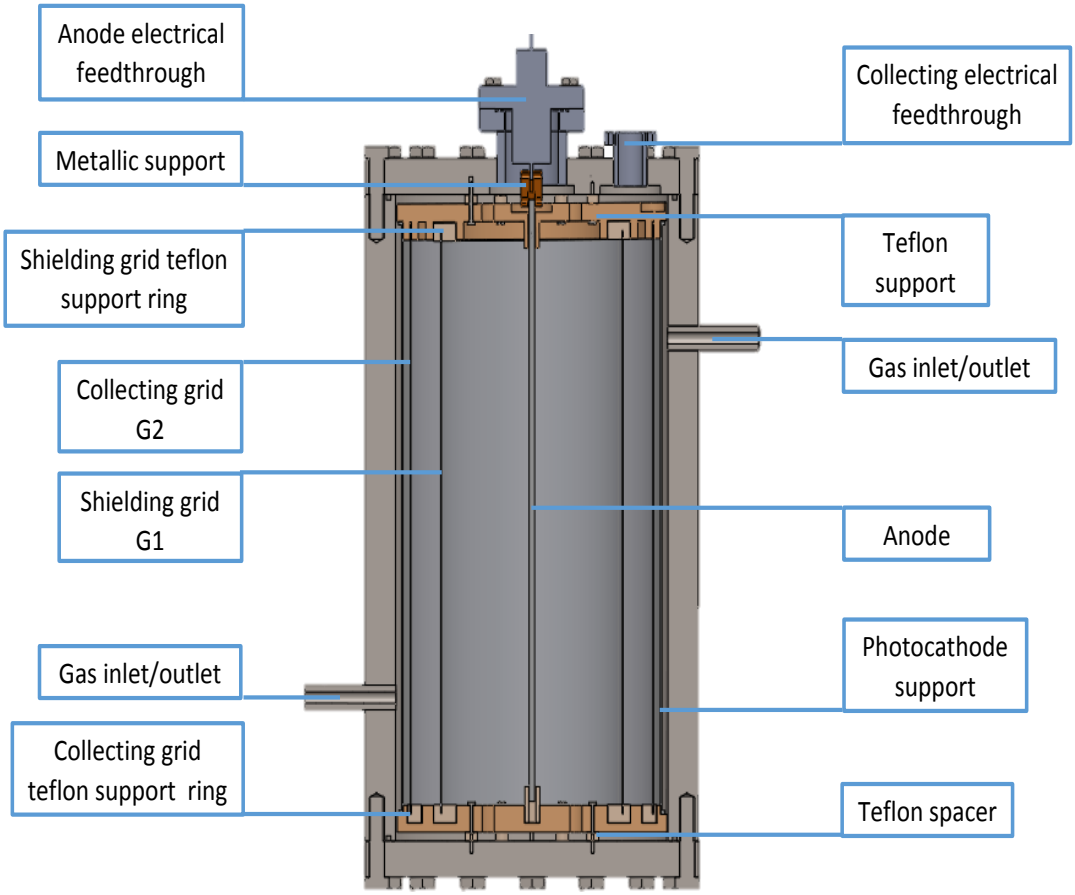

Figure 2.18: Detector schematic.

To support the internal structure elements (anode, grids and photocathode support), two teflon disks were designed to fix these structures to the detector bases. These structures are very important since they must ensure that these components are stable, both electrically and mechanically, avoiding current leaks, virtual gas leaks, and ensuring at the same time an easy assembly of the detector components. Both teflon supports have a cylindrical shape 1.5 cm in height and a radius of 9 cm, with holes drilled to improve the gas flow inside the detector and to avoid virtual gas leaks (Appendix A).

The anode is a stainless steel rod 320 mm long and 2 mm in diameter, and is fixed to a feedthrough on one of the detector bases with the help of a metallic support and kept in its position by a teflon support on the other base.

The two cylindrical grids employed are made of stainless steel 316L sheets, with hexagonal holes and a transmission of 78%, which were bent and then welded. The grids have a length of 320 mm and diameters of 120 mm (shielding grid) and 160 mm (collecting grid). An additional thin mesh of stainless steel (88% transmission) was placed over the collect-

Figure 2.19: Photos of the different assembly stages of the detector.

ing grid, resulting in a overall transmission of about 68%. A feedthrough was welded to the collecting grid, G2, and the shielding grid was grounded to the detector body, both being fixed on both sides to the teflon supports with the help of teflon rings.

Another important feature of the detector is the photocathode support. Because of physical limitations on the evaporation plant available for the photocathode deposition we decided to divide the stainless steel photocathode support into three metal sheets folded in a concave shape, which when assembled together form a cylindrical structure. Two backstops were made in each of the three parts to maintain a fixed distance from the photocathode to the detector wall and ensure that the structure is electrically grounded.

The electrical connections to the anode and collecting grid were made using electrical feedthroughs. The feedthrough chosen to bias the anode was the 21184-01-CF model of Cerameseal, which stands pressures up to 28 bar and a maximum biasing voltage of 50 kV. For the electrical feedthrough of the collecting grid, the 18088-01-CF model of Cerameseal was chosen, since it supports pressures up to 17 bar and a biasing voltage up to 20 kV.

2.5 Preliminary Tests

Since this detector was designed to work at pressures between 5 and 20 bar, high pressure tests had to be performed after its assembly. For safety reasons, these tests are usually conducted for pressures 3 to 4 times higher than the working pressure.

The initial tests were made with water (hydrostatic pressure tests) to provide a safe way in which pressure vessels can be tested for strength and leaks. The test involves repeatedly filling the vessel with water, to the specified test pressure, which in our case was 30 bar. This was considered enough for the initial work in the laboratory.

After the initial hydrostatic tests were concluded, leak tests followed. Leak tests are essential to ensure that the detector's insulation is adequate and therefore the gas losses or the risk of contamination from impurities caused by leaks is negligible.

The leak tests were initially performed under vacuum, followed by the same tests at high pressure. The system was initially vacuum pumped and the vacuum was monitored using the pressure gauge from the pump station. Whenever doubts about possible leaks existed, the identification of these leaks was done evaluating the change in the pressure using a very sensitive pressure gauge, placed at the head of the vacuum pump, after applying acetone in the components and connectors used in the detector. Having concluded this initial leak test under vacuum, where a stable vacuum of 10^{-6} Torr was achieved at the pressure gauge position, the detector was filled with nitrogen up to 10 bar and left for a week with the pressure being constantly monitored to verify if there was any change. This test was repeated and since no relevant change in pressure was observed, the detector was considered able to be filled with the more expensive Xe gas.

In addition, electrical insulation tests were performed to test the design, construction and material problems that might affect the insulation and performance of the detector. Tests verified that a specified level of insulation was met. In these tests the electrical insulation of the different parts of the detector that were to be biased was assessed. The tests consisted of increasing the voltage applied first to the anode and then to the collecting grid, constantly monitoring the current delivered by the sources, which should be zero to guarantee the necessary electrical insulation. These tests revealed that the conditions needed to operate the detector were met, so we proceeded to the assembly of the detector in the gas line.

2.6 Gas Admission, Purification and Storage

After these tests, the detector was assembled in the experimental line. The experimental line should be able to supply, store, circulate and purify the detector filling gas (Xe in our case). The experimental line where the detector was assembled was designed for both high-vacuum and to stand pressures up to 20 bar and is depicted in figure 2.20.

As is known, gas purity is a very important factor that limits the performance of scintillation counters since the amount of light actually collected can be significantly affected

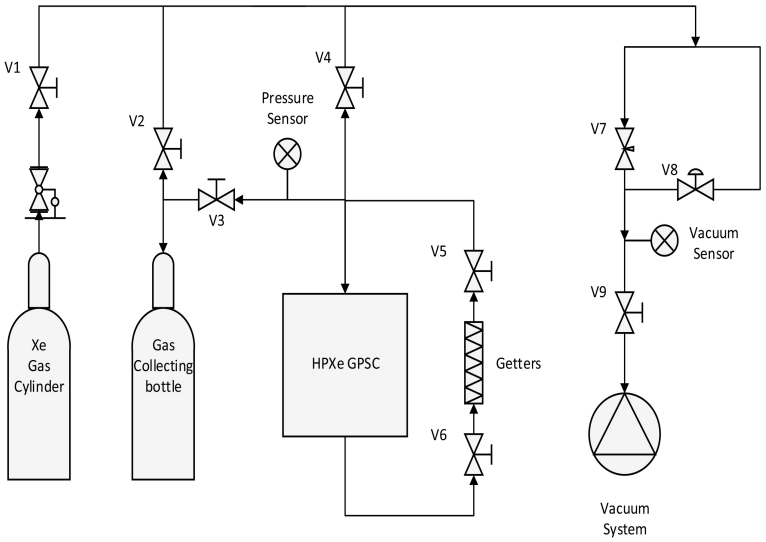

Figure 2.20: Gas system schematic: the left side of the diagram shows the gas cylinders for supply and storage, at the centre the detector and the purification system (*getters*) are shown; on the right side is the vacuum system.

by impurities [46, 82], thus continuous gas purification is essential.

Initially the detector was assembled in a gas line and a high-vacuum (about 10^{-7} Torr between V7 and V9) was achieved. The vacuum system uses a turbomolecular pump (Edwards EXPT Pumping Station) with a pressure gauge (Edwards Wide Range gauge WRG-S-NW25) that measures the vacuum level (between valves V9 and V7) as depicted in figure 2.20. Vacuum was performed for 2-3 days to allow outgassing of the detector and associated pipes but also of the getters (introduced between valves V5 and V6). When a good vacuum (10^{-5} Torr) was established the getters were activated.

These getters are adsorbent alloys that are placed in the detectors' gas system with the purpose of improving the quality of the gas or gases introduced in the detector by removing existing impurities (hydrogen (H_2), water (H_2O), carbon monoxide (CO), carbon dioxide (CO_2) and nitrogen (N_2)) by either combining the impurity molecules chemically or by absorbing them, as they affect not only the electroluminescence yield but also the QE of the photocathode (CsI), which is highly hygroscopic. When selecting the getter material, there are three important characteristics that should be met: low vapour pressure and low activation and operation temperatures [22]. The ones used in our system were the SAES Getters, model ST707/WASHER/833 purifiers (Zirconium: 70.0%, Vanadium: 24.6%, Iron: 5.4%). These getters are activated upon removing the protective film that covers them, by heating them up to 673-773 K. After this activation, the getters should not be in contact with air. To have their operation optimized and extend their lifetime, the getters' temperature should be kept at 473-523 K and should be isolated from the rest of the detector, until it is filled with the gas to be purified.

So, after the activation of the getters, Xe was introduced in the detector. The Xe gas cylinder was assembled on the gas line with two valves that allow control of the amount of gas admitted to the detector. The first valve (V0) is used to decrease the pressure from the gas bottle to an intermediary section, being then released to the detector's interior with the help of a second valve (V1). In the present system, the pressure in the detector is controlled by a pressure sensor placed near the inlet of the detector, and the gas circulation is achieved by convection through the heated getters.

Since Xe is an expensive gas, it might be useful to store it between experiments and for that reason the system includes a gas reclamation cylinder. In these cases, Xe can be cryogenically removed from the detector by placing the reclamation cylinder inside a dewar with liquid nitrogen and cooling it down to 77 K. Knowing Xe's critical point, which is about 56 bar (55.4 atm) at 290 K, and considering the detector dimensions (the detecting gas volume, $V \simeq 9.13$ L) and assuming a working pressure of 15 bar, the reclamation cylinder should have a volume of at least 3.30 L. A reclamation cylinder with this specification was then bought and assembled in the gas line, near V2 and V3.

In addition to the mentioned characteristics, a gas sampling system with a precision leak valve (needle valve, V8) was introduced in the gas line. This valve will enable the use of a residual gas analyser (mass spectrometer) either to verify the purity of the gas or to detect leaks. The remaining valves employed in the current design are important to ensure the protection of the system, equipment and personnel from pressure hazards.

A set of photos of the detector installed in the experimental line are shown in figure 2.21.

Figure 2.21: Photos of different perspectives of the detector and experimental line.

3

Detector Performance

William Crookes (1832-1919), was the inventor of the spinthariscope, considered to be the first particle detector. The idea for the spinthariscope came while observing the apparently uniform fluorescence created by alpha particles on a zinc sulfide screen, its name comes from the Greek word (spinth'ēr) that means "spark". His work on the study of nuclear disintegrations opened the door for Ernest Rutherford, Hans Geiger and Ernest Mardsen to discover the atomic structure in 1909.

–

The initial tests were performed with alpha-particles from an ^{241}Am (5.486 MeV) source to prove the detector concept as they produce a large number of primary electrons and have a relatively small stopping range. So, an alpha particle support was devised to guide the alpha particles directly to the detector absorption/drift region with an optimized geometry, also providing some level of collimation.

Figure 3.1 shows the detail of the supporting structure developed. The alpha-particles support is a hollow tube with a small hole (2 mm in diameter) at one end and completely open at the other. To ensure detector tightness, an aluminized Mylar window was glued to the planar surface facing the interior of the detector, in such a way that the gas pressure, during operation, is applied normally to the mentioned surface, minimizing the surface tension. In order for the alpha-particles to enter directly in the absorption/drift region, two holes were cut in grids G1 and G2. These holes were made as small as possible to minimize the impact in the electric field uniformity in the different detector regions and at the same time providing the necessary electrical insulation from grid G2, which is positively biased. This removable structure is fixed to the detector wall using a commercial flange that seals the detector. To minimize the energy loss of the alpha particles, before crossing the Mylar window, this structure is enclosed in a chamber designed to produce a primary vacuum.

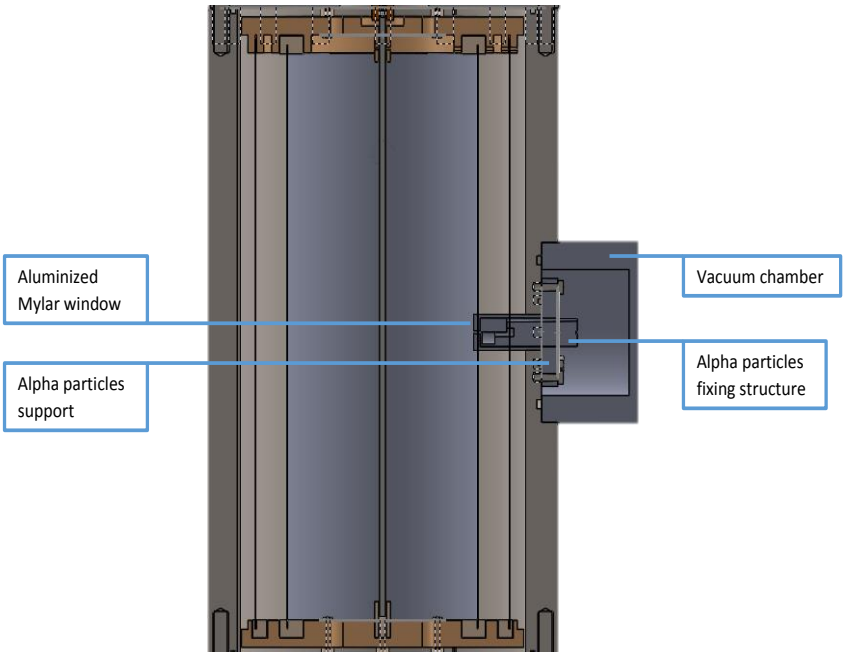

Figure 3.1: Detailed view of the support structure for the alpha particles.

Before starting the experimental measurements, a simulation study of the attenuation of the alpha particles in the entrance window and of the stopping range of the alpha particles in Xe (gas) at different pressures was performed, using the SRIM ("Stopping and Range of Ions in Matter") software.

Following this simulation, the charge collection at the anode was performed varying the reduced electric field at the surface of the anode with the detector biased in ionization chamber mode. Then, the charge at the collecting grid with the detector biased in GPSC mode, *i.e.* with light amplification was measured for different reduced electric fields at the anode surface and in the collecting region. From these values, the detector gain was obtained for different pressures and biasing conditions and then compared with the theoretical values. Finally, the experimental resolution for the alpha particles and the signal-to-noise ratio (SNR) were also obtained.

3.1 Simulation studies for alpha-particles

Alpha-particle attenuation in the entrance window

To determine how the Mylar window could affect the energy dispersion of the alpha particles entering the detector, a simulation using Stopping and Range of Ions in Matter (SRIM)® software was carried out.

Before starting the simulation the minimum window thickness able to support the same pressure difference used in the previous prototype [112] was calculated using different safety factors, to determine which window thickness would offer the best compromise between total energy and energy dispersion.

For the calculation of the window thickness, Th, a formula available in [113] was used:

$$Th = \sqrt{\frac{1.1 \times P \times R^2 \times SF}{MR}} \tag{3.1}$$

where P is the pressure differential (psi), R is the unsupported radius (inches), Safety Factor (SF), and MR is the modulus of rupture (psi) of the Mylar window.

Substituting R=0.03937 in (1 mm), MR=510000 psi [114] and varying the pressure differential from 14.5 up to 72.5 psi (1 to 5 bar) with a safety factor from 1 up to 4 (typical design specification), the window thickness was determined. Figure 3.2 displays the results for the Mylar window thickness as a function of the pressure, for the different safety factors (from 1 to 4).

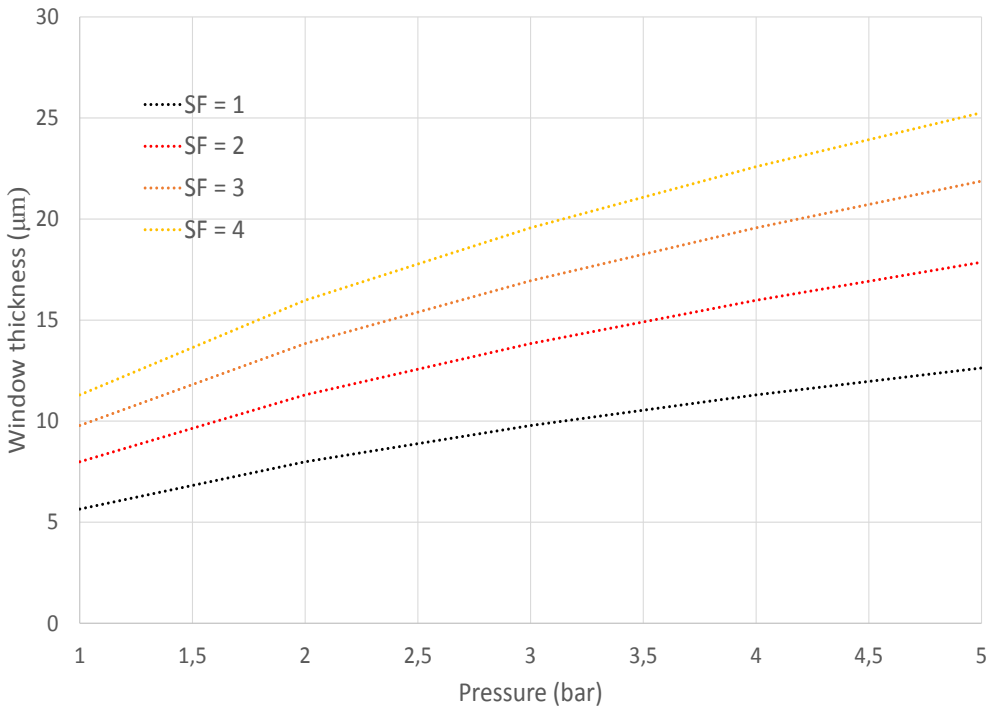

Figure 3.2: Mylar window thickness as a function of the pressure using different safety factors (SF).

Looking at figure 3.2 it is possible to see that the window thickness needed to support a pressure difference of 5 bar with a safety factor of 4, a typical value used for the design of pressure windows is about 25.2 μm, while without using any safety factor it is about 12.6 μm. The influence of the aluminium layer that will be needed to ensure electrical contact between the window and detector wall was not considered and it may eventually contribute to lowering the limits presented here.

Now that the limits for the Mylar window thickness have been found, it is important to understand how the window thickness degrades the energy of the alpha-particles.

A study of the impact of the Mylar thickness on the energy dispersion of the alpha particles with a constant thickness of the aluminium deposit (0.1 μm) was performed using alpha-particles with energy of 5.486 MeV (^{241}Am). The energy distribution of the alpha particles after crossing these two layers was determined for a total number of 10 runs with 500 events, considering normal incidence of the alpha particles in the Mylar window.

The results are displayed in figure 3.3, with the mean energy, E_α, on the left axis and the energy dispersion, $\Delta E/E$, on the right axis.

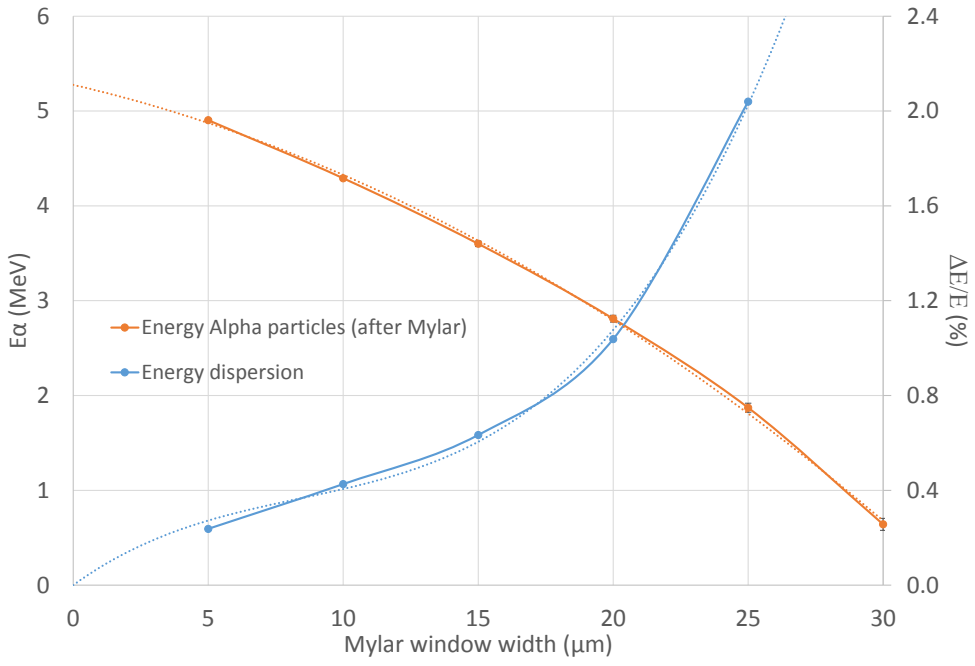

Figure 3.3: Energy of the alpha particles and its energy dispersion ($\Delta E/E$) after crossing the Mylar window and the aluminium layer (0.1 μm) as a function of the Mylar thickness, for normal incidence in the window.

As expected, it is possible to see both a significant decrease in the energy of the alpha particles coming from the window along with an increase in the energy dispersion with the window thickness.

Looking at figure 3.2 we can see that choosing a safety factor of 4 implies, at a pressure of 3 bar, a window thickness of 20 μm, which already gives rise to an energy dispersion above 1%, with the alpha-particles entering the detector with less than 3 MeV (figure 3.3). From previous experience, even working below the advised thickness limit [112], it was found that an aluminized Mylar window of 5 μm could stand a differential pressure of more than 5 bar, enough for our initial tests. So, we chose the 5 μm thick Mylar window as it would minimize the energy dispersion (0.23%) and maximize the energy of the alpha-particles entering the detector (about 4.8 MeV).

With the window selected, the influence of the angle of incidence of the alpha particles in their energy after entering the detector was studied. To assess this information, another simulation was carried out where the incidence angle of the alpha particles was varied from 0° up to 80°, using a Mylar window with 5 μm thickness with an aluminium film of 0.1 μm thickness. The results of this simulation are given in figure 3.4.

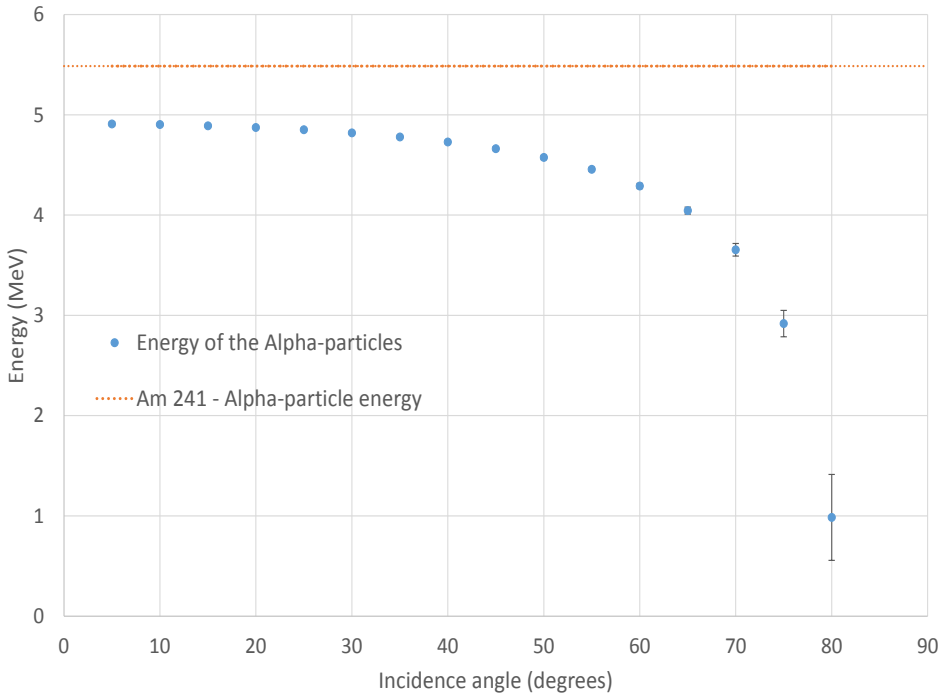

Figure 3.4: Energy of the alpha particles after crossing the 5 μm thick Mylar window and the aluminium layer (0.1 μm) as a function of the incidence angle in the window.

Since in the setup the maximum angle of incidence will be $\sim 22°$, the $\Delta E/E$ due to the incidence angle of the alpha particle will be about 2%, to which must be added the $\Delta E/E$ due to normal incidence (figure 3.3) not considered here, and which is 0.23%.

Alpha-particle absorption in the gas (Xe)

The lower operating pressure limit in these initial tests with α-particles will be defined by the distance travelled by the alpha particles before being completely stopped within the 54 mm absorption region.

Figure 3.5 depicts the stopping range of the alpha particles from ^{241}Am (with an initial energy of 5.486 MeV) after crossing a Mylar window with 5 μm thickness with an aluminium deposit (0.1 μm) as a function of the gas pressure (Xe) (blue line) and the absorption region limit (orange dashed line). The pressure limit needed to stop all the alpha particles in the absorption region is about 0.33 bar, for pure Xe. Since the usual working pressure is above the atmospheric one to prevent contamination of the gas, it will be safe to work at pressures ranging from 1-5 bar for the initial tests with α-particles.

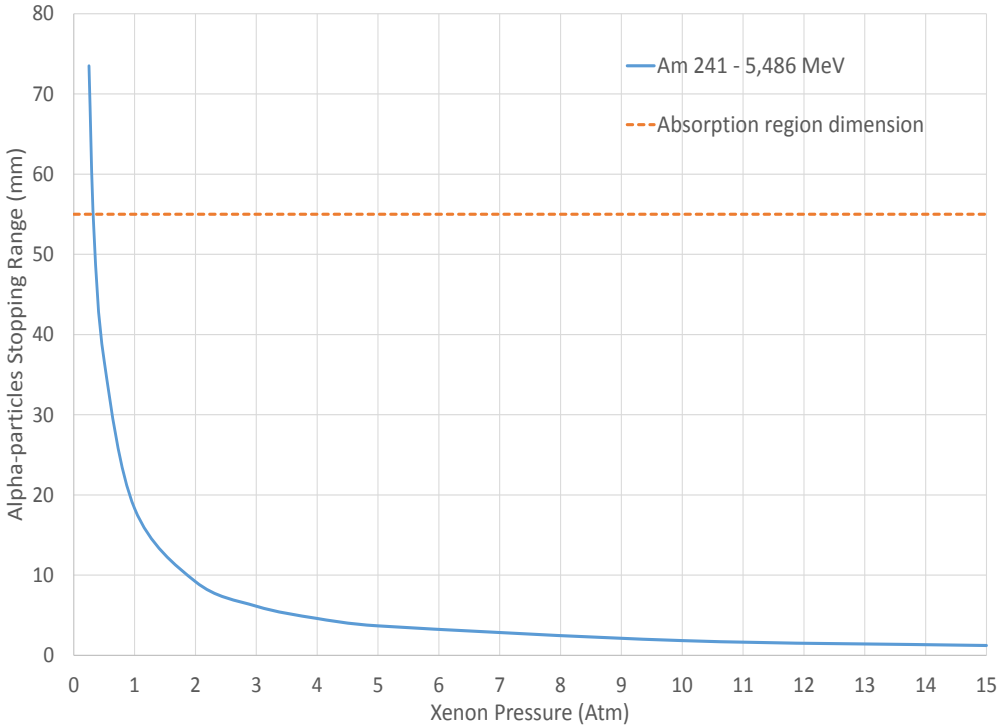

Figure 3.5: Alpha particles stopping range in Xe for pressures ranging from 0.1 atm up to 15 bar, after crossing a Mylar window (5 μm) and the aluminium layer (0.1 μm).

Having calculated that with the Mylar window used a reasonable fraction of the alpha-particles' energy enters the detector and that these are stopped in the absorption region for the defined pressure range (1-5 bar), we then proceeded with experimental characterization of the alpha particles' energy after crossing the Mylar window with a silicon (Si) detector that will be essential to determine the primary charge produced.

3.2 Characterization of the Alpha-particles with a Silicon Detector

Before using α-particles to determine the gain of the detector, it is important to verify their energy after crossing the Mylar window.

To accomplish this task, an existing experimental system based on a silicon (Si) detector placed inside a vacuum chamber (to minimize the α-particles' energy loss in air) was used (figure 3.6).

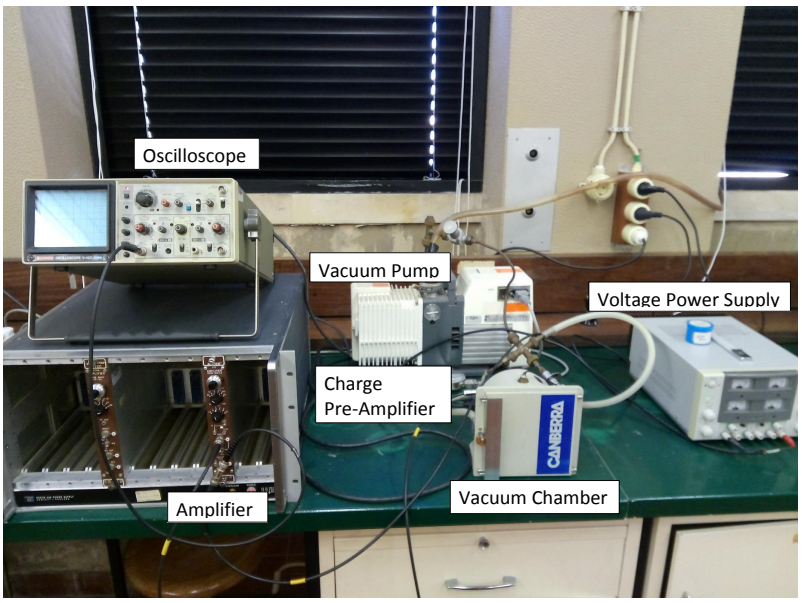

Figure 3.6: Experimental system used in the study of the energy lost by the alpha particle in the Mylar window. The system is composed by a silicon (Si) detector placed inside a vacuum chamber, a power supply, a pre-amplifier, a linear amplifier, a NIM crest, an oscilloscope and a computer that hosts the MCA.

The Si detector was biased according to its specifications. The electronics used consisted of a CANBERRA Model 2004 pre-amplifier and an Ortec 570 linear amplifier, with a shaping time of 2 μs. The signal from the detector was then fed to a multichannel analyser (MCA) where the spectrum was recorded.

To estimate the loss of energy of the alpha-particles in the Mylar window, the entire

supporting structure was placed inside the vacuum chamber (figure 3.7) and spectra were taken with and without the 5 μm Mylar window, placing the source in the same position that would be used during the detector operation, which is as close as possible to the Mylar window. The distance from the silicon detector was the same for all the measurements.

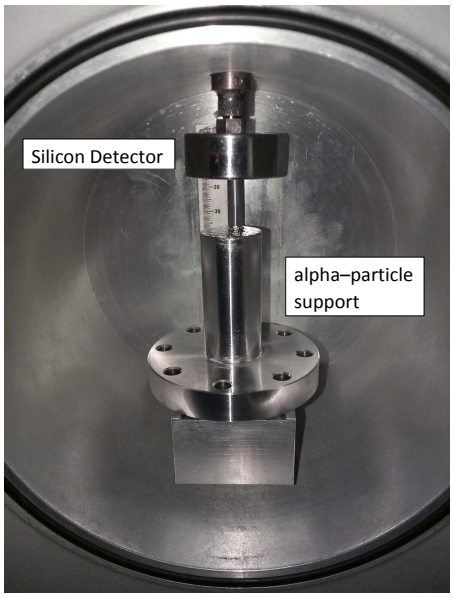

Figure 3.7: Photograph of the interior of the vacuum chamber with the silicon detector and the alpha particle's source support structure.

The loss of energy of the alpha particles from the ^{241}Am source (5.486 MeV) after passing through the Mylar window was assessed comparing the centroid of the peak distribution of the energy spectra obtained with and without the Mylar window, assuming that the MCA has a linear behaviour.

According to our estimate, using the centroids of the peaks observed with and without the window, 19.3±1.5% of the energy of the alpha particles is lost in the Mylar window and so, the energy with which the alpha particles enter the detector will be approximately 4.427 MeV. This information allows us to have a better estimate of the primary charge signal amplitude, important in the determination of the detector gain.

After these tests were concluded we proceeded to the assembly of the support to the detector, followed by leak and pressure tests.

3.3 Primary Charge Collection at the Anode

To study the primary charge collection at the anode, both the anode and grid G2 were positively biased, while grid G1 was placed at ground potential (figure 2.1), with the signal being recorded from the anode. With this polarization the detector is in the ionization

chamber mode of operation, since the primary charge is collected at the anode without amplification. The anode voltage was adjustable so that the reduced electric field at the surface of the anode could be varied, in order to understand its influence in the charge collection at the anode for different Xe pressures (1-3 bar), while the bias of grid G2 was defined for normal operation.

The ^{241}Am alpha source was placed inside its support, which was then evacuated. The alpha particles entering the detector through the Mylar window are then absorbed in the absorption region, with the resulting cloud of primary electrons being accelerated towards the positively biased anode, where they are collected. The charge signal produced is then fed to a pre-amplifier (CANBERRA 2006 with a sensitivity of 47 mV/1-M electron-ion pairs), and then shaped and further amplified by a linear amplifier (TENNELEC TC 243 with a shaping time of 12 μs and a fixed gain of 100). This signal is finally sent to an oscilloscope (Tektronix TDS 2022B), where the 128 pulses are averaged and then stored to be further analysed in a computer. The peaks' centroids of the spectra in the oscilloscope were obtained fitting the distribution to a Gaussian curve over a linear baseline using an interface developed in Matlab.

Figure 3.8 displays a typical signal obtained collecting the charge at the anode for an ^{241}Am (4.427 MeV after crossing the Mylar window) alpha particle source, with an E/p at the surface of the anode of about 4.5 kV·cm^{-1}·bar^{-1} (6 V·cm^{-1}·Torr^{-1}), for a pressure of 2 bar. This signal is an average of 128 pulses, which allows the background noise to be reduced, coming essentially from the associated electronics and the HV power supplies.

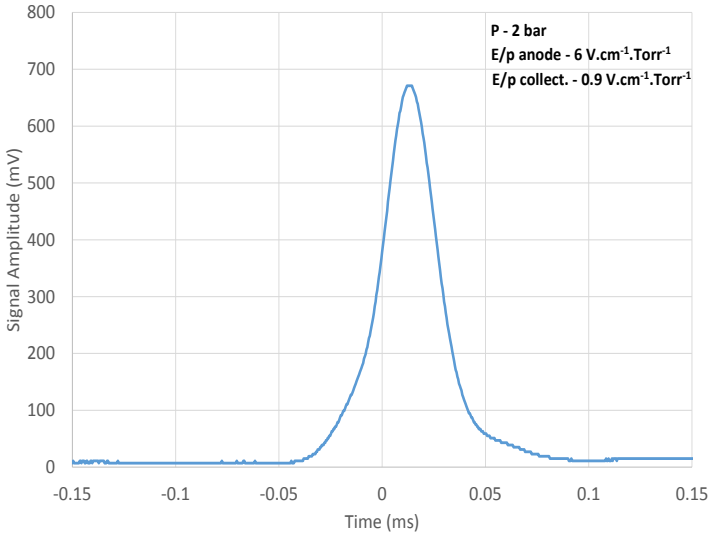

Figure 3.8: Typical signal from the oscilloscope, obtained collecting the primary (^{241}Am - alpha particle source), with an E/p at the surface of the anode of about 4.5 kV·cm^{-1}·bar^{-1} (6 V·cm^{-1}·Torr^{-1}) with 2 bar of Xe. The signal was obtained from an average of 128 pulses.

This procedure was repeated for different pressures (1-3 bar) and different voltages at the anode. Figure 3.9, shows the signal amplitude measured with the oscilloscope as a function of the reduced electric field at the surface of the anode, for the different pressures studied. The measurements were repeated 5 times with the associated error being the standard deviation. Although all error bars are represented, in some cases they are smaller than the symbols used.

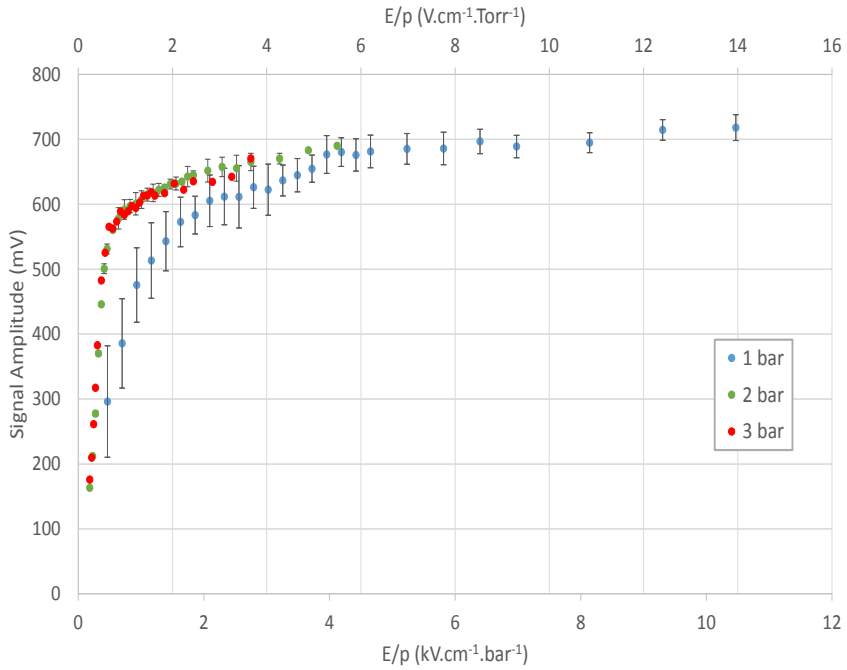

Figure 3.9: Primary charge signal amplitude at the anode as a function of the reduced electric field at the surface of the anode, for different pressures ranging from 1 up to 3 bar of Xe.

The signal amplitude in figure 3.9 is seen to increase with E/p at the surface of the anode, stabilizing faster for increasing pressures, being particular relevant for lower E/p values (about 2 kV·cm^{-1}·bar^{-1}). It can also be observed that the fluctuations are larger for the lower pressures. Above an E/p of 4 kV·cm^{-1}·bar^{-1}, the collected charge stabilises for all pressures, meaning that most of the primary charge is collected at the anode in these conditions.

From the results in figure 3.9, we can also conclude that increasing the E/p above the ionization threshold (4.5 kV·cm^{-1}·bar^{-1} or 6 V·cm^{-1}·Torr^{-1}), apparently has no significant effect on the charge collection at the anode. Although some increase in the collected charge could be expected due to ionization of the Xe atoms, since for this geometry the

range of r values where the E/p is above the ionization threshold is small, this effect is almost negligible for these E/p values. The fact that the E/p at the anode surface can be increased, up to about 10 kV·cm^{-1}·bar^{-1} without significant charge multiplication is important when biasing the detector in scintillation mode, as we will see in the next section.

We believe that the higher statistical fluctuations in the collected charge, that give rise to the higher error bars observed, for lower pressure and lower E/p values, are related to the higher radial primary electron dispersion for these pressures. To verify this, a simulation was carried out using SRIM. Once again, the initial energy of the alpha particles was considered to be 5.486 MeV, a Mylar entrance window was defined with 5 μm thickness with a thin aluminium film (0.1 μm) deposited on one end and a Xe gas with different densities corresponding to 0.5, 1, 2 and 3 bar of Xe. Assuming that these particles are emitted with a normal incidence angle to the window surface, the depth of interaction (range) in the absorption region was determined for the different densities using a total number of 1000 α-particles. In this simulation the electric field was not considered. The profile of the tracks created by the 1000 events generated is represented in figure 3.10 for each Xe pressure considered (0.5, 1, 2 and 3 bar), which gives an indication on the stopping range of the particles in the detector (GPSC). As can be seen, the radial cloud size increases substantially with decreasing pressure, apparently confirming that this effect can be responsible for the stronger electric field required to collect all the charge at lower pressures and also responsible for the large error bars associated with the lower pressure.

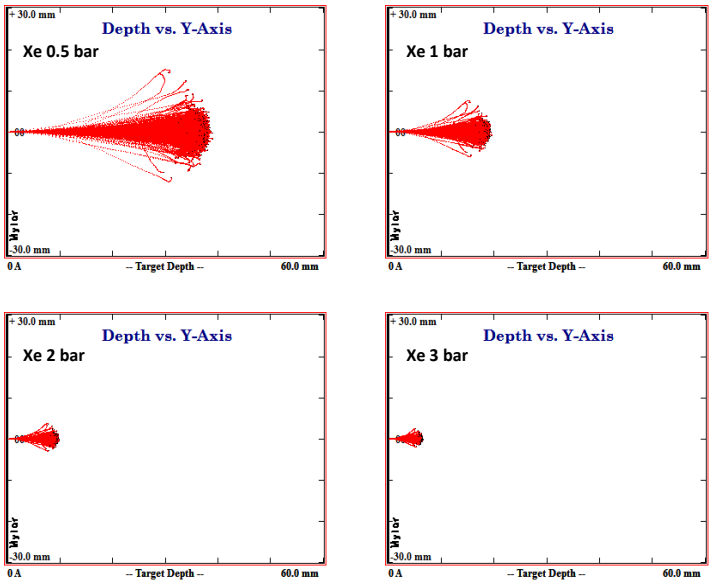

Figure 3.10: ^{241}Am alpha particles' depth of interaction for 0.5, 1, 2 and 3 bar of Xe after crossing an aluminized (0.1 μm) Mylar window of 5 μm. Calculated with SRIM. .

In addition to the track of the alpha-particles inside the detector, the SRIM simulation allowed us to characterize the ionization profile of the alpha particles. Figure 3.11 shows the simulated results of the ionization profile as a function of the depth of interaction inside the detector, for different Xe operating pressures (0.5, 1, 2 and 3 bar) after crossing the Mylar aluminized window. The results displayed in figure 3.11 show, as expected, that most of the ionization occurs at the end of the track of the alpha particles.

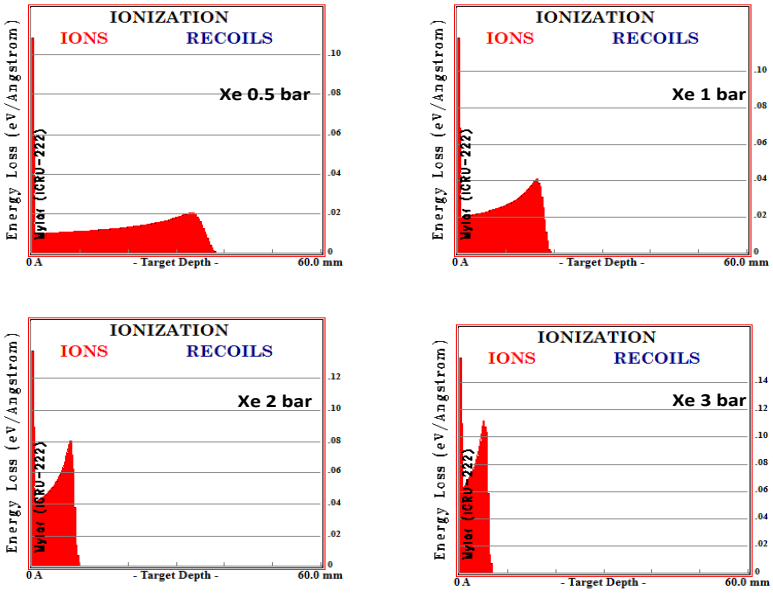

Figure 3.11: ^{241}Am alpha particles' ionization profile as a function of the depth of interaction for 0.5, 1, 2 and 3 bar of Xe after crossing an alluminized (0.1 μm) Mylar window of 5 μm. Calculated with SRIM.

3.3.1 Considerations on the charge collection at the anode

In addition, it is important to understand if we are collecting all the charge at the anode, as it will be fundamental for the determination of the gain of the detector later.

The main factors that can limit the total charge collection at the anode are related to the decay time constant of the preamplifier and with the shaping time of the linear amplifier. So, in order to understand if the all the charge arriving was been collected at the anode in the preamplifier and linear amplifier chain, the charge collection time was determined and the results were compared to the time constant of the preamplifer (τ=50 μs) and the longer shaping time of the available linear amplifier used (12 μs).

Figure 3.12 gives the expected charge collection time as a function of the E/p at the anode surface, which was calculated performing the integral in equation 2.37 with the limits of integration being the beginning of the absorption/drift region and the anode radius, with the drift velocity values that vary with E/p taken from [19].

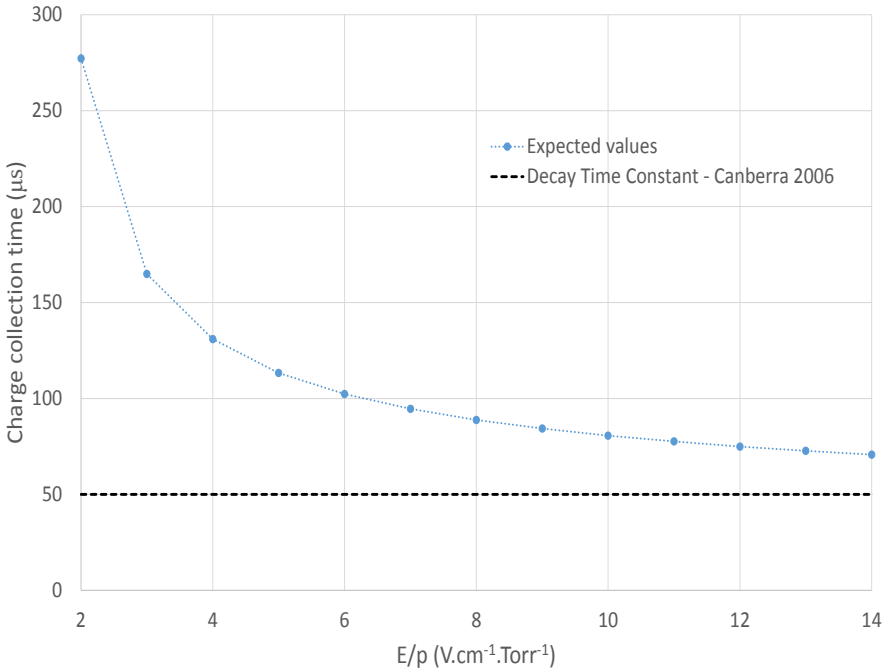

Figure 3.12: Primary charge collection time at the anode as a function of the reduced electric field, E/p, at the anode surface.

As can be seen, the drift time in all cases is larger than both the time constant of the preamplifier and shaping time of the linear amplifier, not allowing the collection at the anode of all the charge produced. So the signal obtained is due to charge induction with the observed increase in the signal amplitude resulting from the faster signals (due to the increasing E/p). This loss by ballistic deficit can only be avoided by keeping the time constants long compared with the charge collection time in the detector or possibly by digital signal processing. For this reason, the determination of the primary charge will be made considering an alternative process that will be described later.

3.4 Detector Operation in Scintillation Mode

Following the charge collection at the anode, we moved to the characterization of the detector signal in scintillation mode. So, the detector was biased to allow scintillation near the anode and the photoelectron collection at the collecting grid (G2), with the shielding grid being at ground potential. Collecting the signal at G2, it was confirmed that light was being produced in the scintillation region (close to the anode) and also allowed to verify the effect in the signal amplitude of both the reduced electric field at the surface of

the anode and in the collection region. The electronics used in these studies were the same as in the previous case of charge collection at the anode. The charge signal produced by the photoelectrons is collected now from grid G2, instead of the anode, with the help of the pre-amplifier CANBERRA 2006 with a sensitivity of 47 mV/1-M electron-ion pairs, and then shaped and further amplified by a TENNELEC TC 243 linear amplifier with a shaping time of 12 μs with a fixed gain of 100. The signal is then sent to an oscilloscope (Tektronix TDS 2022B), where the 128 pulses are averaged and then stored to be further analysed.

In order to better characterize the detector response to the different adjustable parameters, this study was divided in two parts: the effect of the reduced electric field at the surface of the anode, for a constant reduced electric field in the collecting region ($E/p \sim 0.9$ V·cm^{-1}·Torr^{-1}) and the effect of the E/p of the collecting region, for a constant E/p value at the surface of the anode close to the Xe ionization threshold ($E/p \sim 7.5$ V·cm^{-1}·Torr^{-1}).

3.4.1 Signal Amplitude as a function of the E/p at the surface of the anode

The signal amplitude was measured varying the reduced electric field at the surface of the anode to the maximum achievable with the high voltage supplies available, maintaining a constant E/p at the collecting region, just below the threshold for secondary scintillation (0.9 V·cm^{-1}·Torr^{-1}).

Figure 3.13 displays two typical signals: one due to the charge collected at the anode and the other due to the charge at the collecting grid, both obtained using the alpha particle source. The E/p used at the surface of the anode was about 4.5 kV·cm^{-1}·bar^{-1} (6 V·cm^{-1}·Torr^{-1}) while the E/p in the collecting region was about 0.68 kV·cm^{-1}·bar^{-1} (0.9 V·cm^{-1}·Torr^{-1}) for Xe at 2 bar. Observing figure 3.13 it is already possible to see some gain in the signal collected at grid G2 when compared to the signal collected at the anode. This result demonstrates that there is light being produced in the scintillation region with the resulting VUV photons providing some gain. Varying the E/p both at the anode surface and in the collecting region and observing simultaneously the signals collected at the anode and at grid G2 it was possible to verify that the signal observed in grid G2 was only due to the light produced in the scintillation region.

The dependence of the signal amplitude at G2 with the E/p at the anode surface can be observed in figure 3.14, where it is possible to see that the signal amplitude displays an almost linear dependence with the E/p throughout the entire range studied. We can conclude that the reduced electric field at the surface of the anode needed to observe a scintillation signal is not 1 V·cm^{-1}·Torr^{-1}, but significantly higher, displaying a dependence on the pressure. This results from the fact that the electric field has a radial geometry dependence and, as a consequence, its higher values occur only very close to the anode, giving rise to a very small scintillation region that does not produce significant scintillation

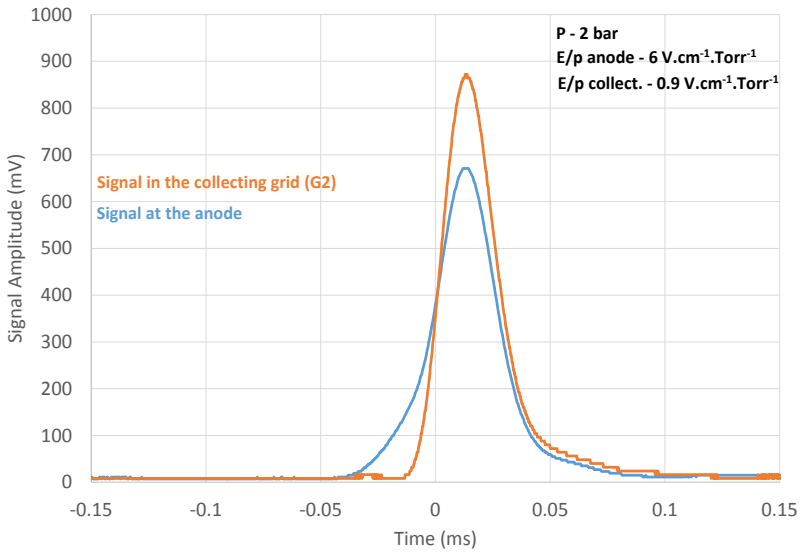

Figure 3.13: Typical signals produced by an ^{241}Am (4.427 MeV) alpha particle source at the anode and in the collecting grid (G2), with an E/p at the surface of the anode of about 4.5 kV·cm^{-1}·bar^{-1} (6 V·cm^{-1}·Torr^{-1}) and with an E/p in the collecting region of about 0.68 kV·cm^{-1}·bar^{-1} (0.9 V·cm^{-1}·Torr^{-1}) with 2 bar of Xe. The signal was obtained from an average of 128 pulses.

until higher E/p values (about 2 V·cm^{-1}·Torr^{-1}), as this process is significantly influenced by the shadow created by the anode, which further decreases the detected photons. In addition to this effect, charge recombination also plays an important role in regions with low reduced electric field, an effect that also decreases with increasing E/p.

When the E/p at the surface of the anode was increased above the Xe ionization threshold (6 V·cm^{-1}·Torr^{-1} for Xe), the signal amplitude was seen to increase accordingly, but maintaining a similar dependence in the range studied. This may be due to the fact that only a small amount of ionization is produced close to the anode, with the additional electrons having a small contribution to the light production, so the small extent of the avalanche will not greatly affect the signal formation with the main contribution coming from the extended scintillation region. This is in accordance with the results obtained for the primary charge, which showed a very slight increase with E/p at the anode for values above 11 V·cm^{-1}·Torr^{-1} (figure 3.9).

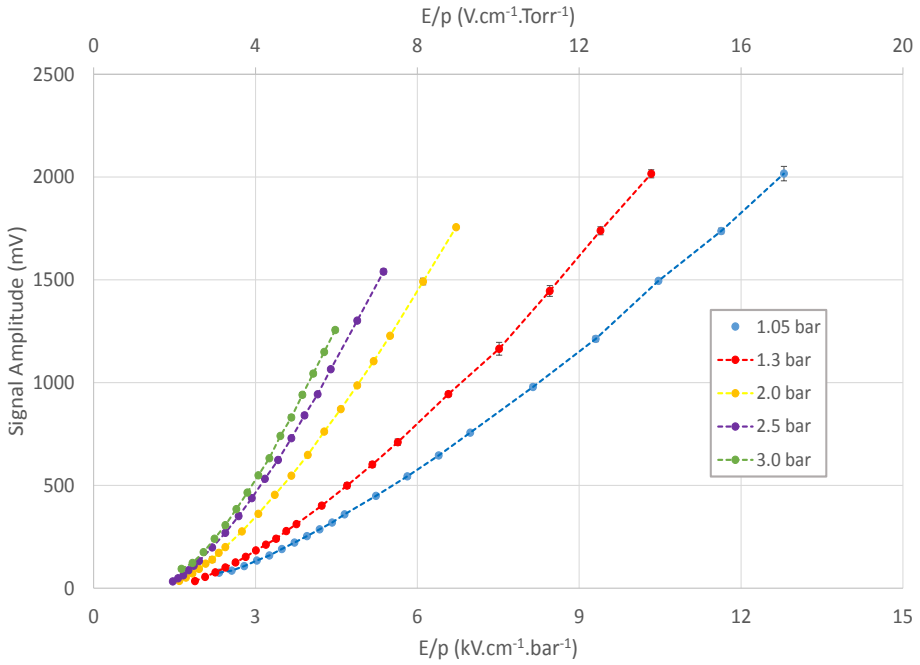

Figure 3.14: Signal amplitude collected at G2 as a function of the E/p at the surface of the anode, for a E/p of 0.9 V·cm^{-1}·Torr^{-1} at the collecting region, for pressures from 1.05 to 3 bar. Error bars are represented but in some cases are of the size of the symbols used.

3.4.2 Signal Amplitude as a function of the E/p in the collecting region

The signal amplitude was also measured, varying the reduced electric field in the collecting region up to a maximum, conditioned by electrical discharges, maintaining a constant E/p at the surface of the anode of about 5.6 kV·cm^{-1}·bar^{-1} or 7.5 V·cm^{-1}·Torr^{-1}, for different pressures. This E/p value at the anode was chosen since it gives a better charge collection there without a significant charge multiplication as already seen in the previous study.

Figure 3.15 displays a typical signal at the collecting grid for the used alpha particle source, for an E/p at the surface of the anode of about 5.6 kV·cm^{-1}·bar^{-1} (7.5 V·cm^{-1}·Torr^{-1}) and with an E/p in the collecting region of about 0.75 kV·cm^{-1}·bar^{-1} (1 V·cm^{-1}·Torr^{-1}) - blue - and 1.05 kV·cm^{-1}·bar^{-1} (1.4 V·cm^{-1}·Torr^{-1}) - orange - for Xe at 2 bar. Both signals are an average of 128 pulses. It is possible to conclude that increasing the E/p in the collecting region above the Xe scintillation threshold and maintaining a constant E/p at the anode surface, the signal increases. This effect is expected and we believe it is related to the more efficient extraction of the photoelectrons from the cathode and possibly to the additional production of VUV photons in the collecting region due

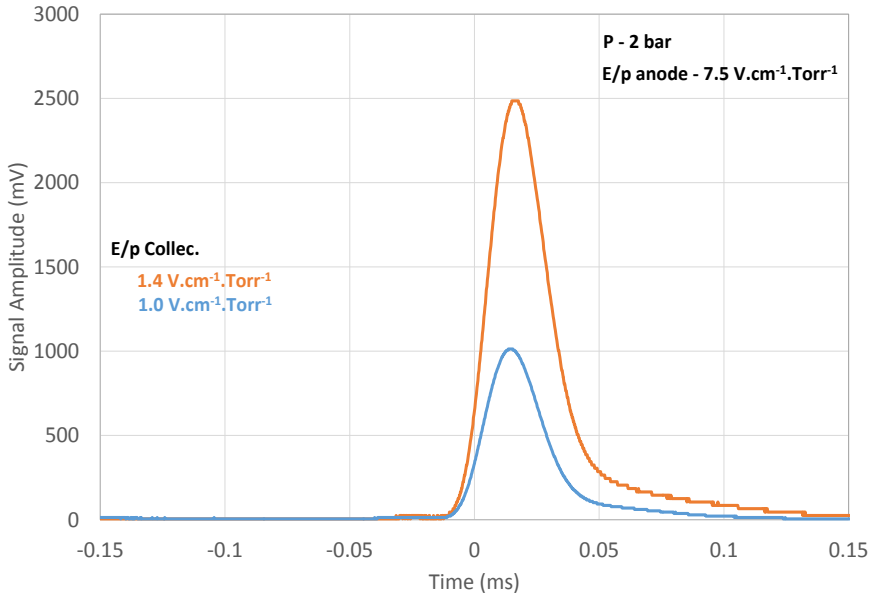

Figure 3.15: Typical signal produced at the collecting grid for an ^{241}Am (5.486 MeV) alpha particle source, with an E/p at the surface of the anode of about 5.6 kV·cm^{-1}·bar^{-1} (7.5 V·cm^{-1}·Torr^{-1}) and with an E/p in the collecting region of about 0.75 kV·cm^{-1}·bar^{-1} (1 V·cm^{-1}·Torr^{-1}) - blue - and 1.05 kV·cm^{-1}·bar^{-1} (1.4 V·cm^{-1}·Torr^{-1}) - orange - with 2 bar of Xe. The signals were obtained from an average of 128 pulses.

to positive feedback conditions in this region. This study was performed for other Xe pressures and E/p values at the collecting region with similar results.

Figure 3.16 shows the amplitude of the signals collected at grid G2 for a fixed E/p value at the anode's surface and varying the E/p in the collecting region, with the signal amplitude being obtained by averaging a total of 128 pulses in the oscilloscope. Error bars are represented, but are smaller than the symbols used.

In figure 3.16 it is possible to see that the signal amplitude increases linearly up to the Xe scintillation threshold (E/p~1 V·cm^{-1}·Torr^{-1}). The linear behaviour can be explained by the increasing extraction efficiency of the photoelectrons due to the higher reduced electric field above the photocathode surface. Above this E/p value, an abrupt increase was observed, a behaviour that is a direct consequence of photon positive feedback, due to an additional production of light close to the photocathode, which produces additional photoelectrons and increases the signal. Although this behaviour is usually avoided, as the multiplication process involved increases the associated statistical fluctuations, it could be used as a second amplification stage if needed, although at the cost of a worse energy resolution, R, as it will be discussed in section 3.6.

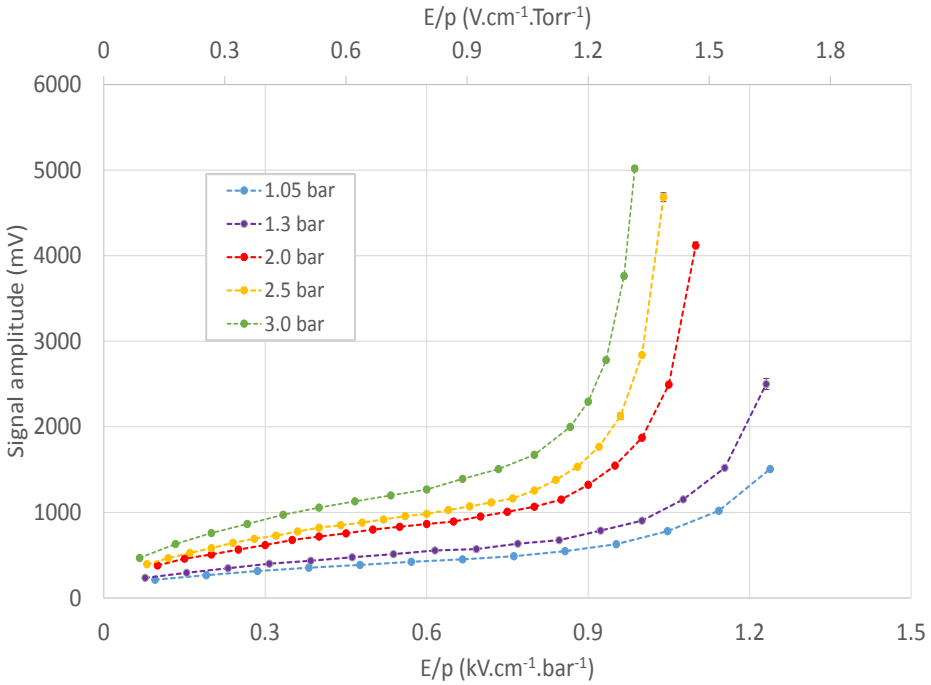

Figure 3.16: Signal amplitude as a function of the E/p in the collecting region, with an E/p at the surface of the anode (of 7.5 V·cm^{-1}·Torr^{-1}), for different pressures (1.05 to 3 bar). Error bars are represented but in some cases are of the size of the symbols used.

As expected, the same behaviour was observed in the signal amplitude with the increase of the E/p at the collecting region for higher pressures (figure 3.16), with the positive feedback being more pronounced for higher pressures.

Figure 3.17 displays the signal amplitude as a function of the E/p in the collecting region, for a pressure of 3 bar (Xe), with the E/p at the surface of the anode of 6 V·cm^{-1}·Torr^{-1} (orange) and 7.5 V·cm^{-1}·Torr^{-1} (blue).
As expected, increasing the electric field at the surface of the anode increases the signal, since more photons are produced in the scintillation region.

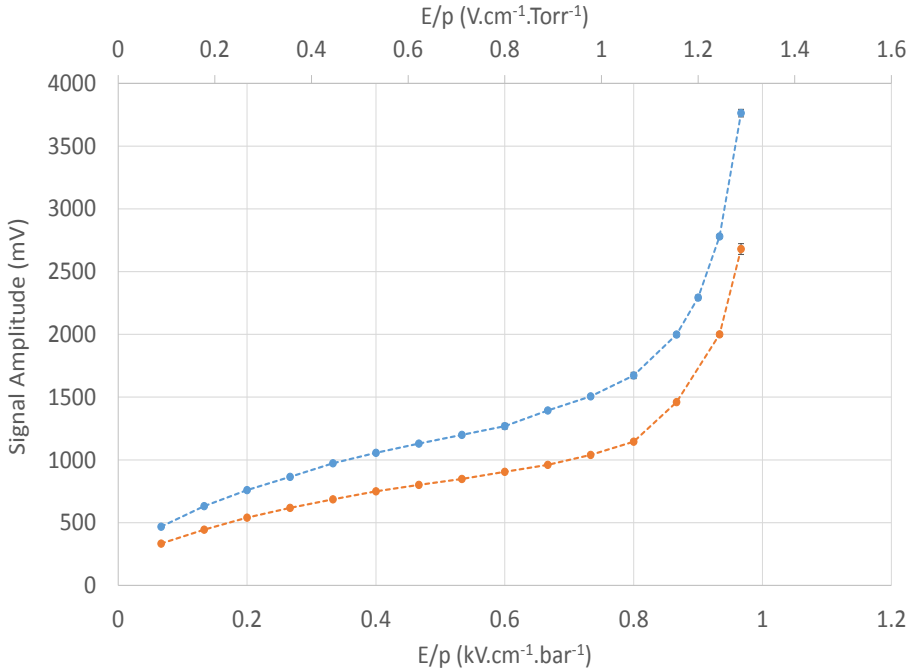

Figure 3.17: Signal amplitude as a function of the E/p of the collecting region, for Xe at 3 bar, for an E/p at the surface of the anode of 6 (orange) and 7.5 (blue) V·cm^{-1}·Torr^{-1}. Error bars are represented but in some cases are of the size of the symbols used.

3.4.3 Considerations on the charge collection in the scintillation mode

To verify if all the charge was being collected at G2, the signal width created by the alpha particles was studied and compared to the time constants of the electronics used.

As mentioned before, the signal width in the scintillation mode results mainly from the dispersion of the primary electron cloud produced by the alpha particles. So, to verify if the conditions necessary to collect all the photoelectrons were met, the difference between the drift time of the electrons at the radial limits of the electron distribution was calculated using equation 2.37 and substituting the limits of integration by their initial position given by the beginning of the absorption region and by the stopping range distance from G1 (determined in section 3.1) for different pressures (1, 2 and 3 bar of Xe). The E/p at the anode surface was varied from 2 to 15 V·cm^{-1}·Torr^{-1}.

Figure 3.18 shows the expected signal width as a function of the E/p at the anode surface for different Xe pressures (1, 2 and 3 bar).

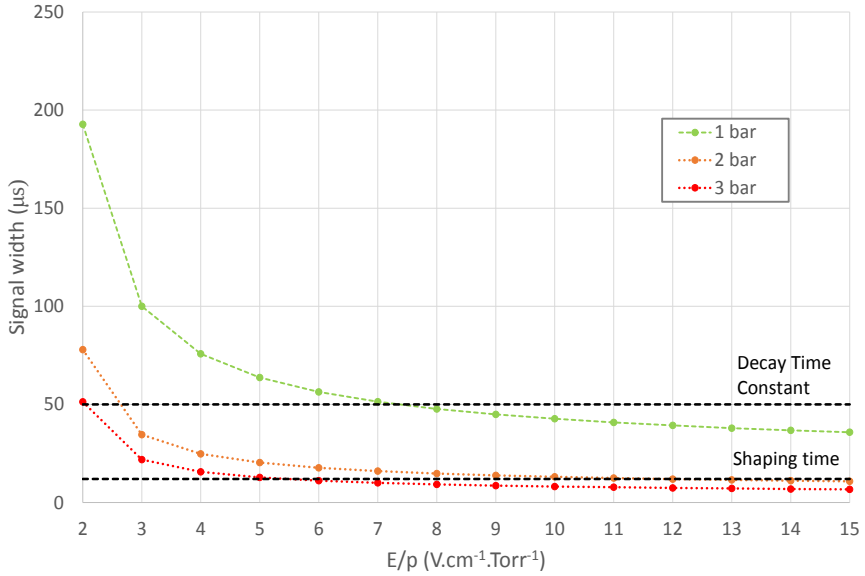

Figure 3.18: Signal width as a function of the E/p at the anode surface for different Xe pressures (1, 2 and 3 bar). Represented in black (dashed lines) are the constraints created by the available electronics, the time constant of the preamplifier CANBERRA 2006 (50 μs) and the shaping time of the TENNELEC TC243 (12 μs).

Looking at figure 3.18, it is possible to see that with the present electronics it is not possible to collect all the charge at 1 bar, with the signal being affected by the time constant of the preamplifier used (τ=50 μs) and by the maximum shaping time allowed by the linear amplifier (12 μs). Nevertheless, increasing the pressure above 2 bar, the majority of the charge is collected, because on one hand the signal width decreases significantly, and on the other hand the majority of the charge is created at the end of the alpha-particle track.

To verify that we were collecting all the charge with the time constants used in the preamplifier and linear amplifier, we studied the charge collected as a function of the shaping time of the linear amplifier. For this purpose, we proceeded with the charge calibration of the detector electronics. Using a pulse generator (ORTEC Model 448 Research Pulser), a known voltage is applied to the terminals of a high precision capacitor with 2 pF. The charge accumulated in the capacitor is then converted to voltage by the pre-amplifier (CANBERRA Model 2006) with a sensitivity of 47 mV/1-M electron-ion pairs that is connected in series to this calibration capacitor. Then, the voltage signal is shaped and further amplified by a linear amplifier TENNELEC TC243 with different

shaping times (2 μs, 4 μs, 8 μs and 12 μs) and maintaining a fixed gain of 100, producing an output voltage related to the charge accumulated in the high precision capacitor. The experimental apparatus is depicted in figure 3.19.

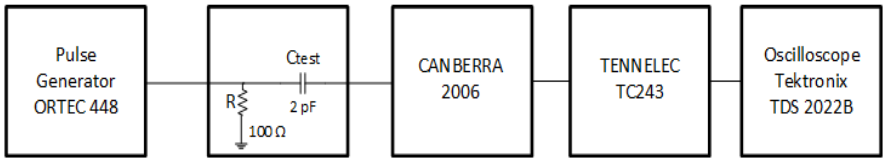

Figure 3.19: Charge calibration schematic.

Varying the pulse amplitude in the pulse generator, we obtain the charge accumulated at the high precision capacitor and the corresponding output voltage. Plotting the input charge as a function of the voltage output, the calibration curves presented in figure 3.20 were obtained.

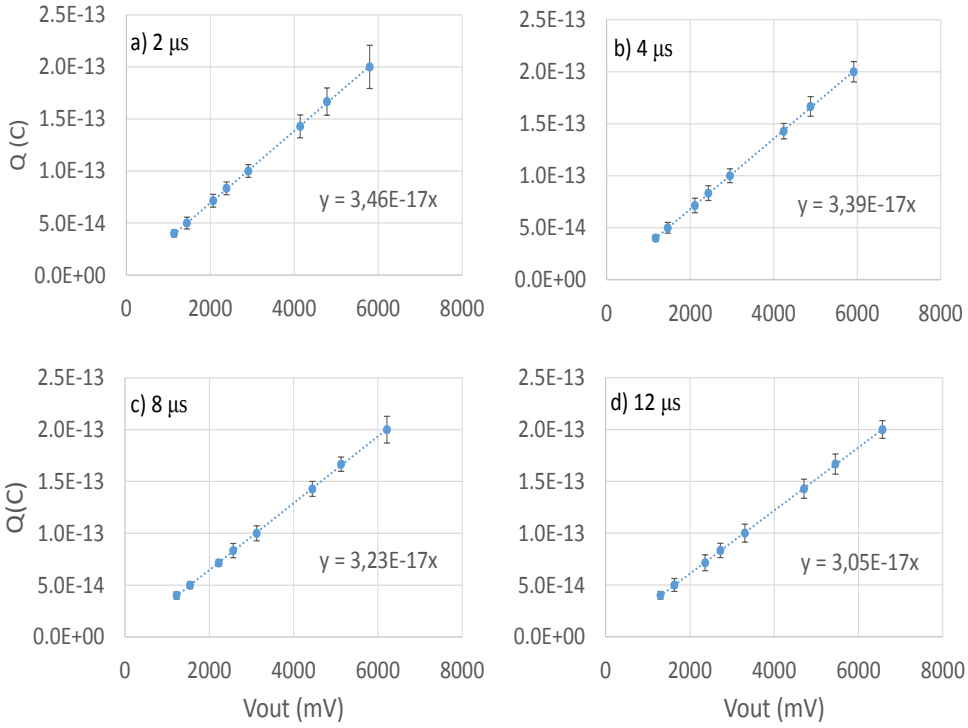

Figure 3.20: Charge calibration curves for the detector's associated electronics (CANBERRA 2006 plus TENNELEC TC243 varying the shaping time between 2 and 12 μs).

Making use of the expressions obtained by fitting the charge calibration curves in figure 3.20, the charge collected at G2 was determined as a function of the shaping time (2, 4, 8 and 12 μs) for 3 bar of Xe, using an E/p at the anode surface of 6 V·cm^{-1}·Torr^{-1} and of about 1 V·cm^{-1}·Torr^{-1} in the collecting region. The results for the collected charge in G2 as a function of the shaping time of the linear amplifier are given in figure 3.21.

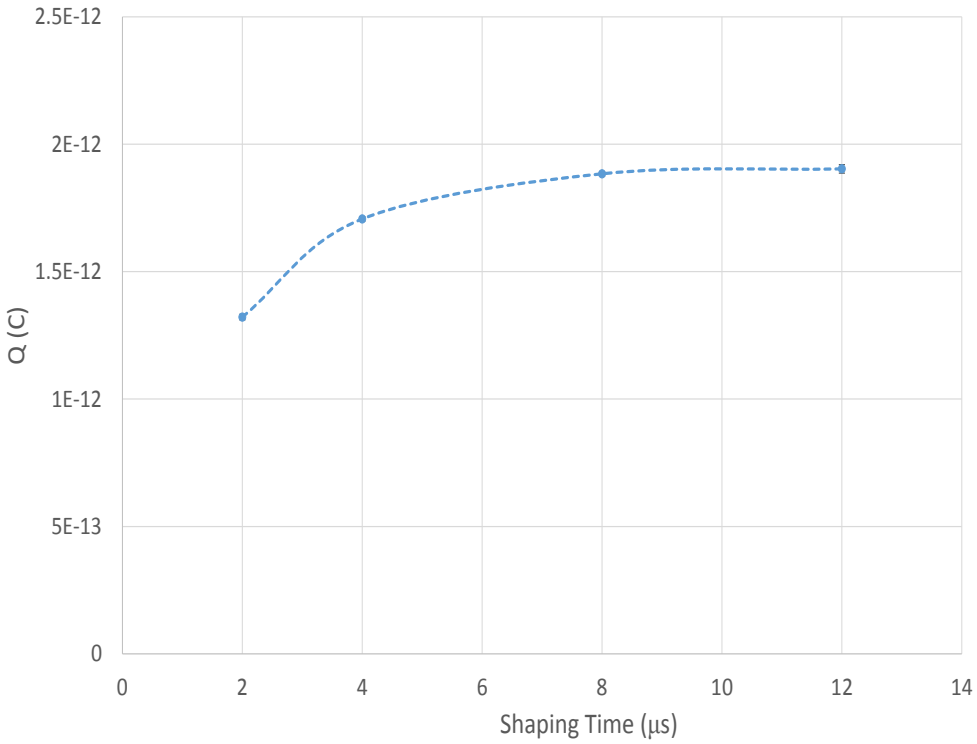

Figure 3.21: Charge calibration curve for the detector's associated electronic (CANBERRA 2006 plus TENNELEC TC243 varying the shaping time between 2 and 12 μs).

Observing figure 3.21, it is possible to see that increasing the shaping time from 8 μs to 12 μs, there is no significant change in the charge collected, meaning that the great majority of the charge is collected in these conditions.

3.5 Detector Gain

This detector's experimental gain can be determined through the ratio between the average number of photoelectrons detected and the number of primary electrons.

$$G_{exp} = \frac{\bar{n}_{photoe^-}}{\bar{n}_{primary\ e^-}} \tag{3.2}$$

This value is usually obtained by dividing the amplitude of the signal after the multiplication stage by the amplitude of the signal collected without this amplification stage. Nevertheless, in our case the direct measurement of the primary electron charge was not possible with the electronics available (as seen subsection 3.3.1), and an alternative method was used.

First from the remaining energy of the alpha particles, after crossing the Mylar window (4.427 MeV obtained previously in section 3.2), the number of primary electrons is estimated using equation 1.7 with the w-value (20.9 eV) of alpha particles taken from [115]. As a result it is possible to find that about 212000 primary electrons are produced.

Now that we have the estimate for the number of electrons collected at the anode, we need to determine the number of photoelectrons collected at grid G2.

The use of the equation, Q=3.05×10^{-17}.V$_{out}$, obtained from the linear fitting performed to the charge calibration data for the 12 μs of shaping time (figure 3.20), allowed us to obtain the charge collected at G2 that corresponds to the V_{out} obtained in the measurements. Knowing the number of photoelectrons collected in the collecting grid and dividing these by the number of primary electrons generated per alpha particle entering the detector, the gain can then be determined as a function of the reduced electric field in both scintillation and collecting region.

Figure 3.22 displays the detector experimental gain obtained for different pressures (from 1 up to 3 bar), maintaining a constant E/p at the surface of the anode (7.5 V·cm^{-1}·Torr^{-1}), for different E/p in the collecting region. Full lines represent the estimated theoretical gain for each condition using the same colour code, obtained through equation 2.8.

Looking at figure 3.22, it is possible to see that the gain experimentally obtained is in agreement with the estimated theoretical gain for the E/p at the collecting region below the Xe scintillation threshold. Fixing the E/p value at the surface of the anode and varying it at the collecting region from 0.63 up to 1.33 V·cm^{-1}·Torr^{-1} the gain was seen to increase more than 4 times, with no significant deterioration of the energy resolution, R, as will be discussed in the next section.

Figure 3.23 shows the estimated theoretical gain for the planar geometry prototype [6] and for the present cylindrical one and the experimental gain obtained in this prototype an E/p at the surface of the anode of 7.5 V·cm^{-1}·Torr^{-1} and an E/p at the collecting region of 1 V·cm^{-1}·Torr^{-1} for different Xe pressures.

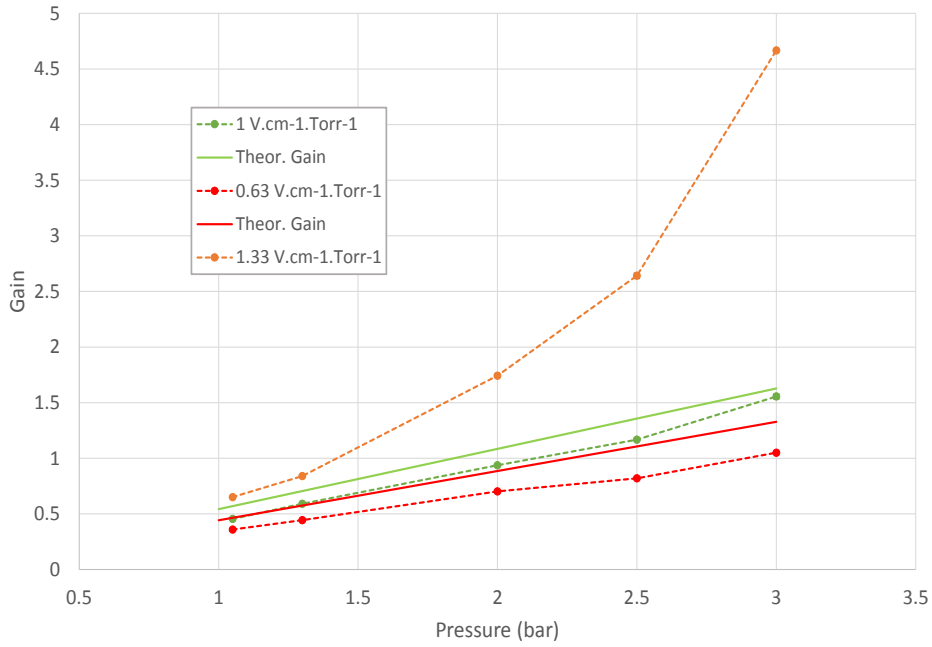

Figure 3.22: Experimental gain of the detector (GPSC) as a function of the pressure maintaining the E/p at the surface of the anode fixed (7.5 V·cm^{-1}·Torr^{-1}) for distinct E/p at the collecting region: 0.63 V·cm^{-1}·Torr^{-1} (dashed red line), 1 V·cm^{-1}·Torr^{-1} (dashed green line) and 1.33 V·cm^{-1}·Torr^{-1} (dashed orange line) together with the estimated theoretical gains for the same conditions (full lines).

Comparing the estimated theoretical gain for the first prototype with the results obtained experimentally it is possible to observe that the gain of the present prototype is about 3 times larger than that expected for the planar geometry at a pressure of 3 bar. These results are in agreement with the previous discussion in section 2.2.2. There are several features that can explain the results pointed out, of which the higher solid angle is the most important. However, a slight difference was observed between experimental and theoretical gains in this new prototype. The differences can be due to non-uniformity of the electric field in the collection region (which will affect the extraction efficiency of photoelectrons from the photocathode), the thickness of the grids (not considered) that affects the optical transmission, and the dependence of the latter with the angle of incidence of the scintillation photons and, not least important, the fact that part of the charge might not be collected due to the limitation on the time constants of the electronics used. Nonetheless, the results are quantitatively close to those expected with the experimental behaviour observed corresponding to that predicted.

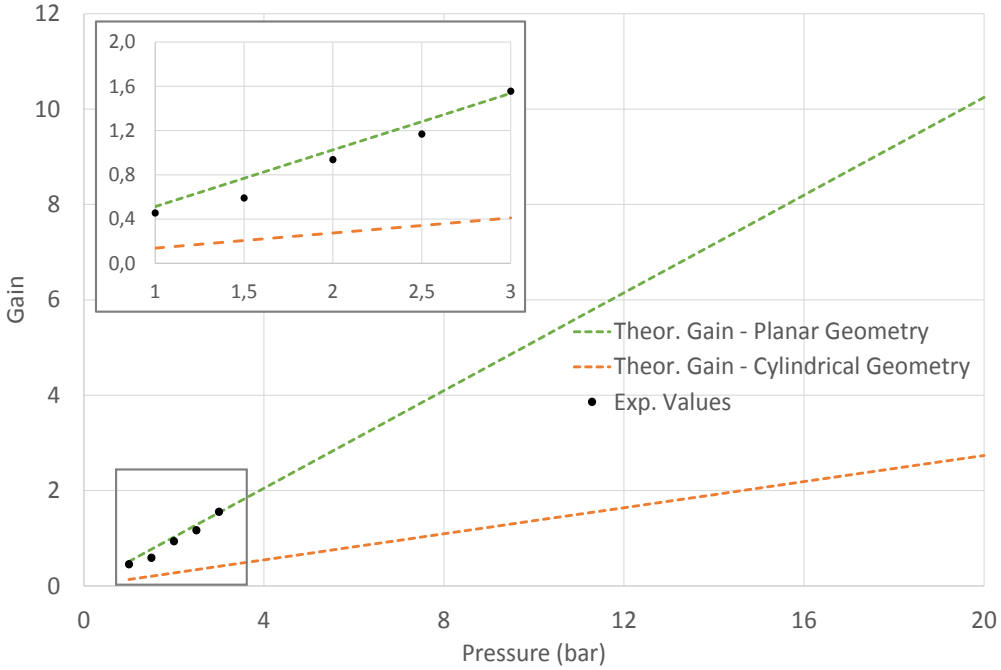

Figure 3.23: Gain of the detector (GPSC) as a function of the pressure maintaining a constant E/p at the surface of the anode (7.5 V·cm^{-1}·Torr^{-1}) and at the collecting region (1 V·cm^{-1}·Torr^{-1}). The black dots are the experimental results and the dashed green line is the theoretical gain for the cylindrical geometry. The dashed orange line represents the theoretical gain for the planar geometry.

Finally, to assess the influence of the anode voltage in the detector gain, the gain value was determined, keeping a constant E/p value at the collecting region and varying the E/p at the anode's surface. The results are presented for 1.05 bar Xe pressure (figure 3.24) since, due to limitations of the available power supplies, this was the pressure for which a wider range of E/p could be studied.

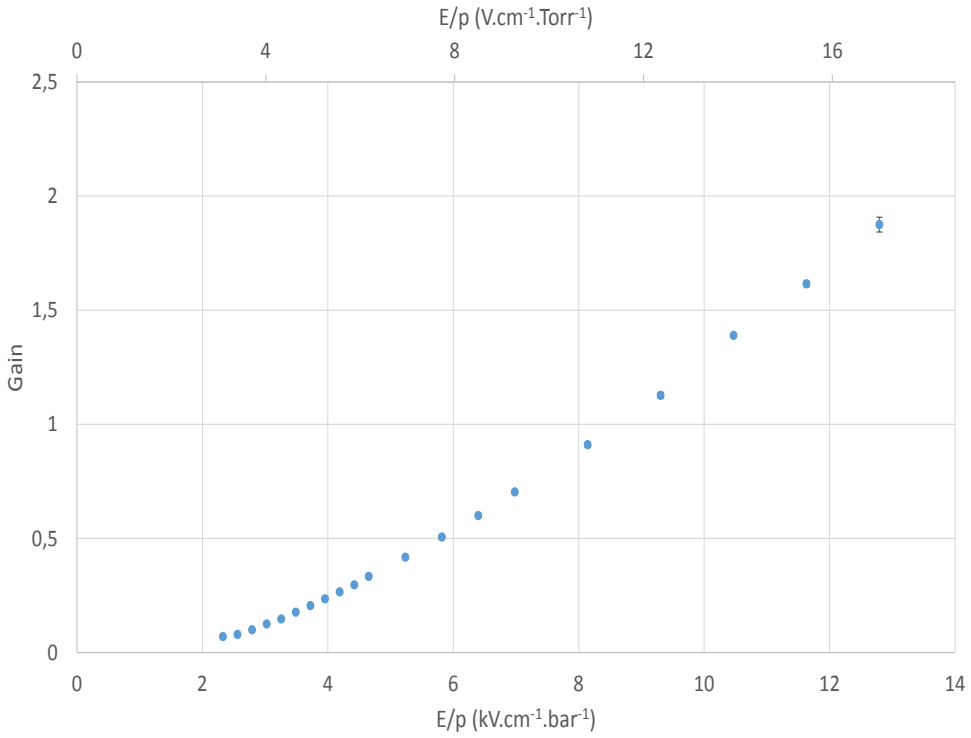

Figure 3.24: Experimental gain for 1.05 bar as a function of the E/p at the anode surface for E/p at the collecting region of about 0.9 V·cm^{-1}·Torr^{-1}.

At this pressure, the gain varies from 0.5 to 1.9, keeping an almost linear behaviour. Assuming that a similar behaviour will be observed for higher pressures, we can expect the detector gain to be about 10 for 5 bar and approximately 29 for 15 bar, which is similar to that obtained in the previous prototype with planar geometry [112]. These estimates should be seen as a lower limit for the experimental gain for the reasons already mentioned. Although limited, the experimental gain can be enhanced increasing either the E/p at the surface of the anode above Xe ionization threshold or the E/p at the collecting region slightly above Xe scintillation threshold.

3.6 Energy Resolution

In order to assess the influence of the different variable parameters (E/p at the anode surface and collecting grid and pressure) in the energy resolution of the detector, the charge signal collected at G2 was amplified and shaped by the electronics described and fed to a multichannel analyser (MCA) where the spectra were recorded and analysed. The spectra were fitted to Gaussian curves using the software associated with the MCA, and from these fittings the energy resolution, R, was obtained.

3.6.1 Energy Resolution vs E/p at the surface of the anode

In this work the energy spectra for the ^{241}Am alpha source was obtained varying the E/p at the anode surface and maintaining constant the E/p in the collecting region. Figure 3.25 shows typical spectra obtained with the MCA for different E/p at the anode surface, for different pressures: a) 2 b) 2.5 and c) 3 bar and keeping a constant E/p in the collecting region of about 1 V·cm^{-1-1}·Torr^{-1}. Above each spectrum the E/p at the anode's surface is represented with matching colour.

From figure 3.25, we can observe that the peak centroid moves towards greater channels for higher anode voltages, indicating the presence of more scintillation light as expected. Figure 3.26 presents the energy resolution obtained for alpha particles as a function of the E/p at the surface of the anode and for a E/p of 0.85 V·cm^{-1}·Torr^{-1}, 1 V·cm^{-1}·Torr^{-1} and 1.05 V·cm^{-1}·Torr^{-1} at the collecting region, for three different Xe pressures: a)1.05 bar, b) 2 bar and c) 3 bar. Again, the information on the E/p at the anode surface is represented in a matching colour to facilitate the identification.

As expected, the energy resolution improved with increasing E/p at the surface of the anode, since the scintillation yield also increases. Because the number of detected photons is larger and the statistical fluctuations associated with the photon-to-photoelectron conversion process and with the amplification process are small, R also improves. The best energy resolution was obtained for an E/p of 7 V·cm^{-1}·Torr^{-1} at the anode surface, at a pressure of 2 bar. Although better results would be expected for higher pressures for this E/p value at the anode's surface, limitations in the power supply for voltages above 8000 V did not allow the reproduction of the same E/p conditions at higher pressures.

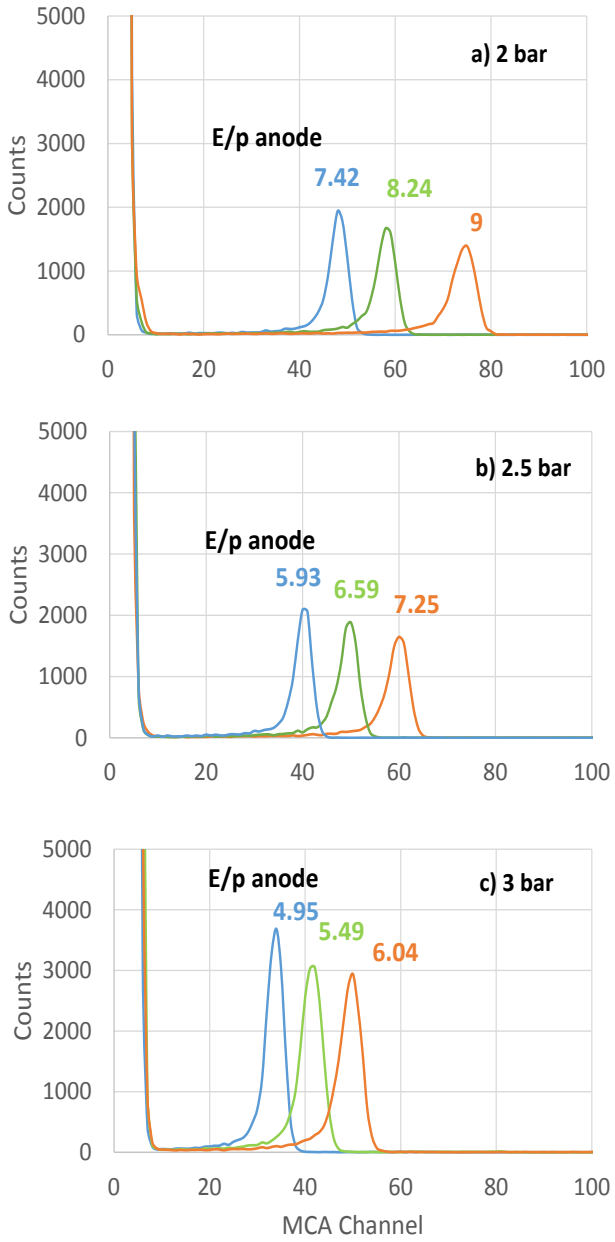

Figure 3.25: Typical spectra obtained with the MCA as a function of the E/p at the anode's surface, for constant E/p at the collecting region of about 1 V·cm^{-1}·Torr^{-1} and for different pressures Xe pressures of a) 2, b) 2.5 and c) 3 bar. The corresponding E/p at the anode surface is represented in the same figure with matching colour.

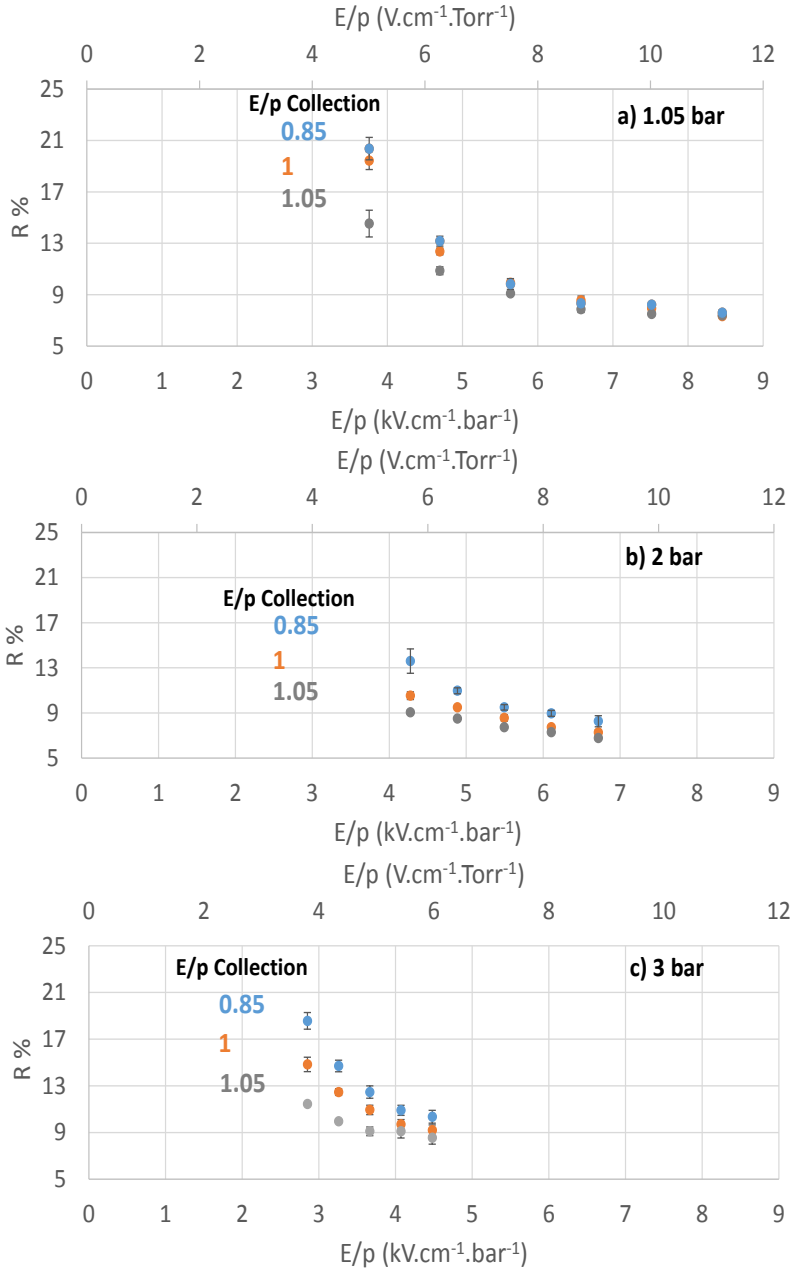

Figure 3.26: Energy resolution as a function of the E/p at the anode surface for different E/p at the collecting region of about 0.85 V·cm^{-1}·Torr^{-1}, 1 V·cm^{-1}·Torr^{-1} and 1.05 V·cm^{-1}·Torr^{-1} and for different pressures Xe pressures of a) 1.05, b) 2 and c) 3 bar.

The dependence of R with the Xe pressure is highlighted in figure 3.27 where the energy resolution is presented as a function of the E/p at the surface of the anode, keeping a constant E/p value in the collection region of 1 V·cm^{-1}·Torr^{-1}, for different pressures between 1.05 and 3 bar. Increasing the pressure it is possible to see that R is improved as expected, since the number of produced photons is higher maintaining the same E/p.

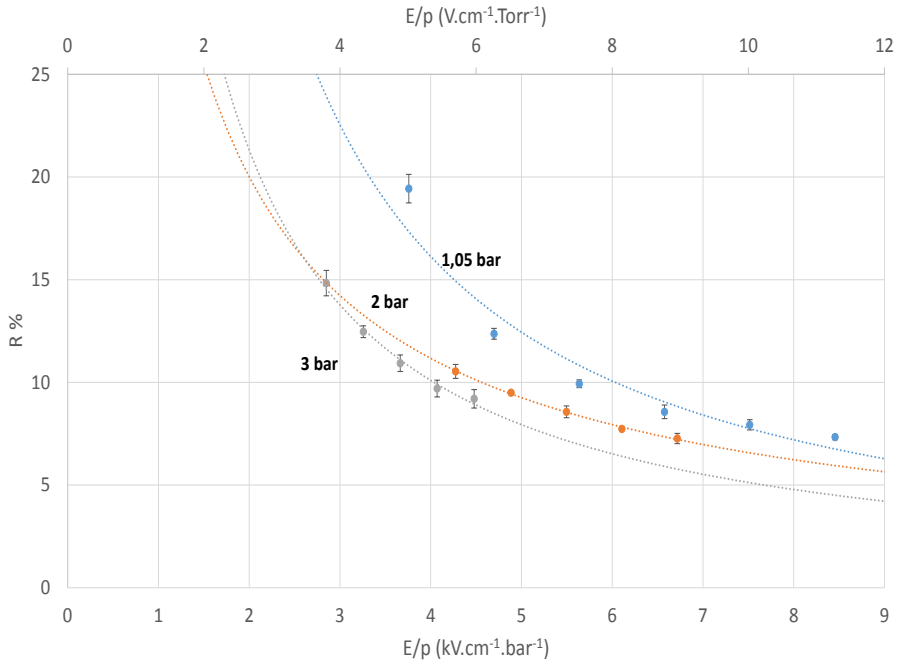

Figure 3.27: Energy resolution as a function of the E/p at the anode surface for constant E/p at the collecting region (∼1 V·cm^{-1}·Torr^{-1}), for various Xe pressures (1.05, 2 and 3 bar) using ^{241}Am alpha-particles (4.427 MeV). The dotted lines represent the fitting to the data.

Also from figure 3.27 it is possible to see that for an E/p value at the anode surface above the ionization threshold and up to 10 there is no significant degradation on the energy resolution; on the contrary, some improvement can be observed for E/p between 6 and 10 V·cm^{-1}·Torr^{-1}. This improvement is related to the fact that increasing the E/p allows additional scintillation photons to be produced in a larger region and if some ionization occurs it is still small taking place near the anode, with little influence on the fluctuations due to the charge production.

From the same figure, an extrapolated R of about 5% for alpha particles is expected at an E/p∼7 V·cm^{-1}·Torr^{-1} and p=3 bar. This energy resolution value is close to the expected 4.75% (as it will be explained in subsection 3.6.5) for the energy entering the

detector (4.427 MeV), and is still a promising value, since the detected beam of alpha particles is far from being monoenergetic as it traversed the Mylar window of the detector. From the results obtained with the SRIM simulation (section 3.1) we could conclude that traversing the window introduces an energy dispersion of at least 2%, considering an incidence angle at the window up to 22°. This effect, together with the contribution of recombination that may also be present, both introducing additional fluctuations, indicates that the energy resolution is promising. The effect of the source collimation was also addressed experimentally and the results obtained will be presented in section 3.6.4.

3.6.2 Energy Resolution vs E/p in the collecting region

Figure 3.28 shows typical spectra obtained with the MCA for different E/p values in the collecting region for an E/p value at the anode surface of about 6 V·cm^{-1}·Torr^{-1} and for different Xe pressures. In these figures the same E/p in the collecting region is represented with matching colour.

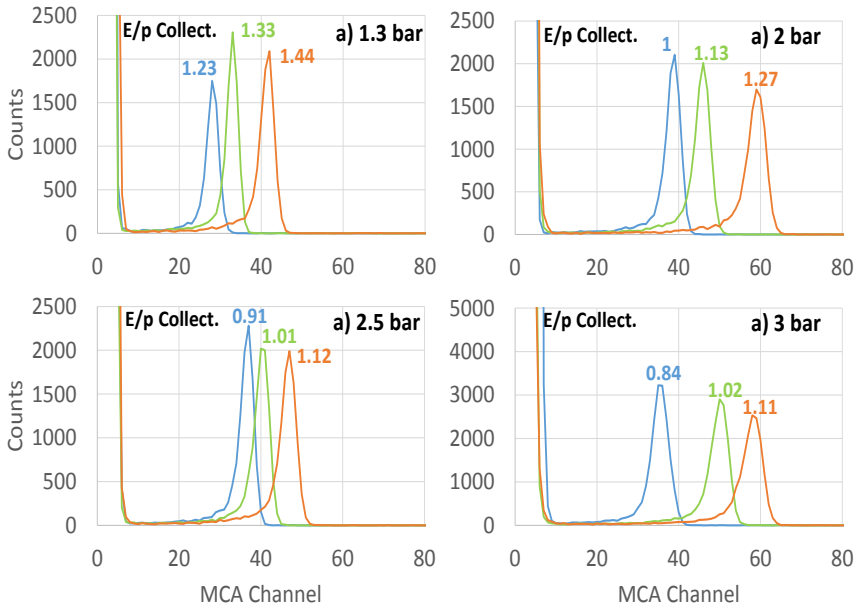

Figure 3.28: Typical spectra obtained with a MCA as a function of the E/p at the collection region, for a fixed E/p at the anode surface of 6 V·cm^{-1}·Torr^{-1} and for Xe pressures of 1.3 (a), 2 (b), 2.5 (c) and 3 bar (d).

From this figure we can observe that, the peak centroid moves towards higher channels with increasing E/p in the collecting region, since the extraction efficiency in the

collecting region is improved by the increasing electric field but also because some light may be produced in this region when E/p is increased above the Xe scintillation threshold (1 V·cm^{-1-1}·Torr^{-1}), due to photon positive feedback.

Figure 3.29 shows the results obtained for the energy resolution, as a function of the E/p at the collecting region and for three different E/p values at the anode's surface and for four different pressures a) 1.3 bar, b) 2 bar, c) 2.5 bar and d) 3 bar. Due to the limitations in the power supply source, it was not possible to obtain the same E/p conditions at the anode surface for all the pressures. The energy resolution improves with increasing E/p at the collecting region, even for E/p slightly above the secondary scintillation threshold. Nevertheless, above 1.3 V·cm^{-1}·Torr^{-1}, the energy resolution is degraded due to the positive feedback in the collecting region, as expected. This effect was only observable at 1 bar, since this E/p value was only achievable at this pressure.

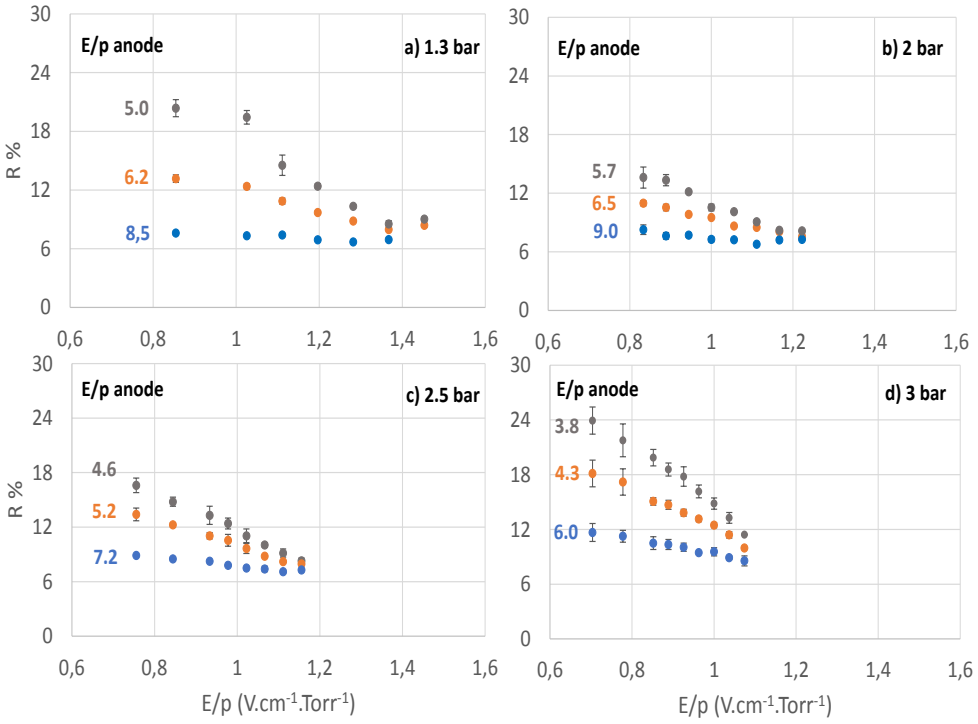

Figure 3.29: Energy resolution as a function of the E/p at the collection region, for different E/p at the anode surface for pressures of a) 1.3, b) 2, c) 2.5 and d) 3 bar Xe.

One interesting feature of the detector, which can be inferred from the previous studies, is that the lesser light produced in this prototype, due to the limited scintillation region, may be compensated by the signal amplification induced by the positive feedback in the

collecting region. Usually positive feedback is avoided due to the fluctuations introduced, but in our case, an additional gain in light due to small amount of photon positive feedback (for a E/p of about 1.1 V·cm^{-1}·Torr^{-1} in the collecting region) gives rise to a small improvement of the energy resolution. This is probably because the collecting region is small (about 0.5 cm), and the amount of positive feedback is not significant.

Figure 3.30 displays the energy resolution obtained as a function of the E/p in the collecting region, maintaining a constant E/p at the anode surface (6.5 V·cm^{-1}·Torr^{-1}), and for different pressures: 1.3 bar, 2 bar and 2.5 bar. In this figure, it is possible to see again that pressure plays an important role in the best energy resolution achieved. In fact, for the same conditions of E/p at the anode and in the collection region, we can observe that the energy resolution improves for higher pressures. This is of course related to the higher scintillation yield for the higher pressure, an effect related with the mean free path between excitation of the gas atoms, which is inversely proportional to the gas density, as the number of collisions between electrons and Xe atoms increases.

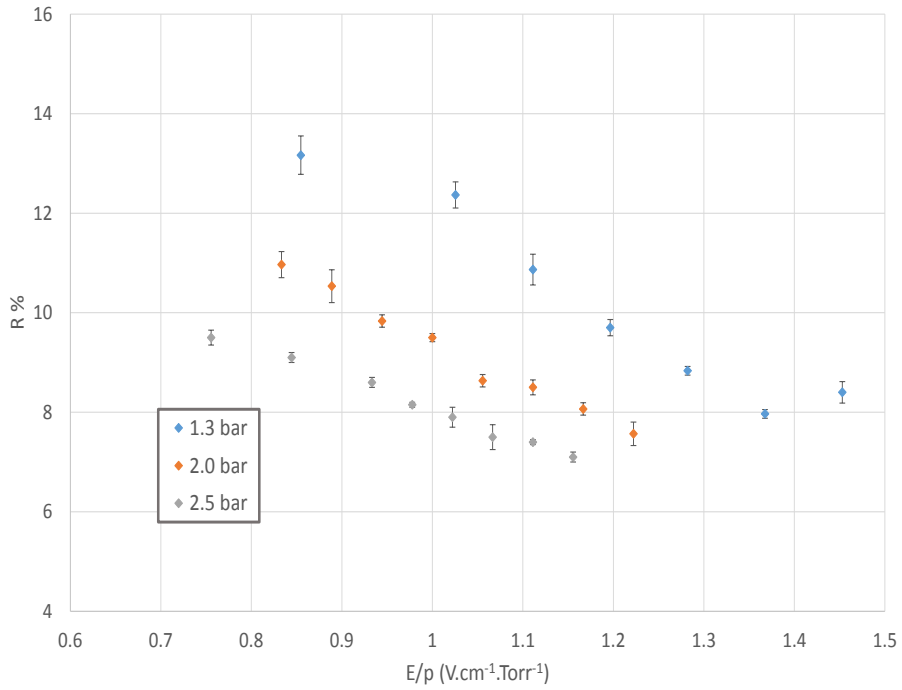

Figure 3.30: Energy resolution as a function of the E/p at the collection region, for a E/p at the anode surface of about 6.5 V·cm^{-1}·Torr^{-1} for pressures of 1.3, 2 and 2.5 bar Xe.

Comparing the energy resolution obtained so far with alpha-particles with the previous planar prototype, it is possible to see that the energy resolution is improved from about 22% to 6.4% in the best conditions. In another paper [41] with alpha-particles of 8.76 MeV, the authors obtained an energy resolution of 4.2% using also a cylindrical geometry, Ar as the detecting medium and a PMT as photosensor.

3.6.3 Influence of source collimation in R (%)

A study was also performed to assess the influence of the source collimation in the energy resolution. In this study, the E/p at the anode was kept constant (6 V·cm^{-1}·Torr^{-1}) and the E/p at the collecting region was 1.15 V·cm^{-1}·Torr^{-1}, for a pressure of 3 bar. Three different positions for the alpha source were selected: just above the Mylar window, at 1 cm and 2 cm from it.

The results showed that increasing the distance of the source to the Mylar window improves the energy resolution by about 0.8%. This is the result of the increased collimation, that leads to a larger uniformity of the alpha particles' energy. This effect is more pronounced as we move from the position just above the window to a distance of 1 cm than from the distance of 1 cm to 2 cm, since for the first case the larger angles of incidence varies from 20° to 8°, while from 1 cm to 2 cm distance, it varies only from 8° to 4.6°. Still, it is clear that the energy resolution can be improved with better collimation.

3.6.4 Signal-to-Noise Ratio

The analysis of the signal-to-noise ratio (SNR) establishes the minimum detectable energy, for the current working conditions.

In this work we used the definition of SNR as SNR=20 $log(A_{signal}/A_{noise})$, where A_{signal} is the signal amplitude and A_{noise} is the noise level. Using the MCA software, both the peak centroid (H_0), that corresponds to the signal amplitude A_{signal}, and the channel (N_0) with about 5% of the number counts observed in H_0, that corresponds to A_{noise}, were identified, and using the definition presented, the SNR can then be calculated.

$$SNR = 20 \cdot log\left(\frac{H_0}{N_0}\right) \tag{3.3}$$

Figure 3.31, displays a sample of the SNR measurements carried out as a function of the E/p at the surface of the anode, for different E/p values in the collecting region: 0.7 V·cm^{-1}·Torr^{-1} (blue), 1 V·cm^{-1}·Torr^{-1} (orange) and 1.07 V·cm^{-1}·Torr^{-1} (grey), for a pressure of 3 bar, since it was the pressure condition which yielded the best SNR results.

As expected, the signal-to-noise ratio is improved when both the E/p at the scintillation and collecting regions are increased. For reduced electric fields below 1 V·cm^{-1}·Torr^{-1} at the collecting region, the noise affects the signal more, which is probably related to the smaller signal amplitude, and so to a smaller SNR value.

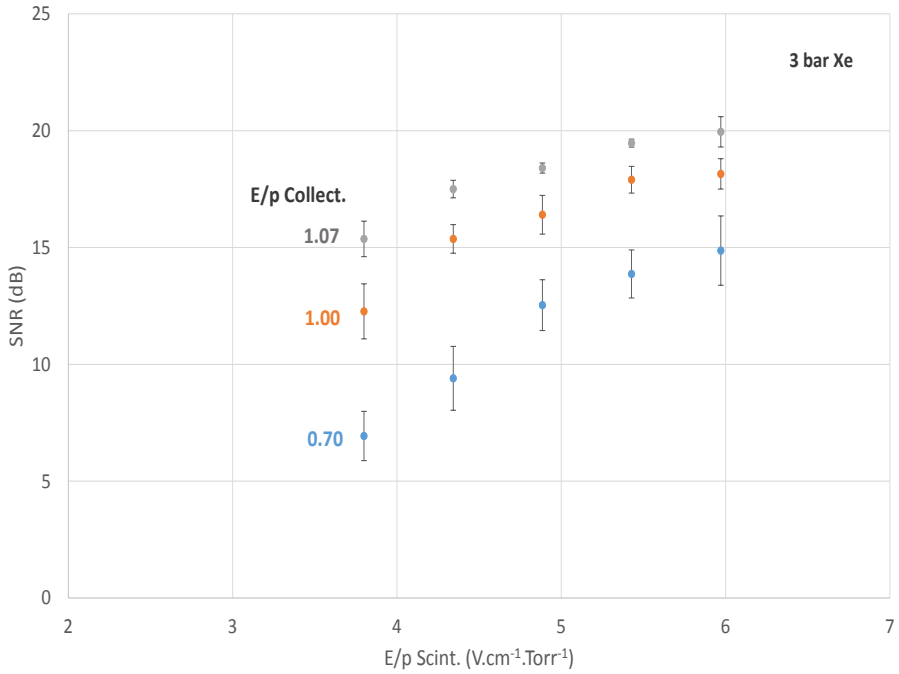

Figure 3.31: Signal-to-noise ratio (SNR) as a function of the E/p at the anode surface for several E/p values at the collection region of 0.7 V·cm^{-1}·Torr^{-1} (blue), 1 V·cm^{-1}·Torr^{-1} (orange) and 1.07 V·cm^{-1}·Torr^{-1} (grey), for Xe at 3 bar.

Increasing the reduced electric field at the surface of the anode brings about a significant improvement in the SNR, due to the increasing secondary photon production in the scintillation region.

The signal obtained in the best conditions was about 10 times the noise fluctuations. From these results, it is possible to establish a minimum detectable energy (MDE) in our current working conditions. Figure 3.32 displays the SNR and MDE as a function of the E/p at the collecting region, for a fixed E/p at the surface of the anode of about 6 V·cm^{-1}·Torr^{-1}, and for Xe at 3 bar. In the present configuration the MDE is about 450 keV. However, the major limitations are not intrinsic: higher voltage power supplies will allow for higher pressure and better results can be anticipated. In fact, optimising the High-Voltage (HV) sources and associated electronics and electrical shielding, which due to time limitations were not possible to perform, the SNR could be further improved.

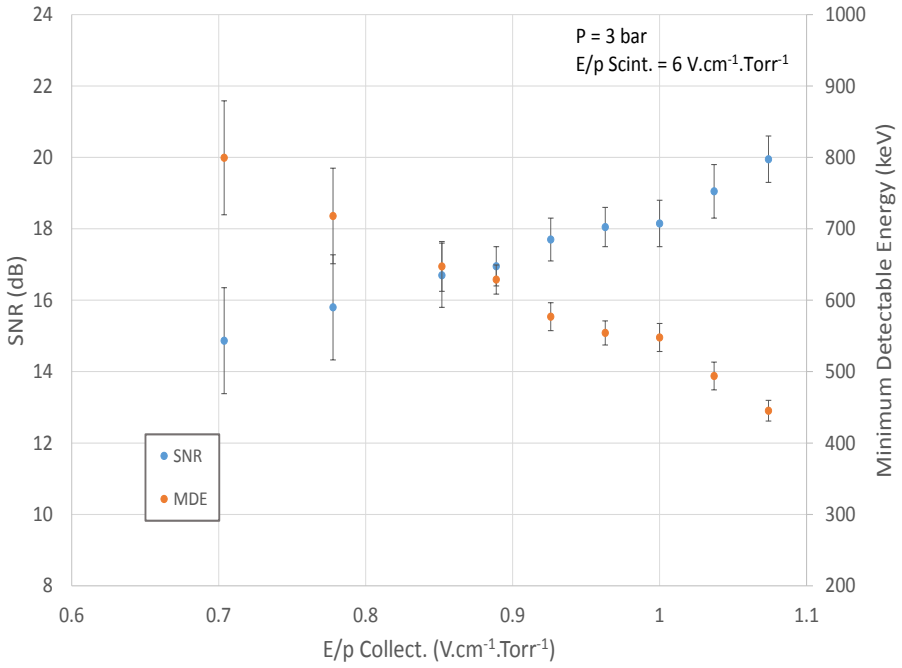

Figure 3.32: Signal-to-noise ratio (SNR) as a function of the E/p in the collecting region for an E/p at the anode surface of 6 V·cm^{-1}·Torr^{-1}, for a pressure of 3 bar of Xe and the corresponding Minimum Detectable Energy (MDE).

3.6.5 Comparison of the experimental and expected R (%)

As discussed previously, the energy resolution, R, of a detector is defined by the $FWHM$ of the energy spectrum peak divided by the incident energy E_r, and as mentioned there are several factors contributing to it, which in our case can be grouped into five different terms:

$$R = \frac{\Delta E}{E_r} = \sqrt{\left(\frac{\Delta E_0}{E_r}\right)^2 + \left(\frac{\Delta E_{amp}}{E_r}\right)^2 + \left(\frac{\Delta E_{photosensor}}{E_r}\right)^2 + \left(\frac{\Delta E_{el}}{E_r}\right)^2 + \left(\frac{\Delta E_{\alpha}}{E_r}\right)^2} \quad (3.4)$$

that correspond to the fluctuations in the primary electron cloud formation (ΔE_0), to the amplification processes involved in the signal formation in the detector that include the amplification (ΔE_{amp}) and the photosensor ($\Delta E_{photosensor}$), the fluctuations introduced by the detector associated electronics (ΔE_{el}) and fluctuations introduced by the fact that the radiation is not monoenergetic when entering the detector (ΔE_{α}). While the first three terms were already introduced in subsection 2.2.3, the term $\Delta E_{el}/E_r$ is inversely proportional to the SNR [6] and $\Delta E_{\alpha}/E_r$ can be estimated from the energy dispersion of the alpha particles upon entering the detector.

Substituting the more detailed information for the different contributions in equation 3.4, we get:

$$R = 2.355\sqrt{\underbrace{\frac{F}{\bar{n}}}_{e^-} + \underbrace{\frac{1}{\bar{n}}\left(\frac{J}{N_S} + \left(\frac{\sigma_{Ns}}{N_S}\right)^2\right)}_{\text{amplification}} + \underbrace{\frac{1}{N_e}\left(1 + \left(\frac{\sigma_q}{G_q}\right)^2\right)}_{\text{photosensor}} + \underbrace{\left(\frac{\frac{ENC}{e}}{\bar{n}G}\right)^2}_{\text{electronics}} + \underbrace{\left(\frac{\sigma_n}{\bar{n}}\right)^2}_{\text{energy}}} \quad (3.5)$$

where F is the Fano factor in Xe, $\bar{n}$ is the number of primary electrons created by the incident radiation, J is the relative variance on the number of photons produced N_S, $\left(\frac{\sigma_{Ns}}{N_S}\right)^2$ is a measure of the fluctuations in the number of scintillation photons able to reach the photocathode, N_e the number of photoelectrons produced in the photosensor per incident ionizing particle or photon absorbed in the detector and $\left(\frac{\sigma_q}{G_q}\right)^2$ is a measure of the fluctuations in the photoelectron multiplication gain, G_q. ENC is the equivalent noise charge of the preamplifier, e is the electron charge and G the gain of the detector, while $\left(\frac{\sigma_n}{\bar{n}}\right)^2$ corresponds to the variance in the energy of the incident radiation (for non-monoenergetic ionizing radiation), as in our case in the tests with the alpha particles used.

Looking at equation 3.5, it is possible to see that there are two limiting resolution values depending on the gain. For high gains, the energy resolution reaches values close to the intrinsic one, only limited by the span in the energy of the incident ionizing radiation, with the limit coming mainly from the variance in the energy of the incident ionizing radiation followed by the statistical fluctuations on the primary charge production as the fluctuations in the amplification process involved are small and the contribution of the photosensor and electronics can be neglected. For low gains, the limit for the resolution of such detectors comes essentially from two sources: the ENC, which depends on the capacitance coupled to the preamplifier, and on the variance of the incident radiation energy.

To determine how the resolution of the GPSC is affected by the ENC, it is necessary to understand how the ENC of the preamplifier used (CANBERRA 2006) behaves with the input capacitance. From the datasheet of this preamplifier, we could obtain the following expression for the ENC:

$$ENC = 2 \times 10^{-22} Cin^2 + 2 \times 10^{-19} Cin + 5 \times 10^{-17} \quad (3.6)$$

To find the ENC in our working conditions, considering only the preamplifier influence, the equivalent input capacitance is assumed to be the detector capacitance (610 pF), calculated previously in subsection 2.3.1, and substituting in the previous equation, we get ENC=2.56×10^{-16} C.

Now that the ENC value has been determined, we can proceed with the determination of the theoretical energy resolution limit for the present detector, for the energy of the alpha particle entering the detector, considering its dispersion due to the Mylar window ($4.486^{+}_{-}0.09$ MeV), and varying the gain.

Before solving equation 3.5 to obtain the expected R, some simplifications can be introduced. Since $J<<F$, $N_S>100$ and assuming that the solid angle effect can be neglected for the alpha particles case, $\left(\frac{\sigma_{Ns}}{N_S}\right)^2=0$, the second term regarding the fluctuations on the amplification of the detector, can also be neglected. In addition, considering that there is no multiplication involved in the extraction of the photoelectrons since E/p in the collecting region is kept below the scintillation threshold, the photosensor term is reduced only to the fluctuations associated with the photoelectron production, $\left(\frac{1}{\bar{n}G}\right)$. Consequently we get:

$$R = 2.355\sqrt{\frac{F}{\bar{n}} + \frac{1}{\bar{n}G} + \left(\frac{\frac{ENC}{e}}{\bar{n}G}\right)^2 + \left(\frac{\sigma_n}{\bar{n}}\right)^2} \tag{3.7}$$

Substituting F by 0.17 in Xe, $\bar{n}=\frac{E_r}{w}$ by 214641 e^-, the ENC by 2.76×10^{-16} C and fluctuations in the alpha particles' energy for a source placed inside the detector $\left(\frac{\sigma_n}{\bar{n}}=0\right)$ and outside having to transverse a Mylar window $\left(\frac{\sigma_n}{\bar{n}}=0.02\right)$, we can infer the expected behaviour in terms of energy resolution with the detector gain. Figure 3.33 shows the limiting energy resolution attainable with the present prototype as a function of the gain, considering monoenergetic alpha particles placed inside the detector (blue), and considering an alpha particles' source with the Mylar window (orange), similar to the one present in our case.

Looking at the values obtained experimentally (section 3.6) and those calculated for the same operating conditions ($G = 1$), obtained using 2.5 bar for E/p of 6 V·cm^{-1}·Torr^{-1} at the anode surface and 1 V·cm^{-1}·Torr^{-1} in the collecting region), it is possible to see that we are relatively close to the limiting value of this detector. The difference observed here can be due to non-uniformity of the electric field in the collecting region or even to a possible recombination effect in the absorption region of the alpha particles in the detector as the electric field in that region is small and this effect is known to be more relevant as the pressure increases and for relatively low electric fields (below 0.1 V·cm^{-1}·Torr^{-1}). In addition to these factors, there are possibly other electronic noise sources that can contribute to the deterioration of the energy resolution and that were not considered and which include the linear amplifier and HV power supplies, which can enhance the contribution of the $\Delta E_{el}/E_r$ term in equation 3.5.

In addition, if we look at equation 3.5, it is possible to see another interesting feature. Increasing the E/p in the collecting region above the excitation threshold will allow an increase in the gain, which means that, despite increasing the fluctuations in the photosensor term, $\left(\frac{\sigma_q}{G_q}\right)^2$, this effect will be compensated by the increased gain eventually resulting in an improvement in R.

From the studies performed we concluded that this detector can reach improved R and G when compared with the previous prototype, allowing the use of E/p values at the surface of the anode above the ionization threshold (up to 7.5 kV·cm^{-1}·bar^{-1}) and slightly above the scintillation threshold (up to 0.825 kV·cm^{-1}·bar^{-1}) at the collecting region.

So, improvements can be foreseen when using limited positive feedback in the collecting region as well.

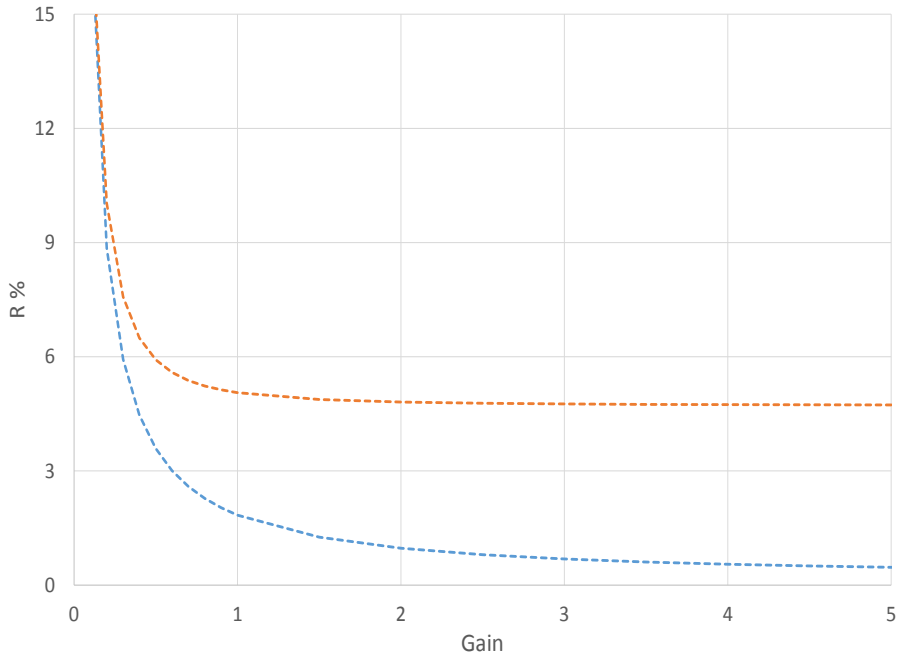

Figure 3.33: Limiting energy resolution with the present prototype as a function of the detector gain: considering a alpha particle source (4.427 MeV) placed inside the detector (blue) and considering a alpha particle source (4.427 MeV) with an energy dispersion of 2% due to the use of a Mylar window (orange).

4

Ion Mobility Measurement in Relevant Gases

Michael Faraday (1791-1867) introduced the term ion for the first time to identify the then-unknown species that were seen moving from one electrode to the other through an aqueous medium. The term ion comes from the Greek word ιόν that means "to go". Within two years after the discovery of X-rays, Ernest Rutherford (1871-1937) measured the mobility of ions formed by X-ray ionization.

This chapter presents and discusses experimental studies of the ion mobility in gas mixures. The work was developed in the scope of the participation in the NEXT Collaboration [116] and RD51/CERN Collaboration [117]. The chapter starts with a brief description of the motivation behind these studies and its relevance for several ongoing experiments [116, 118]. Then, the most relevant concepts regarding ion formation are introduced along with the theory used for the ion identification process, which will be followed by a brief description of the experimental system used and its working principle. Following this, the ion mobility results will be presented; first for the pure gases and then for the gas mixtures studied. Finally, a discussion on the applicability of the Langevin limit will be undertaken and some conclusions will be drawn.

4.1 Introduction

Measuring the mobility of ions in gases is relevant in several areas from physics to chemistry. A good example of its relevance is in gaseous radiation detectors, in particular in the modelling and understanding of the pulse shape formation [4, 5, 7].

Recently, in the search for dark matter, particle physics, high energy and rare events experiments, new gas mixtures are being proposed for which this information is lacking. Namely for the international collaboration NEXT (Neutrino Experiment with Xenon TPC), that uses xenon at high pressure as detection medium, the use of a molecular

additive to increase electron drift velocity and decrease electron diffusion is being considered [119–125]. The mobility of ions in the candidate mixtures may be determinant in the choice.

Nitrogen (N_2) was initially thought as a possible additive gas, as it was expected to increase the charges' drift velocity, decreasing their diffusion as in other molecular gases [19] without seriously affecting the scintillation yield. This option would lead to an improved tracking capability and background rejection, essential in the scope of the experiment.

Another additive proposed was trimethylamine - $(CH_3)_3N$ (TMA) - $(CH_3)_3N$ which, in very small percentages, has been considered as a potential choice since it could also be advantageous in other aspects [122–124, 126, 127] besides the improvement of electron drift parameters, namely in the wavelength shifting of the xenon VUV emission [123–125] and as a partner for xenon in the Penning effect, which could bring an improvement in the energy resolution [122–127].

Regarding other experiments, the same problem has arisen since data for ion mobility in mixtures of two and three gases is scarce. For example in the ALICE TPC, where the build-up of positive space-charge in the large ($\sim$90 m^3) drift volume of the upgraded detector requires on line correction of the track distortions for immediate data compression [118], this information is of utmost importance. The choice of the gas mixture hints at the time it takes the ions to drift back to the central electrode, which will affect the overall performance of the detector. For these reasons, the ALICE TPC collaboration needs detailed information on gas mixtures, which include Ar or Ne with CO_2 and N_2.

In addition, this information might be useful for Transition Radiation Detectors (TRDs). These detectors are used for particle identification at high momenta [128, 129]. The choice of the gas mixture for such detectors is determined by several parameters such as high electron/ion velocity and low electron diffusion, which are of key importance [5] as they influence the rate capability and signal formation of TRDs' of the Multi-Wire Proportional Chamber type (MWPCs) [8]. Xenon (Xe) is considered to be the best choice as the main gas, while the choice for the best quencher is not unanimous [5]. One effective quenching gas is methane, (CH_4) but its use is limited due to its flammability [5] and is usually substituted by carbon dioxide (CO_2). Presently, xenon-carbon dioxide (Xe-CO_2) mixtures are widely used in high energy physics experiments such as ALICE [129, 130] and CBM (Compressed Baryonic Matter experiment) TRD [129, 131]. Still, gas mixtures such as xenon-methane (Xe-CH_4) and xenon-ethane (Xe-C_2H_6) are being used in high energy physics experiments such as DØ [132, 133], HERMES [134] and the Pioneering High Energy Nuclear Interaction eXperiment (PHENIX) TRDs [135, 136]. So the transport properties of ions in these gas mixtures are also needed. Although less commonly adopted, mixtures of argon with ethane or methane (Ar-C_2H_6 and Ar-CH_4) could also be useful.

The experimental set-up used in the present work, developed by P.N.B. Neves and described in detail in [137, 138], allows the measurement of ion mobility in gas mixtures. Initially considered for high pressure, it was converted into a low-pressure gas system.

Lowering the operating pressure provided a wider scope of application and more detailed information on the fundamental processes involved in the ion transport, and also allowed a reduction in the inherent operation cost. Still, the results have been consistently in accordance with data obtained at higher pressure [139].

Several gas mixtures have been studied in recent years to address these issues both in the scope of our participation in the NEXT Collaboration and at the RD51/CERN Collaboration, and have already been published [140–152].

In this chapter, the experimental results on Xe-N_2, Xe-CO_2, Xe-CF_4, Ar-C_2H_6 and Ar-CH_4 will be presented and discussed. First, some discussion of previous results for the pure gases used is made and then the discussion on the gas mixtures, which is followed by a brief comparison between the different gas mixtures in the scope of the different experiments for which they were considered. Some definitions and processes that may affect the ion mobility are introduced before the experimental results.

4.2 Ion Mobility

When a group of ions moves under the influence of a weak and uniform electric field, they collide with atoms or molecules from the medium losing energy, and gaining/losing energy from the electric field. A steady state is reached, when the energy lost in the collisions is balanced by that gained from the electric field and as a result, the average speed of the group of ions, also known as drift velocity v_d, becomes proportional to the electric field intensity [153]:

$$v_\mathrm{d} = KE \tag{4.1}$$

where K is the mobility of the ions, expressed in units of $\mathrm{cm^2{\cdot}V^{-1}{\cdot}s^{-1}}$ and E is the intensity of the drift electric field. This relation is applicable for low E/N, *i.e.*, when the energy gained from the field between collisions is below the thermal energy [153, 154] . The ion mobility, K, is normally expressed in terms of the reduced mobility K_0,

$$K_0 = KN/N_0 \tag{4.2}$$

with N the gas number density and N_0 the Loschmidt number ($N_0 = 2.68678 \times 10^{19}$ $\mathrm{cm^{-3}}$ for 273.15 K and 101.325 kPa according to NIST [155]). The mobility values are commonly presented as a function of the reduced electric field E/N in units of Townsend (1 Td=10^{-17} $\mathrm{V{\cdot}cm^2}$).

When addressing these subjects, there are two important concepts that help in the understanding and prediction of the behaviour of the ions in different gas mixtures. These are the Langevin limit and Blanc's law and due to their importance a brief discussion will follow.

4.2.1 Langevin Limit

According to Langevin's theory, first published in 1905 [156], one limiting value of the ions' mobility is reached when the electrostatic hard-core repulsion becomes negligible compared to the neutral polarization effect [154]. This limit is given by the following equation,

$$K_{pol} = 13.88 \left(\frac{1}{\alpha\mu}\right)^{\frac{1}{2}} \tag{4.3}$$

where α is the neutral polarisability in cubic angstroms (a summary of the values for the different gases used in this study is given in table 4.1) and μ is the ion-neutral reduced mass in unified atomic mass units. Although the Langevin limit is meant to be applied for real ion-neutral systems in the double limit of low E/N and low temperature, it predicts the low-field mobility at room temperature with relatively good accuracy [154]. Although generally accepted, Langevin theory has some known limitations in its application, namely with ions that may interact by resonant charge transfer, where it fails to provide correct values for their mobility [139].

Table 4.1: Neutral polarisabilities for different gases (Xe, Ar, N_2, CO_2, CH_4, C_2H_6 and CF_4). Adapted from [157, 158].

Neutral	Polarisability (Å^3)	Ref.
Xe	4.044 ± 0.013	[159]
Ar	1.64 ± 0.01	[159, 160]
N_2	1.74	[161]
CO_2	2.93	[161]
CH_4	2.62 ± 0.01	[158]
C_2H_6	4.47 ± 0.01	[158]
CF_4	3.86 ± 0.01	[162]

4.2.2 Blanc's law

In 1908, an important pioneering work was carried by A. Blanc in the field of ion transport properties, more specifically, ion mobility in binary gas mixtures [163]. His work resulted in an empirical law, which has proven to be very useful, as the mobility of a group of ions of the same species in a binary gas mixture was found to be the combination of the ions' mobility in each gas.

According to this law, the reduced mobility of the ion in the binary mixture, K_{0mix}, can be expressed as follows:

$$\frac{1}{K_{0mix}} = \frac{f_1}{K_{0g1}} + \frac{f_2}{K_{0g2}} \tag{4.4}$$

where K_{0g1} and K_{0g2} are the reduced mobility of that same ion in an atmosphere of 100% of gas #1 and #2 respectively and f_1 and f_2 are the molar fraction of each gas in the

binary mixture [163].

These concepts are of particular importance in the scope of this work as they will be used in the ion identification process. Although the knowledge of ion mobility is the main goal of this work, it is also important to identify the ions as this might be useful to predict the ageing of detectors.

4.3 Processes Affecting Ion Mobility

The mobility of ions depends on many factors that vary from the ions' charge to their mass, and the composition of the drift medium. In order to understand how these factors influence ion mobility it is important to understand the mechanisms underlying their formation since on one hand it will allow their behaviour to predicted but will also help in the ion identification process.

As discussed previously, the ionization of the gas molecules can be caused either by incident radiation or energetic electrons, which will be referred to as primary ionization or through secondary ionization, due to the transfer of the excess energy of the primary ions to other atoms or molecules, resulting in further ionizations. Besides these direct channels, ion formation can also be achieved by transfer processes, such as the Penning effect [164], charge transfer and the associative reactions (Hornbeck-Molnar process [15]). The "charge exchange" mechanism plays an important role in the ion-atom interaction, its main effect being the change in the magnitude and in the energy dependence of the momentum transfer cross section, at low E/N [165]. Because the exchange forces are usually weak except at very short distances [71], its impact on ion mobility tends to be greater with increasing pressure.

Depending on the type of molecules involved in this "charge transfer" reaction, different nomenclatures are used. The charge exchange reaction can be expressed by:

$$A^+ + B \rightarrow A + B^+ \tag{4.5}$$

If A and B are identical atoms, the reaction is called symmetric, and asymmetric if A and B are different. In addition, the reaction is called resonant if the initial and final states are degenerate and nonresonant if the initial and final states are nondegenerate.

The ease of occurrence of charge exchange between an ion and a parent atom arises from the circumstance that, in the absence of interaction, the electronic energy of the system does not depend on the charge location, so, both states are energetically equivalent. As a result, the weakest electron transfer interaction between A and B, if given sufficient time, will cause charge-exchange [166]. This charge exchange process reduces the mobility of ions involved, and in the case of noble gases, makes the atomic ions slower than the higher mass dimer ones.

In addition, more complex ions can be formed through chemical reactions between the primary ions and the gas atoms/molecules, namely through an important mechanism

which is ion cluster formation, that can produce complex ions. Cluster ions are composed by a central ion with one or more neutral atoms or molecules, bound together by charge-induced dipole forces. Typically the binding energy of cluster ions ranges from 0.1-1.5 eV, with the range of binding energies placing cluster ions between the ionic and covalent bonds and the van der Waals bond [139]. Due to their mass, cluster ions are slower, and may significantly affect the performance of detectors [139].

The formation of a simple cluster with only one neutral from the same species as the main ion, is usually described by the following chemical reaction:

$$A^+ + A + M \rightarrow A^+.A + M \tag{4.6}$$

Knowing the reactions that may take place during the drift time of the ions can be extremely helpful in the ion identification process. The theory used in the present work to estimate the relative concentration of each ion species as a function of the time is called collision theory. The principle behind this theory is that reactant particles must collide for a reaction to occur, and only a certain fraction of the total collisions will transform reactants into products. This is due to the fact that only a portion of the molecules have enough energy and momentum at the instant of impact to break the existing bonds. The reaction rate defines the rate at which a reaction occurs. If we consider two species, A and B, that react leading to the formation of species C and D:

$$aA + bB \rightarrow cC + dD \tag{4.7}$$

where a, b, c and d represent the stoichiometric coefficients. The reaction rate, R, for this reaction can be expressed by:

$$\mathrm{R} = -\frac{1}{a}\frac{d[A]}{dt} = -\frac{1}{b}\frac{d[B]}{dt} = \frac{1}{c}\frac{d[C]}{dt} = \frac{1}{d}\frac{d[D]}{dt} \tag{4.8}$$

where $[A]$, $[B]$, $[C]$, $[D]$ are the concentrations of the different species present at a certain instant. The reaction rate can be rewritten as,

$$\mathrm{R} = \mathrm{k[A]}^m\mathrm{[B]}^n \tag{4.9}$$

where k is the rate coefficient or rate constant and m and n are the order of reaction of A and B, respectively. The reaction order is not necessarily related to the stoichiometry of the reaction, unless the reaction is elementary. In more complex problems an approximation can be made assuming that both the stoichiometry and reaction order are similar.

An elementary reaction is defined as a chemical reaction in which the products are formed in a single reaction step with a single transition state. The elementary reactions can be of first-order ($A \rightarrow products$), second-order ($A + B \rightarrow products$), and so forth.

The reaction rate of a first-order reaction is given by,

$$R = k[A] = -\frac{d[A]}{dt} \tag{4.10}$$

From the time integration of the previous equation, an expression for the concentration of $[A]$ can be obtained:

$$[A]_t = [A]_0.e^{-kt} \tag{4.11}$$

where $[A]_0$ is the initial concentration of A and $[A]_t$ the concentration at an instant t. Knowing the rate constant, k, and the initial concentration of A, it is possible to determine its concentration at any given instant, t, allowing us to predict which ion species will be present in the detector and contribute to the signal formation, at an instant t.

A similar deduction can be made for the second and third-order reactions. For example, the equation for the second-order reaction can be expressed as follows:

$$\mathrm{R} = \frac{d[A]}{dt} = -\mathrm{k}[A][B] \tag{4.12}$$

However, as the complexity of the reactions involved increases, the solution for these differential equations becomes more complicated.

4.4 Method and Experimental Setup

The system in which the experimental measurements were made [137] is based on very simple principles: ions moving in a weakly ionized atmosphere under a uniform electric field will lose the energy gained from the electric field and, after a number of ion-neutral collisions, a steady state is reached. The distance needed for the steady state to be reached depends on the electric field, gas pressure and ion involved. The technique to produce the ions uses a gas electron multiplier (GEM) covered with a 250 nm thick CsI film, acting as a photocathode, a UV flash Xe lamp (Hamamatsu L2439) with a frequency of 10 Hz and a pulse duration of 0.5 μs, and two grids (G1 and G2) separated by 0.5 mm.

The flash lamp releases photoelectrons from the photocathode deposited on the GEM. These electrons, are then guided by the electric field generated by the voltage applied across the GEM through the GEM holes, ionizing the gas molecules found on their paths. While the electrons are collected at the bottom electrode of the GEM, the cations produced drift in the opposite direction, towards grids G2 and G1 under a uniform electric field. Grid G2 acts as a Frisch grid, avoiding signal induction in the collecting grid G1 while ions drift in the chamber and ensuring a constant electric field during the ions' drift. The pulse collected at G1 is converted from current to voltage by a pre-amplifier, giving a time of arrival spectrum that is recorded in a digital oscilloscope (Tektronix TDS 2022B), set to continuously average 128 pulses and fed to a computer for further processing. This procedure is shown schematically in figure 4.1.

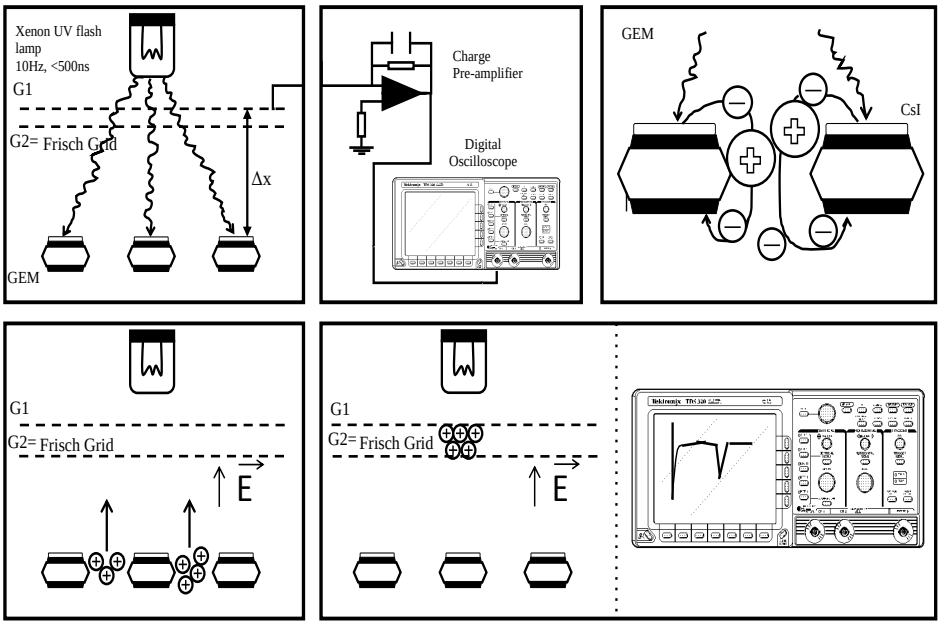

Figure 4.1: Schematic representation of the experimental system and method used to measure the ion mobility [138].

The background spectra, obtained without the voltage applied to the GEM (i.e. without drifting ions), is then subtracted from these time of arrival spectra and Gaussian curves are fitted to the peaks using a Matlab code. The trigger in the system is set by the UV flash lamp, providing the information on the initial time, and since the peaks' centroid in the time spectra corresponds to the average drift time of the ions along a known distance (4.273 cm), the drift velocity is determined and the mobility can then be calculated using expression 4.1.

Results obtained so far have proved that the technique is well established and provides consistent results. Even though the system does not provide direct information on the ion species involved, there are some features that can guide us to their identification. In fact, the capability of controlling the voltage across the GEM, which ultimately is an upper limit of the energy gained by the photoelectrons released from the photocathode, together with the ionization energies of the atomic/molecular species present, are the keys to ion identification. Knowing the primary ions that can be generated, and following their possible paths onto further reactions, helps in the identification and validation of the ions that reach G1. Cross checking of this identification can also be made using Blanc's law, if the required data is available. This method, although indirect, has proven to be most

successful and useful up to the present measurements.

The range of the reduced electric field values used to determine the ions' mobility is limited by two distinct factors: at high E/N by the occurrence of electric discharges, and for very low values of E/N (below 5 Td or 1.2 kV·cm^{-1}·bar^{-1}) by the deterioration of the time of arrival spectra, which has been attributed to collisions between the ions and impurity molecules when the drift time becomes too long.

4.5 Results and Discussion - Pure Gases

The results for pure gases will now be briefly discussed. This introduction will be important since this knowledge is important to interpret the drift spectra of their mixtures with other gases. These are xenon (Xe), argon (Ar), nitrogen (N_2), methane (CH_4), ethane (C_2H_6), carbon dioxide (CO_2) and carbon tetrafluoride (CF_4). The results presented here were all obtained with the present experimental system.

4.5.1 Xenon (Xe)

Regarding the case of pure Xe, one or two peaks can be observed depending on factors such as the pressure or E/N value [137]. The ions possible to be formed are the atomic (Xe^+) and dimer ion (Xe_2^+). While the atomic ion (Xe^+) is a direct result of electron impact ionization [167], Xe_2^+ is the result of the following reaction:

$$Xe^+ + 2Xe \rightarrow Xe_2^+ + Xe \tag{4.13}$$

and its relative abundance depends on the reaction time (that depends on the pressure, electric field, drift distance and temperature), which can be calculated using the rate constant available in table 4.2.

Extrapolating to zero field, the mobility of Xe^+ and Xe_2^+ ions in Xe was found to be 0.578 cm^2·V^{-1}·s^{-1} and 0.642 cm^2·V^{-1}·s^{-1}, respectively. The atomic ion has a lower mobility than the dimer one, due to the resonant charge transfer process between Xe^+ ions and Xe atoms, which results in the slowing down of these ions. Despite of the fact that two ions can be formed in Xe, for the pressures commonly used (6-10 Torr) and for the range of E/N (below 30 Td) studied here, only one peak was observed, which was attributed to Xe_2^+. In figure 4.2 a typical time-of-arrival (drift) spectrum for pure Xe at 8 Torr is shown, using an E/N of 15 Td and a V_{GEM} of 22 V, at room temperature (293 K). This is due to the fact that for this pressure and E/N values, during the drift time, most of the Xe^+ ions will convert into Xe_2^+ through the reaction 4.13.

Table 4.2: Possible ionization products, ionization cross sections for electron impact (16 eV, 20 eV, 22 eV and 25 eV) on Xe [167], appearance energies [168] and respective reaction rates [139, 169].

Reaction	Cross Sec. (10^{-16}cm^2)	A. E. (eV)	Rate Const.
$e^- + Xe \rightarrow Xe^+ + 2e^-$	2.43 ± 0.12 (20 eV) 2.90 ± 0.15 (22 eV) 3.48 ± 0.17 (25 eV)	12.13 ± 0.01	-
$Xe^+ + Xe \rightarrow Xe + Xe^+$	-	-	2.5×10^{-10} cm^3.s^{-1}
$Xe^+ + 2Xe \rightarrow Xe_2^+ + Xe$	-	-	$2.0\pm0.2\times10^{-31}$ cm^{6}s^{-1}

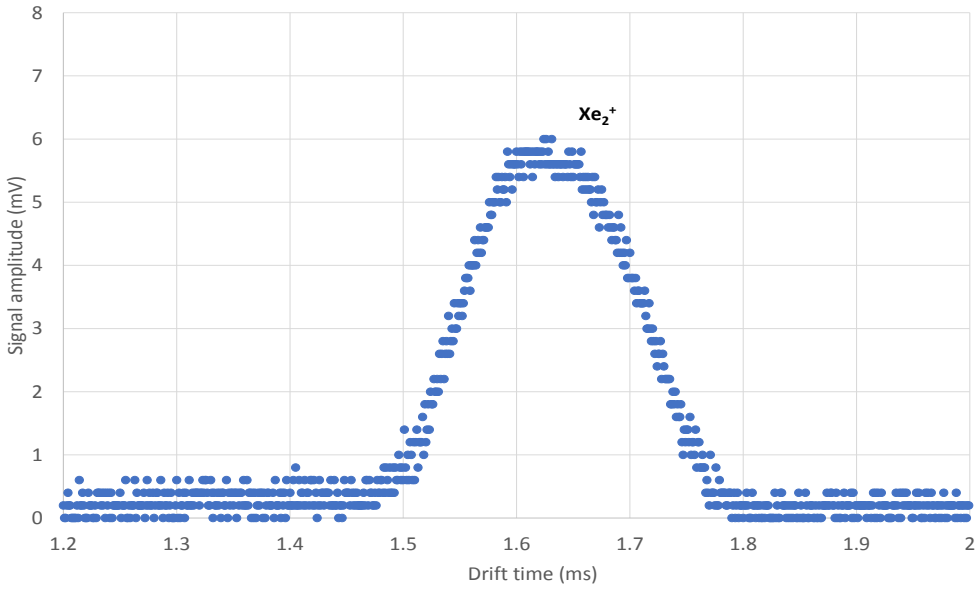

Figure 4.2: Time-of-arrival spectrum of an average of 128 pulses recorded for Xe at a pressure of 8 Torr, temperature of 293 K and for a reduced electric field of 15 Td with a voltage across GEM of 22 V.

4.5.2 Argon (Ar)

Regarding the pure Ar case, two different types of ions can be observed for electron impact ionization up to 20 eV and for pressures between 6 and 10 Torr. These two ions are the atomic and the dimer Ar ions, as in the case of Xe. The atomic ion (Ar^+) is a direct result of electron impact ionization [167], while the dimer ion (Ar_2^+) is, at our working pressures, the result of a three-body collision between Ar^+ and two neutrals, whose formation process

can be expressed by:

$$Ar^+ + 2Ar \rightarrow Ar_2^+ + Ar \tag{4.14}$$

The atomic ion has a lower mobility than the dimer one, also due to the resonant charge transfer process between Ar^+ ions and Ar atoms, that results in the slowing down of these ions, as in the case of Xe.

Table 4.3: Possible ionization products, ionization cross sections for electron impact (20 eV) on Ar [167], appearance energy (A.E.) [168] and respective reaction rates [139, 170].

Reaction	Cross Sec. (10^{-16}cm^2)	A. E. (eV)	Rate Const.
$e^- + Ar \rightarrow Ar^+ + 2e^-$	0.604 ± 0.030	15.76 ± 0.01	-
$Ar^+ + Ar \rightarrow Ar + Ar^+$	-	-	$3.7 \pm 0.37 \times 10^{-10}$ cm^3·s^{-1}
$Ar^+ + 2Ar \rightarrow Ar_2^+ + Ar$	-	-	$2.2 \pm 0.2 \times 10^{-31}$ cm^6·s^{-1}

Extrapolated to zero field, the mobility of Ar^+ and Ar_2^+ ions in Ar was found to be 1.57 cm^2·V^{-1}·s^{-1} and 1.92 cm^2·V^{-1}·s^{-1}, respectively. The results obtained in pure Ar were already reported in a previous work [138], and a typical time-of-arrival spectrum for pure Ar using a pressure of 8 Torr, an E/N of 15 Td and a V_{GEM} of 20 V, at a room temperature can be seen in figure 4.3. The bump observable in the spectrum is thought to be due to impurities, namely H_3O^+ and ArH^+, and for that reason they were not considered in the analysis.

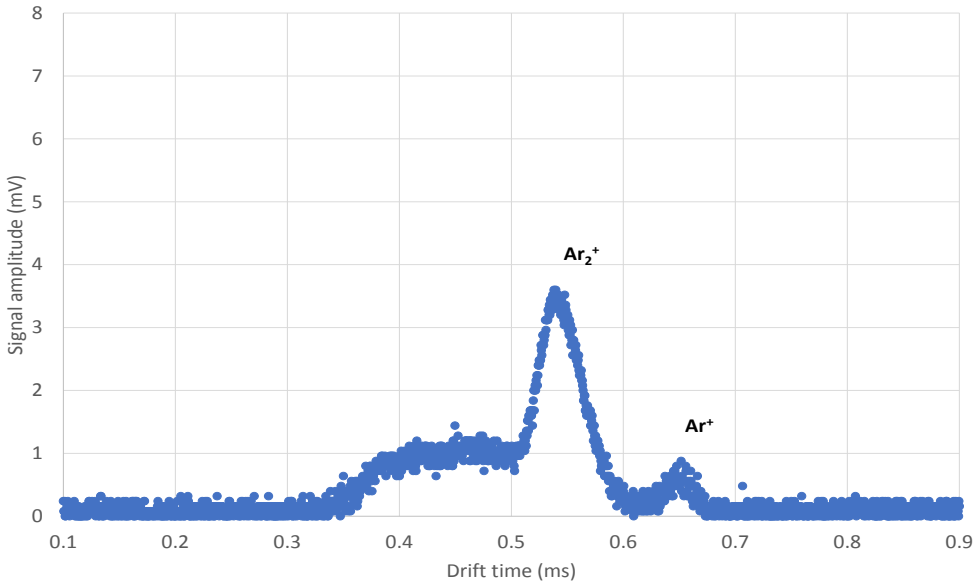

Figure 4.3: Time-of-arrival spectrum of an average of 128 pulses recorded for Ar at a pressure of 8 Torr, temperature of 293 K and for a reduced electric field of 15 Td with a voltage across GEM of 20 V.

4.5.3 Nitrogen (N_2)

In a previous work [171] for N_2 and for electron impact ionization with energies of about 20 eV, using reduced electric fields (E/N) between 15 and 35 Td and for a pressure range of 6-16 Torr at room temperature (298 K), only one peak was reported. The peak was identified as corresponding to N_4^+, as can be seen in figure 4.4.

From the literature it is known that as a result of electron impact ionization, for the above mentioned energies, only N_2^+ is formed at our working pressures. However N_2^+ will quickly react with N_2 molecules producing N_4^+ through:

$$N_2^+ + 2N_2 \rightarrow N_4^+ + N_2 \tag{4.15}$$

with a reaction rate constant of about $5{\times}10^{-29}\text{cm}^6{\cdot}\text{s}^{-1}$ for fields up to about 40 Td [172–174]. Since the dissociation energy of N_4^+ (0.87 eV) is much larger than the kinetic energy of the ion under the low reduced electric field used, the N_4^+ ion, once formed, will not easily dissociate back into N_2^+ and N_2. Extrapolated to zero field, the mobility of N_4^+ ions in N_2 was found to be 2.37 $\text{cm}^2{\cdot}\text{V}^{-1}{\cdot}\text{s}^{-1}$.

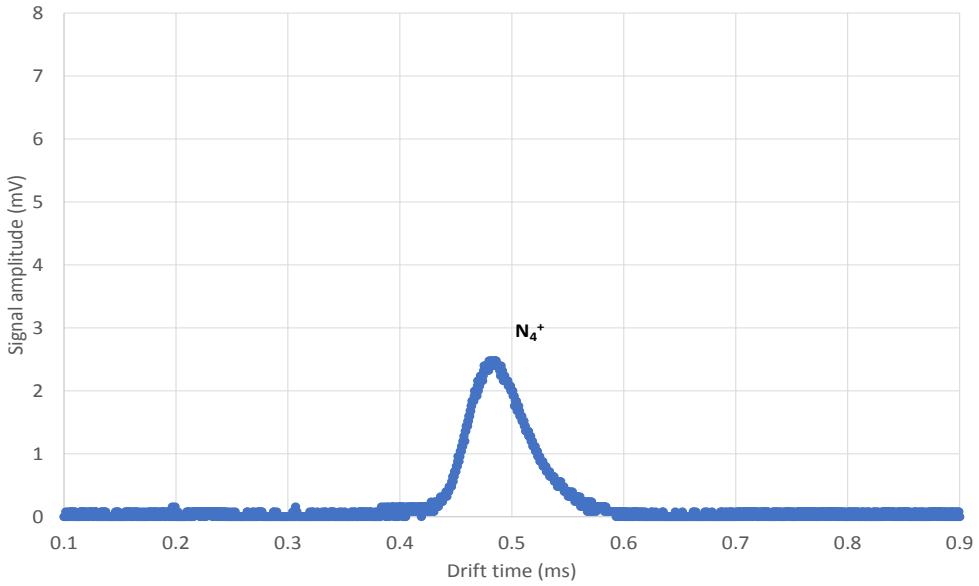

Figure 4.4: Time-of-arrival spectrum of an average of 128 pulses recorded for pure N_2 at a pressure of 8 Torr, temperature of 293 K and for a reduced electric field of 15 Td with a voltage across GEM of 22 V.

4.5.4 Methane (CH_4)

In pure CH_4, two peaks were observed and reported in a previous work [177], although other authors have observed three peaks in the same conditions as discussed in [177]. These two peaks were identified as corresponding to CH_5^+ (peak with higher mobility) and to a 2-carbon ion group ($C_2H_n^+$) together with the $C_3H_7^+$ ion (peak with lower mobility), and result from reactions involving the primary ions and CH_4 molecules. These primary ions can be found in Table 4.5, where we summarize the possible reactions due to electron impact in CH_4 for electron energies up to 20 eV, together with the respective cross-sections, appearance energies and product distribution. The probabilities presented were obtained using the cross sections for CH_4 primary ionization products and the CH_4 total cross section provided in [178], which allowed us to infer the product distribution of the primary ionization.

These primary ions can further react with the gas molecules resulting in more complex ions. Table 4.6 presents a summary of the chemical reactions, their product distribution, and respective reaction rates for the reactions between the primary ions displayed on table 4.5 and CH_4 molecules, at room temperature [180].

The reactions presented in tables 4.5 and 4.6 corroborate the explanation of the results obtained for pure CH_4, justifying the attribution of the most intense peak to CH_5^+ (lighter,

Table 4.4: Ionization products, ionization cross sections for electron impact (20 eV) on N_2 [175], appearance energy (A.E.) [176] and respective reaction rates [174].

Reaction	Cross Sec. (10^{-16}cm^2)	A. E. (eV)	Rate Const.
$e^- + N_2 \rightarrow N_2^+ + 2e^-$	0.013 (16 eV) 0.327 (20 eV) 0.527 (22 eV)	$15.6^{+}_{-}0.1$	-
$N_2^+ + 2N_2 \rightarrow N_4^+ + N_2$	-	-	$5.5^{+}_{-}0.3\times10^{-29}$cm^6·s^{-1}

Table 4.5: Possible ionization products, ionization cross sections for electron impact (20 eV) on CH_4 [178], appearance energies (A.E) [179] and respective product distribution.

Reaction	Cross Sec. (10^{-16}cm^2)	A. E. (eV)	Prod. Dist.
$e^- + CH_4 \rightarrow CH_4^+ + 2e^-$	$0.892^{+}_{-}0.134$	$12.65^{+}_{-}0.40$	56.7 %
$e^- + CH_4 \rightarrow CH_3^+ + H^- + e^-$	$0.512^{+}_{-}0.08$	$13.58^{+}_{-}0.10$	32.6 %
$e^- + CH_4 \rightarrow CH_3^+ + H + 2e^-$		$14.34^{+}_{-}0.10$	
$e^- + CH_4 \rightarrow CH_2^+ + H_2 + e^-$	$0.169^{+}_{-}0.03$	$15.10^{+}_{-}0.10$	10.7 %

thus with higher mobility) and the smaller one to a group of ions which include $C_2H_4^+$, $C_2H_5^+$ and $C_3H_7^+$ (heavier, thus with lower mobility).

4.5.5 Ethane (C_2H_6)

Following the previous work, the mobility of the ions in pure ethane (C_2H_6) was measured in the scope of this thesis for different reduced electric fields E/N (from 6 Td up to 42 Td) and for different pressures (in the 6-10 Torr range) at room temperature (293 K), with the resulting time-of-arrival spectra displaying two distinct peaks [140] as can be seen in figure 4.5 for a pressure of 8 Torr, E/N of 15 Td and V_{GEM} of 20 V and at room temperature (293 K).

For each pressure and reduced electric field studied, the respective mobility was determined by fitting a Gaussian function to the different peaks present in the time-of-arrival spectrum that allowed the average drift time of each ion to be determined. Then, making use of equation 4.1 it was possible to determine the mobility of the peaks identified.

When dealing with molecules with several atoms such as ethane, it is important to have a detailed knowledge of the possible reactions in order to identify the ion species present. By keeping V_{GEM} as low as possible, we are able to reduce the variety of primary ions produced in the GEM holes, reproducing the same ions that usually drift in common gas detectors. Table 4.7 summarizes the possible ionization reactions due to electron impact in C_2H_6 for electron energies up to about 20 eV, together with the respective cross-sections [181], appearance energies [182] and the product distribution. The displayed probabilities

Table 4.6: Ionization reactions, product distribution and rate constants for the collisions of the primary ions with CH_4. Adapted from [180].

Reaction	Rate Const. (10^{-9} $cm^3 \cdot s^{-1}$)	Prod. Dist.
$CH_4^+ + CH_4 \rightarrow CH_5^+ + CH_3$	1.140 ± 0.171	100%
$CH_3^+ + CH_4 \rightarrow C_2H_5^+ + H_2$	1.100 ± 0.165	100%
$CH_2^+ + CH_4 \rightarrow C_2H_4^+ + H_2$	1.300 ± 0.195	70%
$CH_2^+ + CH_4 \rightarrow C_2H_5^+ + H$		30%
$C_2H_5^+ + CH_4 \rightarrow C_3H_7^+ + H_2$	0.00009 ± 0.0000135	100%

were obtained using the cross sections for C_2H_6 primary ionization products and the C_2H_6 total cross section provided in [181], allowing us to infer the product distribution of this primary ionization.

Table 4.7: Possible ionization products, ionization cross sections for electron impact (20 eV) on C_2H_6 [181], appearance energies (A.E) [182] and their respective product distribution.

Reaction	Cross Sec. ($10^{-16}cm^2$)	A. E. (eV)	Prod. Dist.
$e^- + C_2H_6 \rightarrow C_2H_6^+ + 2e^-$	0.168 ± 0.017	11.46 ± 0.04	15.0 %
$e^- + C_2H_6 \rightarrow C_2H_5^+ + H^- + e^-$	0.122 ± 0.012	12.06 ± 0.06	10.9 %
$e^- + C_2H_6 \rightarrow C_2H_4^+ + H_2 + 2e^-$	0.490 ± 0.049	11.90 ± 0.04	43.8 %
$e^- + C_2H_6 \rightarrow C_2H_3^+ + H^- + H_2 + e^-$	0.135 ± 0.014	15.02 ± 0.10	12.1 %
$e^- + C_2H_6 \rightarrow C_2H_2^+ + 2H_2 + 2e^-$	0.080 ± 0.008	15.02 ± 0.10	7.1 %

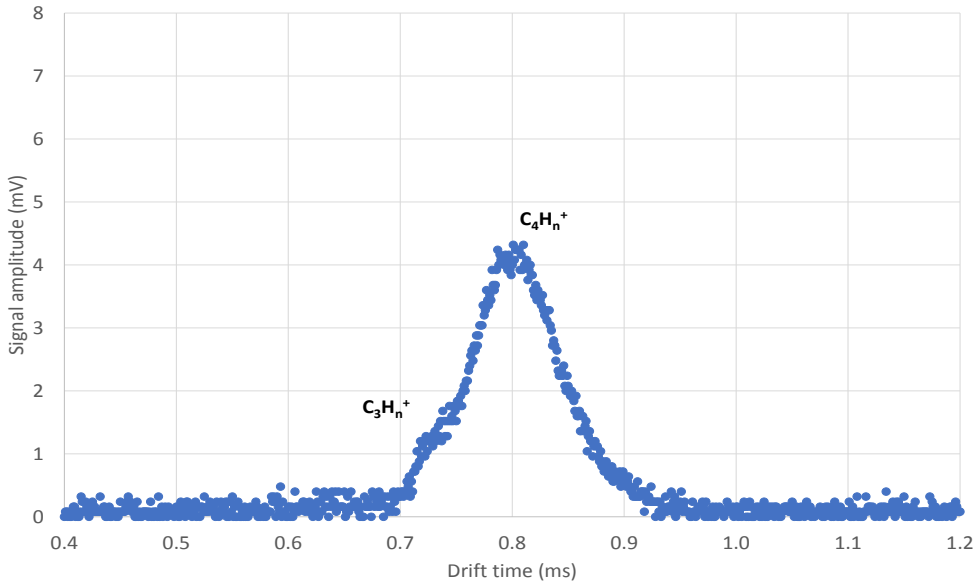

Figure 4.5: Time-of-arrival spectrum of an average of 128 pulses recorded for C_2H_6 at a pressure of 8 Torr, temperature of 293 K and for a reduced electric field of 15 Td with a voltage across GEM of 20 V.

All these primary ions ($C_2H_2^+$, $C_2H_3^+$, $C_2H_4^+$, $C_2H_5^+$ and $C_2H_6^+$) can rapidly undergo reactions that transform them into secondary ions. These reactions are summarized in table 4.8, along with a summary of the product distribution and respective reaction rates at room temperature [180]. Although not mentioned there is also the possible formation of CH_3^+ according to [181], but since it is residual, about 2.8%, it was discarded in the present analysis.

Table 4.8: Ionization reactions, product distribution and rate constants for the collisions of the primary ions with C_2H_6. Adapted from [180].

Reaction	Rate Const. (10^{-9} cm^3·s^{-1})	Prod. Dist.
$C_2H_6^+ + C_2H_6 \rightarrow C_3H_8^+ + CH_4$	$0.019^{+}_{-}0.001$	42%
$C_2H_6^+ + C_2H_6 \rightarrow C_3H_9^+ + CH_3$		58%
$C_2H_5^+ + C_2H_6 \rightarrow C_4H_9^+ + H_2$	$0.040^{+}_{-}0.003$	100%
$C_2H_4^+ + C_2H_6 \rightarrow C_3H_6^+ + CH_4$	$0.0053^{+}_{-}0.0001$	7%
$C_2H_4^+ + C_2H_6 \rightarrow C_3H_7^+ + CH_3$		93%
$C_2H_3^+ + C_2H_6 \rightarrow C_2H_5^+ + C_2H_4$	$0.62^{+}_{-}0.03$	47%
$C_2H_3^+ + C_2H_6 \rightarrow C_3H_5^+ + CH_4$		40%
$C_2H_3^+ + C_2H_6 \rightarrow C_4H_7^+ + H_2$		13%
$C_2H_2^+ + C_2H_6 \rightarrow C_2H_4^+ + C_2H_4$	$1.46^{+}_{-}0.06$	18%
$C_2H_2^+ + C_2H_6 \rightarrow C_2H_5^+ + C_2H_3$		9%
$C_2H_2^+ + C_2H_6 \rightarrow C_3H_3^+ + CH_3 + H_2$		6%
$C_2H_2^+ + C_2H_6 \rightarrow C_3H_5^+ + CH_3$		54%
$C_2H_2^+ + C_2H_6 \rightarrow C_4H_5^+ + H_2 + H$		5%
$C_2H_2^+ + C_2H_6 \rightarrow C_4H_7^+ + H$		9%

From tables 4.7 and 4.8 we can conclude that the most probable ions responsible for the peaks observed are:

$$C_2H_6^+ + C_2H_6 \rightarrow C_3H_8^+ + CH_4 \quad (4.16)$$

$$C_2H_6^+ + C_2H_6 \rightarrow C_3H_9^+ + CH_3 \quad (4.17)$$

$$C_2H_5^+ + C_2H_6 \rightarrow C_4H_9^+ + H_2 \quad (4.18)$$

$$C_2H_4^+ + C_2H_6 \rightarrow C_3H_7^+ + CH_3 \quad (4.19)$$

$$C_2H_3^+ + C_2H_6 \rightarrow C_2H_5^+ + C_2H_4 \quad (4.20)$$

$$C_2H_3^+ + C_2H_6 \rightarrow C_3H_5^+ + CH_4 \quad (4.21)$$

$$C_2H_2^+ + C_2H_6 \rightarrow C_3H_5^+ + CH_3 \quad (4.22)$$

So, it is expected that the ionization of C_2H_6 will lead to the formation of ion species with 3- or 4-carbons, which are responsible for the two peaks observed. We suspect that the peak with lower mobility corresponding to the heavier ions (with 4-carbons) while the peak with higher mobility being due to the lighter 3-carbon ions. The relation between the areas of these two groups of ions is not completely explained by the above reactions, so we shall discuss these reactions now in more detail, starting with reaction (4.19) which involves the most abundant primary ion - $C_2H_4^+$. In fact, even though the end product of this reaction is the $C_3H_7^+$ ion, the authors of [183] state that at room temperature the

reaction between C_2H_6 and $C_2H_4^+$ is a two-step reaction that can be described by the following chemical equations:

$$C_2H_4^+ + C_2H_6 \rightarrow C_4H_{10}^+ \tag{4.23}$$

$$C_4H_{10}^+ \rightarrow C_3H_7^+ + CH_3 \tag{4.24}$$

This intermediary reaction can explain the relationship between the areas of the peaks observed, since at 293 K, the ion $C_4H_{10}^+$ becomes the major product and only at 343 K does the conversion of $C_2H_4^+$ into $C_3H_7^+$ become noticeable [183].

The second most abundant primary ion, $C_2H_6^+$, reacts with the parent gas forming either $C_3H_9^+$ or $C_3H_8^+$ (Table 4.8). However, according to [184] there is the possibility of this primary ion forming a cluster, $(C_2H_6)_2^+$.

$$C_2H_6^+ + C_2H_6 \rightarrow (C_2H_6)_2^+ \tag{4.25}$$

Although not mentioning the rate constant and not including the mentioned products, this reaction could make the explanation plausible for the results obtained.

Concerning $C_2H_5^+$, it will produce a 4-carbon ion species, the $C_4H_9^+$ ion according to reaction 4.18. We are left with the $C_2H_3^+$ and the $C_2H_2^+$ primary ions, which are likely to produce $C_3H_5^+$ or $C_2H_4^+$. So, according to the reactions just mentioned, the most abundant secondary ions that are responsible for the observed peaks are: $C_2H_4^+$, $C_3H_5^+$, $C_3H_7^+$, $C_3H_8^+$, $C_3H_9^+$, $C_4H_9^+$, $C_4H_{10}^+$ and $C_4H_{12}^+$. Concerning all the possible secondary ions, we believe that the presence of $C_2H_4^+$ is residual, due to minor abundance of its corresponding primary ion, justifying that its corresponding peak in the spectra is not visible.

In figure 4.6 we can see the resulting mobilities, K, plotted against the reduced electric field, E/N. Extrapolating these values to $E/N \rightarrow 0$ Td (Langevin's limit), values of 1.46 and 1.57 $cm^2 \cdot V^{-1} \cdot s^{-1}$ were obtained.

Since this experimental technique does not allow the distinction between the mobilities of ions which differ by only a few protons, we can only divide the remaining ions into 2 groups, those with 4-carbon atoms and those with 3-carbon atoms. Calculating the Langevin limits of these ions: $C_2H_4^+$ (1.715 $cm^2 \cdot V^{-1} \cdot s^{-1}$), $C_3H_5^+$ (1.568 $cm^2 \cdot V^{-1} \cdot s^{-1}$), $C_3H_7^+$ (1.553 $cm^2 \cdot V^{-1} \cdot s^{-1}$), $C_3H_8^+$ (1.545 $cm^2 \cdot V^{-1} \cdot s^{-1}$), $C_3H_9^+$ (1.539 $cm^2 \cdot V^{-1} \cdot s^{-1}$), $C_4H_9^+$ (1.472 $cm^2 \cdot V^{-1} \cdot s^{-1}$), $C_4H_{10}^+$ (1.468 $cm^2 \cdot V^{-1} \cdot s^{-1}$), $C_4H_{12}^+$ (1.460 $cm^2 \cdot V^{-1} \cdot s^{-1}$) and comparing these values with our experimental mobilities, the results seem to be consistent with the most intense peak with lower mobility (1.47 $cm^2 \cdot V^{-1} \cdot s^{-1}$) being due to the 4-carbon ion species and the smaller peak with higher mobility (1.58 $cm^2 \cdot V^{-1} \cdot s^{-1}$) being due to the 3-carbon ion species, which are close to the expected Langevin limit. Given the amplitude of the most intense peak (which corresponds to the 4-carbon ion species) we are inclined to believe that the most abundant primary ions ($C_2H_4^+$ and $C_2H_6^+$) do, in fact, produce

$C_4H_{10}^+$ and $C_4H_{12}^+$ ions, as stated in [183,184] and as already explained with equations 4.23 and 4.24.

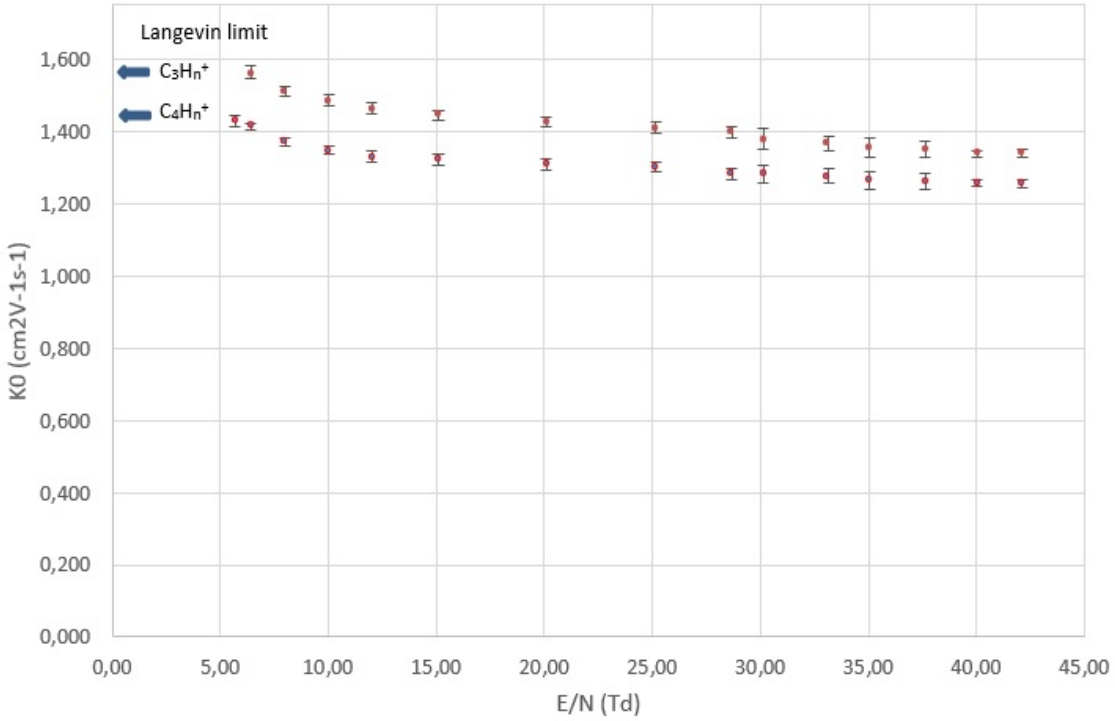

Figure 4.6: Reduced mobility of the ions produced in C_2H_6 for a pressure range of 6-10 Torr and for E/N values in the 6-42 Td range. Taken from [140].

4.5.6 Carbon Dioxide (CO_2)

Concerning pure carbon dioxide (CO_2), the measurements performed previously in our group [144] revealed only one peak for different reduced electric fields, E/N, (6-40 Td) and for pressures in the 8-12 Torr range at room temperature (298 K), which was attributed to CO_2^+ in [144] or to $CO_2^+(CO_2)$ cluster in [139]. The experimental measurements led to a reduced mobility value, K_0, of 1.17 $cm^2V^{-1}s^{-1}$ which is in good agreement with the ones obtained by other authors [185–187].

A typical example of this time of arrival spectra is displayed in figure 4.7. In this particular case the pressure used was 8 Torr, the reduced electric field was 15 Td, and the voltage across the GEM, V_{GEM}, was 25 V.

Table 4.9 summarizes the possible reactions due to electron impact in CO_2 for electron energies up to 25 eV, together with the respective cross-sections, appearance energies and product distribution. The displayed probabilities were obtained using the cross sections for CO_2 primary ionization products and the total cross section provided in [188], allowing us to infer the product distribution of this primary ionization. All these primary ions (CO_2^+, CO^+, O_2^+) will rapidly undergo reactions producing secondary ions, as displayed

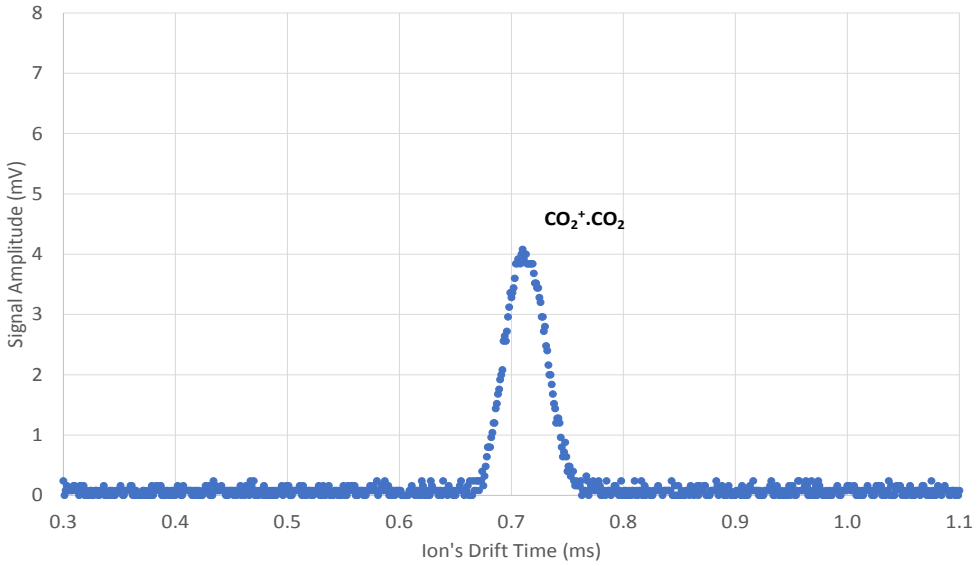

Figure 4.7: Time-of-arrival spectrum averaged over 128 pulses for pure CO_2 at a pressure of 8 Torr, temperature of 298 K and for a reduced electric field of 15 Td with a voltage across GEM of 25 V.

in table 4.10 which presents a summary of the possible secondary reactions, product distributions, and reaction rates, for these ions with CO_2 molecules at room temperature.

Table 4.9: Possible ionization products, ionization cross sections for electron impact (25 eV) on CO_2 [188], appearance energies (A.E) [189], and respective product distribution.

Reaction	Cross Sec. (10^{-16}cm^2)	A. E. (eV)	Prod. Dist.
$e^- + CO_2 \rightarrow CO_2^+ + 2e^-$	1.00 ± 0.10	13.83 ± 0.05	84.7 %
$e^- + CO_2 \rightarrow CO^+ + \frac{1}{2} O_2 + e^-$	0.044 ± 0.004	19.42 ± 0.075	3.7 %
$e^- + CO_2 \rightarrow O^+ + CO + e^-$	0.064 ± 0.006	19.05 ± 0.05	5.4 %

Taking a closer look at table 4.9 it is possible to see that the most probable ion is CO_2^+. Despite the good experimental agreement with [185–187], the mobility values substantially differ from the theoretical ones for CO_2^+ (K_0=1.81 cm^2·V^{-1}·s^{-1}), obtained using the Langevin limit.

Table 4.10: Ionization reactions, product distribution and rate constants for the collisions of the primary ions of CO_2 in their parent gas. Adapted from [190].

Reaction	Rate Const. (10^{-9} cm^3·s^{-1})	Prod. Dist.
$CO_2^+ + CO_2 \rightarrow CO_2^+ + CO_2$	$0.370^{+}_{-}0.037$	100%
$CO^+ + CO_2 \rightarrow CO_2^+ + CO$	$1.10^{+}_{-}0.11$	100%
$O^+ + CO_2 \rightarrow O_2^+ + CO$	$1.10^{+}_{-}0.22$	100%

In [144], the authors suggest that the difference observed in the mobility value (when compared to the Langevin limit) may be due to the charge transfer process between CO_2^+ and a neutral from its parent gas, expressed by:

$$CO_2^+ + CO_2 \rightarrow CO_2 + CO_2^+ \tag{4.26}$$

which lowers the ion velocity. The reaction constant of this process is $3.7\pm0.37\times10^{-10}$ cm^6·s^{-1} [190]. On the other hand, it is proposed in [139] that the ion responsible for the peak observed is a CO_2 ion cluster. In this work, it is assumed that under these conditions (E/N of 6-40 Td and pressures of 8-12 Torr at room temperature) the most important reaction of CO_2^+ with the gas molecules is a three-body reaction (4.27) instead of the well-known resonant charge transfer reaction (4.26), leading to the formation of a $CO_2^+(CO_2)_n$, with n equal to 1.

$$CO_2^+ + CO_2 + M \rightarrow CO_2^+.CO_2 + M \tag{4.27}$$

with a reaction constant equal to $k = 2.1\times10^{-28}$ cm^6·s^{-1} [191]. In the discussions that follows in the gas mixtures it is assumed that the ion appearing in pure CO_2 is the cluster one, which is more generally accepted by the scientific community.

4.5.7 Carbon Tetrafluoride (CF_4)

In pure carbon tetrafluoride (CF_4), the mobilities of the ions formed in the parent gas were measured for different reduced electric fields E/N (10 - 45 Td) and for pressures in the 6-10 Torr range at room temperature (293 K) for a constant V_{GEM} of 25 V.

A typical example of a time of arrival spectrum is shown in figure 4.8, for a pressure of 8 Torr, a reduced electric field of 15 Td, and voltage across the GEM, V_{GEM}, of 25 V, at room temperature, where a peak can clearly be observed, with another possible one of higher mobility. The origin of the two peaks will now be discussed.

In table 4.11 the possible reactions resulting from the electron impact in CF_4 for electron energies up to 25 eV, together with their respective cross-sections, appearance energies and the product distribution are summarized. Once again, the probabilities indicated for the product distribution were calculated using the cross sections for CF_4 primary

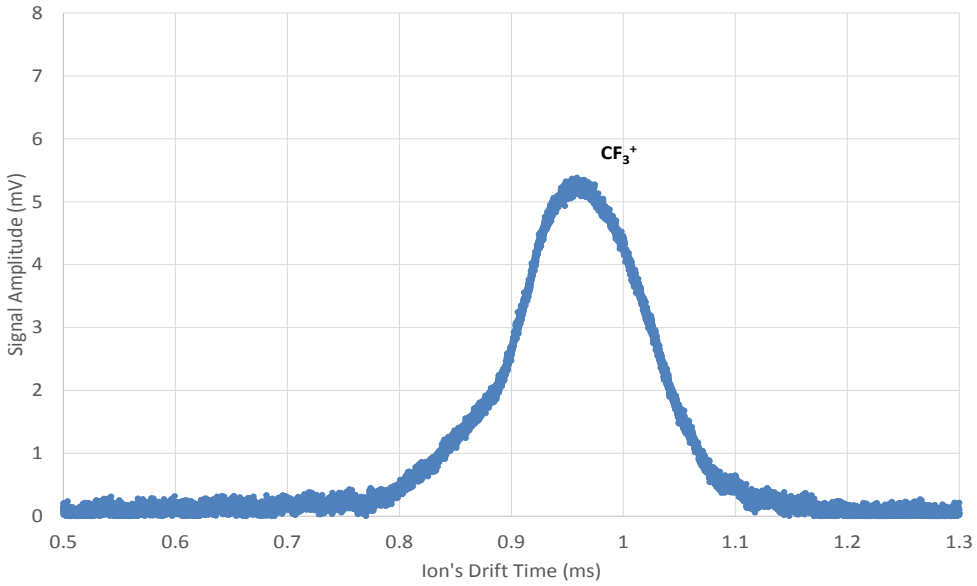

Figure 4.8: Time-of-arrival spectrum averaged over 128 pulses for pure CF_4 at a pressure of 8 torr, temperature of 293 K and a reduced electric field of 15 Td, with a voltage across GEM of 25 V.

ionization products and the total cross section provided in [192], which allowed us to infer the product distribution of the primary ionization. To the best of our knowledge these primary ions (CF_3^+, CF_2^+, CF^+, F^+ and C^+) are long lived at our working pressures, which means that once formed they will remain unaltered during the drift time.

Table 4.11: Possible ionization products, ionization cross sections for electron impact 25 eV on CF_4 [192], appearance energies (A.E.) [193], and respective product distribution.

Reaction	Cross Sec. (10^{-16}cm^2)	A. E. (eV)	Prod. Dist.
$e^- + CF_4 \rightarrow CF_3^+ + F + 2e^-$	1.011 ± 0.101	15.69 ± 0.05	96.1 %
$e^- + CF_4 \rightarrow CF_2^+ + 2F + e^-$	0.038 ± 0.004	21.47 ± 0.1	3.6 %
$e^- + CF_4 \rightarrow CF^+ + F + e^-$	0.0017 ± 0.0003	29.14 ± 0.2	0.16 %
$e^- + CF_4 \rightarrow C^+ + 2F_2 + e^-$	0.0007 ± 0.0001	34.77 ± 0.2	0.007 %
$e^- + CF_4 \rightarrow F^+ + CF_3 + e^-$	0.0007 ± 0.0001	35.00 ± 0.2	0.007 %

As seen in Table 4.11, the most probable ion is CF_3^+. In addition, CF_2^+, CF^+, C^+ and F^+ are also produced but with a much lower probability, up to 3.9 % of the total number of primary ions. Considering the relative abundance expected and our experimental system's limitations (e.g. signal-to-noise ratio), it is highly probable that it will only be possible to

observe the peak corresponding to the CF_3^+ ion, eventually with the residual (up to 3.6%) contribution of CF_2^+, which would be expected to have a slightly higher mobility due to its smaller mass.

In order to confirm this assumption, the trend of the experimental mobility values was compared with the polarization limit from Langevin's formula (equation 4.3). Figure 4.9 shows the reduced ion mobility as a function of the reduced electric field in the 10 to 45 Td range, at 8 Torr, with a V_{GEM} of 25 V and at room temperature, together with the polarization Langevin limit ($E/N \rightarrow 0$ Td) for the CF_3^+ ion.

The measured mobility tends to 1.12 $cm^2 \cdot V^{-1} \cdot s^{-1}$, a value in good agreement with the Langevin limit (equation 4.3) for CF_3^+, 1.13 $cm^2 \cdot V^{-1} \cdot s^{-1}$. Nonetheless, it deviates from those obtained by other authors [194,195]. The difference can be explained by the possibility of the cluster formation [196], $CF_3^+(CF_4)$, which would be favoured at higher pressures (close to atmospheric) and whose expected value is close to those observed experimentally by these authors. Another explanation could be the fact that the measurements in those references were taken in conditions where the Langevin limit is not strictly applicable, as discussed in [154].

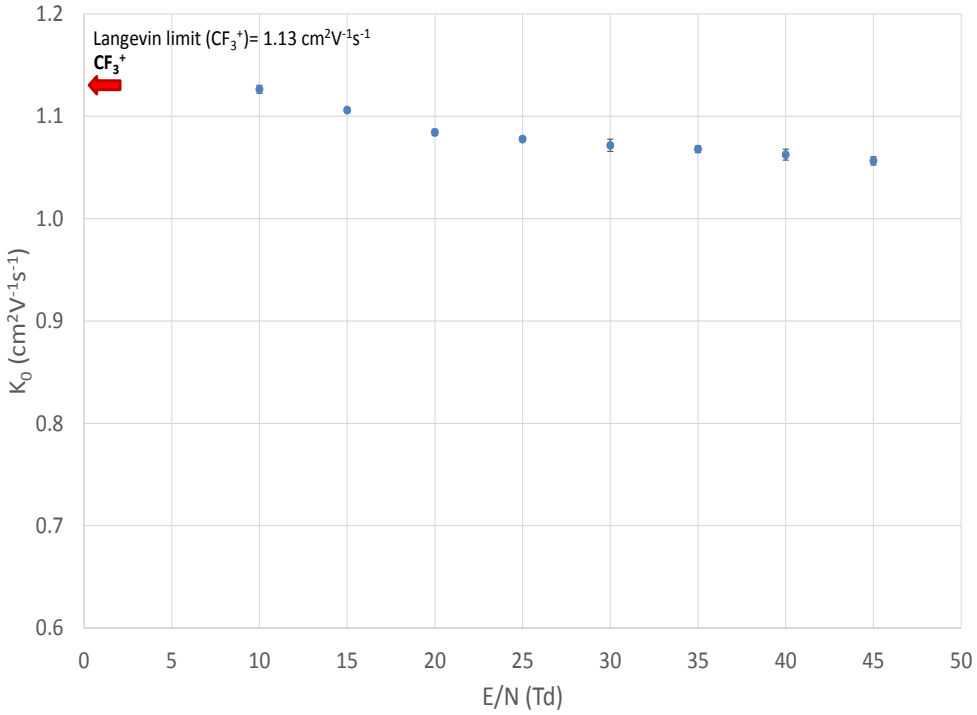

Figure 4.9: Reduced mobility of the ions produced in CF_4 for a pressure range of 6-10 Torr and for E/N vales in the range 10-45 Td range.

4.6 Results and Discussion - Gas Mixtures

4.6.1 Xenon-Nitrogen (Xe-N_2) mixtures

Measurements were made for Xe-N_2 mixtures, ranging from 0 to 100% Xe, for reduced electric fields between 15 and 30 Td and a pressure of 8 Torr, at room temperature, 293 K.

Figure 4.10 displays typical time-of-arrival spectra for 30%, 50%, 75% and 90% of Xe, for a pressure of 8 Torr, a E/N of about 15 Td and a V_{GEM} of 22 V, averaged for 128 pulses and with the background subtracted.

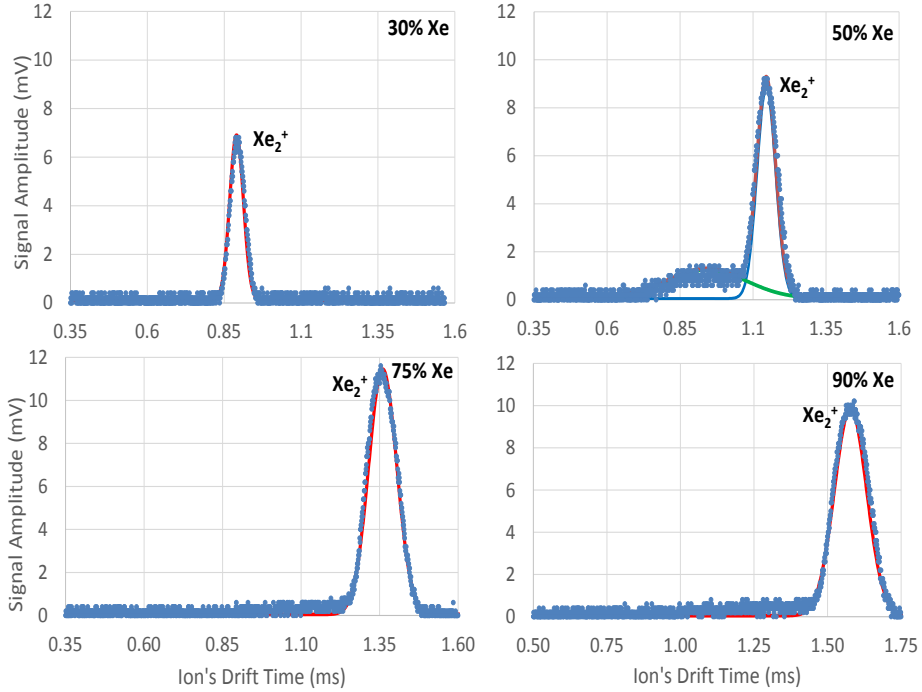

Figure 4.10: Time-of-arrival spectra obtained in Xe-N_2 mixtures, for different percentages of Xe in Xe-N_2 mixtures for a reduced electric field of 15 Td, at 8 Torr and room temperature (293 K), using a V_{GEM} of 22 V.

Looking at figure 4.10, it is possible to see that only one peak is present in the different spectra displayed. Increasing the percentages of Xe in the mixture results in two effects: a reduction in the mobility of the ions observed due to an increase in the drift time and an apparent increase in the peak area, hinting at the origin of the peak observed, which is expected to be due to Xe. Although the obtained spectra, shown in figure 4.10, already provided a hint as to the origin of the peak, the mobility of the most likely candidate ions using Blanc's law was calculated and compared with the experimental mobility and the

origin of the peak was confirmed to be Xe_2^+, due to the proximity of the theoretical and experimental values.

Figure 4.11 shows the measured ion mobilities, also displayed in table 4.12, in Xe-N_2 mixtures as a function of the Xe percentage, together with the calculated ion mobility using Blanc's law for the ions most likely to be formed (Xe^+, Xe_2^+, N_2^+ and N_4^+). The K_{0g1} and K_{0g2} values in equation 4.4, that is, the mobilities of Xe^+, Xe_2^+, N_2^+ and N_4^+ in pure Xe and in pure N_2, were either values experimentally obtained (when existing) or calculated using Langevin's formula (equation 4.3).

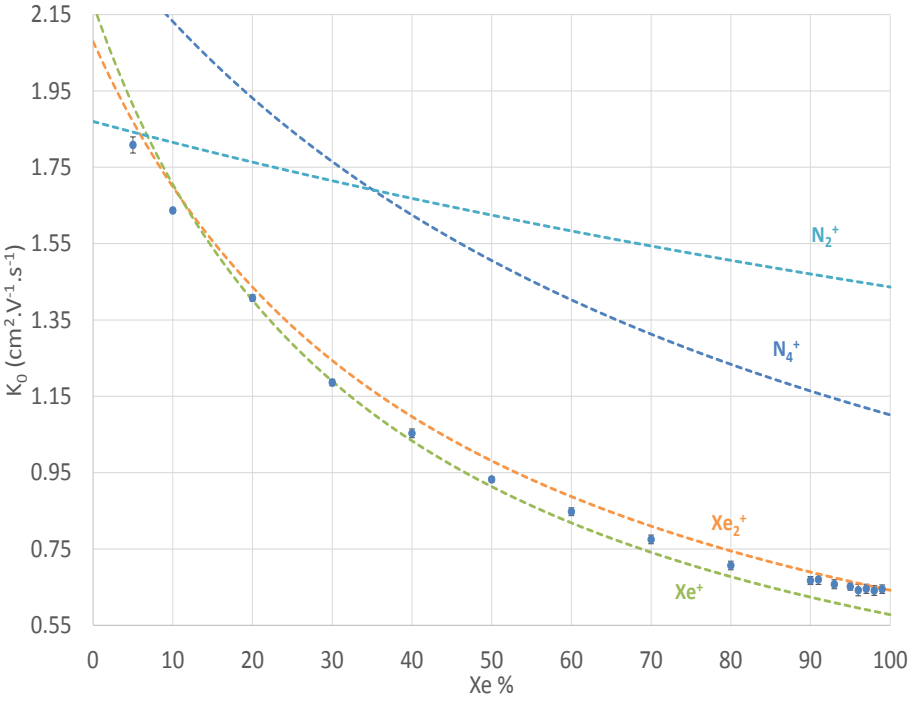

Figure 4.11: Experimental ion mobility data, K_0, for different percentages of Xe in Xe-N_2 mixtures for a reduced electric field of 15 Td, at 8 Torr and room temperature, using a V_{GEM} of 22 V. Adapted from [143].

In fact, for the determination of the Blanc's law curves displayed in figure 4.11, the mobilities used were either obtained experimentally in this work or taken from literature in the case of the ions in their parent gases (such as Xe^+ and Xe_2^+ in Xe [137], N_2^+ [197] and N_4^+ [171] in N_2) or calculated using the Langevin polarization limit (equation 4.3), with the neutral polarizability taken from table 4.1.

Looking at figure 4.11, it is possible to see that the ion mobility data obtained experimentally is consistent with the values predicted by Blanc's law for Xe^+/Xe_2^+ in the entire range of mixtures studied. Xe_2^+ is the dominant ion species in pure xenon at 8

Torr [137, 138, 198].

If we now consider the V_{GEM} used in the measurements (22 V), it is possible to see that the electron impact ionization cross section for the formation of Xe^+ is about 6 times larger than that for N_2^+. As a result, the formation of N_2^+ ions only becomes relevant for low Xe concentrations, below about 17% of Xe, conditions for which the same number of ionizations of both Xe and N_2 are expected.

At about 15% of Xe, for which both primary ions (Xe^+ and N_2^+) have equal probabilities of being produced at the GEM, only one peak is observed even when the GEM voltage was varied between 16 and 22 V. Since the experimental values are in accordance with the theoretical ones given by Blanc's law for Xe^+/Xe_2^+, this could hint at a possible charge transfer reaction between N_2^+ and Xe for which there is no data in the literature, even though it is energetically favourable.

Observing figure 4.11, it is possible to see that by decreasing the Xe concentration, the corresponding ion mobility slightly deviates from that of Xe_2^+ given by Blanc's law. In fact, in the intermediate region (figure 4.11), experimental results are more consistent with the Blanc's law values for Xe^+ ion, hinting that, as we add N_2, the probability for the three body process involved in the Xe_2^+ production (reaction 4.15) decreases. This seems plausible, given that it is a three-body process, highly dependent on the partial pressure of the gas involved. As a result, the mobility of the Xe_2^+ predecessor ion, namely Xe^+, will increasingly affect the drifting ion mobility, eventually reaching Xe^+ mobility, for low Xe content in the mixture.

Also from figure 4.11, for even lower concentrations of Xe ($< 5\%$), our results also deviate from the Xe^+ Blanc's curve. It is possible that for very high concentrations of N_2, the major primary ion formed will be N_2^+, which will react with N_2 molecules forming N_4^+, eventually following the behaviour found in pure N_2. In fact, the mobility measured, 2.379 ± 0.026 $\mathrm{cm^2 \cdot V^{-1} \cdot s^{-1}}$, is consistent with the results obtained for N_4^+ in pure N_2 [171].

Deviations from Blanc's law can be also explained by some limitation exhibited by the Langevin limit which sometimes underestimates or overestimates the ion mobility. This topic will be addressed as the end of this chapter.

Table 4.12: Mobility of the ions observed for the Xe-N_2 mixture ratios studied, obtained for E/N of 15 Td, at 8 Torr and 293 K, using a V_{GEM} of 22 V. Adapted from [143].

Xe-N_2 Mixture	Mobility ($cm^2 \cdot V^{-1} \cdot s^{-1}$)	Ion
5% Xe	1.81 ± 0.03	Xe^+
10% Xe	1.64 ± 0.02	Xe^+/Xe_2^+
20% Xe	1.41 ± 0.01	Xe_2^+
30% Xe	1.19 ± 0.01	Xe_2^+
40% Xe	1.05 ± 0.01	Xe_2^+
50% Xe	0.93 ± 0.01	Xe_2^+
60% Xe	0.85 ± 0.01	Xe_2^+
70% Xe	0.78 ± 0.01	Xe_2^+
80% Xe	0.71 ± 0.01	Xe_2^+
90% Xe	0.67 ± 0.01	Xe_2^+
91% Xe	0.67 ± 0.01	Xe_2^+
93% Xe	0.66 ± 0.01	Xe_2^+
95% Xe	0.65 ± 0.01	Xe_2^+
96% Xe	0.64 ± 0.01	Xe_2^+
97% Xe	0.65 ± 0.02	Xe_2^+
98% Xe	0.64 ± 0.01	Xe_2^+
99% Xe	0.65 ± 0.01	Xe_2^+

4.6.2 Xenon-Carbon Dioxide (Xe-CO_2) mixtures

In xenon-carbon dioxide (Xe-CO_2) mixtures, only one peak is observed in all mixture compositions studied, from pure Xe to pure CO_2. In figure 4.12 typical drift spectra for several are given Xe-CO_2 mixtures (5%, 25%, 50% and 95% of Xe), which were obtained at a total pressure of 8 Torr, with a E/N of 15 Td, V_{GEM} of 20 V, at room temperature (293 K).

Nevertheless, it was concluded that the ion responsible for the peak is not the same for all the mixtures, and it depends on the mixture ratio. In fact, according to the cross sections and rate constants in table 4.13, for Xe concentrations larger than 15%, the ions are from Xe, Xe_2^+ and Xe^+, while below this concentration the main ion is believed to be a CO_2 ion cluster ($CO_2^+.CO_2$). From the total ionization cross section for electron impact (table 4.13) at an energy of 20 eV we can observe that the probability of ionization of Xe atoms is about 5 times higher than that of the CO_2 molecule, thus it is expected that even at low Xe concentrations (down to 15% Xe), Xe ions are still the ones preferentially produced.

Using the appropriate reaction rates together with the electron impact ionization cross sections, the time evolution of the ion species for a total pressure of 8 Torr was calculated and the results for 5% and 50% Xe are shown in figure 4.13 and figure 4.14, respectively. As can be seen, the fraction of the different ion species present at the end of the drift distance depends on the reaction time and on the total drift time. Figure 4.13 and 4.14 can help to interpret figure 4.12, where it can be seen that down to about 8% Xe the production of Xe^+ ions will be favoured, leading to the same ions as in pure Xe (Xe_2^+ and Xe^+), while

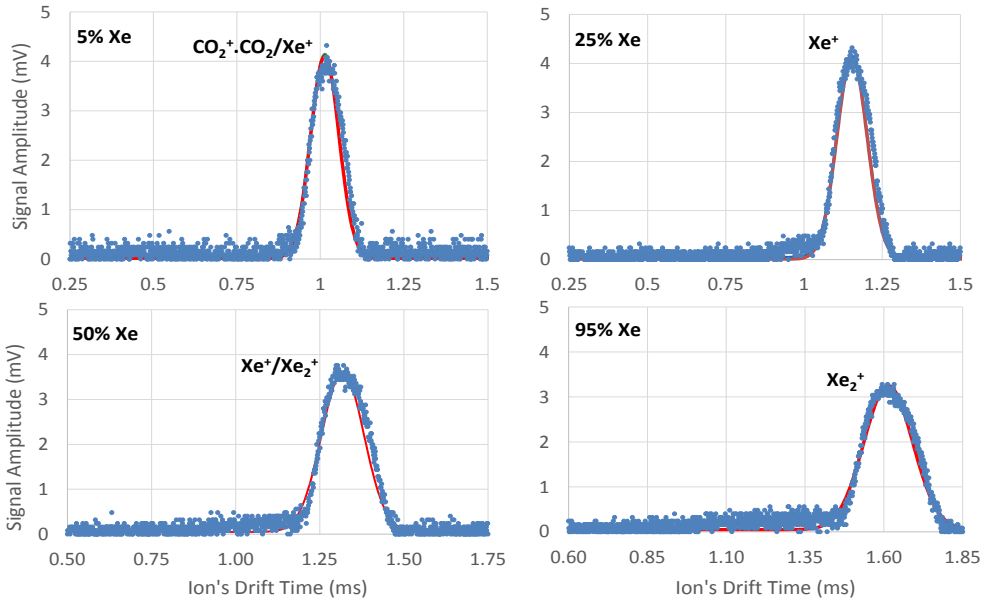

Figure 4.12: Time-of-arrival spectra averaged over 128 pulses for several Xe-CO_2 mixtures (5%, 25%, 50% and 95% of Xe) at a pressure of 8 Torr, temperature of 293 K and for a reduced electric field of 15 Td with a voltage across GEM of 20 V (background noise subtracted). Taken from [147].

below this Xe concentration, $CO_2^+.CO_2$ ions will be produced more abundantly.

For 5% Xe (figure 4.13), the species expected at the instant corresponding to the detected ions' average drift time (estimated from the peak's centroid of figure 4.12 at 5% Xe, to be about 1 ms) are: 39.8% of Xe^+, 1.4% of Xe_2^+ and 58.8% of $CO_2^+.CO_2$. In spite of the fact that two different ions are expected ($CO_2^+.CO_2$ and Xe^+) from the analysis of figure 4.13, only one peak was observed in figure 4.12. This can be explained by the fact that both ions have similar mobilities at low Xe concentrations according to Blanc's law, and contribute to the same peak in the time spectra. As it is energetically favourable, the charge transfer from $CO_2^+.CO_2$ to Xe could also explain the fact that only one peak was observed in figure 4.12. However, since no reference to this reaction exists in the literature it was not considered in the analysis performed in figures 4.13 and 4.14.

Further increasing the concentration of Xe will lead first to the formation of Xe^+ and ultimately to Xe_2^+. In fact, looking at figure 4.14, at the instant corresponding to the detected ions' average drift time inferred from figure 4.12 for 50% Xe (about 1.3 ms), the estimated fraction of each ion species is 96.1% of Xe_2^+ and 3.1% of Xe^+ (adding up to 99.2%), while the ions formed at the GEM are 84.4% Xe^+ and 15.6% CO_2^+.

Table 4.13: Summary of possible reactions and respective rate constants or cross section for electron impact ionization at 20 eV (references on the last column).

Reaction	Rate Const. ($^{*}cm^3 \cdot s^{-1}$ or $^{**}cm^6 \cdot s^{-1}$)	Cross Sec. (10^{-16} cm^2)	Ref.
$e^- + Xe \rightarrow Xe^+ + 2e^-$	-	2.43 ± 0.12	[167]
$Xe^+ + Xe \rightarrow Xe + Xe^+$	2.5×10^{-10} *	-	[199]
$Xe^+ + 2Xe \rightarrow Xe_2^+ + Xe$	$2.0 \pm 0.2 \times 10^{-31}$ **	-	[169]
$e^- + CO_2 \rightarrow CO_2^+ + 2e^-$	-	0.452 ± 0.032	[200]
$CO_2^+ + CO_2 \rightarrow CO_2 + CO_2^+$	$3.7 \pm 0.37 \times 10^{-10}$ *	-	[190]
$CO_2^+ + CO_2 + M \rightarrow CO_2^+.CO_2 + M$	$2.1 \pm 0.3 \times 10^{-28}$ **	-	[191]
$CO_2^+ + Xe \rightarrow Xe^+ + CO_2$	$6.0 \pm 1.8 \times 10^{-10}$ *	-	[201]

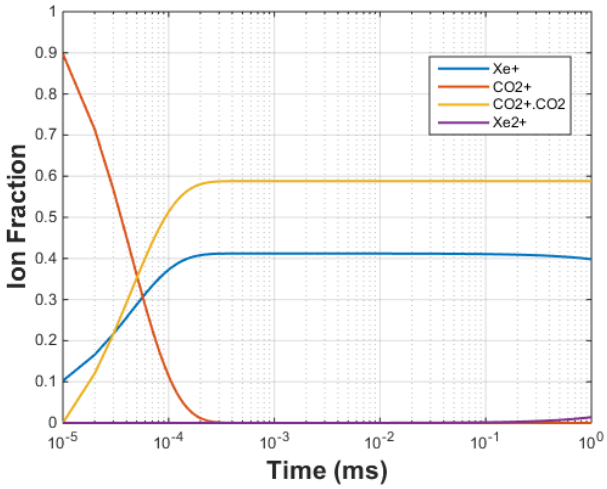

Figure 4.13: Fraction of ions that can be formed as a function of time for Xe-CO_2 mixtures with 5% Xe, for a total pressure of 8 torr. Taken from [147].

Thus, although CO_2^+ ions are produced at the GEM in both cases, with a comparatively higher abundance at 5% Xe, the end product is essentially a Xe ion, namely Xe_2^+.

As for the Xe^+ ion, it can be produced either by direct electron impact ionization of Xe or by the charge transfer reaction,

$$CO_2^+ + Xe \rightarrow Xe^+ + CO_2 \tag{4.28}$$

which in the pressure conditions of this experiment is a much faster reaction than the three-body competing one (M being either CO_2 or Xe):

$$CO_2^+ + CO_2 + M \rightarrow CO_2^+.CO_2 + M \tag{4.29}$$

as can be seen in figure 4.14 for 50% of Xe.

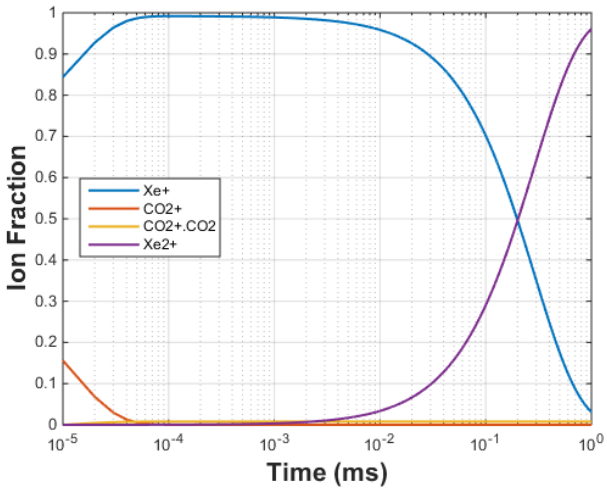

Figure 4.14: Fraction of ions that can be formed as a function of time for Xe-CO_2 mixtures with 50% of Xe, for a total pressure of 8 torr. Taken from [147].

Since according to [202] there is no charge transfer between Xe_2^+ and CO_2 we expect that, once formed, this ion will remain unaltered through the rest of the drift distance.

Other relevant features include the variation of the FWHM and peak position (drift time) in the drift spectra that can also be observed in figure 4.12. The larger FWHM for the peak as Xe concentration increases can be explained by the higher longitudinal diffusion of the Xe_2^+ ion in the medium due to higher energy loss probability in collisions with higher mass particles (Xe).

As for the shift of the peak in the drift spectrum towards lower drift times (increasing ion mobility) with the decrease in Xe concentration, it can be explained by the lower CO_2 mass compared to the Xe atom, which implies a lower reduced mass (μ in the Langevin limit eq. 4.3) in ion-neutral collision, and so a higher mobility.

In figure 4.15 we plot the inverse reduced mobility obtained for the ions produced in Xe-CO_2 mixtures as a function of Xe percentage, for 8 Torr and 15 Td, at room temperature (293 K), together with Blanc's law prediction for Xe_2^+ (blue dashed line), Xe^+ (green dashed line) and $CO_2^+.CO_2$ (orange dashed line). K_{0g1} and K_{0g2} in Blanc's law (eq. 4.4), were obtained either using experimental values from literature or, when not available, by extrapolating from existing experimental data or calculated using Langevin's formula.

As mentioned before, Langevin theory has some limitations, namely in CO_2, yielding mobilities higher than the experimental values. To address the lack of experimental values for Xe^+ and Xe_2^+ in pure CO_2 an alternative method was devised using the data in [139] for pure CO_2.

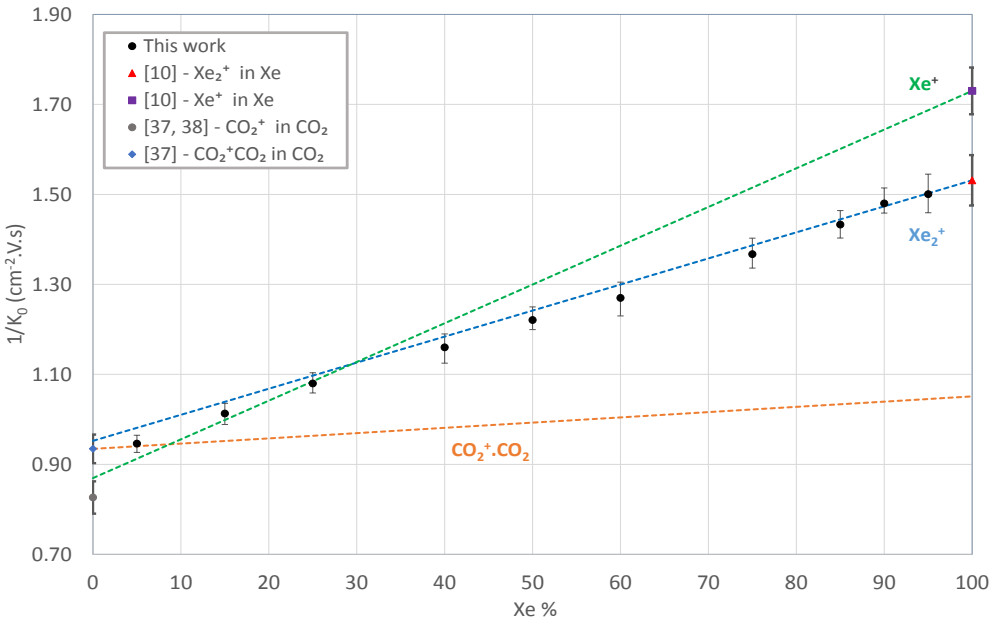

Figure 4.15: Inverse of the reduced mobility of the ions produced in the Xe-CO_2 mixture for a pressure of 8 Torr and for a E/N of 15 Td at room temperature. The dotted lines represent the mobility values expected from Blanc's law for Xe_2^+ (blue), Xe^+ (green) and for $CO_2^+.CO_2$ (orange). Taken from [147].

This alternative method for obtaining an estimate of the ion mobilities in CO_2 uses the mass-mobility data for CO_2 [139] and the masses of Xe^+ and Xe_2^+. The mobility values obtained were 1.15±0.05 $cm^2 \cdot V^{-1} \cdot s^{-1}$ and 1.05±0.10 $cm^2 \cdot V^{-1} \cdot s^{-1}$, respectively. A similar analysis of the mass-mobility data in Xe, obtained from [203] showed that in pure Xe the experimental ion mobility follows the values obtained from the Langevin polarization limit fairly well. The good agreement obtained using this approach in pure Xe corroborates it and for this reason the mobility value of $CO_2^+.CO_2$ ion in Xe used in this work was obtained from the Langevin limit, 1.05 $cm^2 \cdot V^{-1} \cdot s^{-1}$.

As seen in figure 4.15, the experimental ion mobility follows, within error bars, Blanc's law prediction for the most abundant ion in the different Xe percentages studied. In fact, from 100% down to 25% Xe the behaviour of Xe_2^+ is followed, while between this concentration and 15% it deviates towards Xe^+ predicted behaviour, and below 15% Xe it follows Blanc's law prediction for $CO_2^+.CO_2$. This behaviour is consistent with reaction rates and pressure data: in pure Xe the ion present is Xe_2^+. However, as Xe concentration decreases, this ion spends an increasing part of its drift time as Xe^+, with its mobility reflecting this growing contribution. As a result, the mobility of Xe_2^+ will decrease, eventually reaching

the predicted value (Blanc's law) of Xe^+, for Xe concentrations from 25% to around 15%. At about 15% Xe, both primary ions (CO_2^+ and Xe^+) are equally produced at the GEM, although only below 8% Xe the most abundantly ion collected changes to $CO_2^+.CO_2$, as until then the charge exchange between CO_2^+ and Xe still makes Xe^+ the more abundant ion. As a consequence, the mobility of the observed ion deviates towards the predicted value for the CO_2 cluster ion. In spite of the fact that Xe^+ and $CO_2^+.CO_2$ have different masses, according to Blanc's law they have similar mobilities between 5% and 15% Xe, thus becoming indistinguishable in the drift spectra. So, despite the presence of two different ions, only one peak is visible in the spectrum, in accordance with what was discussed earlier.

Finally, for high Xe concentrations, the introduction of CO_2 leads to an increase in the mobility of the Xe ions present (Xe_2^+). The ion mobility values measured in this experiment range from 1.06±0.02 (5% Xe) to 0.67±0.02 $cm^2V^{-1}s^{-1}$ (95% Xe), for E/N of 15 Td and 8 Torr. No significant variation of the mobility was observed in the range of pressures (6-8 Torr) and of E/N (10-25 Td) studied. The results presented here are in good agreement with the experimental values obtained by other authors when available [8,204] at standard pressure and similar E/N values. Table 4.14 summarizes the results obtained.

Table 4.14: Mobility of the ions observed for the Xe-CO_2 mixture ratios studied, obtained for E/N of 15 Td, at 8 Torr and 293 K. Adapted from [147].

Xe-CO_2 Mixture	Mobility ($cm^2 \cdot V^{-1} \cdot s^{-1}$)	Ion
5% Xe	1.06 $\pm$ 0.02	$CO_2^+CO_2$
10% Xe	1.03 $\pm$ 0.02	$CO_2^+CO_2/Xe^+$
15% Xe	0.99 $\pm$ 0.02	Xe^+
25% Xe	0.93 $\pm$ 0.02	Xe^+/Xe_2^+
40% Xe	0.86 $\pm$ 0.02	Xe_2^+
50% Xe	0.82 $\pm$ 0.01	Xe_2^+
60% Xe	0.79 $\pm$ 0.02	Xe_2^+
75% Xe	0.73 $\pm$ 0.02	Xe_2^+
85% Xe	0.70 $\pm$ 0.01	Xe_2^+
90% Xe	0.68 $\pm$ 0.01	Xe_2^+
95% Xe	0.67 $\pm$ 0.02	Xe_2^+

4.6.3 Xenon-Carbon Tetrafluoride (Xe-CF_4) mixture

In xenon-carbon tetrafluoride (Xe-CF_4) mixtures, one or two peaks can be observed depending on the mixture composition, from pure Xe to pure CF_4, as can be seen in figure 4.16, where the drift spectra for several Xe-CF_4 mixtures (20%, 50%, 80% and 90% of Xe) obtained at 8 Torr, 293 K and 15 Td with a V_{GEM} of 25 V, are displayed.

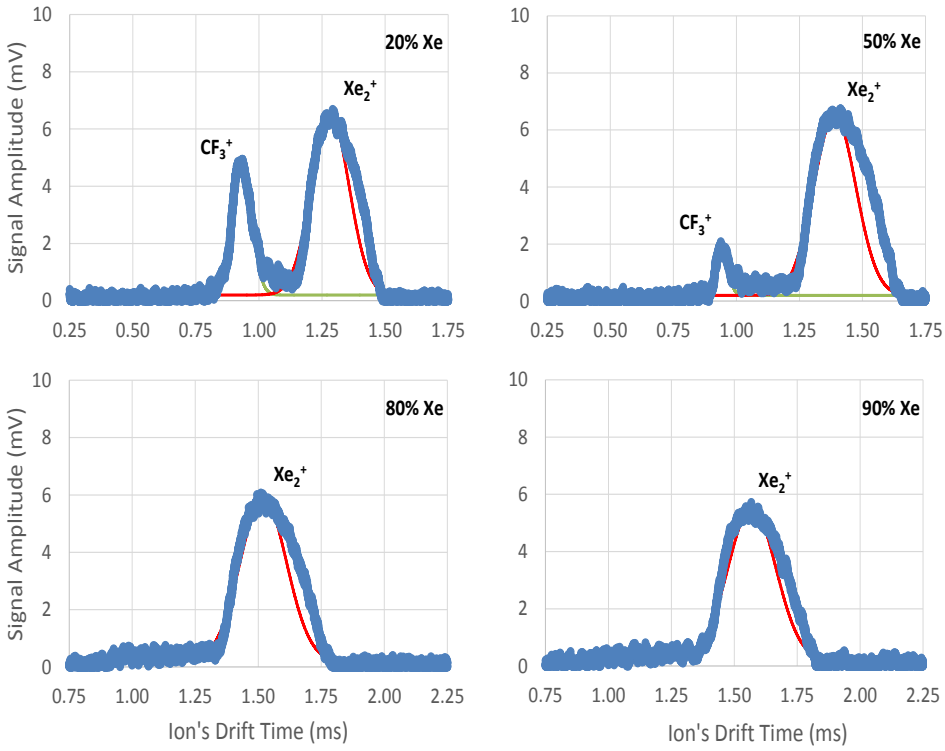

Figure 4.16: Time-of-arrival spectra of an average of 128 pulses recorded for several Xe-CF_4 mixtures (20%, 50%, 80% and 90% of Xe) at a total pressure of 8 Torr, a reduced electric field of 15 Td, a V_{GEM} of 25 V and at room temperature (293 K).

In figure 4.16 there are two striking features both of which are a result of the increasing Xe concentration in the mixture: the decrease in mobility of the different ions observed - more pronounced in the lower mobility peak - and the change in the relative abundance ion species present (even changing the dominant ion species), which can be perceived by a decrease in the area of the peak corresponding to the higher mobility, and an increase in the area of the other peak. Considering the shift of the peaks towards higher drift times with increasing Xe concentration (decreasing ion mobility), it can be explained by the higher Xe mass when compared to that of the CF_4 molecule, which implies a higher reduced mass in ion-neutral collisions (μ in equation 4.3), thus a lower mobility. Regarding the changes observed in the area of the different peaks, it suggests that the faster group of ions comes from CF_4, while the second, and slower group, comes from Xe atoms.

The evolution of the proportion of the peaks observed (from CF_4 and Xe ions) with the mixture composition was compared with the relative abundance of primary ions after traversing the GEM holes, using a Monte Carlo simulation code described in detail in [205].

The simulation code uses the cross-sections for the scattering of electrons by Xe atoms and CF_4 molecules described in [206]. As in [205], a uniform field between anode and cathode inside the GEM holes was considered. Although this is not the real field geometry, it can provide sufficient information for the present purpose. The simulation reproduces the drift of 10^8 photoelectrons released from a CsI photocathode into Xe-CF_4 mixtures (at a typical pressure of 8 Torr and temperature of 293 K) until they reach the anode at a distance of 50 μm from the photocathode and calculates the proportion of primary ions (CF_3^+ or Xe^+) after this drift for the different gas mixtures. The results are displayed in figure 4.17, where it can be seen that, even at low Xe concentrations (down to about 15% of Xe), Xe ions are still the ones preferentially produced.

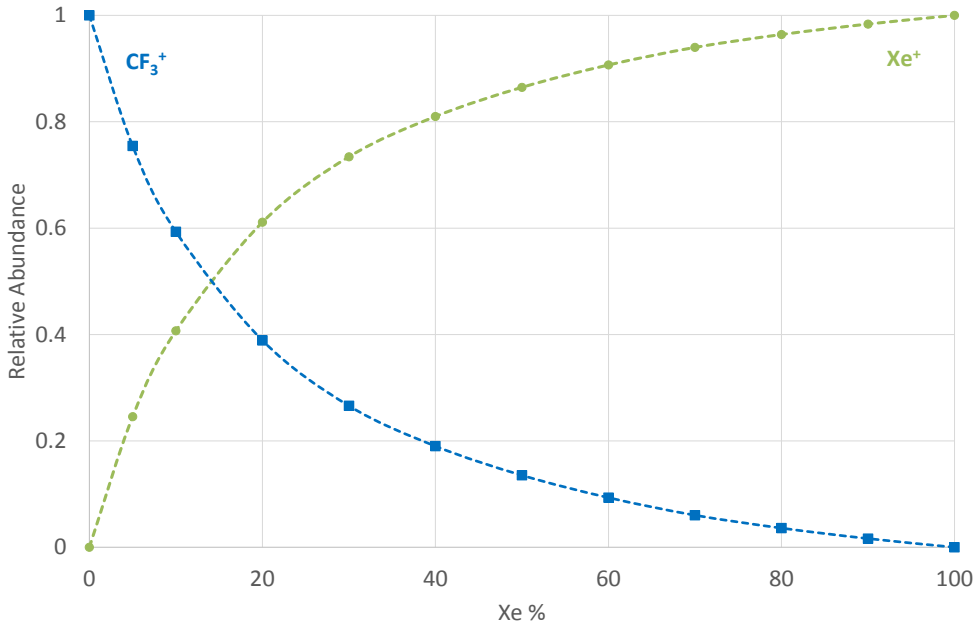

Figure 4.17: Monte Carlo calculated relative abundance of the fraction of ions produced at the GEM holes as a function of the Xe percentage in the mixture.

Comparing the results from figure 4.17 for the relative abundance of the ions in Xe-CF_4 calculated through the Monte Carlo simulation with the peak area, obtained by adjusting a Gaussian fit to each peak in the experimental time spectra (figure 4.16), it is possible to see a good agreement between the two, indicating that once the primary ions are formed the relative abundance of CF_4 and Xe ions will remain approximately constant. In addition, Blanc's law was also used as a cross-checking method to verify the ion identification.

Figure 4.18 shows the reduced mobility of the ions produced in different Xe-CF_4 mixtures at 8 Torr and for E/N of 15 Td at room temperature, together with Blanc's law prediction for the main candidate ions - CF_3^+ (orange), Xe^+ (red) and Xe_2^+ (green). K_{0g1} and K_{0g2} in Blanc's law (equation 4.4), were obtained either using experimental values from literature or, when not existing, by using the Langevin limit formula (equation 4.3).

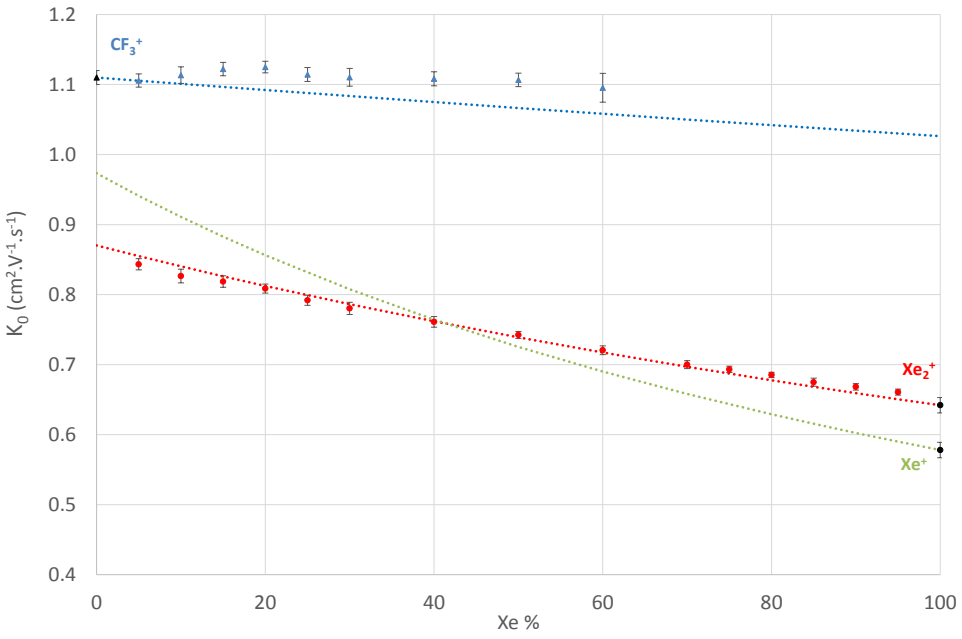

Figure 4.18: Reduced mobility of the ions produced in the Xe-CF_4 mixture for a pressure of 8 Torr and for a E/N of 15 Td at room temperature. The dotted lines represent the mobility values expected from Blanc's law for CF_3^+ (blue), Xe^+ (green) and Xe_2^+ (red).

Figure 4.18 shows that while the peaks corresponding to higher drift times follow closely Blanc's law curve for Xe_2^+, those corresponding to lower drift times are also well described (3% maximum deviation) by the same law for CF_3^+. The slight deviation observed may be caused by the collision-induced dissociation reaction between CF_3^+ and Xe [207],

$$CF_3^+ + Xe \rightarrow CF_2^+ + Xe + F \tag{4.30}$$

which is energetically favourable and would lead to an increasing formation of CF_2^+ with increasing concentration of Xe in the mixture and for which there is no reaction rate available. In table 4.15 the results obtained for the ion mobilities of CF_3^+ and Xe_2^+ in Xe-CF_4 mixtures are summarized. No significant variation of the mobility was observed in the range of E/N values (10-25 Td) studied.

Table 4.15: Mobility of the peaks observed for the Xe-CF_4 mixture ratios studied, obtained for E/N of 15 Td, a pressure of 8 Torr at room temperature (293 K).

Mixture	Mobility ($cm^2 \cdot V^{-1} \cdot s^{-1}$)	Ion
5% Xe	1.106 ± 0.009	CF_3^+
	0.843 ± 0.008	Xe_2^+
10% Xe	1.113 ± 0.012	CF_3^+
	0.827 ± 0.011	Xe_2^+
15% Xe	1.122 ± 0.009	CF_3^+
	0.819 ± 0.008	Xe_2^+
20% Xe	1.125 ± 0.008	CF_3^+
	0.809 ± 0.006	Xe_2^+
25% Xe	1.114 ± 0.009	CF_3^+
	0.792 ± 0.007	Xe_2^+
30% Xe	1.100 ± 0.013	CF_3^+
	0.780 ± 0.009	Xe_2^+
40% Xe	1.108 ± 0.001	CF_3^+
	0.761 ± 0.008	Xe_2^+
50% Xe	1.107 ± 0.009	CF_3^+
	0.742 ± 0.005	Xe_2^+
60% Xe	1.095 ± 0.021	CF_3^+
	0.721 ± 0.006	Xe_2^+
70% Xe	0.700 ± 0.006	Xe_2^+
75% Xe	0.693 ± 0.005	Xe_2^+
80% Xe	0.685 ± 0.004	Xe_2^+
85% Xe	0.675 ± 0.006	Xe_2^+
90% Xe	0.668 ± 0.005	Xe_2^+
95% Xe	0.661 ± 0.004	Xe_2^+

4.6.4 Argon-Ethane (Ar-C_2H_6) mixtures

Regarding the argon-ethane (Ar-C_2H_6) mixture from 0% (pure C_2H_6) up to 80% Ar concentration, two peaks are observed while above 80% Ar a new peak seems to emerge on the right side of the main one as can be seen in figure 4.19. The ions responsible for the two main peaks are the two groups identified in pure C_2H_6: $C_3H_n^+$ (the peak with higher mobility) and $C_4H_n^+$ (the most intense peak). Since the electron impact ionization cross section for Ar^+ production [167] is much higher than that of pure C_2H_6 [181], we expect that even for low concentrations of Ar primary ions, Ar^+, will be produced. These Ar^+ ions rapidly undergo one of the possible reactions with C_2H_6, displayed in table 4.16. In fact, the rate constants in table 4.16 show that Ar^+ ions are more likely to react with C_2H_6 rather than with Ar through reaction 4.14 with k=1.2×10^{-31}cm^{6}s^{-1}.

As seen in Xe-C_2H_6 mixtures [150], the reactions involving Ar^+ and C_2H_6 also lead to the same ions as in pure C_2H_6, which again will react with C_2H_6 molecules produce 3 and 4-carbon ions, but with slight differences from the pure C_2H_6 case reported in [140]: instead of $C_2H_4^+$ being the main primary ion produced, $C_2H_3^+$ becomes increasingly important when adding Ar to the mixture. With increasing Ar concentration, Ar^+ is produced more

Table 4.16: Reactions involving Ar^+ and C_2H_6 molecules. Authors of [208] believe that the $C_2H_6^+$, resulting from the charge transfer process between C_2H_6 and Ar^+, is not observed due to a possible fragmentation of $C_2H_6^+$. Adapted from [180].

Reaction	Rate Const. (10^{-9} $cm^3 \cdot s^{-1}$)	Prod. Dist.
$Ar^+ + C_2H_6 \rightarrow C_2H_6^+ + Ar$		0%
$Ar^+ + C_2H_6 \rightarrow C_2H_5^+ + H + Ar$		8%
$Ar^+ + C_2H_6 \rightarrow C_2H_4^+ + H_2 + Ar$		22%
$Ar^+ + C_2H_6 \rightarrow C_2H_3^+ + H_2 + H + Ar$	$1.15^{+}_{-}0.17$	42%
$Ar^+ + C_2H_6 \rightarrow C_2H_2^+ + H_2 + H + Ar$		23%
$Ar^+ + C_2H_6 \rightarrow CH_3^+ + CH_3 + Ar$		5%

abundantly leading to an increase of $C_2H_3^+$, which will further react with C_2H_6 forming 3- and 4-carbon ions with a slight predominance of the 3-carbon group. This feature explains the decrease in abundance of the 4-carbon ion group with the increase of Ar concentration, while the overall decrease in both ion groups with increasing Ar fraction in the mixtures, is related to the decrease in the C_2H_6 availability.

In figure 4.19 we can observe that, besides the already discussed features related to the peaks' amplitude, for Ar concentrations above 80% a small bump starts to show up at the right of the $C_4H_n^+$ peak, which may be due to the ion $C_5H_{11}^+$ [190], produced through:

$$C_3H_5^+ + C_2H_6 \rightarrow C_5H_{11}^+ \tag{4.31}$$

where $C_3H_5^+$ ion is the product of a reaction involving the $C_2H_3^+$ ion and C_2H_6 molecules (Table 4.8). As said before, the amount of $C_2H_3^+$ ions increases with concentration of Ar in the mixture. This can explain why the $C_5H_{11}^+$ only becomes visible for concentrations of Ar above 80%, whereas until then it is overshadowed by the $C_4H_n^+$ peak. Since the $C_5H_{11}^+$ ion is slightly heavier than the $C_4H_n^+$ ion group, it seems coherent that it should lie at the right of $C_4H_n^+$ and in an almost symmetric position relative to the $C_3H_n^+$ peak.

Concerning the mobility of $C_5H_{11}^+$, it increases with increasing Ar concentration, in the same way that $C_4H_n^+$ does, since the relative positions of the two peaks seem to remain constant in the various mixtures. Although the rate constant for the formation reaction is not mentioned in [190] it can justify the appearance of the peak for high Ar concentrations (above 80%).

Besides the different features mentioned in the time-of-arrival spectra, a shift of the peaks towards lower drift times can also be seen. While the $C_4H_n^+$ shift is described almost correctly by Blanc's law for all the mixtures studied as we will see later, the shift seen for $C_3H_n^+$ is much more pronounced than that expected from Blanc's law for high Ar concentrations (above 80% Ar).

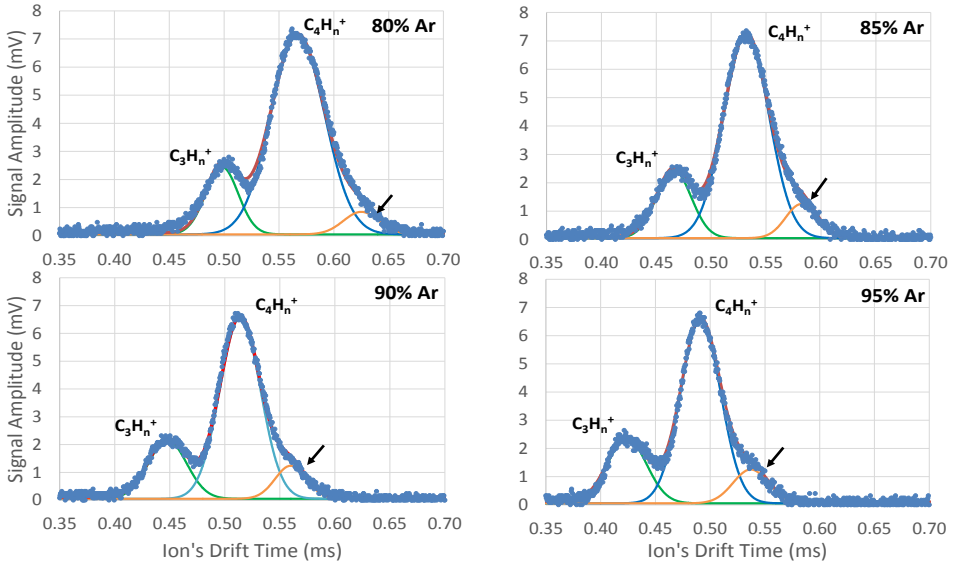

Figure 4.19: Time-of-arrival spectra of an average of 128 pulses recorded for several Ar-C_2H_6 mixtures (80%, 85%, 90%, 95% of Ar) at a pressure of 8 Torr, temperature of 293 K and for a reduced electric field of 15 Td with a voltage across GEM of 20 V (background noise was already subtracted). The ions responsible for the peaks appearing in this time-of-arrival spectra are $C_3H_n^+$ (n = 7, 8, 9), $C_4H_n^+$ (n = 9, 10, 12) and the most probable candidate for the bump present at the right side of the main peak is $C_5H_{11}^+$ (identified by the arrow). Taken from [141].

Figure 4.20 presents the reduced mobility of the ions produced in the Ar-C_2H_6 mixture for different mixture ratios for 6-10 Torr range, E/N of 15 Td at room temperature. Also, full lines representing Blanc's law for the most probable candidate ions are displayed. For the representation of Blanc's law (4.4), K_{0g1} and K_{0g2} are the mobilities of the mentioned ions in pure Ar and in pure C_2H_6. These mobility values were calculated using Langevin's formula (equation 4.3). Even though both $C_3H_n^+$ and $C_4H_n^+$ consist of several ions, a mean value of the reduced mobility was calculated using the lightest and heaviest ion of each group of ions.

Looking at figure 4.20 it is possible to see that the $C_4H_n^+$ ions group roughly follows Blanc's law throughout the entire mixture range. As for the $C_3H_n^+$ ion group, a significant deviation from Blanc's law behaviour can be seen for Ar concentrations above 80%. This discrepancy is thought to be related to the intermediate channels that benefit from the increase in the Ar^+ abundance, which yields a product distribution that, among the 3-carbon group, favours the formation of lighter ions. This is corroborated by the broadening of the peak and slight asymmetry observed in figure 4.19 with increasing Ar concentration.

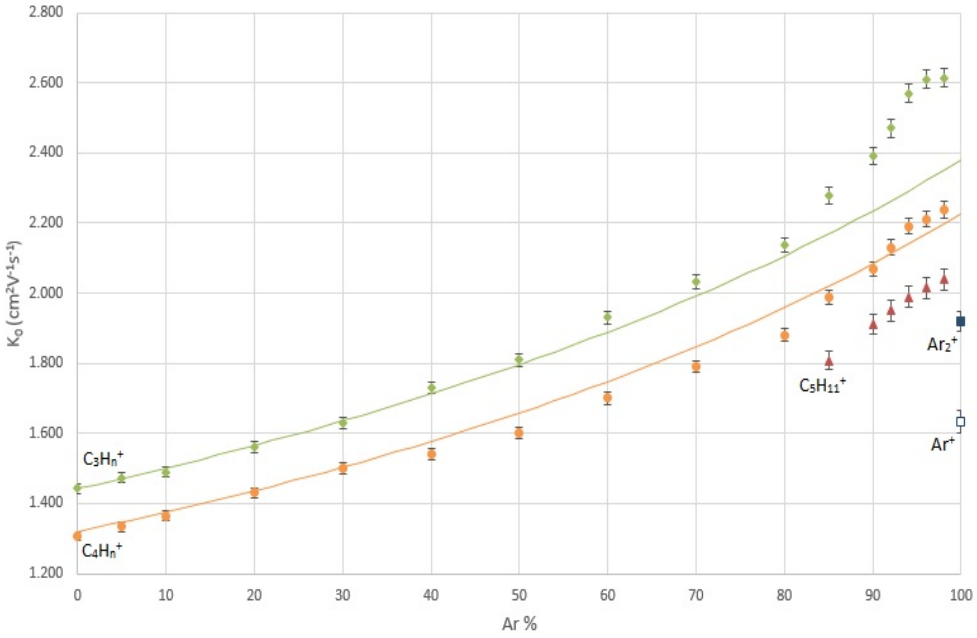

Figure 4.20: Reduced mobility of the ions produced in the Ar-C_2H_6 mixture for a pressure range of 6-10 Torr and for a E/N of 15 Td at room temperature. Taken from [141].

As for the $C_5H_{11}^+$ peak, its presence only appears for Ar concentrations above 80%, preventing an adequate analysis using Blanc's law, not performed for this reason.

So, from 0 to 100% Ar, the peaks observed were seen to vary, demonstrating that the mixture properties depend on the ratio of the two gases used. The mobility values of the peaks observed for the Ar-C_2H_6 mixture ratios of 80%, 85%, 90% and 95% of Ar, for a E/N of 15 Td, at 8 Torr and room temperature (298 K) are displayed in table 4.17.

Table 4.17: Mobility of the peaks observed in Ar-C_2H_6 mixture ratios of 80%, 85%, 90% and 95% of Ar, obtained for E/N of 15 Td, 8 Torr and V_{GEM} of 20 V at room temperature (298 K). Adapted from [141].

Ar-C_2H_6 Mixture	Mobility ($cm^2 \cdot V^{-1} \cdot s^{-1}$)	Ion
80% Ar	2.14 ± 0.02	$C_3H_n^+$
	1.86 ± 0.02	$C_4H_n^+$
85% Ar	2.28 ± 0.02	$C_3H_n^+$
	1.99 ± 0.02	$C_4H_n^+$
	1.81 ± 0.02	$C_5H_{11}^+$
90% Ar	2.37 ± 0.02	$C_3H_n^+$
	2.07 ± 0.02	$C_4H_n^+$
	1.91 ± 0.02	$C_5H_{11}^+$
95% Ar	2.47 ± 0.02	$C_3H_n^+$
	2.14 ± 0.02	$C_4H_n^+$
	1.96 ± 0.02	$C_5H_{11}^+$

In the range of pressures considered (6-10 Torr) and E/N range studied (from 10 to 25 Td) no significant change of the mobility was observed.

4.6.5 Argon-Methane (Ar-CH_4) mixtures

Regarding the argon-methane (Ar-CH_4) mixture, the focus of our study was the mixtures usually used in gas-filled radiation detectors from 90% up to 100% Ar concentration, where three peaks were observed. We concluded that the ions responsible for these peaks are the ones observed in pure CH_4 [177]: CH_5^+, $C_2H_n^+$ ($C_2H_4^+$ and $C_2H_5^+$) and $C_3H_7^+$.

Figure 4.21 displays a typical time-of-arrival spectrum for a P-10 mixture (Ar + 10% of CH_4), obtained at a pressure of 7 Torr, for a reduced electric field of 32 Td and a voltage across the GEM, V_{GEM}, of 19.5 V, where the background noise has already been subtracted.

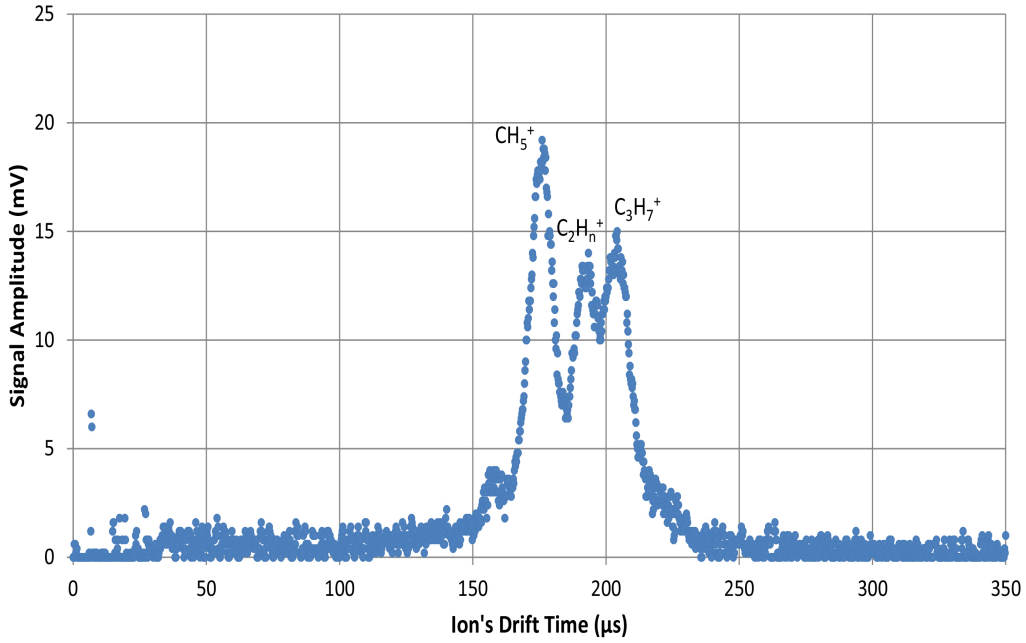

Figure 4.21: Time-of-arrival spectrum of an average of 128 pulses recorded for a P-10 Ar-CH_4 mixture at a pressure of 7 Torr, temperature of 298 K and for a reduced electric field of 32 Td with a voltage across GEM of 19.5 V (background noise was already subtracted). Taken from [142].

Since the electron impact ionization cross section for 20 eV in Ar [167] is about one half of the total ionization cross section in CH_4 [178], it is expected that even at fairly low CH_4 concentrations, CH_4 ions will be produced more abundantly than Ar^+ ions. Also, since the appearance energies for CH_4 ions are lower than those for Ar ions, charge transfer from Ar^+ to CH_4 is expected and for that reason Ar^+ ions will rapidly undergo one of the possible reactions with CH_4, shown in table 4.18, preventing Ar^+ from appearing in the time-of-arrival spectra.

Table 4.18: Reactions involving Ar atomic ions and its ionization products with CH_4, adapted from [180]. Authors of [208] believe that the CH_4^+, resulting from the charge transfer process between CH_4 and Ar^+, is not observed due to a possible fragmentation of CH_4^+.

Reaction	Rate Const. (10^{-9} $cm^3 \cdot s^{-1}$)	Prod. Dist.
$Ar^+ + CH_4 \rightarrow CH_4^+ + Ar$		N/A
$Ar^+ + CH_4 \rightarrow CH_3^+ + H + Ar$	$0.98^{+}_{-}0.01$	85%
$Ar^+ + CH_4 \rightarrow CH_2^+ + H_2 + Ar$		15%

Furthermore, the only competing process is the three-body reaction (equation 4.14), much slower than the charge transfer reactions ($k = 0.98\times10^{-9}$ cm^3s^{-1}) (table 4.18). As a result, the Ar ions will lead to the formation of the same ions as in pure CH_4 (CH_2^+ and CH_3^+) but with different ratios than in pure CH_4. These will further react with CH_4 (table 4.6).

The ions responsible for the three peaks observed in figure 4.21 are believed to be CH_5^+, a 2-carbon ions group ($C_2H_4^+$ and $C_2H_5^+$) and $C_3H_7^+$, which at some mixture compositions was distinguishable from the 2-carbon ion group. These peaks were observed in all Ar-CH_4 spectra, although with minor differences as can be seen in figure 4.22 for 95% (P-5), 97.5% (P-2.5) and 98.75% (P-1.25) of Ar in the mixture. The small peaks almost unnoticeable in figure 4.21 at the left side of CH_5^+ and at the right side of $C_3H_7^+$ were attributed to impurities.

As for the origin of the peaks we believe that, even though $C_2H_5^+$ is expected to form $C_3H_7^+$, both species are present in the time-of-arrival spectra. The reactions involving $C_2H_5^+$, that lead to the formation of $C_3H_7^+$ are:

$$CH_3^+ + CH_4 \rightarrow C_2H_5^+ + H_2 \tag{4.32}$$

$$CH_2^+ + CH_4 \rightarrow C_2H_5^+ + H \tag{4.33}$$

which will then lead to,

$$C_2H_5^+ + CH_4 \rightarrow C_3H_7^+ + H_2 \tag{4.34}$$

As reaction 4.34 has a much lower rate constant ($\leq10^{-15}cm^3s^{-1}$) than reactions 4.32 and 4.33, we expect both $C_2H_5^+$ and $C_3H_7^+$ ions to be present in the time-of-arrival spectra, in agreement with results presented in [209] that also identify a substantial decrease in the $C_2H_5^+$ concentration and increase in the $C_3H_7^+$ with time.

As can be seen in figure 4.22, with increasing concentration of CH_4 the signal amplitude increases, as expected.

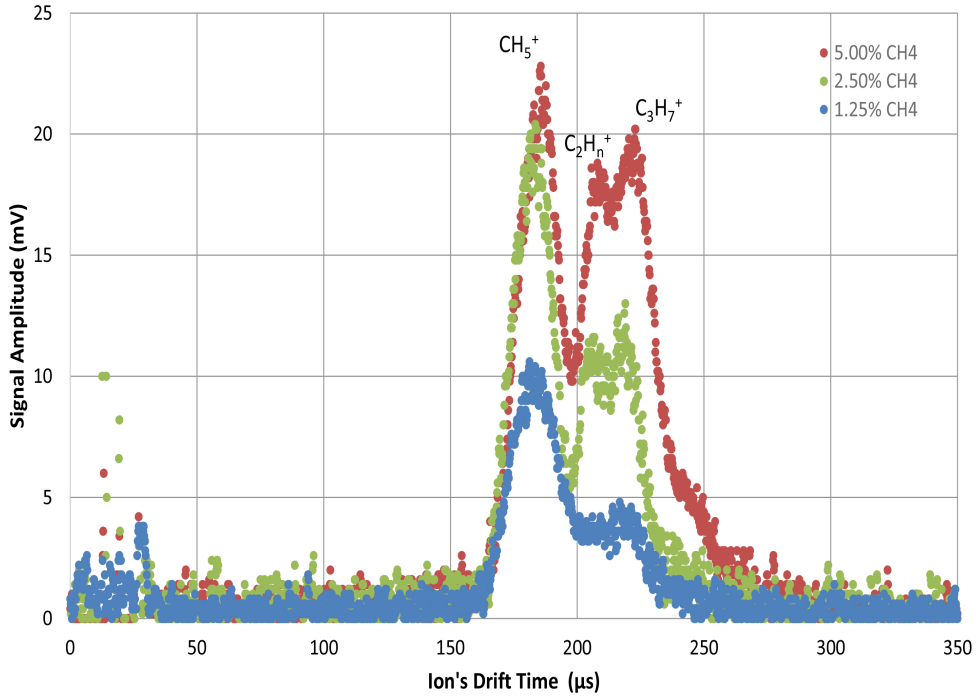

Figure 4.22: Time-of-arrival spectrum of an average of 128 pulses recorded for a P-1.25, P-2.5 and P-5 Ar-CH_4 mixture at a pressure of 7 Torr, temperature of 298 K and for a reduced electric field of 32 Td with a voltage across GEM of 20 V (background noise was already subtracted). Taken from [142].

Besides this difference, for CH_4 concentrations above 1.25% the peak with lowest mobility separates into two well defined peaks as already mentioned: the 2-carbon ion ($C_2H_4^+$ and $C_2H_5^+$) and a 3-carbon ion ($C_3H_7^+$) groups. In fact, the amount of $C_2H_5^+$ ions increases with the presence of Ar in the mixture, since the charge transfer reactions between Ar^+ and CH_4 favours its formation. However, higher abundance of CH_4 is needed in order to produce $C_2H_5^+$ and $C_3H_7^+$ through reaction 4.34. This explains why the 2-carbon ion group and the 3-carbon ion peaks only become clearly defined for concentrations higher than 1.25% CH_4, whereas below that they are indistinguishable, mainly due to the low amplitude of $C_3H_7^+$ ion and the peaks' resolution. Another relevant feature in figure 4.22 is the slight decrease in the mobility of the peaks with increasing CH_4 concentration in accordance with Blanc's law.

Figure 4.23 presents the reduced mobility of the ions produced in Ar-CH_4 for different mixture ratios for a pressure range of 5-8 Torr and for E/N in the 17 to 43 Td range, at room temperature. The full lines represent the trend in the mobility as function of E/N.

From 0 to 10% CH_4, the peaks' mobility was seen to vary, demonstrating that the transport properties of the ions produced in the mixture depend on the ratio of the two gases used. Table 4.19 shows the mobility values of the peaks observed for Ar-CH_4 mixture

ratios of 2.5%, 5% and 10% of CH_4, obtained for E/N of 32 Td, at a pressure of 7 Torr and at room temperature.

Although the results presented for the mobility of $C_3H_7^+$ are in good agreement with those predicted from Blanc's law, we believe they are an upper limit to their mobility. In fact, since the reaction time (equation 4.34) is of the order of the ions' transit time in their drift towards G2, the ions collected and identified as $C_3H_7^+$ spend some of their drift time as $C_2H_5^+$, thus the mobility measured for the ion collected is, in fact, a combination of the drift of both ions.

In the range of pressures considered in this work (5-8 Torr) and E/N (from 17 to 43 Td) no significant dependence of the mobility was observed.

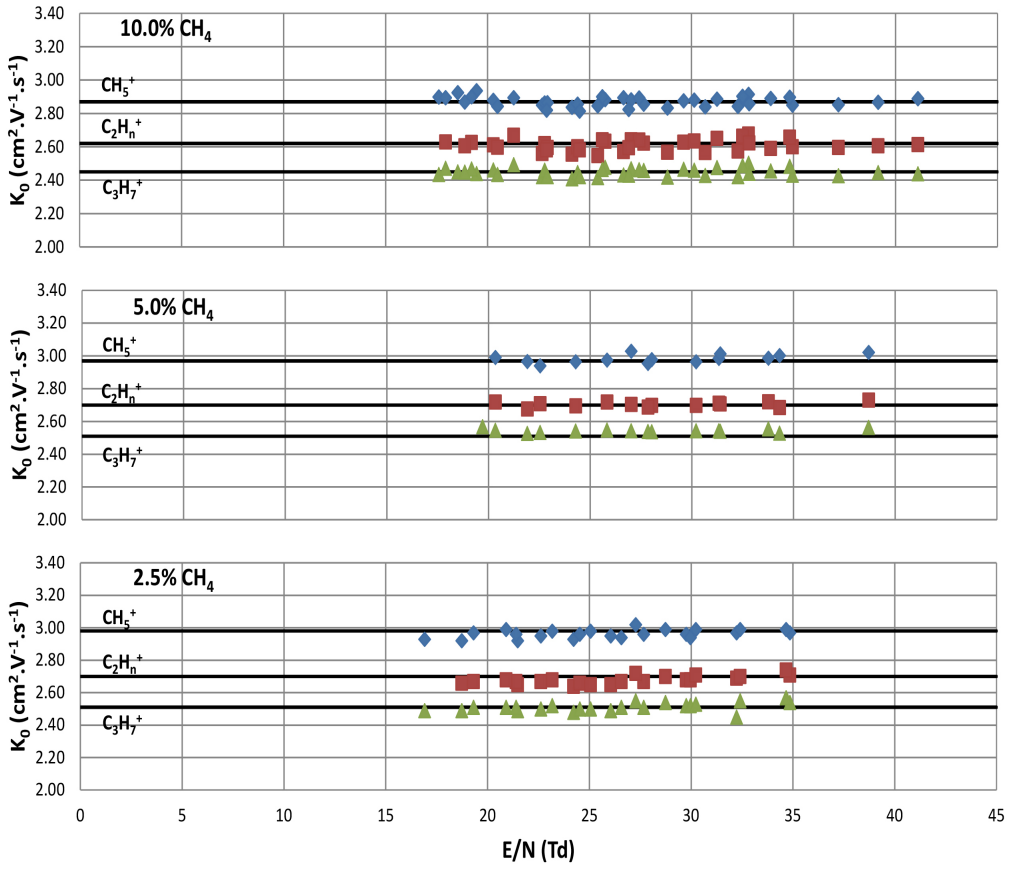

Figure 4.23: Reduced mobility of the ions produced in different Ar-CH_4 mixtures (2.5%, 5% and 10% of CH_4) for a pressure range of 5-8 Torr, E/N in the 17-43 Td range and at room temperature. The several peaks observed in the time-of-arrival spectra correspond to: CH_5^+, $C_2H_n^+$ ($C_2H_4^+$ and $C_2H_5^+$) and $C_3H_7^+$ ions. Taken from [142].

Table 4.19: Mobility of the ions observed in the Ar-CH_4 mixture ratios of 2.5%, 5% and 10% of CH_4, for E/N of 32 Td, a pressure of 7 Torr and 298 K. Adapted from [142].

Ar-CH_4 Mixture	Mobility ($cm^2 \cdot V^{-1} \cdot s^{-1}$)	Ion
90% Ar	2.87 ± 0.03	CH_5^+
	2.62 ± 0.04	$C_2H_n^+$
	2.45 ± 0.03	$C_3H_7^+$
95% Ar	2.97 ± 0.03	CH_5^+
	2.70 ± 0.04	$C_2H_n^+$
	2.51 ± 0.04	$C_3H_7^+$
97.5% Ar	2.98 ± 0.04	CH_5^+
	2.70 ± 0.05	$C_2H_n^+$
	2.52 ± 0.05	$C_3H_7^+$

4.7 Validity of the Langevin Limit

According to the Langevin theory, when the interaction between the ion and the gas atoms or molecules is dominated by the charge-induced dipole force, the ion mobility is determined by the neutral polarisability, α. In such cases, the Langevin formula (equation 4.35) gives relatively good estimates for the mobility because α is accurately known for most gases [157].

Despite the good agreement, a problem arises when the gas atoms or molecules are weakly polarisable, or when the molecules are large [139]. In these cases, the Langevin formula switches from the polarization limit (equation 4.35) to hardsphere elastic scattering (equation 4.36), whose estimate accuracy is far from desirable as d (the sum of the ion and gas radii) is not known with precision [139]. The complete expressions for K_{pol} and K_{elast} can be found in [153], where K_{pol} and K_{elast} are the polarization and elastic mobility limits according to the Langevin theory, respectively.

$$K_{pol} \propto \frac{1}{\sqrt{\alpha\mu}} \tag{4.35}$$

$$K_{elast} \propto \frac{1}{d^2\sqrt{\mu}} \tag{4.36}$$

To understand the implications of the observations made, the reduced mobility of ions in pure Ar, Xe, Ne and CO_2 as a function of the ion mass are represented in figure 4.24, along with the Langevin limit and in some cases a fitting to the experimental data. The results presented were obtained from the data compilation available in [203]. The fitting performed is in fact a correction to the Langevin polarization limit that provides a better fitting to the experimental data, which is obtained by varying the neutral polarisability, α, in the Langevin formula (equation 4.3) presented in section 4.2.1.

In figure 4.24 it is possible to see that the mobility of ions in Ar and in Xe are relatively well described by the polarisation limit of the Langevin formula, except for Ar^+ and Xe^+ whose mobility is not correctly described because they are slowed down in their parent

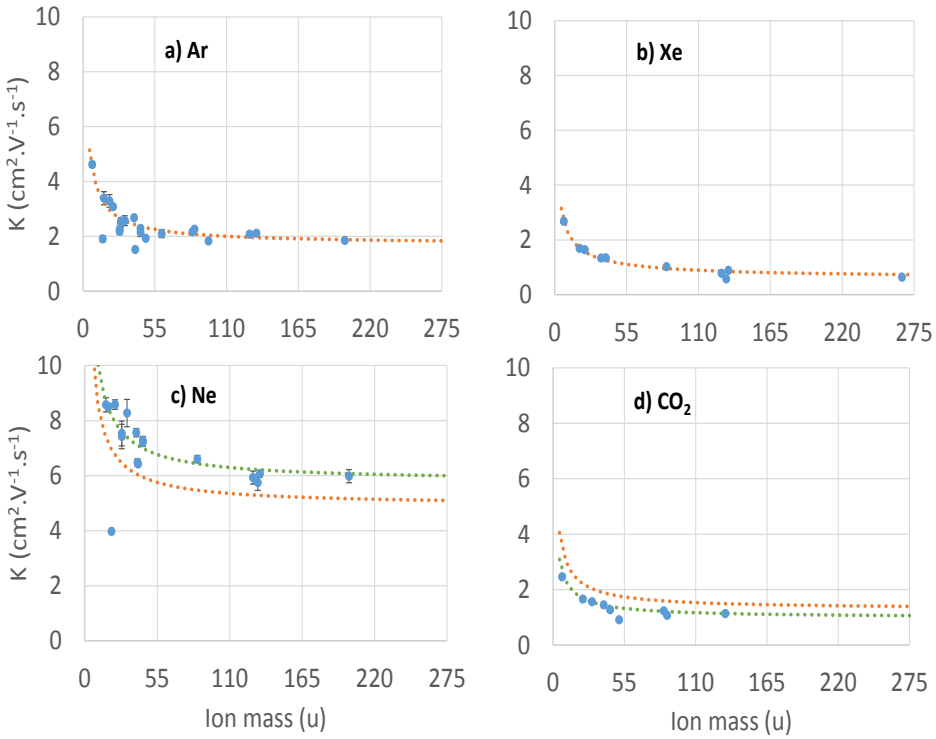

Figure 4.24: Reduced mobility of ions in a) Ar, b) Xe, c) Ne and d) CO_2 at, or extrapolated to 15 Td, error bars are represented. The results presented are a compilation from [203], selecting measurements at or near 300 K. Curves show the polarisation limit of the Langevin mobility formula (orange) and by fitting the experimental data (green).

gas due to resonant charge exchange.

If we look now at the case of ions moving in Ne or CO_2 in figure 4.24, we can see that the Langevin polarization limit systematically underestimates the mobility in Ne, while overestimating the mobility in CO_2 by 20 – 25%. In Ne, this underestimation of the mobility can be explained by the neon's weak polarisability. As a consequence the polarisation limit of the Langevin formula is no longer valid, with the mobility of the ions being almost correctly described by the hardsphere elastic scattering limit. As for CO_2, the scattering in CO_2 is, in part inelastic because of the numerous internal degrees of freedom, responsible for reducing the mobility by 10% only, as pointed out in [157]. Authors in [139] suggest that the tendency of CO_2 to form molecular clusters would help to explain the difference observed.

So in such cases, an alternative way of predicting the mobility of different ions can be performed by fitting the experimental data available for a certain gas and plotting

it as mass-mobility diagrams. Knowing the ion's mass, it is possible then to determine its mobility with the information obtained by the fitting. This way, it is possible to obtain more accurate estimates on the ion mobility for a specific ion in other gases. One good example of how well this approach works is the Xe-CO_2 case, where it was first implemented, giving very interesting results in terms of the understanding of the origin of the ions present [147].

The same principle can be used in mixtures with CH_4 or N_2 where these corrections can improve the accuracy of the mobility estimates.

4.8 Gas mixtures discussion

The measurements performed in this work were part of wider group of mixtures studied [144–150] in the scope of our participation both in the NEXT Experiment and RD51/CERN.

Regarding all the mixtures studied for the NEXT Experiment (Xe-N_2 [143] and Xe-TMA [148]), the results indicate that the gas mixture that provides the best results on ion mobility is Xe-TMA up to 10% of TMA.

As for the RD51 Collaboration/CERN for the ALICE TPC, the two gas mixtures studied in the scope of our participation were Ar-CO_2 [144] and Ne-CO_2 [145]. Based on the results, the ion responsible for the signal in CO_2-quenched mixtures of Ar and Ne is the $CO_2^+ \cdot (CO_2)_n$ cluster ion. Comparing Ar-CO_2 and Ne-CO_2, we concluded that Ne-CO_2 displays better results in terms of ion mobility in the range of interest for the ALICE TPC (0-10% CO_2), mainly because of the smaller Ne mass which results in lower energy losses in collisions. Another important feature of this gas mixture is that a small amount of CO_2 increases the ion mobility. Additional studies were performed for different gases such as Ar-C_2H_6 [141] and Ar-CH_4 [142]. Although not being initially part of work developed in the scope of the RD51/CERN for the ALICE TPC, these mixtures may also be considered. If we compare these results with Ar-CO_2 and Ne-CO_2 it is possible to see that the mixture that presents the best results in terms of ion mobility is still Ne-CO_2.

In addition, several other Xe based mixtures were studied. These are particularly important in TRD detectors based on MWPCs (ALICE and CBM TRDs) as they influence their rate capability. In such applications, Xe is considered to be the best choice for the main gas while the choice of the quencher is not unanimous. Thus, the mobility of ions produced in Xe-CH_4 [149], Xe-C_2H_6 [150] and Xe-CO_2 [147] mixtures were studied. The results revealed that, for the range of interest (typically 0-10% of CH_4, C_2H_6 and CO_2), only one peak was observed in the time-of-arrival spectrum for Xe mixtures with CH_4 and CO_2, while three peaks were observed for mixtures of Xe with C_2H_6. The ion in the first two mixtures was Xe_2^+, with a similar mobility. In the Xe-C_2H_6 mixture, in addition to the Xe_2^+ ion, two ions related with C_2H_6 appear. Although, Xe-C_2H_6 presents the highest mobility, the presence of more than one group of ions is expected to affect more deeply the rate capability of these detectors, as a result of the mobility span. Since CH_4 is highly flammable, the choice falls to carbon dioxide (CO_2). Comparing these results with the

previous mixtures that use CO_2 as quencher, it is possible to see that the best results (faster ions with smaller spread) are obtained with Ne followed by Ar, and only then Xe, as expected from theory.

Other mixtures studied are more difficult to compare as their use in gaseous detectors is not common, but still represent an important step in trying to predict the ion mobility behaviour in gas mixtures with three gases. Examples include Ne-N_2 [146] and CO_2-N_2 [145], which were also taken in the scope of our work at RD51/CERN Collaboration.

5

Conclusions and Future Work

In this chapter, a summary of conclusions and remarks are presented together with suggestions for future work for the two topics addressed: High Pressure Gas Proportional Scintillation Counter and Ion Mobility Measurement in Relevant Gases.

The main goal of this work was to design, construct and test a new detector of the gas proportional scintillation counter type for high energy that would compete with the state of the art contenders. In addition, a study of charge transport properties in some targeted gases and mixtures was also performed. The major objective was to study the ion mobility in gas mixtures of interest in the scope of our participation in the NEXT Collaboration and in the RD51 Collaboration/CERN, as this parameter influences the performance of large volume detectors.

5.1 HPXe Gas Proportional Scintillation Counter

In this work a new design concept for the detection of gamma-rays was explored and the results seem promising. A gas proportional scintillation counter has been developed to improve the performance of a previous prototype, based on the same concept. This geometry was expected to have a better photon collecting geometry (approximately 4 times higher) and a detection efficiency 20 times higher for 662 keV photons, resulting in a higher gain, for pressures of about 15 bar.

Despite the promising theoretical characteristics, during the development stage, several difficulties were encountered namely in the construction of the prototype and its assembly. The process used for the construction of the grids was far from perfect; this is especially relevant in the case of the collecting grid, as it affects the signal collection. In this case, obtaining a constant radial distance between the grids and the different structures is more challenging. As a result, the performance of the detector is influenced by such factors. Another important constraint was the availability of adequate HV power sources and signal processing electronics, which limited the present study.

To prove the feasibility of the concept, the detector was tested with alpha particles. This test allowed us to understand the role/influence of the reduced electric field in the

different regions and to study the performance of the detector. The role of the reduced electric field in the signal amplitude was determined varying the E/p at the surface of the anode and in the collecting region separately, seeking the optimization of the operating voltages. This study allowed us to understand the influence of the E/p in the light production process, but also its effect in the extraction of photoelectrons from the photocathode. It was also possible to identify an interesting feature: using non conventional E/p values, above the ionization threshold in the scintillation region and above the excitation threshold in the collecting region, provided higher gains, and also a better energy resolution, which was not expected since the introduction of ionization in the scintillation region usually brings about a deterioration of the energy resolution. This can be explained by the fact that, although ionization exists, since it occurs only in the vicinity of the anode, its extent is limited and the increase in fluctuations it implies is compensated by the larger scintillation yield, due to the presence of more electrons.

In terms of the detector performance, the energy resolution and gain of the detector were also assessed. In normal operating conditions, limiting the E/p in both regions to the theoretical maximum values allowed, the measured gain was in fair agreement with that predicted. Increasing the operating voltages to non-conventional E/p ranges, both energy resolution and gain were improved, with the gain surpassing the initial predictions, almost 5 times greater than expected. When the source was placed farther from the window, the energy resolution was also seen to improve approximately 1%, corresponding to the improved collimation of the alpha particle source. In the best conditions (p=3 bar), the signal was about 10 times greater than the noise. This result can be improved as the E/p in the scintillation region was not optimized.

The present results should be analysed keeping in mind that alpha particles were used instead of hard X and gamma-rays in this initial stage. The energy dispersion in alpha particles smears the energy resolution. So, the use of conventional hard X and gamma-ray sources, is expected to yield better results. Unfortunately, it was not possible to carry on the test of the detector with gamma-rays as initially proposed due to problems related with the HV supplies, when the pressure was increased above 5 bar.

We could conclude that introducing a cylindrical geometry, the solid angle and the detection efficiency were significantly improved. However, this new design makes the construction issues much more challenging. The non-uniformity of the detector response, which results from solid angle effects has to be compensated. This compensation, as seen in this work, can be made through different methods which may be active or passive. In this work, a new method was devised varying the electric field in the scintillation region, which will help to compensate for the number of photons lost due to the solid angle effects. This method was only studied theoretically with some simulation work, and its implementation is being considered as future work.

Another important improvement needed in such detector is the optical transmission of the grids. In the present prototype, the grid system developed was not optimized which resulted in a low optical transmission. There are two solutions for this problem. One is

to place both the shielding and collecting grid as close as possible to reduce the impact on the overall optical transmission and the other is to choose a different grid with better optical transmission. Alternatively, the use of a different polarization of the grids may allow to reduce the number of grids. An increase in the optical transmission at this stage will be essential to improve the detector performance.

The major limitations met in these initial tests, however, were not intrinsic. Higher voltage power supply sources (not available at the time) will allow the use of higher gas pressure, which allows us to anticipate better results.

So, in the near future we intend to address these problems and test the detector performance for gamma rays of different energies. Before that, solid angle effect corrections may also need to be implemented to achieve a detector response independent of the interaction position. This issue was only partially addressed in this work and, its implementation is not simple, so the test of several possible options should be devised.

Alternative modular low-power and compact electronics should be considered as the current available options limit the performance of the detector. Optocoupling electronics is a valid alternative to the capacitive high-voltage coupling used and may solve some of the limitations encountered. The search for valid alternatives for the electronics using digital signal acquisition and processing techniques should also be considered, since they have a significant advantage mainly due to the powerful signal pulse manipulation. In this case, the use of digital signal processing techniques can be most useful to surpass the limitations of using standard linear amplifiers not optimized for these applications, as the ones used in the initial tests.

More studies are needed to validate this prototype for commercial applications. Nevertheless, contacts have already been made with knowledge transfer institutes to adapt this technology and introduce it to industry.

Still, alternative geometries to this prototype are being considered, adapting the knowledge obtained with this prototype, with the aim of further improving its performance.

5.2 Ion mobility measurement in relevant gases

Ion mobility has been the focus of research over the past decades because of their influence in the performance of large volume detectors. Interest has been growing as new upgrades are being prepared for the large volume detectors in CERN experiments such as ALICE and NEXT Experiments, and LIP-Coimbra has been providing experimental data in this area, in particular through our participation in the RD51 Collaboration (CERN). To obtain the predicted values, usually simulation programs (Garfield) are used, but experimental data is very important in the validation of these results. The experimental setup used in the present work (described in detail in [138]) has been specially designed to study ion mobility. Within the scope of this thesis a total of 12 gas mixtures were studied, providing valuable information for several major experiments. The mixtures studied were discussed and grouped according to the property requirements specified in each case.

The studies performed in the scope of our participation at RD51 Collaboration/CERN for the ALICE TPC (Ar-CO_2 and Ne-CO_2), showed that the ion drifting in CO_2-quenched mixtures of Ar and Ne is $CO_2^+ \cdot (CO_2)_n$. Comparing both mixtures, Ne-CO_2 has better results in terms of ion mobility in the range of interest for the ALICE TPC (0-10% CO_2) as Ne has smaller mass, making energy losses in the collision of the ions with the medium gas atoms/molecules much lower. Another feature of this gas mixture is that just a small amount of CO_2 increases the mobility of the ions present.

In addition to the previous mixtures, Xe based mixtures were studied, as they are important in TRD detectors based on MWPCs (ALICE and CBM TRDs) to assess their rate capability. For these applications, Xe is considered to be the best choice of the main gas, but the best quencher is still under discussion. To answer this question, the mobility of ions produced by electron impact in Xe-CH_4, Xe-C_2H_6, Xe-CO_2 and Xe-CF_4 mixtures was studied. The results revealed that ions tend to move faster in gas mixtures with low mass additives. In theory, the use of lighter additive gases improves the mobility, which is a great advantage, especially in MWPCs where it has a significant impact on the rate capability. Comparing the results obtained with Xe based gas mixtures in the range of interest (typically 0-10% of CH_4, C_2H_6 and CO_2), it was possible to verify that Xe-C_2H_6 presented the highest mobilities, but the existence of more than one group of ions is expected to affect the rate capability of these detectors, because of the span observed in the mobilities. Looking at mixtures with CO_2, the best results are obtained with neon followed by argon, and only then xenon, which is in agreement with the theory. As for the mixtures of Ar with CH_4 and with C_2H_6, it was possible to see that Ar-CH_4 displayed the highest mobility values, as expected.

Moreover, with this work an alternative method was devised to improve the accuracy of the mobility estimates, in particular when the gas atoms or molecules are weakly polarisable, or when the molecules are large, as in Ne-CO_2. In spite of the good results obtained so far, the system has some limitations, which will be discussed next together with new opportunities that emerged during the course of this work.

So, in the future, we expect to carry out the experimental measurements for several new gas mixtures to be used eventually at the ILC Experiment which include Ar-iC_4H_{10}, Ar-CF4-iC_4H_{10} and alternative mixtures to these, Ar-CF_4-CO_2 Ar-CF_4-CH_4 Ar-CF_4-C_2H_6 as well as Ne-CF_4.

Although the results have been consistently in accordance with data obtained by other authors, several limitations have been identified. The detection of light ions constitutes a limitation, as their mobility is relatively high for the current chamber specifications (pressure, drift distance, pulse duration of the lamp, etc.). The introduction of a variable drift distance will allow the mobility of lighter ions to be measured but may also improve the ion discrimination in signals which, in the present configuration, overlap. Another application of this new feature is the study reaction rates, adding valuable information for the performance of gaseous detectors.

In order to address the mentioned limitations, a new detector is being designed. This detector will be a dual-polarity ion drift chamber, that will allow us to study the drift of both positive and negative ions, in a variable distance. The study of negative ions has been suggested by several research groups from the University of Arlington (Texas, U.S.A.) and Istituto Nazionale di Fisica Nucleare - Laboratori Nazionali di Frascati - INFN-LNF (Frascati, Italy), whose interest in this subject is growing, in part due to the rising interest in Negative Ion TPCs, for which the ion mobility is very important.

At the present moment, simulations are being carried out to help in the optimization of the design of the new prototype. A group from the Technological University of Warsaw (Poland) will help to perform experimental work within the scope of a collaboration that started recently.

To improve our knowledge of the transport properties of ions, it would be interesting to study the ion diffusion, since the tracking capabilities of future negative ion TPCs will depend on such properties. Interesting results should be expected in the near future in this area.

Appendices

Appendix A

Prototype Development Considerations

A.1 Initial Considerations on Material Selection

While all internal elements of the detector, except the feedthroughs, are made of stainless steel 316L or teflon, the external elements are made of stainless steel, copper (rings for the feedthroughs), and viton (O-rings for vacuum).

Stainless steel is typically used for these applications due to its intrinsic characteristics: general corrosion resistance, resistance to pitting from chloride ion solutions, and increased strength at elevated temperatures and very low outgassing. Another well recognized characteristic of stainless steel is the resistance to oxidation. Moreover, the 316L type is an extra-low carbon version of type 316 that minimizes harmful carbide precipitation due to welding which is an important characteristic for the development of detectors that need to be partially welded.

To seal the detector two kinds of o-rings are used: viton o-rings which make the detector versatile since they can be used several times and are inexpensive when compared with the copper ones, used for sealing components that are not intended to be re-opened.

A.2 External Structure

The external structure of the detector is formed by two flanges fixed at the top and bottom of a cylindrical tube. The main objective of this structure is to support the differential pressure between the internal and the external environment, allow to introduce and retrieve the gas and provide the support to the feedthroughs needed.

Based on our earlier discussion on the detector definition topic, we are able to calculate the detector dimensions, which were the basis of the detector design and development and that are summarized below.

Radius:

- Anode - 0.1 cm
- Scintillation region - 0.5 cm
- Absorption region - 5.5 cm
- Electric field barrier region - 2 cm
- Photoelectron collecting region - 0.5 cm

Length:

- Effective absorption length - 30 cm

As a result, the detector must have a total radius of more than 8.07 cm and an effective length of at least 30 cm. Still, there are some features that need to be taken into consideration when developing the detector and which will significantly contribute to the overall detector volume. Included in these features are: grids dimensions, supporting structure for the anode and grids, and some considerations regarding electrical discharges and vacuum virtual leaks. Since grids are usually thin and will not greatly affect the detector dimension, our focus will be on the development of the supporting structure which is essential for our system performance. For practical reasons an extra 0.5 cm will be added in the radius to make the detector versatile in its internal configuration and an additional 4 cm will be added to the detector length to comprise the internal supporting structure.

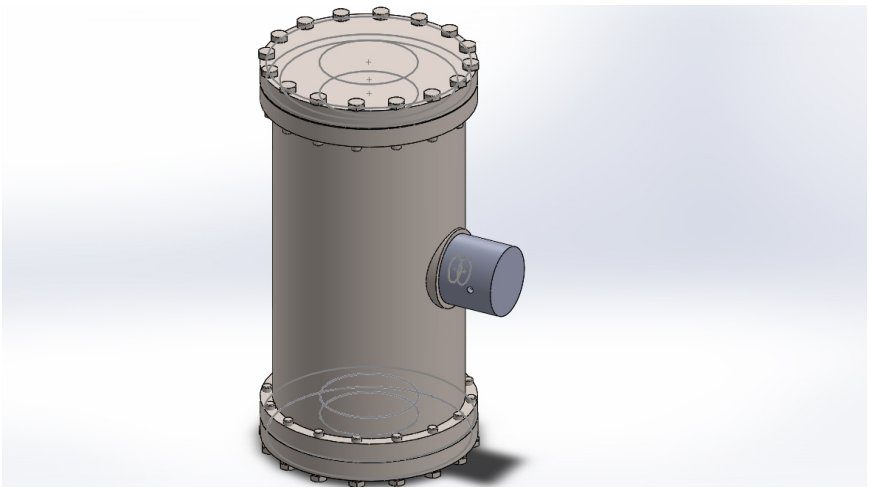

Figure A.1: External structure of the detector.

i) Tube Structure

As mentioned before a key feature of the detector is the supporting structure where the anode, grids and photocathode will be fixed. This supporting structure must ensure

on one hand that these components are stable (both electrical and mechanically) while on the other hand precluding current leaks, virtual gas leaks and ensuring at the same time an easy assembly of the detector components.

To avoid virtual gas leaks, spacers will be introduced in the top and bottom flange of the detector, with 0.5 cm height. Additionally, to facilitate the gas flow inside the detector, 0.7 cm will be added to the photocathode radius. As a consequence the detector will have an internal radius of 9.28 cm. Since it is far more convenient and cheaper to have a detector made of a single piece of stainless steel (seamless tube/hollow cylinder) it is imperative to search for the available tubes with an internal radius of this order.

ii) Wall Thickness Considerations

A simple way to calculate the minimum wall thickness needed to support a pressurized gas inside a detector is by making use of the Barlow formula that is a simplification of Lame's formula for thin walled cylinders and which can be expressed as follows:

$$P = \frac{2St}{D} \tag{A.1}$$

where P is the maximum internal pressure, S the allowable stress, t the minimum wall thickness and D is the outside diameter. Since S values are only material dependent, for stainless steel it is approximately 25000 psi [210]. For the operating conditions defined the thickness wall comes:

$$t = \frac{PD}{2S} \tag{A.2}$$

Since the outer diameter is unknown and the value for the inner diameter of the detector based in the premises discussed earlier in this section, we can rearrange eq. 4.7 where D_i is the internal diameter and obtain the desired wall thickness for the detector.

$$t = \frac{PD_i}{2S - P} \tag{A.3}$$

For a maximum pressure of 20 bar (293.92 psi), a inner diameter of 18.5 cm, a allowable stress of 25000 psi the wall thickness needed for the detector is 0.11 cm.

A simplified way to ensure that the detector wall is designed to support the pressures intended is done usually by adding a safety factor to the pressure (typically between 3 to 4 times the minimum wall thickness according to European Union (EU) norms) and use that value of the wall thickness as reference. For a safety factor of 4 the wall thickness needed for the detector is 0.44 cm, for practical reasons we will use 0.5 cm, which will be enough for the purposed work.

A.3 Internal Structure

A.3.1 Anode

The anode structure is a stainless steel cylinder, with a 0.1 cm radius and 32 cm length. The voltage applied to the anode is done using a high voltage feedthrough which is welded to the anode. The feedthrough is fixed at the top flange of the detector and copper rings are used to seal the detector. The feedthrough chosen was the 21184-01-CF model of Cerameseal, which supports pressures up to 28 bar and with a limit voltage supply of 50 kV.
An important situation that must be considered while developing new detectors are the unwanted discharges in high-voltage systems which in our case can lead to a catastrophic failure. As known from literature, the key to high-voltage anode design is smoothness, both microscopically and macroscopically. For that reason and in order to avoid electrical discharges the anode's end will be made spherical and left loose, since it is important for the anode to be physically smooth and have gently curving features with large radii while being without any contact with other materials [211].

A.3.2 Grid

The grids employed in the detector are essential for its performance, since they will establish the electric fields inside the detector, which will define the different regions presented earlier in section 4.1.

The grids that will be employed in the detector are of cylindrical shape and made of stainless steel, one with a 6 cm radius (shielding grid) and another with 8 cm radius (collecting grid) and 32 cm length. Although the dimensions are defined, it is important to define another characteristic of those grids, once it will have important implications on the detector gain and which is the optical transmission of the grids. As seen earlier, the detector working principle relies on the production of secondary scintillation photons from excited Xe atoms. These photons will be produced in the scintillation region which is close to the detector's anode and since these photons will be collected in the photocathode they need to cross the two grids so a good optical transmission is imperative to avoid a decrease in the amount of photons that arrive at the photocathode. For the proposed detector, we believe that a combined optical transmission of about 50% will suffice.

i) Grid structure

Another factor that needs to be considered is the way the grid will be shaped in a cylinder. The easier way to do so, is to use a material strong enough to maintain the shape given to it, fold it in a cylindrical shape and then weld both ends.

This solution has two important limitations: one is the optical transmission and the other is the electric field uniformity in the photoelectron collecting region which is a very thin region making the region E/p very sensitive to small variations in the distance between the collecting grid and photocathode.

ii) Electric Field Simulation Study

As mentioned, the transmission of both grids must be as high as possible without changing the uniformity of the electric field inside the different detector regions. In order to ensure that the electric field is uniform inside the collecting region, which is essential for the detector performance, an initial simulation was done using different openings (distance between wires) and, to simplify the problem, a linear configuration was considered for the simulation since the radius of the collecting grid and photocathode will be much higher than the distance between them. For the present simulation, the software Ansoft Maxwell V.14 was used. To simulate the electric field inside the region of photoelectron collection a bar of stainless steel of 2 cm length and 0.5 cm thickness was used to simulate the photocathode, which was considered to be at 0 V. To represent the two grids full circles made of stainless steel with a radius of 0.02 cm were considered and then placed at different distances between them and parallel to the bar at a constant distance of 0.5 cm (collecting grid) and 2.5 cm (shielding grid) of the bar at a voltage of 5000 V and 0 V respectively. For the environment definition, vacuum was considered in this simulation.

The results of this simulation are represented in figure A.2.

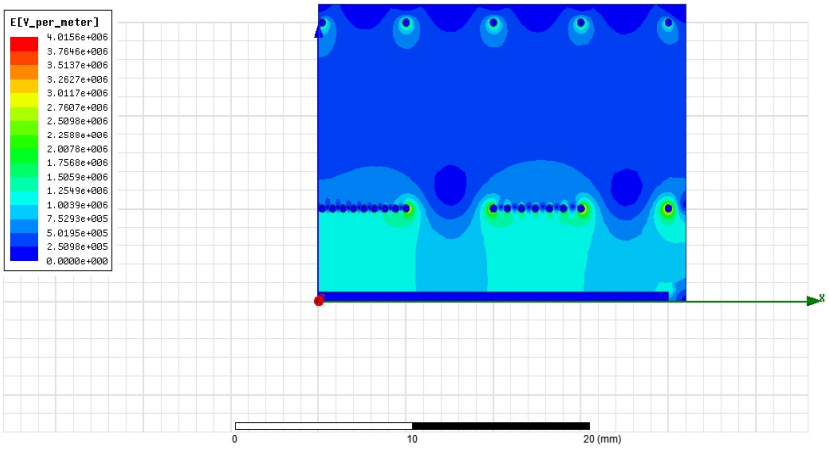

Figure A.2: Electric field simulation of the photoelectron collecting region. In this simulation is possible to see the resulting electric field for different distances between the wires defined (0.01 cm, 0.04 cm and 0.5 cm, from left to right. In this simulation the shieding grid, collecting grid and photocathode represented here as the set of dots and bar at the bottom) were defined to be made of stainless steel and was considered an excitation voltage of 5000 V for the collecting grid. As for the distance between the wires in the shielding grid, a constant distance of approximately 0.5 cm was considered.

From the simulation results we concluded that to have a uniform electric field the distance between the grid wires should be at most 0.04 cm. For the definition of the opening are a square shape was considered, resulting in a opening of 0.0016 cm^2.

A.3.3 Photocathode

As seen before, one of the crucial features of the detector is the photocathode. The main function of a photosensor is to convert the incident scintillation light into photoelectrons which will be collected in the collecting grid afterwards.

Alternatively to traditional methods used to convert light into charge, which include, as seen in section 2.2, PMTs and photodiodes, in this project we will use three metal sheets folded in a concave shape in a way so that together they will form a cylinder and coated in the concave side with a thin photocathode film.

i) Photocathode Selection

Essentially the choice of a photocathode depends on the wavelength of the incident radiation, in our case since we are working with VUV photons, with a wavelength of 170 nm, the photocathode that has the higher quantum efficiency is Cesium Iodide (CsI) corresponding to 25-30% for 170 nm incident radiation [39]. Along with the high quantum efficiency for the Xe VUV wavelength, CsI films are easy to prepare which makes them attractive for application in radiation detectors using photocathodes.

Usually the thickness of the CsI films is of few hundred nanometers, obtained by vacuum deposition. The typical evaporation rate is about 1-10 $nm.s^{-1}$, with no significant difference in the quantum efficiency of the photocathode to vacuum conditions between 10^{-5} and 10^{-8} Torr. For poorer vacuum conditions, it is recommended to increase the evaporation rate to reduce contamination.

As known from literature the substrate is a vital component for the performance of photocathodes. To improve the quality of the substrates surface, CsI can be deposited on aluminium thin films (100 nm) which in turn are deposited on the metal substrate, although several authors deposit CsI directly on metal substrates, usually stainless steel [64].

One drawback to consider in CsI photocathodes is their degradation when exposed to moist air, which leads to a performance decay in the photoelectron emission due to hydrolysis of the material surface. This effect was already studied by several authors that concluded that a decrease of 25% in the quantum efficiency for 170 nm was observed for 100 minutes at a relative humidity of 25% [212]. Other authors that include Dangendorf [213] and Krizan [214] reported a decay of 50 % in quantum efficiency after exposure to air for 100 minutes at a relative humidity of 50%. It has been observed that the degradation of emission of photoelectrons is greater for higher wavelengths, probably due to

an increase in electron affinity [212]. It was found, however, that the CsI photocathodes that were heat treated after the evaporation have a considerably slower deterioration, are more stable when exposed to air [215]. Eventually CsI photocathodes damaged by water absorption may still be recovered by heating to 373 K for a few hours.

ii) CsI Photocathode Deposition

The CsI photocathodes used in the HPXe GPSC were deposited on one side of the photocathode support structure by Joule effect, on the evaporation setup available at the Department of Physics from LibPhys. The stainless steel support was cleaned beforehand with the standard procedure:

1. flushed with deionized water followed by
2. 60 minutes in an ultrasonic bath of iso-propyl alcohol followed by
3. baking for 24 hours at 60 ^{o}C

The aim is to maximize the CsI photocathode quantum efficiency and to improve resistance to short term exposure to air during the transfer and installation, from the evaporation plant to the detector.

The CsI film was deposited directly on a thin stainless steel sheet which will improve the versatility of the detector, facilitating the substitution of the photocathode in a case of need. The thickness chosen for the CsI film needs to be at least 200 nm, although typical thickness in reflective photocathode applications are of about 500 nm.

Before starting the evaporation of CsI in the plant, the CsI mass required to make a deposit of a minimum of 200 nm was calculated. Due to the fact that we were dealing with a non conventional deposition geometry a simulation was carried out to identify possible problems during the evaporation process and to tentatively predict the CsI thickness distribution during the deposition process.

The result of the simulation for the masses used during the deposition process is displayed in figure A.3.

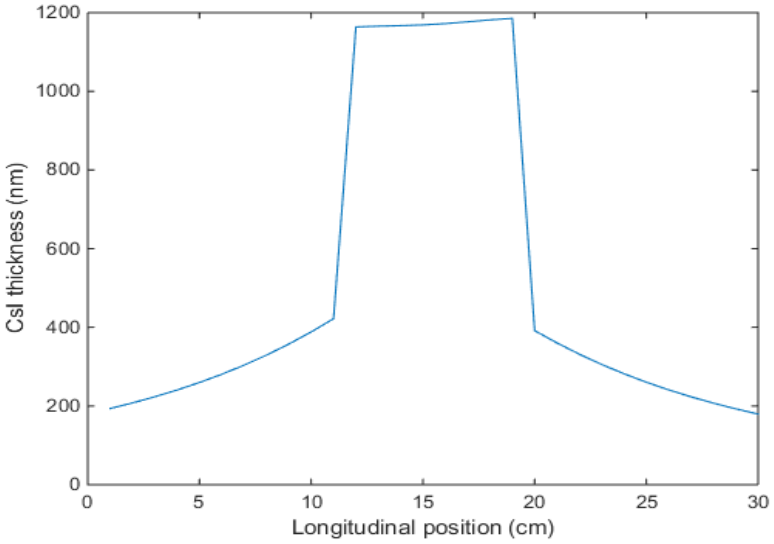

Figure A.3: CsI thickness as a function of the longitudinal position simulated using MATLAB.

iii) CsI Photocathode Treatment

As mentioned before, the quantum efficiency of CsI is generally lower after the evaporation process as a result from several factors that include surface impurities and exposure of the substrate to moisture during the evaporation inside the evaporation plant or during the transportation to the detector.

There are numerous ways of improving the photoemission properties of the photocathode. These properties can be simply improved by streaming pure CH_4 for a few hours on the surface of photocathode, which is probably a result of the removal of impurities and contaminants from the surface to evaporate (Seguinot [65] and Anderson [216]) or alternatively by heating the photocathode in circulation gas to approximately 373 K for several hours to remove the water existing on its surface [216].

A.3.4 Teflon Structure

The teflon structure developed has two distinct objectives, provide the supporting structure for the detector elements (anode, grids and CsI photocathode support) and, at the same time, provide the electrical insulation between the different detector components. The connections to the anode and collecting grid are made with wires capable of carrying the required currents and suitable vacuum feedthroughs, were incorporated in the design. This teflon structure was designed to allow fixing the different components in the flanges, making the detector versatile at the same time. Additionally, it allows an easy access to the detector interior whenever needed.

This structure was split into two distinct supports, one fixed to the top flange of the

detector and the second one that was mounted on the bottom flange of the detector. Both structures have a cylindrical shape with 1,5 cm height and a 9 cm radius. These structures were machined in order to produce the support to the anode, grids and CsI photocathode. Holes were drilled to improve the gas flow inside the detector and to avoid virtual gas leaks. Additionally spacers were introduced in both top and bottom flanges of the detector, with 0.5 cm height.

The details on the different internal supporting structures as well as a detailed schematic will be provided in the following subsections.

i) Bottom Flange Teflon Supporting Structure

Since the electrical feedthroughs are mounted in the bottom flange of the detector , this internal support must be fixed at all times to the stainless steel flange of the detector. To prevent electrical current leaks, the several components were placed in this structure at distinct heights protected by teflon rings, or teflon rings with a slit to support the different structures of the detector (anode, grids and CsI photocathode) machined in the initial cylindrical piece of teflon. A schematic image of the flange can be seen in figure A.4.

As it can be seen, this structure was fixed to the flange using teflon screws that are inside the teflon spacers.

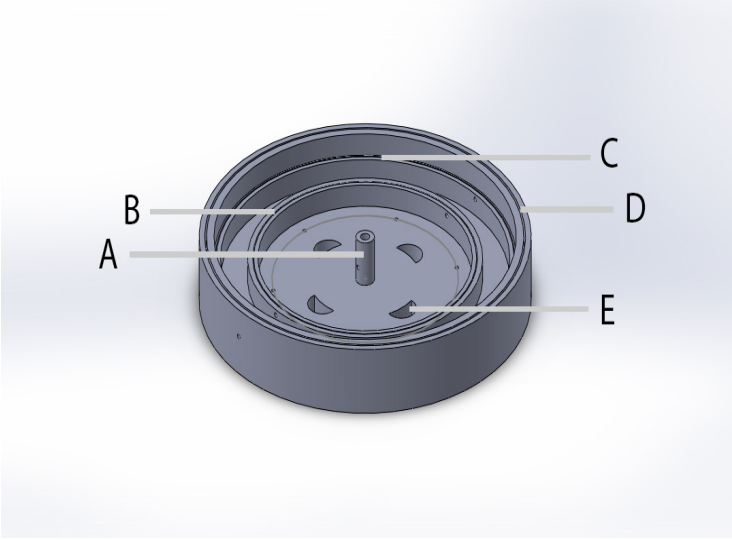

Figure A.4: Schematic of th bottom flange teflon supporting structure. In this image it is possible to see the anode support (A), the shielding grid support (B), the collecting grid support (C), the CsI photocathode support (D) and holes to help the gas flow inside the detector (E).

ii) Top Flange Teflon Supporting Structure

There were several details that were considered when the top teflon supporting structure was designed. An important aspect of the top teflon support is that it must ensure an easy access to the different components of the detector and at the same time facilitate the structure mounting after the different elements are fixed in the top teflon structure. A schematic image of the flange can be seen in figure A.5.

To make it versatile this structure was divided into three separated structures. The main is fixed to the stainless steel flange through the teflon spacers using screws (as in the previous teflon support described). This main structure, represented in figure A.6 by A is the supporting structure of the other two structures, here represented by B and C, that will settle in this structure. The other two teflon rings (B and C) have a slit for the grids to fit. These rings have 1 cm height with the slit radius being defined by the grid intended position. In such teflon rings a thickness of 1 cm was defined with the slit being positioned at the middle of each ring.

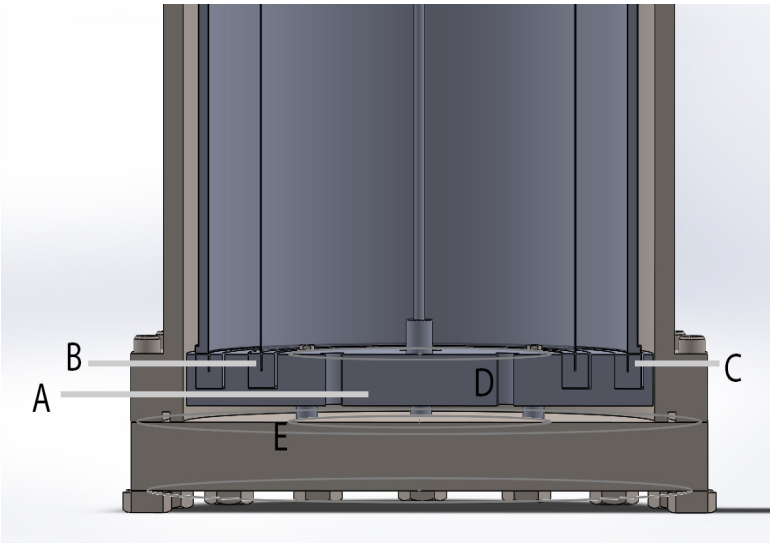

Figure A.5: Schematic of the top flange teflon supporting structure. In this image it is possible to see the main teflon support (A), the shielding grid support ring (B), the collecting grid support ring (C), holes to help the gas flow inside the detector (D), and teflon spacers (E).

In figure A.6 is possible to see both top (A) and bottom (B) teflon supports, the anode (C), the shielding (D) and collecting grids (E), the CsI photocathode (F) and the alpha particle window and supporting structure (G). The alpha particle supporting structure was incorporated in the detector design for proof concept (which will be addressed in section 4.6.2), and can be easily removed after this test is finished.

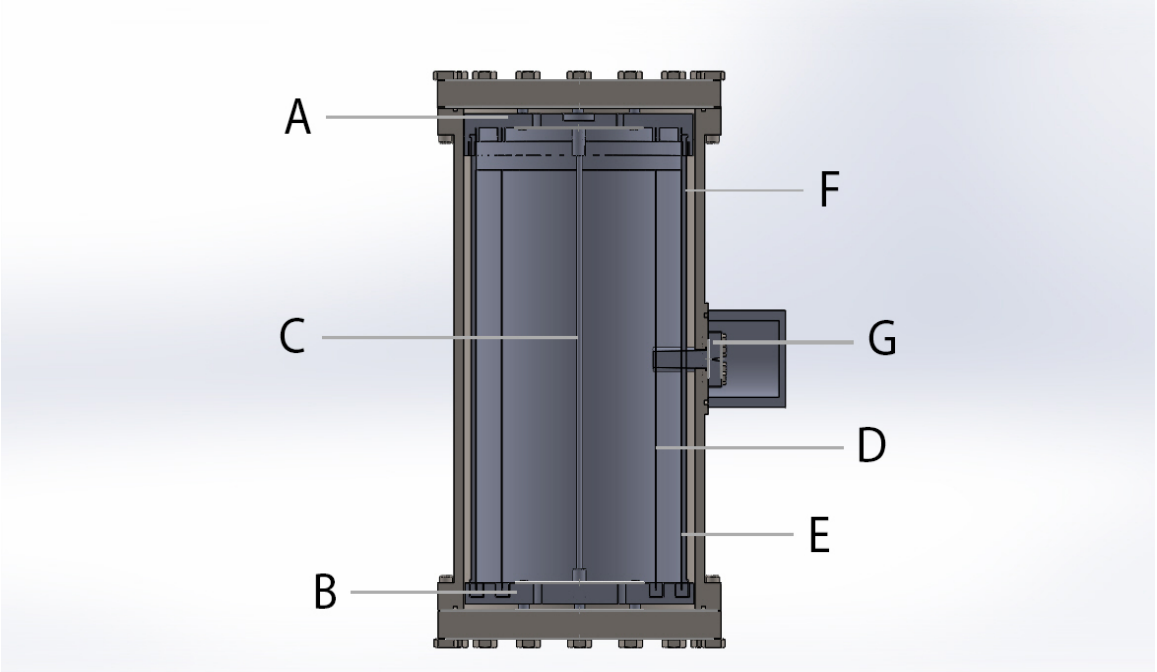

Figure A.6: Schematic of the complete detector. In this image it is possible to see both top (A) and bottom (B) Teflon supports, the anode (C), the shielding (D) and collecting grids (E), the CsI photocathode (F) and the alpha particle window and supporting structure (G).

Bibliography

[1] G. Charpak, *Some Steps in the Evolution of Gaseous Detectors*, *IEEE Trans. Nucl. Sci.* **NS-27 1** (1980) 119.

[2] E. Aprile, A.E. Bolotinikov, A.I. Bolozdynya, T. Doke, *Noble Gas Detectors*, Wiley-VCH Verlag GmbH & Co. KGaA, Weinheim 2006.

[3] C.A.N. Conde, *Gas Proportional Scintillation Counters for X-ray Spectrometry, X-Ray Spectrometry: Recent Technological Advances*, Ch. 4.2, John Wiley and Sons, Inc., New York 2004.

[4] W. Blum, L. Rolandi, *Particle Detection with Drift Chambers*, Springer-Verlag, Berlin 1994.

[5] F. Sauli, *Gaseous Radiation Detectors: Fundamentals and Applications*, Cambridge Monographs on Particle Physics, Nuclear Physics and Cosmology, Cambridge: Cambridge University Press, 2014.

[6] F.I.G.M Borges, S.J.C. do Carmo, J.C.R. Mariquito, A.M.F. Trindade and C.A.N. Conde, *A New Technique for Gaseous Radiation Detectors: The Multigrid High-Pressure Xenon Gas Proportional Scintillation Counter*, *IEEE Trans. Nucl. Sci.* **57** (2009) 4.

[7] G.F. Knoll, *Radiation detection and measurements*, John Wiley and Sons, Inc., New York 2000.

[8] A. Andronic, C. Garabatos, D. Gonzalez-Diaz, A. Kalweit and F. Uhlig, *A comprehensive study of rate capability in Multi-Wire Proportional Chambers*, *JINST* **4** (2009) P10014.

[9] W.R. Leo, *Techniques for Nuclear and Particle Physics Experiments*, Springer-Verlag, Berlin 1994.

[10] F.I.G.M. Borges, *Detectores de radiação X de baixa energia baseados em misturas de Xenon e Neon*, Dissertação de Doutoramento, Departamento de Física, Universidade de Coimbra, Portugal, 2003.

[11] F.P. Santos, *Detectores Gasosos para Raios-X: Simulação e Estudo Experimental*, Dissertação de Doutoramento, Departamento de Física, Universidade de Coimbra, Portugal, 1994.

[12] R. Johnsen, M.A. Biondi, *Thermal Energy Charge Transfer, Quenching and Association Reactions of Doubly Charged Ions in Rare Gases*, *Phys. Rev. A* **20**, (1979) 87.

[13] R. Morgenstern, A. Niehaus and G. Zimmermann, *Auto-ionization States Formed by Electron-Capture in Collisions of Multiply Charged Ne Ions with He, H_2 and Xe*, *J. Phys. B* **13**, (1980) 4811.

[14] W. Groh, A. Muller, A.S. Schlachter and E. Salzborn, *Transfer Ionization in Slow Collisions of Multiply-Charged Ions with Atoms*, *J. Phys. B* **16**, (1983) 1997.

[15] J.A. Hornbeck and J.P. Molnar, *Mass spectrometric studies of molecular ions in the noble gases*, *Physical Review* **84**, (1951) 621.

[16] R.E. Huffman, D.H. Katayama, *Photoionization Study of diatomic-Ion Formation in Argon, Krypton and Xenon*, *J. Chem. Phys.* **45**, (1966) 138.

[17] S.J.C. do Carmo, F.I.G.M. Borges, F.L.R. Vinagre and C.A.N. Conde, *Experimental Study of the w-Values and Fano Factors of Gaseous Xenon and Ar-Xe Mixtures for X-Rays*, *IEEE Trans. Nucl. Sci* **55** (2008) 2637.

[18] E.W. McDaniel, *Atomic Collisions - Electron and Photon projectiles*, John Wiley and Sons, Inc., New York 1989

[19] J. Escada, *Detetores Gasosos de Radiação: Efeitos da retrodifusão na emissão de fotoeletrões por fotocátodos de CsI em meio gasoso e eletroluminescência em Xe dopado com CH4 e CF4*, Ph.D. Thesis, University of Coimbra, 2012.

[20] G.D. Alkhazov, A.P Komar, and A.A. Vorob'ev, *Ionization fluctuations and resolutions of ionization chambers and semiconducter detectors*, *Nucl. Instrum. and Meth.* **48** (1967) 1.

[21] P.J. Campion, *A Study of Proportional Counter Mechanisms*, *International Journal of Applied Radiation and Isotopes* **19** (1968) 219.

[22] J.M.F. dos Santos, J.A.M. Lopes, J.F.C.A. Veloso, P.C.P.S. Simões, T.H.V.T. Dias, F.P. Santos, P.J.B.M. Rachinhas, L.F. Requicha Ferreira and C.A.N. Conde, *Development of portable gas proportional scintillation counters for x-ray spectrometry*, *X-Ray Spectrom.* **30** (2001) 373.

[23] M. Suzuki and S. Kubota, *Mechanism of Proportional Scintillation in argon, krypton and xenon*, *Nucl. Instr. Meth.* **164**, (1979) 197.

[24] M.S.C.P. Leite, *Radioluminescence of Rare Gases*, *Portgal Phys.* **11**, (1980) 53.

[25] A. Gedanken, J. Jortner, B. Raz and A. Szoke, *Electronic Energy Transfer Phenomena in Rare Gases*, *J. Chem. Phys.* **57**, (1972) 3456.

[26] A.J.P.L. Policarpo, *Light Production and Gaseous Detectors*, *Physica Scripta* **23**, (1981) 539.

[27] G.N. Gerasimov, B.E. Krylov, A.V. Loginov and S.A. Shchukin, *UV Emission for Excited Inter-Gas Molecules*, *Sov. Phys. Usp.* **35**, (1992) 400.

[28] T.E. Stewart, G.S. Hurst, T.E. Bortner, J.E. Parks, F.W. Martin and H.L. Weidner, *Photon Excitation of Continuous Emission in Noble Gases*, *J. Opt. Soc. Am.* **60**, (1970) 1290.

[29] T.H.V.T. Dias, *Simulação do transporte de electrões em gases raros*, Dissertação de Doutoramento, Departamento de Física, Universidade de Coimbra, Portugal, 1986.

[30] C.A.N. Conde, L.R. Ferreira and M.F.A. Ferreira, *Secondary scintillation output of xenon in a uniform field gas proportional scintillation counter*, *IEEE Trans. Nucl. Sci* **24** (1977) 221.

[31] R.D. Andresen, E.A. Leimann, A. Peacock, *The nature of the light produced inside a gas scintillation proportional counter*, *Nucl. Instrum. and Meth.* **140** (1977) 371.

[32] T.H.V.T. Dias, F.P. Santos, A.D. Stauffer and C.A.N. Conde, *Monte Carlo simulation of x-ray absorption and electron drift in gaseous xenon*, *Phys. Rev. A* **48** (1993) 2887.

[33] F.P. Santos, T.H.V.T. Dias, A.D. Stauffer and C.A.N. Conde, *Three-dimensional Monte Carlo calculation of the VUV electroluminescence and other electron transport parameters in xenon*, *J. Phys. D: Appl. Phys.* **27** (1994) 42.

[34] F.P. Santos, T.H.V.T. Dias, P.J.B.M. Rachinhas, A.D. Stauffer and C.A.N. Conde, *Three-dimensional Monte Carlo calculation of the VUV electroluminescence and other electron transport parameters in xenon*, *IEEE Trans. Nucl. Sci.* **45** (1998) 754.

[35] F.I.G.M. Borges and C.A.N. Conde, *Experimental W-values in gaseous Xe, Kr and Ar for low energy X-rays*, *Nucl. Instr. Meth. Phys. Res. A* **381** (1996) 91.

[36] S. Kubota, *Non-metastable Pening Effect in Alpha-particle Ionization of Inert Gas Mixtures*, *J. Phys. Soc. Japan* **29** (1970) 1017.

[37] M. Jarvinen and H. Sipila, *Effects of Pressure and Admixture of Neon Pening Mixtures on Proportional Counter Resolution*, *Nucl. Instr. and Meth.* **193** (1982) 53.

[38] F. Favata, A. Smith, M. Bavdaz, T.Z. Kowalski, *Light yield as a function og gas pressure and electric field in gas scintillation proportional counters*, *Nucl. Instr. Meth. Phys. Res. A* **294** (1990) 595.

[39] A. Breskin, *CsI UV photocathodes: History and mystery*, *Nucl. Instrum. Meth. A* **371** (1996) 116.

[40] C.A.N. Conde and A.J.P.L. Policarpo, *A Gas Proportional Scintillation Counter*, *Nucl. Instrum. Meth.* **53** (1967) 7.

[41] A.J.P.L. Policarpo, M.A.F. Alves, C.A.N. Conde, *The argon-nitrogen proportional scintillation counter*, *Nucl. Instrum. Meth.* **55** (1967) 105.

[42] A.J.P.L. Policarpo, M.A.F. Alves, M.J.T. Carvalho, M.A.G. Da Rocha, *The gas proportional scintillation counter under X-rays bombardment: Resolution and pulse correlations*, *Nucl. Instrum. Meth.* **77** (1970) 309.

[43] J.A.M. Lopes, J.M.F. Dos Santos, C.A.N. Conde, *A large area avalanche photodiode as the VUV photosensor for gas proportional scintillation counters*, *Nucl. Instr. and Meth. A* **454** (2000) 421.

[44] L.C.C. Coelho, J.A.M. Lopes, D.S. Covita, A.S. Conceição, J.M.F. dos Santos, *Xenon GPSC high-pressure operation with large-area avalanche photodiode readout*, *Nucl. Instrum. Meth. A* **575** (2007) 444.

[45] C.M.B. Monteiro, L.M.P. Fernandes, J.F.C.A. Veloso, C.A.B. Oliveira, J.M.F. dos Santos, *Secondary scintillation yield from GEM and THGEM gaseous electron multipliers for direct dark matter search*, *Physics Letters B* **714** (2012) 18.

[46] J.A.M. Lopes, *Contadores Gasosos de Cintilação Proporcional: Novas Aplicações e Tecnologias de Fotossensores Integrados*, Ph.D. Thesis, University of Coimbra, 2002.

[47] A.J.P.L. Policarpo, *Coupling the Gas Scintillation Proportional Counter to Photoionization Detectors*, *Nucl. Instr. and Meth.* **153** (1978) 389.

[48] D.F. Anderson, *A xenon gas scintillation proportional counter coupled to a photoionization detector*, *Nucl. Instr. and Meth.* **178** (1980) 125.

[49] J.C. Van Standen, J. Foh, M. Mutterer, J. Pannicke, K.P. Schelhas and J.P. Theobald, *A xenon gas scintillation proportional counter coupled to a photoionization detector*, *Nucl. Instr. and Meth.* **157** (1978) 301.

[50] A.J. de Campos, *A Silicon Photodiode Based Gas Proportional Scintillation Counter*, *IEEE Trans. Nucl. Sci.* **NS-31 1** (1984) 133.

[51] J.F.C.A. Veloso, *Detectores Gasosos de Radiação Baseados em Microestruturas*, Ph.D. Thesis, University of Coimbra, 2000.

[52] J.F.C.A. Veloso, D.S. Covita, L.F. Requicha Ferreira, J.M.F. dos Santos, *Gas proportional scintillation counters with a CsI-covered microstrip plate UV photosensor for high-resolution X-ray*, *Nucl. Instr. and Meth. A* **457** (2001) 253.

[53] J.A.M. Lopes and C.A.N. Conde, *A large-area VUV photosensor with high gain by means of photoelectron acceleration and concentration*, *IEEE Trans. Nucl. Sci.* **NS-42 4** (1995) 364.

[54] L.C.C. Coelho, J.F.C.A. Veloso, D.S. Covita, L.F. Requicha Ferreira, J.M.F. dos Santos, *High-pressure operation of a xenon-GPSC/MSGC hybrid detector for hard X-ray spectrometry*, *Nucl. Instr. and Meth. A* **569** (2006) 796.

[55] C.D.R. Azevedo, C.A.B. Oliveira, H. Natal da Luz, L.F. Carramate, A.L. Ferreira, J.M.F. dos Santos, J.F.C.A. Veloso, *Gas VUV photosensors operating face to face*, *Nucl. Instr. and Meth. A* **610** (2009) 238.

[56] F.D. Amaro, M. Ball, J.F.C.A. Veloso and J.M.F. Dos Santos, *Zero Ion Backflow electron multiplier operating in noble gases*, *JINST* **9** (2014) P02004.

[57] W. E. Spicer, *Photoconductive, and Optical Absorption Studies of Alkali-Antimony Compounds*, *Phys. Rev.* **112** (1), (1958) 114.

[58] W. E. Spicer, A. Herrera-Gomez, *Modern theory and applications of photocathodes*, *Proceedings of the International Society for Optical Engineering (SPIE) Symposium on Optics, Imaging and Instrumentation, San Diego*, (1993) 18.

[59] G.R. Carruthers, *Magnetically Focused Electronographic Image Converters for Space Astronomy Applications*, *Appl. Opt.* **8** (1969) 633.

[60] P. Miné, *Photoemissive materials and their application to gaseous detectors*, *Nucl. Instr. and Meth. A* **343** (1994) 99.

[61] A. Akkerman, T. Boutboul, A. Breskin, R. Chechik and A. Gibrekhterman, *Low-energy electron transport in alkali halides*, *J. Appl. Phys.* **76** (1994) 4656.

[62] J. Va'vra, A. Breskin, A. Buzulutskov, R. Chechik and E. Shefer, *Study CsI photocathodes: Volume resistivity and aging*, *Nucl. Instrum. Meth. A* **387** (1997) 154.

[63] A. Breskin, A. Buzulutskov, R. Chechik, *New ideas in CsI-based photon detectors: wire photomultipliers and protection of the photocathodes*, *IEEE Trans. Nucl. Sci.* **90** (1989) 7143.

[64] A. Breskin, A. Buzulutskov, R. Chechik, A. DiMauro, E. Nappi, G. Paic and F. Piuz, *Field dependent photoelectron extraction from CsI in different gases*, *Nucl. Instrum. Meth. A* **367** (1995) 342.

[65] J. Seguinot, G. Charpak, Y. Giomataris, V. Peskov, J. Tischhauser, T. Ypsilantis, *Reflective UV photocathodes with gas phase electron extraction: Solid, liquid, and adsorbed thin films*, *Nucl. Instrum. Meth. A* **297** (1990) 133.

[66] M.A. Stoletow, *Sur les courants actino-électriques dans l'air raréfié*, *J. Physique* **9** (1890) 468.

[67] E.R. von Schwidler, *Cpmptes Rendus* **127** (1898) 224.

[68] P. Lenard, *Erzeugung von kathodenstrahlen durch ultraviolettes licht*, *Ann. Physik* **2** (1900) 359.

[69] W.M. Varley, *On the photo-electric discharge from metallic surfaces in different gases*, *Phil. Trans. A* **202** (1904) 439.

[70] J.J. Thomson, *Conduction of electricity through gases*, *Cambridge University Press* **90** (1928) 466.

[71] L.B. Loeb, *Basic processes of gaseous electronics*, University of California press, California 1955.

[72] V. Dangendorf, A. Breskin, R. Chechik and H. Schimdt-Böcking, *As gas-filled UV-photon detector with CsI photocathode for the detection of Xe light*, *Nucl. Instrum. Meth. A* **289** (1990) 322.

[73] A. Breskin, A. Buzulutskov, R. Chechik, D. Vartsky, G. Malamud, P. Miné, *Electric-Field Effects on the Quantum Efficiency of Csi Photocathodes in Gas Media*, *Nucl. Instrum. Meth. A* **344** (1994) 537.

[74] A. Buzulutskov, A. Breskin and R. Chechik, *Field Enhancement of the Photoelectric and Secondary-Electron Emission from Csi*, *J. Appl. Phys.* **77** (1995) 2138.

[75] J. Escada, P.J.B.M. Rachinhas, T.H.V.T. Dias, J.A.M. Lopes, F.P. Santos, and C.A.N. Conde, *Photoelectron Collection Efficiency in Xe-CF4 Mixtures*, *IEEE Trans. Nucl. Sci.* **43** (2007) 585.

[76] J. Escada, T.H.V.T. Dias, P.J.B.M. Rachinhas, F.P. Santos, J.A.M. Lopes, L.C.C. Coelho, C.A.N. Conde and A.D. Stauffer, *A Monte Carlo study of photoelectron extraction efficiency from CsI photocathodes into Xe–CH4 and Ne–CH4 mixtures*, *J. Phys. D: Appl. Phys.* **43** (2010) 065502.

[77] L.C.C. Coelho, J.A.M. Lopes, J. Escada, T.H.V.T. Dias and J.M.F. dos Santos, *Photoelectron transmission efficiency in Ar-CH4 and Xe-CH4 mixtures: Experimental results*, *Nucl. Instrum. Meth. A* **607** (2009) 587.

[78] D.S. Covita, C.D.R. Azevedo, C.C. Caldas and J.F.C.A. Veloso, *Photoelectron extraction efficiency from cesium iodide photocathodes in a pressurized atmosphere of argon and xenon up to 10 bar*, *Physics Letters B* **701** (2011) 151.

[79] G. Manzo, A. Peacock, R.D. Andresen and B.G. Taylor, *High Pressure Gas Scintillation Spectrometers for X-ray Astronomy*, *Nucl. Instr. Meth. Phys. Res. A* **294** (1990) 595.

[80] C.A.N. Conde, J.M.F. dos Santos, A.C.S.S.M. Bento, *New concepts for the design of large area gas proportional scintillation counters*, *IEEE Trans. Nucl. Sci.* **40** (1993) 452.

[81] J.F.C.A. Veloso, J.M.F. dos Santos, C.A.N. Conde, *Large-window gas proportional scintillation counter with photosensor compensation*, *IEEE Trans. Nucl. Sci.* **42** (1995) 369.

[82] NEXT collaboration, V. Álvarez et al., *Ionization and scintillation response of high-pressure xenon gas to alpha particles*, 2013 *JINST* **8** P05025.

[83] F.I.G.M. Borges, J.M.F. dos Santos, T.H.V.T. Dias, F.P. Santos, P.J.B.M. Rachinhas and C.A.N. Conde, *Operation of gas proportional scintillation counters in a low charge multiplication region*, *Nucl. Inst. Meth. A* **422** (1999) 321.

[84] J.F.C.A. Veloso and C.A.N. Conde, *Incidence angle dependence of the output response uniformity of photomultipliers*, *IEEE Trans. Nucl. Sci.* **40** (1993) 434.

[85] J.M.F. dos Santos, A.C.S.S. Bento and C.A.N. Conde, *The effect of the photomultiplier nonuniformity on the performance of gas proportional scintillation counters*, *Nucl. Instr. Meth. A* **238-241** (1992) 238.

[86] D.F. Anderson, W.H.M. Ku, D.D. Mitchel, R. Novick, and R.S. Wolff, *Recent developments in parallel-grid gas scintillation proportional counters*, *IEEE Trans. Nucl. Sci.* **24** (1977) 283.

[87] J.M.F. dos Santos, A.C.S.S. Bento and C.A.N. Conde, *The dependence of the energy resolution of gas proportional scintillation counters on the scintillation region to photomultiplier distance*, *IEEE Trans. Nucl. Sci.* **39** (1992) 541.

[88] V.V. Dmitrenko, V.M. Gratchev, S.E. Ulin, Z.M. Uteshev, K.F. VIasik, *High-pressure xenon detectors for gamma-ray spectrometry*, *Applied Radiation and Isotopes* **52** (2000) 739.

[89] V.V. Dmitrenko, S.E. Ulin, V.M. Grachev, K.F. Vlasik, Z.M. Uteshev, I.V. Chernysheva, K.V. Krivova, and A.G. Dukhvalov, *Perspectives of High Pressure Xenon Gamma-ray Spectrometers to Detect and Identify Radioactive and Fissile Materials*, *Prevention, Detection and Response to Nuclear and Radiological*, Springer, New York 2008.

[90] A. Bolotnikov, A. Bolozdynya, R. DeVito, J. Richards, *Dua-Anode High-Pressure Xenon Cylindrical Ionization Chamber*, *Applied Radiation and Isotopes* **52** (2000) 739.

[91] A.Bolozdynya, A. Arodzero, and R. DeVito, *High-pressure xenon detectors for applications in portal safeguard systems and for monitoring nuclear waste*, *INMM 43rd Annual Meeting*, Orlando (U.S.A), *June 23-27* (2002).

[92] R. A. Austin, *High-pressure xenon detector development at Constellation Technology Corporation*, *Nucl. Instr. and Meth. A* **579** (2007) 58.

[93] S.E. Ulin, K.F. Vlasik, A.M. Galper, V.M. Grachev, V.V. Dmitrenko, V.I. Liagushin, Z.M. Uteshev, Yu.T. Yurkin, *Influence of proton and neutron fluxes on spectrometric characteristics of a high-pressure xenon gamma spectrometer*, *Proc. SPIE 3114, EUV, X-Ray, and Gamma-Ray Instrumentation for Astronomy VIII* **499** (1997).

[94] S. Kopernya, T.Z. Kowalskia, *Performance of proportional counters under high count rate, high gas gain and at high working gas pressure*, *Nuclear Physics B - Proceedings Supplements* **197** (2009) 370.

[95] D. Akimov, S. Belogurov, A. Burenkov, D. Churakov, V. Kuzichev, V. Morgunov, G. Smirnov, V. Solovov, *Scintillation proportional Xe counter with WLS fiber readout for low-energy X-rays*, *Nucl. Instrum. Meth. A* **391** (1997) 468.

[96] D. Akimov, A. Burenkov, V. Kuzichev, V. Morgunov, V. Solovov, *Cylindrical Scintillation Proportional Counter with WliS Fiber Readout*, *IEEE Trans. Nucl. Sci.* **45** (1998) 497.

[97] A. Bolozdynya and R. DeVito, *Vibration-proof High-pressure Xenon Electroluminescence Detector*, *IEEE Trans. Nucl. Sci.* **77** (2004) 309.

[98] F. Resnati, U. Gendotti, R. Chandra, A. Curioni, G. Davatz, H. Friederich, A. Gendotti, L. Goeltl, R. Jebali, D. Murer, A. Rubbia, *Suitability of high-pressure xenon as scintillator for gamma ray spectroscopy*, *Nucl. Instrum. Meth. A* **715** (2013) 87.

[99] F.Resnati, *Pressurised xenon as scintillator for gamma spectroscopy*, *Light Detection in Noble Elements (LIDINE 2013)* Illinois (U.S.A.), *May 29-31* (2013)

[100] A. Goldschmidt, T. Miller, D. Nygren, J. Renner, D. Shuman, H. Spieler, and J. White, *High-Pressure Xenon Gas TPC for Neutrino-Less Double-Beta Decay in 136Xe: Progress Toward the Goal of 1% FWHM Energy Resolution*, *IEEE Nucl. Sci. Sym.* **23** (2011)1–4.

[101] G. Tepper, J. Losee, R. Palmer, *A cylindrical xenon ionization chamber for high resolution room temperature gamma radiation spectroscopy*, *Nucl. Inst. Meth. A* **413**, (1998) 467.

[102] T.H.V.T. Dias, P.J.B.M. Rachinhas, J.A.M. Lopes, F.P. Santos, L.M.N. Távora, C.A.N. Conde and A.D. Stauffer, *The transmission of photoelectrons emitted from CsI photocathodes into Xe, Ar, Ne and their mixtures: a Monte Carlo study of the dependence on E/N and incident VUV photon energy*, *J. Phys. D: Appl. Phys.* **37** (2004) 540.

[103] National Institute of Standards and Technology, Available in *http://www.nist.gov/*, Last access on 05-09-2014.

[104] Frostburg State University's Chemistry, *Gaseous Equation of State Calculator*, Available in http://antoine.frostburg.edu/chem/senese/javascript/realgas.shtml , Last access on 05-09-2014.

[105] J.A.M. Lopes and C.A.N. Conde, *VUV efficiency of chevron type CsI vacuum photocathodes*, *Journal Optics*, **24** (1993) 15.

[106] A.S. Tremsin, O.H.W. Siegmund, *The dependence of quantum efficiency of alkali halide photocathodes on the radiation incidence angle*, *Proc. SPIE* **3765** (1999) 441

[107] F.C. Rolo, *Study of the relative extraction efficiency of photocathodes in gaseous atmosphere*, MS. Thesis, Universidade de Coimbra, 2016.

[108] G. Fraser, *The characterisation of soft X-ray photocathodes in the wavelength band 1-300 Å*, *Nucl. Inst. Meth. Phys. Res.*, **206** (1983) 251.

[109] J. Marcoux, *Dielectric constants and indices of refraction of Xe, Kr and Ar*, *Canadian Journal of Physics* **48** (1970) 244.

[110] A. Thompson, D. Attwood, E. Gullikson, M. Howells, K.J. Kim, J. Kirz, J. Kortright, I. Lindau, Y. Liu, P. Pianetta, A. Robinson, J. Scofield, J. Underwood, G. Williams and H. Winick, *X-Ray Data Booklet*, *LBNL/PUB-490* **Rev. 3**, California 2009.

[111] T. Menezes, *Room temperature CdZnTe X- and γ-ray detectors for nuclear physics applications*, PhD thesis, University of Surrey, 2000.

[112] J.C.R. Mariquito, *Detector Gasos de Contilação Proporcional Multi-Grelhas para Radiação X de Alta Energia e Radiação Gama*, Dissertação de Mestrado, Universidade de Coimbra, 2009.

[113] ISPOPTICS LightPath Technology, Available in *http://www.ispoptics.com/articles/8/DESIGN%20OF%20PRESSURE%20WINDOW*, Last access on 05-09-2017.

[114] DuPont Teijin Films, *Mylar polyester film - Physical-Thermal Properties*, *Product Information*, Virginia 2003.

[115] M. Mimura, S. Kobayashi, N. Masuyama, M. Miyajima and N. Hasebe, *Average Numbers of Scintillation Photons and Electrons Produced by an Alpha Particle in High-Density Xenon Gas*, *Jpn. J. Appl. Phys.* **48** (2009) 076501.

[116] J.J. Gomez-Cadenas, *The NEXT Experiment*, **273-275** (2016) *Nucl. Part. Phys. Proc.* **8** 1732.

[117] M. Chefdeville and the Rd51 collaboration, *RD51, a world-wide collaboration for the development of Micro Pattern Gaseous Detectors*, *J. Phys.: Conf. Ser.* **309** (2011) 012017.

[118] The ALICE Collaboration et al, *The ALICE experiment at the CERN LHC*, 2008 *JINST* **3** S08002.

[119] NEXT collaboration, F. Granena et al., *A HPGXe TPC for neutrinoless double beta decay searches*, (2009) [arXiv:0907.4054].

[120] NEXT collaboration, V. Álvarez et al., *The NEXT-100 experiment for neutrinoless double beta decay searches (Conceptual Design Report)*, (2011) [arXiv:1106.3630].

[121] NEXT collaboration, J. Renner et al., *Ionization and scintillation of nuclear recoils in gaseous xenon*, *Nucl. Instr. and Meth. A* **793** (2015) 62 [arXiv:1409.2853v1].

[122] V.M. Gehman, A. Goldschmidt, D. Nygren, C.A.B. Oliveira and J. Renner, *A plan for directional dark matter sensitivity in high-pressure xenon detectors through the addition of wavelength shifting gaseous molecules*, 2013 *JINST* **8** C10001.

[123] D. Nygren, *Can the "intrinsic" energy resolution in xenon be surpassed?*, 2011 *J. Phys.: Conf. Ser.* **309** 012006.

[124] NEXT collaboration, V. Álvarez et al., *Characterization of a medium size Xe/TMA TPC instrumented with microbulk Micromegas, using low-energy γ–rays*, 2014 *JINST* **9** C04015 [arXiv:1311.3535v2].

[125] D.R. Nygren, *Columnar recombination: a tool for nuclear recoil directional sensitivity in a xenon-based direct detection WIMP search*, 2013 *J. Phys.: Conf. Ser.* **460** 012006.

[126] S. Cebrián et al., *Micromegas-TPC operation at high pressure in xenon-trimethylamine mixtures*, 2013 *JINST* **8** P01012 [arXiv:1210.3287v3]. (Erratum: 2015 *JINST* **10** E07001).

[127] NEXT collaboration, V. Álvarez et al., *Description and commissioning of NEXT-MM prototype: first results from operation in a Xenon-Trimethylamine gas mixture*, 2014 *JINST* **9** P03010 [arXiv:1311.3242v2].

[128] B. Dolgoshein, *Transition radiation detectors*, *Nucl. Instrum. Meth. A* **326** (1993) 434.

[129] A. Andronic, J.P. Wessels, *Transition radiation detectors*, *Nucl. Instrum. Meth. A* **666** (2012) 130.

[130] K. Aamodt *et al*, *The ALICE experiment at the CERN LHC*, *JINST* **3** (2008) S08002, p.70.

[131] A. Andronic, *The TRD of the CBM experiment*, *Nucl. Instrum. Meth. A* **563** (2006) 349.

[132] J.-F.Detoeuf *et al*, *The D0 transition radiation detector*, *Nucl. Instrum. Meth. A* **265** (1988) 157.

[133] H. Piekarz, *Transition radiation detector in the DO colliding beam experiment at Fermilab*, *Nucl. Instrum. Meth. A* **367** (1995) 220.

[134] K. Ackerstaff *et al*, *The HERMES spectrometer*, *Nucl. Instrum. Meth. A* **417** (1998) 230.

[135] E. O'Brien *et al*, *A Transition Radiation Detector which features accurate tracking and dE/dX particle identification*, *IEEE Trans. Nucl. Sci.* **40** (1993) 153.

[136] E. O'Brien, *Electron identification in the PHENIX experiment using a tracking TRD*, *Nucl. Phys. A* **566** (1993) 615C.

[137] P.N.B. Neves, *Studies on the mobility of monoatomic and dimer noble gas ions in their parent gases*, PhD thesis, Universidade de Coimbra, 2009.

[138] P.N.B. Neves, C.A.N. Conde and L.M.N. Távora, *Experimental measurement of the mobilities of atomic and dimer Ar, Kr and Xe ions in their parent gases*, *J. Chem. Phys.* **133** (2010) 124316.

[139] Y. Kalkan, M. Arslandok, A.F.V. Cortez, Y. Kaya, I. Tapan and R. Veenhof, *Cluster ions in gas-based detectors*, *JINST* **10**, (2015) P07004.

[140] A.F.V. Cortez, A.N.C. Garcia, P.N.B. Neves, F.P. Santos, F.I.G.M. Borges, J.A.S. Barata and C.A.N. Conde, *Experimental measurement of the mobility of ions originated in ethane in their parent gas*, *JINST* **8** (2013) P07013.

[141] A.F.V. Cortez, A.N.C. Garcia, P.N.B. Neves, F.P. Santos, F.I.G.M. Borges, J.A.S. Barata and C.A.N. Conde *Experimental measurements of the mobility of ethane ions in Ar-C_2H_6*, *JINST* **8** (2013) P12012.

[142] A.M.F. Trindade, A.F.V. Cortez, P.N.B. Neves, A.N.C. Garcia, J.Escada, F.P. Santos and C.A.N. Conde *Experimental study on ion mobility in Ar-CH_4 mixtures*, *JINST* **9** (2014) P06003.

[143] A.N.C. Garcia, P.N.B. Neves, A.M.F. Trindade, A.F.V. Cortez, F.P. Santos and C.A.N. Conde *Experimental measurements of the mobility of Xenon- Neon ions mixtures*, *JINST* **9** (2014) P07008.

[144] P.M.C.C. Encarnação, A.F.V. Cortez, M.G.A. Pinto, P.N.B. Neves, A.M.F. Trindade, J. Escada, F.P. Santos, F.I.G.M. Borges, J.A.S. Barata and C.A.N. Conde *Experimental Ion Mobility measurements in Ar-CO_2 mixtures*, *JINST* **10** (2015) P01010.

[145] P.M.C.C. Encarnação, A.F.V. Cortez, R. Veenhof, P.N.B. Neves, F.P. Santos, A.M.F. Trindade, F.I.G.M. Borges and C.A.N. Conde *Experimental Ion Mobility measurements in Ne-CO_2 and CO_2-N_2 mixtures*, *JINST* **11** (2016) P05005.

[146] A.F.V. Cortez, P.M.C.C. Encarnação, R. Veenhof, P.N.B. Neves, F.P. Santos, F.I.G.M. Borges and C.A.N. Conde *Experimental Ion Mobility measurements in Ne-N_2*, *JINST* **11** (2016) P11019.

[147] A.F.V. Cortez, M.A.G. Santos, R. Veenhof, R.N. Patra, P.N.B. Neves, F.P. Santos, F.I.G.M. Borges and C.A.N. Conde *Experimental ion mobility measurements in Xe-CO_2*, *JINST* **12** (2017) P06012.

[148] A.M.F. Trindade, J. Escada, P.M.C.C. Encarnação, A.F.V. Cortez, P.N.B. Neves, F.P. Santos, F.I.G.M. Borges and C.A.N. Conde *Experimental ion mobility measurements in xenon-trimethylamine*, *JINST* **12** (2017) P07007.

[149] J.M.C. Perdigoto, A.F.V. Cortez, R. Veenhof, P.N.B. Neves, F.P. Santos, F.I.G.M. Borges and C.A.N. Conde *Experimental ion mobility measurements in Xe-CH_4*, *JINST* **12** (2017) P09003.

[150] J.M.C. Perdigoto, A.F.V. Cortez, R. Veenhof, P.N.B. Neves, F.P. Santos, F.I.G.M. Borges and C.A.N. Conde *Experimental ion mobility measurements in Xe-C_2H_6*, *JINST* **12** (2017) P10011.

[151] A.F.V. Cortez, M.A. Kaja, J. Escada, M.A.G. Santos, R. Veenhof, P.N.B. Neves, F.P. Santos, F.I.G.M. Borges and C.A.N. Conde *Experimental ion mobility measurements in Xe-CF_4*, *JINST* **13** (2018) P04006.

[152] M.A.G. Santos, M.A. Kaja, A.F.V. Cortez, R. Veenhof, P.N.B. Neves, F.P. Santos, F.I.G.M. Borges and C.A.N. Conde *Experimental ion mobility measurements for the LCTPC Collaboration - Ar-CF_4*, *JINST* **13** (2018) P04011.

[153] G. A. Eiceman, Z. Karpas, and H. H. J. Hill, *Ion Mobility Spectrometry*, CRC Press - Taylor & Francis Group, third ed., 2014.

[154] E.W. McDaniel, J.B.A. Mitchell, M.E. Rudd, *Atomic collisions – heavy particle projectiles*, Wiley, New York, U.S.A. (1993).

[155] National Institute of Standards and Technology, Gaithersburg, Maryland, 20899-8320, web address: http://physics.nist.gov/cuu/Constants/Table/allascii.txt.

[156] P. Langevin, *Une formule fondamentale de théorie cinetique*, *Annal. Chimie Physique* **5** (1905) 245.

[157] E.A. Mason, E.W. McDaniel, *Transport Properties of Ions in Gases*, John Wiley and Sons, Inc., New York 1988.

[158] J.O. Hirschfelder, C.F. Curtis, and R.B. Bird, *Molecular Theory of Gases and Liquids*, John Wiley and Sons, Inc., New York 1954, p.950 Fundamental information on molecular polarizabilities.

[159] R.R. Teachout and R.T. Pack, *The static dipole polarizabilities of all the neutral atoms in their ground states*, *Atom. Data Nucl. Data tables* **3** (1971) 195.

[160] B.K. Chatterjee, R. Johnsen, *An estimating formula for ion-atom association rates in gases*, *J. Chem.Phys.* **93** (1990) 5681.

[161] A.A. Maryott and F. Buckley, *Table of dielectric constants and electric dipole moments of substances in the gaseous state*, *National Bureau of Standards*, Circular **573** (1953), Washington, DC.

[162] A.B. Tipton, A.P. Deam and J.E. Boggs, *Atomic Polarization of Sulfur Hexafluoride and Carbon Tetrafluoride*, *J.Chem. Phys.* **40** (1964) 1144

[163] A. Blanc, *Recherches sur le mobilités des ions dans les gaz*, *J. Phys. Theor. Appl.* **7**, (1908) 825.

[164] M.F. Penning, *Über Ionisation durch metastabile Atome*, *Naturwissenschaften* **40** (1927) 818.

[165] S.L. Lin and E.A. Mason, *Influence of resonance charge transfer on ion mobility*, *Journal of Physics B: Atomic, Molecular and Optical Physics* **12**, (1978) 783.

[166] T. Holstein, *Mobilities of positive ions in their parent gases*, *The Journal of Chemical Physics* **56**, (1952) 832.

[167] R. Rejoub, B.G. Lindsay, and R.F. Stebblings, *Determination of the absolute partial and total cross sections for electron-impact ionization of the rare gases*, *Phys. Rev. A* **65**, (2002) 042713.

[168] B. Gstir, S. Denifl, G. Hanel, M. Rummele, T. Fiegele, P. Cicman, M. Stano, S. Matejcik, P. Scheier, K. Becker, A. Stamatovic and T. D. Mark, *Electron impact multiple ionization of neon, argon and xenon atoms close to threshold: appearance energies and Wannier exponents*, *J. Phys. B: At. Mol. Opt. Phys.* **35** (2002) 2993.

[169] A.P. Vitols and H.J. Oskam, *Reaction rate constant for* $Xe^+ + 2Xe \rightarrow Xe_2^+ + Xe$, *Phys. Rev. A* **8** (1973) 1860.

[170] K. Hiraoka and T. Mori, *Formation and stabilities of cluster ions* Ar_n^+, *J. Chem. Phys.* **90** (1989) 7143.

[171] A.N.C. Garcia, P.N.B. Neves, A.M.F. Trindade, F.P. Santos and C.A.N. Conde, *A new contribution to the experimental measurement of the* N_4^+ *and* $N_2{}^+$ *ion mobility in N2 at 298K*, *JINST* **7** (2012) P02012.

[172] A. Bekstein, *Données de base des ions polyatomiques dans les gaz d'echappment: modélisation et validation experimentale*, Ph.D. Thesis, University of Toulouse, 2009.

[173] W. Lindinger et al., *Reactions of N_4^+ with O_2, CO_2, H_2, and D_2 and mobilities of N_4^+ in nitrogen*, *J. Chem. Phys.* **68** (1978) 2607.

[174] P.A.M. van Koppen et al., *Ion-molecule association reactions: A study of the temperature dependence of the reaction $N_2^+ + N_2 + M \rightarrow N_4^+ + M = N_2$, Ne, and He: Experiment and theory*, *J. Chem.Phys.* **81** (1984) 288.

[175] H.C. Straub, P. Renault, B.G. Lindsay, K.A. Smith and R.F. Stebbings, *Absolute partial cross sections for electron-impact ionization of H_2, N_2 and O_2 from threshold to 1000 eV*, *Phys. Rev. A* **54**, (1996) 2146.

[176] R.K. Asundi et al., *Studies of N_4^+ and N_3^+ ion formation in nitrogen using high-pressure mass spectrometry*, *J. Chem. Phys.* **47** (1967) 1584.

[177] A.M.F. Trindade, J. Escada, P.N.B. Neves, T.H.V.T. Dias, J.A.S. Barata, F.P. Santos and C.A.N. Conde, *Experimental measurements of the mobility of methane ions in methane*, 2012 *JINST* **7** P06010.

[178] H.C. Straub, D. Lin, B.G. Lindsay, K.A. Smith, and R.F. Stebbings, *Absolute partial cross sections for electron-impact ionization of CH_4 from threshold to 1000 eV*, *J. Chem. Phys* **106** (1997) 4430.

[179] M. Stano, Š. Matejčík, J.D. Skalný and T.D. Märk, *Electron impact ionization of CH_4: ionization energies and temperature effects*, *J. Phys. B: At. Mol. Opt. Phys.* **36** (2003) 261.

[180] W.T. Huntress Jr., *Laboratory studies of bimolecular reactions of positive ions in interstellar clouds, in comets, and in planetary atmospheres of reducing composition*, *Astrophys. J. Suppl.* **33** (1977) 495.

[181] Cechan Tian and C.R. Vidal, *Electron impact dissociative ionization of ethane: Cross sections, appearance potentials, and dissociation pathways*, *J. Chem. Phys* **109(5)** (1998) 1704.

[182] E. Vašeková, M. Stano, Š. Matejčík, J.D. Skalný, P. Mach, J. Urban, T.D. Märk, *Electron impact ionization of C_2H_6: ionization energies and temperature effects*, *International Journal of Mass Spectrometry* **235** (2004) 155.

[183] K. Hiraoka and P. Kebarle, *Ion molecule reactions in ethane. Thermochemistry and structures of the intermediate complexes: $C_4H_{11}^+$* and $C_4H_{10}^+$ formed in the reactions of $C_2H_5^+$ and $C_2H_4^+$ with C_2H_6, *Can J. Chem.* **58** (1980) 2262.

[184] S.K. Searles, L. Wayne Sieck and P. Ausloos, *Reactions of $C_2H_6^+$: Formation of the $(C_2H_6)_2^+$ Ion*, *J. Chem.Phys.* **53** (1970) 849.

[185] G. Schultz, G. Charpak anf F.Sauli, *Mobilities of positive ions in some gas mixtures used in proportional and drift chambers*, *Revue de Physique Appliqueé* **22**, 67 (1977).

[186] M. Saporoschenko, *Drift Velocities of O_2^+, CO_2^+, and CO_4^+*, *Phys. Rev. A* **82**, (1972) 1044.

[187] P.A. Coxon and J.L. Moruzzi, *Positive Ion Mobilities in Carbon Dioxide*, *J. Physique* **40**, Colloq. C7 (1979) 117.

[188] C. Tian and C.R. Vidal, *Electron impact dissociative ionization of CO_2: Measurements with a focusing time-of-flight mass spectrometer*,*J. Chem. Phys* **108(5)**,927 (1998).

[189] N. Bussieres, P. Marmet, *Ionization and dissociative ionization of CO_2 by electron impact*, *Can. J. Phys.* **55**, (1977) 1889.

[190] V.G. Anicich, *Evaluated Bimolecular Gas Phase Kinetics of Positive Ions for Use in Modeling Planetary Atmospheres, Cometary Comae, and Insterstellar Clouds*, *J. Phys. Chem.* **22**, 6 (1993).

[191] A.B. Rashit and P. Werneck, *Rate Coefficients and Product Ion Distributions for Reactions of CO_2.CO_2^+ Ions with Neutral Molecues at 300K*, *Z. Naturforsch* **34a**, (1979) 1410.

[192] I. Torres, R. Martínez and F. Castaño, *Electron-impact dissociative ionization of fluormethanes CHF_3 and CF_4*, *J. Phys. B: At. Mol. Opt. Phys.* **35** (2002) 2423.

[193] T. Fiegele, G. Hanel, I. Torres, M. Lezius and T.D. Märk, *Threshold electron impact ionization of carbon tetrafluoride, trifluoromethane, methane and propane*, *J. Phys. B: At. Mol. Opt. Phys.* **33** (2000) 4263.

[194] E. Basurto and J. de Urquijo, *Mobility of CF_3^+ in CF_4, CHF_2^+ in CHF_3 and C^+ in Ar*, *J. Appl. Phys.* **91** (2002) 36.

[195] V. Stojanovic, Z. Raspopovic, J. de Urquijo and Z.Lj. Petrovic, *Mobility of positive ions in CF_4*, *J. Phys: Conf. Ser.* **514** (2014) 012059.

[196] National Institute of Standards and Technology, Gaithersburg, Maryland, 20899-8320, web address: http://webbook.nist.gov/cgi/cbook.cgi?ID=C75730&Mask=1EFF

[197] J.T. Moseley, R.M. Snuggs, D.W. Martin and E.W. McDaniel, *Mobilities, Diffusion Coefficients, and Reaction Rates of Mass-Indentified Nitrogen Ions in Nitrogen*, *Phys. Rev.* **178** (1969) 240.

[198] P.N.B. Neves, C.A.N. Conde and L.M.N. Távora, *The $X^+ + 2X \rightarrow X_2^+ + X$ reaction rate constant for Ar, Kr and Xe, at 300 K*, *Nucl. Instrum. Meth. A* **619** (2010) 75.

[199] H. von Köding, F.A. Pinkse and N.M.M. Nibbering, *Rate Coefficients of Single and Double Electron Transfer from Xe to Xe^{2+} at Low Collision Energies as Determined by Use of Fourier Transform Ion Cyclotron Resonance Mass Spectrometry* , *Physica Scripta.* **T59** (1995) 418.

[200] Y. Itikawa, *Cross Sections for Electron Collisions with Carbon Dioxide*, *J.Phys. Chem. Ref. Data* **31(3)**, (2002) 749.

[201] M. Durop-Fergunson, H. Bohringer, D.W. Fahey, E.E. Fergunson, *Enhancement of charge transfer reaction rate constants by vibrational excitation at kinetic energies below 1 eV*, *J. Chem. Phys.* **79**, (1983) 265.

[202] K. Giles, N.G. Adams and D. Smith, *Reactions of Kr^+, Kr_2^+, Xe^+ and Xe_2^+ ions with several molecular gases at 300 K*, *J. Phys. B: At. Mol. Opt. Phys.* **22** (1989), 873.

[203] H.W. Ellis, R.Y. Pai, E.W. McDaniel, L.A. Viehland and E.A. Mason, *Transport Properties of Gaseous Ions over a Wide Energy Range*, *At. Data Nucl. Data tables* **60**, (1995) 37.

[204] G.C. Smith and E.Mathieson, *Gain Reduction Due to Space Charge at High Counting Rates in Multiwire Proportional Chambers*, *IEEE Trans. Nucl. Sci.* **34** (1987) 410.

[205] A.M.F. Trindade, J. Escada, P.N.B. Neves, T.H.V.T. Dias, J.A.S. Barata, F.P. Santos and C.A.N. Conde, *Experimental measurements of the mobility of methane ions in methane*, *JINST* **7** (2012) P06010.

[206] J. Escada, T.H.V.T. Dias, F.P. Santos, P.J.B.M. Rachinhas, C.A.N. Conde and A.D. Stauffer, *A Monte Carlo study of the fluctuations in Xe electroluminescence yield: pure Xe vs Xe doped with CH_4 or CF_4 and planar vs cylindrical geometries*, *JINST* **6** (2011) P08006.

[207] E.R. Fisher and P.B. Armentrout, *The Appearance Energy of CF_3^+ from CF_4: Ion/Molecule Reactions Related to the Thermochemistry of CF_3^+*, *Int. J. Mass Spectrom. Ion Proc.* **101** (1990) R1-R6.

[208] M. Tsuji, H. Kouno, K. Matsumura, T. Funatsu, Y. Nishimura et al., *Dissociative charge transfer reactions of Ar+ with aliphatic hydrocarbons at thermal energy*, *J. Chem. Phys.* **98**, 2011 (1993).

[209] K. Hiraoka and P. Kebarle, *Temperature dependence of bimolecular ion molecule reactions. The reaction $C_2H_5^+ + CH_4 = C_3H_7^+ + H_2$*, *Can. J. Chem.* **63**, (1975) 394.

[210] Shangai Stal Precision Stainless Steel Co., Available in *http://www.stal.com.cn/pdffile/316316l317317l.pdf*, Last access on 05-09-2014.

[211] D.C. Faircloth, *Technological Aspects: High Voltage*, *CERN Yellow Report* **CERN-2013-007** (2012) 381.

[212] D.G. Simons, G.W. Fraser, P.A.J. De Korte, J.F. Pearson, L. De Jong, *UV and XUV quantum detection efficiencies of CsI-coated microchannel plates*, *Nucl. Instrum. Meth. A* **261** (1987) 579.

[213] V. Dangendorf, A. Breskin, R. Chechik, H. Schmidt-Böcking, *A Gas-Filled UV-Photon Detector with CsI Photocathode for the Detection of Xe Light*, *Nucl. Instrum. Meth. A* **289** (1990) 322.

[214] P. Krizan, M. Cindro, V. Cindro, S. Korpar, G. Omahen, A. Stanovnik, M. Staric, *Measurements of the quantum efficiency of CsI photocathodes in a multiwire proportional chamber*, *Nucl. Instrum. Meth. A* **364** (1995) 243.

[215] J. Almeida, A. Braem, A. Breskin, A. Buzulutskov, R. Chechik, S. Cohen, C. Coluzza, E. Conforto, G. Margaritondo, E. Nappi, G. Paic, F. Piuz, T. Dell'Orto, T. Scognetti, S. Sgobba and B.P. Tonner, *Microanalysis surface studies and photoemission properties of CsI photocathodes*, *Nucl. Instrum. Meth. A* **367** (1995) 337.

[216] D.F. Anderson, S. Kwan, B. Hoeneisen and V. Peskov, *Technical Memo on New Results on Csl Photocathodes:Enhancement and Aging*, *FNAL TM-1753 Fermi National Accelerator Laboratory* (1991).